UNIVERSITY OF SOUTHAMPTON

FACULTY OF ENGINEERING AND THE ENVIRONMENT

Institute of Sound and Vibration Research

Target Discrimination in Bubbly Water

by

Gim Hwa Chua

Thesis for the degree of Doctor of Philosophy

September 2012

UNIVERSITY OF SOUTHAMPTON

ABSTRACT

FACULTY OF ENGINEERING AND THE ENVIRONMENT

Institute of Sound and Vibration Research

Doctor of Philosophy

TARGET DISCRIMINATION IN BUBBLY WATER

by Gim Hwa Chua

A man-made sonar that can operate in bubbly water is relevant: decades of active sonar experience built up for deep water applications are insufficient for shallow water operations required of a changed maritime security landscape. In many instances, military-trained dolphins represent the only viable sonar option, and this study adds to the limited number of solutions that could in future be developed into standard military tools. A series of laboratory tests is described which examines the ideas put forward. The necessary sonar simulation model (based on current state-of-the-art techniques) is also developed. The efficacy of the Twin Inverted Pulse Sonar (TWIPS), is first demonstrated with a linear frequency modulated (LFM) waveform. While TWIPS arose in response to a video showing dolphins generating bubble nets when hunting, existing evidence of TWIPS-like pulses produced by odontocetes suggests their amplitudes appear too low for TWIPS. Instead, the review of the echolocation behaviour of other species of odontocetes yields several results and techniques, which can possibly enhance sonar performance in bubbly water. Parameters like chirp structure and pulse duration are found to be important because of the nonlinear time-dependent characteristics of bubbles. A two-pulse technique, the Biased Pulse Summation Sonar (BiaPSS), which arose from the review, is extensively tested in both simulations and measurements here. Like TWIPS, BiaPSS exhibits the primary advantage of distinguishing a solid target (linear scatterer) from the bubble cloud (nonlinear scatterers) by exploiting nonlinearities with a secondary advantage of outperforming standard sonar processing in target detection. While this does not conclusively prove that dolphins use such nonlinear processing, it demonstrates that a man-made system can classify and detect targets in bubbly water using dolphin-like sonar pulses, raising intriguing possibilities for dolphin sonar when they make bubble nets

Table of Content

List of Figures

List of Tables

List of Publications

Journal Papers

- Leighton, T.G., G.H. Chua, and P.R. White. *Do dolphins benefit from nonlinear mathematics when processing their sonar returns?* Proceedings of the Royal Society A, 2012, doi: 10.1098/rspa.2012.0247

- Chua, G.H., P.R. White, and T.G. Leighton. *Use of clicks resembling those of the Atlantic bottlenose dolphin (Tursiops truncatus) to improve target discrimination in bubbly water with Biased Pulse Summation Sonar (BiaPSS).* IET Radar Sonar Navig., 2012, **6**(6), p.510-515.

- Finfer, D.C., P.R. White, G.H. Chua, and T.G. Leighton. *Review of the occurrence of multiple pulse echolocation clicks in recordings from small odontocetes.* IET Radar Sonar Navig., 2012, **6**(6), p.545-555.

- Leighton, T.G., D.C. Finfer, G.H. Chua, P.R. White, and J. Dix. *Clutter suppression and classification using Twin Inverted Pulse Sonar in ship wakes.* J. Acoust. Soc. Am., 2011. **130**(5), p. 3431-3437.

- Leighton, T.G., D.C. Finfer, P.R. White, G.H. Chua, and J. Dix. *Clutter suppression and classification using Twin Inverted Pulse Sonar (TWIPS).* Proceedings of the Royal Society A, 2010. **466**: p. 3453-3478.

Conference Papers

- Chua, G.H., T.G. Leighton and P.R. White. *Use of clicks resembling those of the Atlantic bottlenose dolphin (Tursiops truncatus) with Biased Pulse Summation Sonar (BiaPSS) to improve target discrimination in bubbly water*, Proceedings of 11th European Conference on Underwater Acoustics (ECUA 2012), Heriot-Watt University, Edinburgh, UK, 2-6 July 2012, p. 1903-1908.

- Leighton, T.G., D.C. Finfer, P.R. White, G.H. Chua, and J. Dix. *Wake penetrating sonar*, Proceedings of 1st EAA Congress on Sound and Vibration (EuroRegio 2010), Ljubljana, Slovenia, 15-18 September 2010, Paper 163, 8pp.

Poster

- Chua, G.H., T.G. Leighton, and P.R. White. *Poster: Target discrimination in bubbly water using dolphin-like signals*. Multidisciplinary Research Showcase 2011, University of Southampton.

Commendations

- 11th European Conference for Underwater Acoustics (ECUA 2012), Heriot-Watt University, Edinburgh, UK, 2 -6 July 2012.
    - Student prize for outstanding presentation

- University of Southampton Multidisciplinary Postgraduate Research Showcase, University of Southampton, 31 March 2011.
    - Gold Award

Declaration of Authorship

I, Gim Hwa Chua

declare that the thesis entitled

Target Discrimination in Bubbly Water

and the work presented in the thesis are both my own, and have been generated by me as the result of my own original research. I confirm that:

- this work was done wholly or mainly while in candidature for a research degree at this University;
- where any part of this thesis has previously been submitted for a degree or any other qualification at this University or any other institution, this has been clearly stated;
- where I have consulted the published work of others, this is always clearly attributed;
- where I have quoted from the work of others, the source is always given. With the exception of such quotations, this thesis is entirely my own work;
- I have acknowledged all main sources of help;
- where the thesis is based on work done by myself jointly with others, I have made clear exactly what was done by others and what I have contributed myself;
- parts of this work have been published as:

    - Leighton, T.G., G.H. Chua, and P.R. White. *Do dolphins benefit from nonlinear mathematics when processing their sonar returns?* Proceedings of the Royal Society A, 2012, doi: 10.1098/rspa.2012.0247

    - Chua, G.H., P.R. White, and T.G. Leighton. *Use of clicks resembling those of the Atlantic bottlenose dolphin (Tursiops truncatus) to improve target discrimination in bubbly water with Biased Pulse Summation Sonar (BiaPSS).* IET Radar Sonar Navig., 2012, **6**(6). p.510-515.

    - Finfer, D.C., P.R. White, G.H. Chua, and T.G. Leighton. *Review of the occurrence of multiple pulse echolocation clicks in recordings from small odontocetes.* IET Radar Sonar Navig., 2012. **6**(6), p.545-555.

- Leighton, T.G., D.C. Finfer, P.R. White, G.H. Chua, and J. Dix. *Clutter suppression and classification using Twin Inverted Pulse Sonar (TWIPS)*. Proceedings of the Royal Society A, 2010. **466**: p. 3453-3478

Signed: …………………………………………………………………………..

Date:……………………………………………………………………………….

Acknowledgements

First and foremost, I will like to offer my heartfelt gratitude to my supervisor, Prof. Timothy Leighton, for his guidance throughout my time in Institute of Sound Vibration Research (ISVR). He sets an example of a world-class researcher for his rigor and passion on research. His perpetual energy and enthusiasm in acoustics have been the source of constant motivation for me. He has also been extremely generous with his time and insights without which my PhD would not have been so enriching. I will also like to attribute my understanding of this work to his encouragement and effort. One simply could not wish for a better supervisor.

I am also privileged to have the advice of Prof. Paul White. His insights to sonar systems and theory of signal processing are second to none. He has been a tremendous resource in discussions related to these topics and has always encouraged my work and kept me focused on the important issues.

I am grateful to have Prof. Phillip Joseph as my review board member. His probing questions and insightful comments during review meetings have helped to improve my work. For the sonar work, I have been aided in the collection of the experimental data by Mr. Ping-Chang Hsueh and Mr. Bo Yuan. Dr. Justin Dix and Dr. Mark Vardy deserve special thank for the use of their transducers. The smooth running of the A.B. Woods Laboratory would not be possible without the technical support of Mr. Nigel Davies, Mr. Antony Wood and Mr. Andy Westerman.

In my daily work, I have been blessed with a friendly and cheerful group of fellow students who have provided the intellectual support when needed, and filled my time in ISVR with fun and laughters.

This work was carried out under a full-time PhD scholarship funded by DSO National Laboratories, Singapore and I express my gratitude for their generous support. I am also indebted to Dr. Yew Wing Chan and Dr. Joo Thiam Goh for their encouragements and advice, without which I will not have embarked on this journey.

Finally, I most want to thank my wife, Hang Ching, for her love, sacrifice and kind indulgence and credit our children, Xin En and Zhi En, for inspiring and amazing me every day.

List of Symbols

A	Amplitude of the particular integral describing steady-state displacement response of a general oscillator (may be complex)
A_1, A_2, and A_3	Empirical constants associated with Eq (3.7)
b	Resistive dissipation constant
b_c	Variable as defined in Eq. (3.3)
b_{RP}	Resistive dissipation constant in the radius-pressure frame
b_{VP}	Resistive dissipation constant in the volume-pressure frame
b_{RF}^{rad}	Radiation dissipation constant in the radius-force frame
b_{RP}^{rad}	Radiation dissipation constant in the radius-pressure frame
b_{RP}^{vis}	Viscous dissipation constant in the radius-pressure frame
b_{VF}^{rad}	Radiation dissipation constant in the volume-force frame
b_{VP}^{rad}	Radiation dissipation constant in the volume-pressure frame
B	Frequency bandwidth of a pulse
B_1, B_2, and B_3	Empirical constants associated with Eq (3.7)
c	Speed of sound in the liquid
c_m	Speed of sound in a mixture
$c_1(t), c_2(t)$	Pulses of finite duration
d	Damping constant
d_{rad}	Radiation damping constant
d_{th}	Thermal damping constant

d_{vis}	Viscous damping constant
d_{tot}	Total damping constant: $d_{tot} = d_{rad} + d_{th} + d_{vis}$
D	Diameter of the tranducer
D_g	Thermal diffusivity of a gas
E_{cloud}	The "energy" associated with the backscatters from the cloud
E_{target}	The "energy" associated with the backscatters from the target
f_1, f_2	Empirical constant associated with Eq (3.7)
F or $F(t)$	Force
F_r	Restoring force pointing towards the centre of a bubble
F_s	Force exerted to a ‘spring’
F_A	Amplitude of driving force (may be complex)
F_o	Amplitude of general driving force of an oscillator
G	An amplitude factor
$h(t)$	Impulse response of the system
$h_{lin}(t)$	Kernel or impulse function incorporating the linear effects of propagation and scattering from the object
$h_Q(...,...,...)$	The Qth-order Volterra kernel
$H_{lin}[\ ]$	Operator that computes, from its argument, the signal received from the linear scatterer
$H_Q[\ ]$	The Qth-order Volterra functional
i	$i^2 = -1$
k	Wavenumber = $2\pi/\lambda$
K	Spring constant

K_{RF}	Stiffness constant in the radius-force frame
K_{RP}	Stiffness constant in the radius-pressure frame
K_{VP}	Stiffness of a bubble for volume-pressure frame
l_D	Width of thermal boundary layer
m	Inertia of a general oscillator
m_{RF}^{rad}	Radiation mass in the radius-force frame
m_{RP}^{rad}	Radiation mass in the radius-pressure frame
m_{VP}^{rad}	Radiation mass in the volume-pressure frame
N	Near-field length of transducer
n	Number of bubbles per cubic metre in a population of identical bubbles
$p(t)$	Pressure signal
p	Reduced form of $p(t)$
$p_g(t)$	Instantaneous gas pressure within a pulsating bubble
p_g	Reduced form of $p_g(t)$
Δp_g	Elemental change in instantaneous gas pressure within a pulsating bubble
$p_i(t)$	Instantaneous total pressure within a pulsating bubble
p_i	Reduced form of $p_i(t)$
Δp_i	Elemental change in total pressure within a pulsating bubble
$p_{i,e}$	Pressure within the bubble at equilibrium
$p_L(t)$	Liquid pressure just outside a bubble or cavity, at the wall
$p_{lin}(t)$	Component of the received echo scattered by a linear scatterer

$p_{nl}(t)$	Component of the received echo scattered by a nonlinear scatterer
$p_{Rx}(t)$	Received echo of a scatterer
p_v	Vapour pressure within the bubble
p_∞	Pressure in the liquid far from the bubble
p_o	Hydrostatic liquid pressure outside the bubble
$p_-(t)$	Difference of delayed versions of the received signal
$p_{m-}(t)$	Difference of delayed versions of the received signal after applying a matched filter whose centre frequency is *m* times the centre frequency of the driving frequency
$p_+(t)$	Sum of delayed versions of the received signal
$p_{m+}(t)$	Sum of delayed versions of the received signal after applying a matched filter whose centre frequency is *m* times the centre frequency of the driving frequency
P_A	Amplitude of the driving pressure field
P_d	Probability of detection or true positive
P_{fa}	Probability of false alarm or false positive
$P_{Rx}(t)$	The processed version of $p_{Rx}(t)$
$P_-(t)$	The processed version of $p_-(t)$
$P_{m-}(t)$	The processed version of $p_{m-}(t)$
$P_+(t)$	The processed version of $p_+(t)$
$P_{m+}(t)$	The processed version of $p_{m+}(t)$
r	The radial coordinate in the spherical frame, with origin at centre of a bubble (if present)
$\dot{r}$	First temporal derivative of r, the velocity term

$\ddot{r}$	Second temporal derivative of r, the acceleration term
dr	Thickness of a given shell of liquid
$R(t)$	Radius of curvature of liquid/ gas interface (e.g. radius of a spherical bubble)
R	Reduced form of $R(t)$
ΔR	Elemental change in radius
$\dot{R}(t)$	Velocity term of a spherical bubble
$\dot{R}$	Reduced form of $\dot{R}(t)$
$\ddot{R}(t)$	Acceleration term of a spherical bubble
$\ddot{R}$	Reduced form of $\ddot{R}(t)$
$R_{\max}$	The maximum radius reached by a bubble during expansion, prior to the collapse phase
$\dot{R}_{\max}$	The maximum velocity reached by a bubble, which is at equilibrium position
R_r	The radius of a bubble that would be in pulsation resonance with the incident sound field
R_o	The radius of a rigid sphere or equilibrium radius of a spherical bubble
$R_\varepsilon(t)$	Displacement of bubble radius from the equilibrium, such that $R(t) = R_o + R_\varepsilon(t)$
R_ε	Reduced form of $R_\varepsilon(t)$
$s_0, s_1, s_2, \ldots$	Coefficients
t	Time
Δt	A finite increment of time or a delay in time
T	Duration of a pulse
V	Volume

ΔV	Elemental change in volume within the gas bubble, $V = V_o + \Delta V$
V_o	Equilibrium volume of a pulsating bubble
x	A distance coordinate in the Cartesian frame
y	A distance coordinate in the Cartesian frame
$y_k(t)$	Response of the system to an input pulse, $c_k(t)$, where k=1 and 2
$Y_k(t)$	The output of the matched filter for $y_k(t)$ with k=1 and 2
¥(t)	The general response of a bubble to an acoustic field
Z	Complex component of $-c/c_\mathrm{m}$
ﬁ(t)	The general driving force of an oscillator
α_1, α_2	Variables for matched filters
β	A resistive constant leading to damping, equal to $b/2m$
γ	Ratio of specific heat of a gas at constant pressure to that at constant volume
$\frac{\partial a}{\partial b}$	‘partial differential of a with respect to b’
Δ	‘a finite increment of …’ (such that $\Delta a \equiv$’a finite increment of a’)
Δ_d	Time interval between two successive pulses in a pulse pair
ε	Displacement in an oscillatory system
$\dot{\varepsilon}$	Velocity in an oscillatory system
$\ddot{\varepsilon}$	Acceleration in an oscillatory system
ε_o	General displacement amplitude in an oscillatory system
π	pi ≈3.14159
ϑ	A phase factor

ϑ_1, ϑ_2	Phase of oscillation of a bubble relative to driving sound field
ϕ_K	Kinetic energy of an oscillator system (specifically of the fluid around a freely pulsating bubble)
Φ	Variable as defined in Eq. (3.4)
κ	Polytropic index
σ	Surface tension of a liquid
$\sigma_{x'}$	Standard deviation of the spatial density of the bubble cloud along the x'-axis
$\sigma_{y'}$	Standard deviation of the spatial density of the bubble cloud along the y'-axis
$\Gamma(t), \Gamma_1(t), \Gamma_2(t)$	Pulses of finite length
$\Gamma(t-\Delta_d)$	Pulse, $\Gamma(t)$, delayed by a time interval of Δ_d
λ	Wavelength
ν	Linear frequency
ν_o	Linear resonance frequency for pulsating bubble
η	Shear viscosity
ρ	Density (generally of a fluid, specifically of the fluid surrounding a bubble)
ρ_o	Equilibrium fluid density
ω	Circular frequency = $2\pi\nu$
ω_d	Oscillatory frequency of a damped system: $\omega_d = \sqrt{\omega_o^2 - \beta^2}$
ω_o	Resonance circular frequency of an oscillator (specifically that of the breathing mode of a bubble)
$\psi_1(t)$, $\psi_2(t)$	Filters
χ	Variable as defined in Eq. (3.5)

List of Abbreviations

AM	Amplitude-modulation
AP	Alternate Pulse
BiaPSS	Biased Pulse Summation Sonar
HF	High frequency
IED	Improvised explosive device
ISVR	Institute of Sound Vibration Research
LF	Low frequency
LFM	Linear frequency modulated
LPM	Linear period modulated
MCM	Mine countermeasures
PI	Pulse inversion
ROC	Receiver operating characteristics
SPL	Sound pressure level
SNR	Signal noise ratio
TR	Time Reversed
TS	Target strength
TWIPS	Twin Inverted Pulse Sonar
UCAs	Ultrasonic contrast agents

Chapter 1. Introduction

The performance of active sonar for target detection and classification has always been limited in a bubble-filled environment by the clutter and excess attenuation caused by bubbles. A sonar designed to minimize these two effects will improve its target detection and classification abilities in such an environment.

From observing behaviour of dolphins in coastal waters, Leighton [1] first proposed the use of the Twin Inverted Pulse Sonar (TWIPS) [2-6] to exploit the nonlinear relationship of bubbles with a sound field to enhance sonar performance in bubbly water. TWIPS is a two-pulse technique, which makes use of two identical pulses, one of opposite polarity to the other. TWIPS has received extensive testing through simulation, tank and field experiments using a Gaussian-modulated eight-cycle 6 kHz sine wave [3, 6], which indicate that it holds possibilities for improved detection and classification of objects, and clutter reduction, by enhancing and suppressing linear and nonlinear components of the echoes. The possibility of applying the principle of TWIPS for radar applications was also suggested by Leighton *et al.* [3, 6].

Another possibility for enhancing sonar performance in bubbly waters is by exploiting the nonlinear and time-dependent characteristics of the bubbles, for example, through the use of very short duration signals [7]. By manipulating the duration of the driving pulse, the bubbles may not reach steady-state oscillations, and prior to reaching steady-state oscillation, the acoustic scattering will be greatly reduced. In nature, the use of relatively short duration and broadband signals by some species of dolphins and porpoises, coupled with their remarkable ability to operate in coastal waters with some even generating bubble ‘nets’ when hunting, raises the possibility that by studying their pulse characteristics, sonar performance in a bubble-filled environment can be enhanced.

1.1. Background

Sea mines has played an important role in naval warfare in many past conflicts. One of the earliest accounts of successful mining came in the 19th century from the American Civil War. During the Civil War, the Confederate forces at the Battle of Mobile Bay, unable to meet the Union fleet on equal terms, used mines as a defensive barrier [8].

Since then, sea mines have caused major damage to naval forces, slowed or stopped naval actions and commercial shipping, and forced changes to strategic and tactical plans. A wide range of naval mines are easily available in global marketplace because of the vast proliferation of the number of countries using, producing and exporting mines. The number of types of mine available in the commercial market is in the order of hundreds, with an increasing level of sophistication in both how the mines are triggered and how they avoid detection from acoustic sensors [8, 9]. The low cost and wide availability of modern sea mines means that their threat to shipping and naval force operations is growing rapidly.

Naval mines represent major threats to naval operations such as landings, and protection of harbours and shipping lanes for military, commercial and aid crafts. They are capable of major disruptions to naval operations while causing significant amount of damage to ships (Table 1.1). In fact, a majority of documented damage suffered by naval ships has been caused by naval mines. Using the US navy as an example, it has been reported that most of the damage suffered by the US naval forces in the past fifty years was from mines. Fourteen incidents involving mines were recorded, while missile, torpedo, or air attack accounted for a total of four [8, 9].

Ship	Cost of ship repair	Cost of the mine inflicting the damage
USS Samuel B. Roberts	US$ 96 millions	US$ 1500
USS Tripoli	US$ 3.5 millions	US$ 1500
USS Princeton	US$ 24 millions	US$ 10 000

Table 1.1. Comparison of ship repair as a result of mine attack in recent years [9].

The limitations of active sonar in shallow water have also become of paramount importance in the last couple of decades. The demise of the sophisticated Soviet blue-water, air and undersea threats after the Cold War, also means that the threat of an air, missile and submarine attack is reduced. Increasingly, the threat is now posed by a much smaller number of countries and non-state forces with the use of underwater mines. Thus, the need has changed from deep sea battles to a requirement to manoeuvre and project power to the world’s littorals. The decades of sonar experience built up for deep water applications during the Cold War [10] are now insufficient to counter the threat posed by naval mines to naval operations such as mine detection, landings, and the protection of harbours and shipping lanes for military, commercial and aid crafts.

The mine threat in littoral water is extensive and varied [11]. Very large numbers of anti-invasion craft mines are laid in shallow water regions. These include whip mines, which may be bottom mounted or tethered to an anchor so as to encounter the bottom of the target craft as it approaches the beach. There are tethered electric switch contact mines designed to attack these craft in the deeper portion of the surf zone. In addition, bottom laid anti-vehicle pressure activated mines may be submerged in water or on the beach depending on the state of the tide. These mines are subjected to burying due to the surf and current. These mines may also be moved to new surf zone depths not planned by those who originally laid the mine, as a result of ocean storms. The threat mix also includes larger warhead bottom influence mines laid in the deeper bottom areas of the surf zone to attack mine countermeasures (MCM) or invasion craft [8].

Another of the shallow water threats is the anti-invasion obstacles which are mostly large non-resonant targets designed to prevent both invasion craft, and the landed marine force personnel from reaching the beach. These vary from concrete Jersey Barriers, steel hedgehogs, steel tetrahedrons, concrete 5-ton cubes to single or triple 36-inch high concertina wire mounted on steel or wooden posts. These obstacles may be submerged at high tide at a depth capable of ripping out the bottom of a landing craft or insurmountable at low tide by the same craft. Anti-personnel mines are usually laid near the obstacles to protect them from destruction by special warfare forces. Detection and classification of all these mines in the shallow water region can be facilitated by a sonar that can penetrate bubbly water [12].

In many instances, military-trained dolphins represent the only viable sonar alternative to manual searches by divers. Quoting Rear Admiral W. E. Landay (Chief of Naval Research, Marine Corps for Science and Technology) Kreisher [13], '*The explosive ordance disposal divers and the marine mammals run counter to the drive to get people out of the minefields, Landay said, but they provide "so much flexible capability" that they are likely to remain. The divers and the mammals work mainly in very shallow water and the surf zone, which "continues to be the most challenging environment" for mine warfare, he said'.* It is thus clear that very shallow water and the surf zone represent some of the most complicated and dynamic environments for sonar operation. This is a direct consequence of the presence of bubbles which occur in millions per cubic metre in coastal water. A sonar designed to work effectively in bubble clouds would have great implications for safety, cost and tactics.

In addition, advances in shallow-water sonar are also required because of the increasing requirements of commercial and leisure crafts. These increasing requirements include to assist fishing, surveying and to cope with bottom sensing (for example, depth sounding) in waters which are becoming increasingly crowded and wake-filled. A requirement to design such sonar forms the basis of this dissertation.

1.2. The problem of target detection in bubbly water

Using acoustic means to detect a target in bubble-filled water has always been a long-standing problem, which has never been adequately solved. This is because the presence of these bubbles generates clutter and excess attenuation, both of which affect the performance of active sonar. The former depends heavily on the frequency. The scattering of these air bubbles can be very strong; bubbles in resonance are very strong scatterers of sound with scattering cross sections typically 1000 times their geometric cross sections [14]. For the latter, the attenuation of bubbles in a sound field, through scattering and absorption losses, can be as great as tens of decibels per metre [15] significantly reducing the operational range of the sonar. This attenuation tends to be higher at higher frequencies. Reducing the effects of clutter and excess attenuation, which are by no means uncoupled from each another, will facilitate better target detection and classification by active sonar in bubbly water.

Air bubbles are thus an important consideration for target detection using active sonar. In the next section, the interactions between bubbles and a sound field are introduced. A single bubble in sound field is first modelled as a linear oscillator with a forcing term introduced. This is followed by the concept of a bubble as a non-linear oscillator.

1.3. Bubble dynamics

1.3.1. Bubble as a linear oscillator

The bubble is a nonlinear oscillator. For a bubble, the relationship between the incident acoustic pressure and its responses is nontrivial: in a low pressure acoustic field, the bubble radiates the acoustic energy by contracting and expanding about its equilibrium radius in response to pressure variations in the compression and rarefaction phases of the acoustic beam. As the peak pressures of the insonating pulse increases, the expansion and compression of the bubble becomes nonlinear, resulting in the emission of harmonics. However, in a low pressure acoustic field, the response of a bubble can be modelled as a simple linear oscillator analogous to a bob of mass m, attached to a spring of stiffness K [16]. This can be described by the equation of motion:

$$m\ddot{\varepsilon} + b\dot{\varepsilon} + K\varepsilon = F(t) \tag{1.1}$$

where $F(t)$ is the excitation force. For a harmonic excitation of F_0 and angular frequency ω, a single degree of freedom equation of motion will be:

$$m\ddot{\varepsilon} + b\dot{\varepsilon} + K\varepsilon = F_0 \sin(\omega t) \tag{1.2}$$

where ε is the displacement, b is the dissipation constant and $\dot{\varepsilon}$ and $\ddot{\varepsilon}$ are the velocity and acceleration respectively. A sine term is used for the driving field for simplicity in determining the constants. The solution of this non-homogenous differential equation can be found by adding the general solution of the homogeneous equation to the particular solution of Eq. (1.2). The solution to the homogenous equation, which is the equation for the damped free vibration, is:

$$\varepsilon = \varepsilon^{-\beta t}(A_1 e^{i\omega_d t} + A_2 e^{-i\omega_d t}) \tag{1.3}$$

where $i = \sqrt{-1}$, the damped frequency $\omega_d = \sqrt{\omega_o^2 - \beta^2}$, ω_o is the resonance circular frequency of an oscillator, β is the resistive constant leading to damping, and A_1 and A_2 are constants determined by the initial conditions. Eq. (1.3) can be written in the more recognizable form of

$$\varepsilon = Ae^{-\beta t}\cos(\omega_d t + \vartheta_1) \tag{1.4}$$

In this equation, the initial amplitude, A and the phase, ϑ_1 are constants determined by the initial conditions. By assuming a solution of the form, $\varepsilon = \varepsilon_0 e^{i\omega t}$ the particular solution of Eq. (1.2) can be found and written in a similar form to Eq. (1.4) as

$$\varepsilon = \frac{F_0 \cos(\omega t - \vartheta_2)}{\sqrt{b^2\omega^2 + (K - \omega^2 m)^2}} \tag{1.5}$$

Here, ϑ_2 is a constant determined by the initial conditions.

The solution of the non-homogenous differential equation, Eq. (1.2) can thus be found by the addition of Eq. (1.4) and Eq. (1.5):

$$\varepsilon = Ae^{-\beta t}\cos(\omega_d t + \vartheta_1) + \frac{F_0 \cos(\omega t - \vartheta_2)}{\sqrt{b^2\omega^2 + (K - \omega^2 m)^2}} \tag{1.6}$$

For a bubble, the height of the bob relates to the position of the bubble wall so that the displacement or extension of the spring ε from the equilibrium position corresponds to the difference in the bubble radius R_ε between its present and equilibrium values (given by R and R_0 respectively). The mass models the liquid around the bubble which must move as the bubble wall pulsates. The dissipation term is because of the presence of a viscous medium within which the bob moves. The spring, which provides the restoring force, models the gas within the bubble. Upon compression and rarefaction, the gas causes pressure differentials which acts to restore the bubble to the equilibrium volume.

To apply the equation of motion (Eq. (1.2)) to a bubble, several reference frames can be used. The exact values of the terms mass, stiffness, and the dissipative constant appropriate to the bubble depend on the way the system is defined. In particular, there are two alternative ways to define each of a particular pair of system parameters, leading in combination to four commonly used reference frames [17]. Firstly, the driving term can be defined as either a force or an acoustic pressure. Secondly, the displacement can either be in terms of the bubble volume or of the radius displacement. Here, the radius-pressure reference frame (denotes by the subscript RP) is used with the mass, stiffness, and the dissipative constant represented by m_{RP}^{rad}, K_{RP}, and b_{RP} respectively. This frame of reference is chosen so as to be consistent with the other models used in this thesis. Hence Eq. (1.2) can be written in the radius-pressure frame to give:

$$m_{RP}^{rad}\ddot{R} + b_{RP}\dot{R} + K_{RP}R_\varepsilon = P_A \sin(\omega t) \tag{1.7}$$

Here P_A is the amplitude of the driving pressure field, and $\dot{R}$ and $\ddot{R}$ are the velocity and acceleration term respectively.

Similarly, Eq. (1.6) can be re-written to give:

$$R_\varepsilon = Ae^{-\beta t}\cos(\omega_d t + \vartheta_1) + \frac{P_A \cos(\omega t - \vartheta_2)}{\sqrt{b_{RP}^2\omega^2 + (K_{RP} - \omega^2 m_{RP}^{rad})^2}} \tag{1.8}$$

To obtain the linear response of the bubble, the terms m_{RP}^{rad}, b_{RP} and K_{RP} will have to be determined. A statement of the effective inertia of the pulsation (m_{RF}^{rad} and consequently m_{RP}^{rad}) can be determined by considering the kinetic energy ϕ_K of a bubble which is pulsating with small-amplitude simple harmonic wall motion in an infinite body of liquid of equilibrium density ρ such that the bubble radius $R(t) = R_0 + R_\varepsilon(t)$ is characterized by a displacement $R_\varepsilon(t)$. The kinetic energy ϕ_K associated with this pulsation can be obtained by integrating over shells of liquid from the bubble wall to infinity, treating the liquid around the bubble as concentric spherical shells of liquid. A given shell at radius r has thickness dr, and mass of $4\pi r^2\rho dr$. The kinetic energy of the liquid is thus

$$\phi_K = \frac{1}{2}\int_{R_0}^{\infty}(4\pi r^2\rho dr)\dot{r}^2 dr \tag{1.9}$$

The mass of liquid flowing in time Δt through any spherical surface around the bubble is $4\pi r^2\dot{r}\rho\Delta t$. If the liquid is assumed to be incompressible, then by conservation of mass this general flow can be equated to the flow at the bubble surface to give:

$$\frac{\dot{r}}{\dot{R}_{\max}} = \frac{R_0^2}{r^2} \tag{1.10}$$

This is because in time, Δt, a mass of liquid $4\pi r^2 \rho \dot{r} \Delta t$ flows across a surface at some general radius r outside the bubble. Substituting Eq. (1.10) into Eq. (1.9) gives $\phi_K = 2\pi R_0^3 \rho \left|\dot{R}_{\max}\right|^2$ which takes a maximum value at the equilibrium position, when $R = R_0$. Thus the value of the kinetic energy is

$$\phi_K = \frac{1}{2} m_{RF}^{rad} \left|\dot{R}_{\max}\right|^2$$

$$\Rightarrow m_{RF}^{rad} = 4\pi\rho R_0^3 \qquad (1.11)$$

which allows a statement of the effective inertia of the pulsation (m_{RF}^{rad}) for such linear oscillations. Using the relationship $m_{RF}^{rad} = 4\pi R_0^2 m_{RP}^{rad}$ [17], this gives:

$$m_{RP}^{rad} = \rho R_0 \qquad (1.12)$$

The stiffness K_{RP} can be obtained using the bob-spring system analogy. The stiffness of a spring is the ratio of the force the spring exerts to the extension which produces that force, that is:

$$K = -\frac{F_s}{\varepsilon} \qquad (1.13)$$

where the force F_s is restoring (hence the minus sign) and ε is the extension. The stiffness of a bubble can be found by calculating the same ratio. For a bubble previously at equilibrium in a liquid of static pressure p_o, is compressed. This corresponds to a change of $-R_\varepsilon$ in radius, from R_0 to $R_0 - R_\varepsilon$. As the volume changes by ΔV, from V_0 to V, the pressure in the bubble therefore changes by Δp_i. Having at equilibrium the value $p_{i,e} = p_\infty + \frac{2\sigma}{R_0}$, it changes to a new non-equilibrium value of p_i. The variable, p_∞, is the static pressure in the liquid far from the bubble, usually equal to the sum of the atmospheric plus hydrostatic pressures.

The gas in the bubble with pressure p_i is assumed to behaves polytropically such that $p_i V^{\kappa}$ is constant where the polytropic index is κ. Depending on the behaviour of the gas (adiabatic, isothermal, or in some intermediate manner), the value of κ varies between γ and unity where γ is the ratio of the heat capacity of the gas at constant pressure to that at constant volume. The constant value of κ used most frequently describes reversible heat transfer. Hence, the assumption of polytropic behaviour of the gas in the bubble will imply

$$\Delta p_i = -\frac{\kappa}{V_0} p_{i,e} \Delta V \tag{1.14}$$

If $R_\varepsilon \ll R_0$ the change in volume ΔV equals $4\pi R_0^2 R_\varepsilon$ such that

$$\frac{\Delta V}{V_0} = \frac{-4\pi R_0^2 R_\varepsilon}{\frac{4}{3}\pi R_0^3} = -3\frac{R_\varepsilon}{R_0} \tag{1.15}$$

Using a similar approximation, the force exerted upon the bubble to produce this change in radius is the product of the excess pressure with the area over which it acts:

$$F_A = -4\pi R_0^2 \Delta p_i \tag{1.16}$$

Substituting Eq. (1.14) into Eq. (1.16), F_A is obtained which gives the stiffness of a bubble as

$$K_{RF} = 12\pi\kappa R_0 p_{i,e} \tag{1.17}$$

Using the relationship $K_{RF} = 4\pi R_0^2 K_{RP}$ [17], from Eq. (1.17), this gives:

$$K_{RP} = \frac{3\kappa}{R_0} p_{i,e} \tag{1.18}$$

The undamped natural circular frequency of bubble pulsation is found from the ratio of the stiffness equation (Eq. (1.17)) to the inertia equation (Eq. (1.11)) as follows:

$$\omega_0 = \sqrt{\frac{K_{RF}}{m_{RF}}} = \frac{1}{R_0}\sqrt{\frac{3\kappa p_{i,e}}{\rho}} \approx \frac{1}{R_0}\sqrt{\frac{3\kappa}{\rho}(p_\infty + \frac{2\sigma}{R_0})} \tag{1.19}$$

The so-called 'Minnaert' frequency is thus found by assuming adiabatic conditions ($\kappa = \gamma$) and neglecting the vapour pressure (p_v) and surface tension (σ) when replacing $p_{i,e}$ with p_∞. With the terms m_{RF}^{rad} and K_{RF} derived, the damping term represented by b_{RP} [18], the dissipation constant, is then given by:

$$b_{RP} = \frac{d_{tot} K_{RP}}{\omega}(4\pi R_0^2) \tag{1.20}$$

The equation (Eq. (1.20)) is obtained by utilizing the relationship [17]:

$$\frac{K_{RP}}{K_{VP}} = \frac{b_{RP}}{b_{VP}} = 4\pi R_0^2 \tag{1.21}$$

and

$$d_{tot} = \frac{\omega b_{VP}}{K_{VP}} = d_{rad} + d_{th} + d_{vis} \tag{1.22}$$

The dimensionless damping constant d_{tot} is expressed as the ratio of the terms in the volume-pressure frame (denoted by the subscript VP) as the standard papers on bubble damping by Devin [19] and Eller [20] are all presented in the volume-pressure frame.

The term d_{tot} in Eq. (1.22) is applicable to all frames of references [21]. Each of the dissipative and damping constants can be associated with each of the three distinct mechanisms [22] by which energy loss from a bubble can occur. They are:

- Energy is radiated away from the bubble as acoustic waves (radiation damping d_{rad}).
- Energy is lost through thermal conduction between the gas and the surrounding liquid (thermal damping d_{th}).
- Work is done against viscous forces at the bubble wall (viscous damping d_{vis}).

The radiation damping d_{rad} is first determined in the radius-force frame by considering the radiation impedance of the bubble [23]. This is defined as the ratio of the applied force to the particle speed. Since it relates to the radius-force frame, it is numerically equal to the product of the specific acoustic impedance and the surface area. It is this impedance that characterizes the coupling between the acoustic source and the radiated waves. The resistive and inertial properties of the source are given by the real and imaginary parts of this impedance respectively. For the limit of $kR_0 \ll 1$, where k is the wavenumber and R_0 is the equilibrium bubble radius, the real part of the radiation impedance is the radiation resistance b_{RF}^{rad}, the resistive term responsible for the damping that results from the radiation of energy away from the bubble as sound. This is derived by Leighton [23] as follows:

$$b_{RF}^{rad} = 4\pi R_0^2 \rho c (kR_0)^2 \tag{1.23}$$

Using the relationship $b_{RF} = (4\pi R_0^2)^2 b_{VP}$ [17], Eq. (1.23) becomes

$$b_{VP}^{rad} = \frac{\rho c k^2}{4\pi} \tag{1.24}$$

Assuming the gas within the bubble behaves polytropically, the stiffness of the bubble, K_{VP}, is given by [21]:

$$K_{VP} = \frac{\kappa p_0}{V_0} = \frac{3\kappa p_0}{4\pi R_0^3} \tag{1.25}$$

where p_0 is the hydrostatic pressure outside of the bubble. From an equation of motion in the volume-pressure frame similar to Eq. (1.2), where the driving force is zero,

$$m_{VP}^{rad}\ddot{V}_\varepsilon + b_{VP}\dot{V}_\varepsilon + K_{VP}V_\varepsilon = 0 \tag{1.26}$$

The dimensionless damping constant d_{rad} can thus be obtained by considering b_{VP}^{rad} and K_{VP} [24] and $d_{tot} = \frac{\omega b_{VP}}{K_{VP}}$ as described in Eq. (1.22),

$$d_{rad} = \frac{\omega b_{VP}^{rad}}{K_{VP}} = \frac{\rho\omega^3 R_0^3}{3\kappa p_0 c} \tag{1.27}$$

This constant d_{rad} obtained is equally applicable to the damping of displacements in any frame [18].

Viscous damping occurs as a result of the viscous stresses. It can be shown that, by application of the Stokes assumption to the Navier-Stokes for a fluid of constant viscosity, there is no net viscous force acting in the body of an incompressible viscous liquid around the pulsating spherical bubble [21]. However, net viscous forces can still occur at the liquid surface of the bubble wall, where they result in excess pressure.

Mallock [25] describes how viscous forces can cause the distortion of spherical shell volume elements concentric with the bubble. For an incompressible liquid, these distortions of the element cannot be caused by compression of the liquid comprising the element. Instead they are the result of the viscous stresses. This causes a net energy loss on compression.

The viscous damping term represented by b_{RP}^{vis} derived by Devin [19] is:

$$b_{RP}^{vis} = \frac{\eta}{\pi R_0^3} \tag{1.28}$$

Using this, the dimensionless equivalence [24] will be:

$$d_{vis} = \frac{\omega b_{VP}^{vis}}{K_{VP}} = \frac{4\omega\eta}{3\kappa p_0} \tag{1.29}$$

where η is the shear viscosity of the liquid.

Amongst the three damping terms that make up the total damping constant, the thermal damping term is the most complicated to derive. In adiabatic conditions, volume and pressure changes take place in a fixed mass of gas without heat being able to transfer between that gas and its surroundings. In such processes, $p_g V^{\gamma}$ is constant. The term κ has the value of γ while in isothermal conditions, the heat transfer between the gas and its surroundings is unhindered, and if those surroundings are assumed to be an infinite reservoir, then compression or expansion of the gas will occur at constant temperature. For a fixed mass of gas at constant temperature, κ is equal to unity.

Eller [20] derived the thermal damping in the volume-pressure frame in terms of l_D, the width of the thermal boundary layer, to give:

$$d_{th} = \frac{3(\gamma-1)\{(R_0/l_D)[\sinh(R_0/l_D)+\sin(R_0/l_D)]-2[\cosh(R_0/l_D)-\cos(R_0/l_D)]\}}{(R_0/l_D)^2[\cosh(R_0/l_D)-\cos(R_0/l_D)]+3(\gamma-1)(R_0/l_D)[\sinh(R_0/l_D)-\sin(R_0/l_D)]} \tag{1.30}$$

With d_{rad}, d_{vis} and d_{th} defined, the total dimensionless damping constant, and consequently b_{RP}, the linear response of a bubble can be obtained. For a real gas bubble in a liquid, the gas next to the bubble wall behaves isothermally because of the high thermal conductivity and specific heat of the liquid, whilst towards the centre of the bubble the gas behaves adiabatically. For a real gas bubble in a liquid, there is a net flow of heat from the bubble into the liquid, resulting in a non-reversible heat transfer (i.e. net losses) across the bubble wall with κ varying throughout the acoustic cycle [26]. As a result, the polytropic index for the bubble as a whole takes an intermediate value between γ and unity. As the bubble pulsates, there is a hysteresis effect, the driving pressure doing more work in compressing the bubble than the gas in the bubble does in moving the liquid on expansion. There is therefore a net flow of heat from the bubble into the liquid, and this loss of energy represents thermal damping.

1.3.2. Nonlinear dynamics of a bubble

The oscillation of a bubble in a sound field is an inherently nonlinear process. When the bubble oscillates in a sound field, its expansion and compression are not symmetrical. This is because whilst the bubble could expand without limit, upon compression, the radial displacement cannot exceed the size of the equilibrium bubble radius.

In addition, a real bubble as a system is generally continuously changing. The equilibrium bubble radius may decrease as the bubble dissolves, or the bubble may fragment [27]. However, by examining the physics of the oscillation process, it is possible to obtain the relationships between the driving acoustic pressure and the response of the bubble (subjected to simplifying approximations), and examine the nature of the nonlinearity.

One source of the nonlinearity can be observed by assuming that the bubble contains only gas at pressure p_g which behaves polytropically, such that $p_g V^{\kappa}$ is constant such that:

$$\frac{\Delta p_g}{p_g} = -\kappa \frac{\Delta V}{V} = -3\kappa \frac{\Delta R}{R} \tag{1.31}$$

Neglecting for a moment surface tension and vapour effects, in the absence of an insonifying field, the net force on the bubble wall arises from the difference between p_g and the constant static pressure in the liquid outside the bubble, p_0 [23].

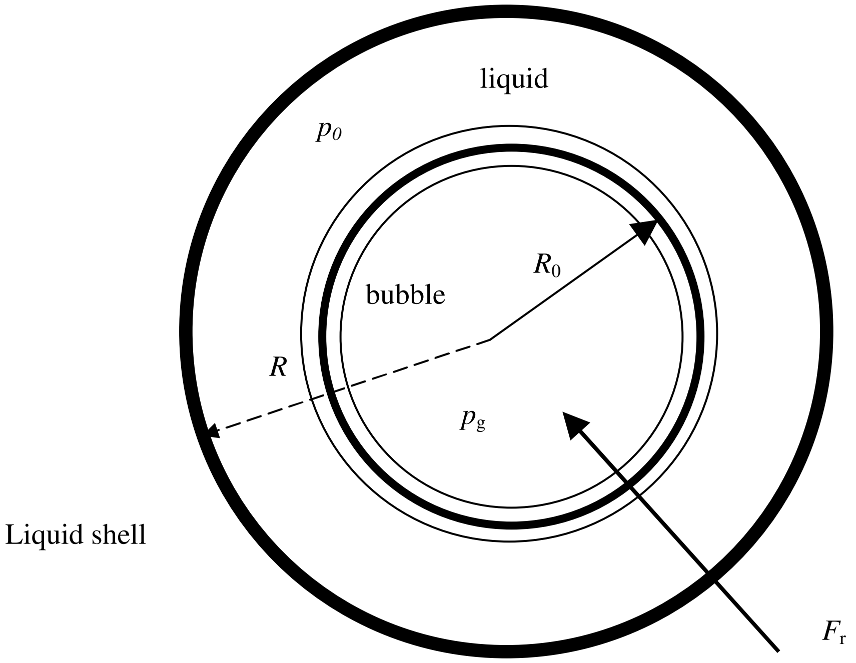

Figure 1.1. A bubble of radius R_0 which is surrounded by spherical shells of liquid with a restoring force F_r pointing towards the centre of the bubble.

As shown in Figure 1.1, if a positive wall displacement occurs ($R_\varepsilon > 0$), the restoring force F_r is towards the origin (the bubble centre), i.e. $F_r = 4\pi R^2(p_g - p_0) < 0$. Using Eq. (1.31), the stiffness of the gas is therefore given by

$$K_{RF} = -\frac{\partial F_r}{\partial R} = 8\pi R(p_0 - p_g) + 4\pi R^2 \frac{\partial(p_0 - p_g)}{\partial R} \approx 12\pi\kappa p_g(t)R(t) \tag{1.32}$$

Eq. (1.32) shows that the dynamics of a bubble is inherently nonlinear as the stiffness is dependent on the instantaneous values of the internal gas pressure, $p_g(t)$, and the bubble radius, $R(t)$, which varies over the oscillation cycle. Another reason is the value of κ may also vary throughout the acoustic cycle of the bubble because of the hysteresis effect.

Consider the case when the amplitude of pulsation is small, specifically $\left|8\pi R(p_0 - p_g)\right| \ll \left|12\pi\kappa p_g(t)R(t)\right|$, and the time-varying quantities $(p_g(t), R(t))$ are replaced by the internal gas pressure $p_{i,e}$, which occurs in the bubble when the radius takes the equilibrium value R_0 (and the magnitude of the wall speed is $\left|\dot{R}_{\max}\right|$), and the common assumption of constant κ. Then the formulation of the bubble model becomes Eq. (1.19), the well-known linear approximation. In the linear approximation model, the stiffness is constant. However, with increasing pulsation amplitude, the discrepancy between the time-varying quantities $p_g(t)$ and $R(t)$ in Eq. (1.32) and their constant counterparts in Eq. (1.17) becomes significant and the amplitude-dependence of the stiffness term cannot be neglected.

Consequently, the nonlinear nature of the bubble pulsation becomes increasingly apparent as the amplitude of the pulsation grows, usually as a result of a high-amplitude driving pressure signal $p(t)$ or closeness to resonance. These nonlinearities are commonly expressed in three families of nonlinear equations of which the simplest is the Rayleigh-Plesset equation. The Rayleigh-Plesset equation only includes the model for viscous damping, with formulations from the Herring-Keller/Keller-Miksis or Gilmore-Akulichev families being required to incorporate the effects of radiation damping.

In the Rayleigh-Plesset family of equations of dynamics for the pulsating bubble, of which Eq. (1.33) is a member, terms resembling ($R\ddot{R}+\frac{3}{2}\dot{R}^2$) are associated with the inertia (as can be seen by differentiating the term $2\pi\rho_0 R^3\dot{R}^2$ in Eq. (1.11) with respect to *R*, noting that $\frac{\partial\dot{R}^2}{\partial R}=\frac{\partial\dot{R}^2}{\partial t}/\dot{R}=2\ddot{R}$). The terms on the right-hand side incorporates the stiffness, as in Eq. (1.17). The effects of viscosity is include in the term $\frac{4\eta\dot{R}}{R}$.

$$R\ddot{R}+\frac{3}{2}\dot{R}^2=\frac{1}{\rho}\left\{\left(p_0+\frac{2\sigma}{R_0}-p_v\right)\left(\frac{R_0}{R}\right)^{3\kappa}+p_v-\frac{2\sigma}{R}-\frac{4\eta\dot{R}}{R}-p_0-p(t)\right\} \tag{1.33}$$

Using the Rayleigh-Plesset equation, it can be demonstrated that the bubble approximates to a linear resonator at low amplitude of oscillation, giving the direct small-amplitude approximation to the resonant frequency of a bubble as [28]:

$$\omega_0=\frac{1}{R_0\sqrt{\rho}}\sqrt{\left\{3\kappa\left(p_0+\frac{2\sigma}{R_0}-p_v\right)-\frac{2\sigma}{R_0}+p_v-\frac{4\eta^2}{\rho R_0^2}\right\}} \tag{1.34}$$

In the sonar simulation model to be presented in Chapter 3, the numerical solution of the Keller-Miksis equation [29] (as shown in Eq. (1.35)) is used so as to incorporate both the viscous and radiation damping through the terms involving η and c respectively. Thermal damping is not included. While being more sophisticated than the Rayleigh-Plesset equation, it is as easy to implement numerically.

$$\begin{aligned}&\left(1-\frac{\dot{R}}{c}\right)R\ddot{R}+\frac{3}{2}\dot{R}^2\left(1-\frac{\dot{R}}{3c}\right)\\&=\left(1+\frac{\dot{R}}{c}\right)\frac{1}{\rho}\left[p_L(t)-p\left(t+\frac{R}{c}\right)-p_\infty\right]+\frac{R}{\rho c}\frac{dp_L(t)}{dt}\end{aligned} \tag{1.35}$$

In Eq. (1.35), $p(t)$ is the driving pressure signal, p_∞ is the pressure far away from the bubble and $p_L(t)$ is the liquid pressure on the external side of the bubble wall, which is related to the internal bubble pressure $p_i(t)$ given by

$$p_i(t)=p_L(R,t)+\frac{2\sigma}{R}+4\eta\frac{\dot{R}}{R} \tag{1.36}$$

In Chapter 3, the numerical implementation of the Keller-Miksis equation in the sonar simulation model used will be described.

1.4. Structure of the thesis

This dissertation presents theoretical and experimental work on the potential of exploiting the relationship of bubbles with an incident acoustic pressure so as to enhance sonar performance in a bubble-filled environment. The first chapter introduces the background and motivation behind this thesis, followed by the introduction of the dynamics of a single bubble in an acoustic field.

Chapter 2 reviews previous work on sonar enhancement in ocean acoustics. The Twin Inverted Pulse Sonar (TWIPS) will be described in this chapter. While the use of two-pulse techniques is uncommon for sonar applications, numerous two-or multi-pulse techniques have been proposed for biomedical applications.

In the field of biomedicine, they are used to enhance the presence of microbubbles called ultrasonic contrast agents (UCAs) inserted into blood stream to enhance scatter from the blood flow relative to the surrounding tissue. The aim of these biomedical imaging techniques is thus opposite to that of TWIPS. TWIPS seeks to enhance the presence of a target in a bubble-filled environment while biomedical imaging techniques aim to enhance the presence of the microbubbles. UCAs are designed such that the bubbles all have similar radii. This is contrary to the sonar case where a wide range of bubble size is typically found. This wide size distribution is one factor complicating the sonar problem, since it rules out the option of choosing a sonar frequency which induces a large response in all the bubbles. Despite the different aims and levels of difficulty, applications in both fields strive to exploit the nonlinearity of bubbles in a sound field. Consequently, it is appropriate to review such techniques in biomedical imaging field and such a review is presented in Chapter 2.

Chapter 3 describes both the sonar simulation model developed and the experimental set-up used to test the efficacy of the techniques identified. The criterion for determining performance of the proposed techniques is also described in this chapter.

In order to enhance sonar performance in a bubble-filled environment, it is important to understand the interaction of a single bubble with a sound field. Chapter 4 gives a detailed examination of the theoretical response of a single bubble when excited by an incident acoustic pulse. This chapter studies the dependence of the peak pressure radiated by a single bubble on different parameters of an acoustic pulse and its implications on sonar enhancement. Both narrowband and wideband pulses will be examined.

While TWIPS has been extensively tested theoretically, and experimentally (in both tank tests and ship trials), it has always been tested using a Gaussian-modulated eight-cycle 6 kHz sine wave. In Chapter 5, the efficacy of TWIPS will be demonstrated using a different waveform (a chirp waveform) theoretically and experimentally. With dolphin behaviour being the main inspiration of TWIPS, the possibility of TWIPS-like processing being implemented in nature by odontocetes to improve target detection and classification in a bubbly environment is also discussed. This discussion mainly centres on odontocetes that have been observed to give out multiple pulses, some of which have been recorded to be of opposite polarity to each other. Current evidence, though limited, has shown these pulses to be usually of low amplitude and higher frequency in the order of 100 kHz. This suggests similar TWIPS-like techniques are unlikely to be used by these odontocetes.

Other odontocetes like the Atlantic bottlenose dolphins (*Tursiops truncatus*), on the other hand, are known to emit trains of high amplitude and high frequency pulses during target interrogation. Discussion of odontocete behaviour with regard to sonar enhancement thus continues in Chapter 6 with a review of the current understanding of the echolocation ability of these odontocetes for possible insight into other potential sonar enhancement solutions. Characteristics of these dolphin-like pulses such as amplitude and chirp structure are investigated and their implications on the detection of targets in a bubble-filled environment discussed. Another main characteristic of these pulses studied is the implication of the short pulse duration of these dolphin-like signals. Using such signals, the effects of different pulse duration on the response of a bubble cloud are investigated by comparing similar pulses of different duration.

Reviews of possible strategies adopted by dolphins during target echolocation experiments have showed that the trains of dolphin pulses emitted would vary in both frequency and amplitude. Chapter 7 thus investigates the use of such pulse variations for possible sonar enhancement. As a form of simplification, a pair of pulses is used in the study. The variation of amplitude between a pair of dolphin-like pulses forms the basis of the Biased Pulse Summation Sonar (BiaPSS). Other two-pulse techniques identified in the reviews are also investigated and their efficacy in target discrimination in bubbly water compared.

Chapter 8 concludes by summarising the main considerations and techniques described for sonar enhancement in bubbly water. Possible future work is also described.

Chapter 2. Enhancing target discrimination in bubbly water

2.1. Review of work in ocean acoustics

There has been a number of works on enhancing target detection by minimizing the degradation of acoustic signal by bubbles. Most of the work is directed towards the effects bubbles have on signal attenuation and the reduction of backscatter or clutter from the bubbles.

With a few exceptions [26, 30], most of this concentrated on the steady state response of bubbles [31-33]. Akulichev *et al.* [31] investigated whether pulsing might decrease backscatter and so mitigate against the adverse effect of sonar on bubble. In the 1986 paper, Akulichev *et al.* [31] noted a pulse-length dependence of the backscatter observed from the microbubbles in the near surface ocean medium. The experimental data was also compared with the predictions from a simple growth model, based on an exponential time constant, for the growth of the bubble acoustic cross-section. It was found that a longer pulse resulted in more significant scattering from bubbles compared to other micro-inhomogeneities in seawater while a shorter pulse introduced less bubble scattering especially if the concentration of solid particles was greater than the bubble density. The decrease in the acoustic backscatter behaviour was found at 5, 15 and 35 kHz and for fewer than 5 to 10 cycles. In the study, the effect of off-resonant bubbles was not accounted in the model which was essentially a linear model based on the steady state response of resonant bubbles. It was also difficult to ascertain the effects of bubble nonlinearity on the finding since the source level used in the experiment was not stated.

However, using similar theoretical models, both Suiter [32] and Pace and Cowley [34] were not able to observe such pulse dependency effects in their bubble cloud attenuation experiments. Unlike the at-sea measurements of Akulichev *et al.* [31], the experiments of Suiter [32] and Pace and Cowley [34] were carried out in laboratory tanks. All three of these studies used simple growth model, based on an exponential time constant, for the growth of the bubble acoustic cross-section.

Clarke and Leighton [30] showed that the ring-up period was more complicated, developing appropriate time-dependent acoustic cross-sections. Using such a theoretical scheme which enabled the investigation of ring-up times of gas bubbles in fresh water, they showed that presence of large bubbles would have a significant effect on the transient response of the cloud as a whole. If the difference between an off-resonant bubble and a bubble oscillating at its resonant frequency, even at small amplitude, is significant when considering pulse length dependence in the study of transient response of a bubble, the presence of a number of off-resonant bubbles may be the reason why Suiter [32] and Pace and Cowley [34] did not detect any reduction in scattering. While not specifically for sonar enhancement, the importance of bubble ring-up and pulse length in estimating the bubble distribution from sea measurements highlighted by Meers *et al.* [35] suggests that some form of pulse-length dependency with bubble responses exists.

As with the previous works [31, 32, 34], the cross-sections developed by Clarke and Leighton [30] were only for semi-infinite insonifications since the cross-section ceased to be definable after the end of the pulse. Leighton *et al.* [26] subsequently developed a strategy for the period after the pulse ended which allowed for prediction of attenuation of an inhomogeneous and time-dependent bubble clouds. This was extended with the proposal of a two-pulse technique: the Twin Inverted Pulse Sonar (TWIPS) which seeks to enhance the detection and classification of targets in bubbly water through exploitation of any bubble nonlinearity that may be generated [3]. TWIPS operates by reducing clutter and has no effect against the attenuation. The principle by which TWIPS operates will be described next.

2.2. Principles of TWIPS

In a scenario where conventional sonar fails to detect a linear scatterer (the ‘target’, e.g. a fish, mine or seabed) because the returned sonar signal is cluttered by the scatter from bubble clouds, TWIPS exploits bubble nonlinearity to enhance the detection and classification of such targets in bubbly water. Assuming the insonifying field has sufficient amplitude to generate a nonlinear response from the bubbles, it may be possible to enhance backscatter from the target (‘detection’) while simultaneously suppressing the nonlinear backscatter from the bubbles, allowing the sonar operator to distinguish between the two (‘classification’).

The principle by which TWIPS operates can be described by first considering the insonifying TWIPS field $p(t)$ which contains pairs of identical pulses of finite length but having opposite phase, with a pulse interval of Δ_d, emitted by the transmitter. A mathematical description of such a pair is as follows [3]:

$$p(t) = \Gamma(t) - \Gamma(t - \Delta_d) \qquad (2.1)$$

The received echoes are processed to take account of any nonlinearity. The received echo of a linear and nonlinear scatterer, $p_{Rx}(t)$ can be described as:

$$p_{Rx}(t) = p_{lin}(t) + p_{nl}(t) \tag{2.2}$$

where $p_{lin}(t)$ is the received component from the linear scatterers, and $p_{nl}(t)$ is the component received from the nonlinear scatterers. The signal arising from a linear scatterer can be related to the emitted pulse $p(t)$ via a convolution integral:

$$p_{lin}(t) = \int_{-\infty}^{t} h_{lin}(t-\tau)p(\tau)d\tau = H_{lin}\left[p(t)\right] = H_{lin}\left[\Gamma(t)\right] - H_{lin}\left[\Gamma(t-\Delta_d)\right] \tag{2.3}$$

where the kernel function (or impulse function) $h_{lin}(t)$ incorporates the effects of propagation (assumed to be linear) and scattering from the object. The operator, $H_{lin}[\ ]$ computes, from its argument, the signal received from the linear scatterer.

To obtain an expression for the received signal from a nonlinear scatterer $p_{nl}(t)$, a Volterra series [36] representation is used. This is used as it has been successfully used to model single bubble scattering by White *et al.* [37]. Using this representation, the signal $p_{nl}(t)$ is given by:

$$\begin{aligned} p_{nl}(t) = &\int_{-\infty}^{t} h_1(t-\tau)\,p(\tau)\,d\tau + \int_{-\infty}^{t}\int_{-\infty}^{t} h_2(t-\tau_1,t-\tau_2)\,p(\tau_1)\,p(\tau_2)\,d\tau_1 d\tau_2 \\ &+\int_{-\infty}^{t}\int_{-\infty}^{t}\int_{-\infty}^{t} h_3(t-\tau_1,t-\tau_2,t-\tau_3)\,p(\tau_1)\,p(\tau_2)\,p(\tau_3)\,d\tau_1 d\tau_2 d\tau_3 + \ldots \end{aligned}$$

$$\therefore\ p_{nl}(t) = H_1\left[p(t)\right] + H_2\left[p(t)\right] + H_3\left[p(t)\right] + \ldots \tag{2.4}$$

where τ, τ_1, τ_2 and τ_3 are dummy variables within the integrals. Here $h_Q(\ldots,\ldots,\ldots)$ and $H_Q[\ ]$ are referred to as the *Q*th-order Volterra kernels and functionals respectively. The Volterra kernels can also be related to harmonic generation in the nonlinear system. In particular if Q is odd, then the Qth-order functional gives rise only to odd harmonics of order less than equal to Q. Similarly, when Q is even, only even harmonics less than or equal to Q are generated. The functionals also satisfy symmetry properties that reflect the oddness and evenness of their arguments Q. Hence:

$$H_Q\left[-\Gamma(t)\right] = H_Q\left[\Gamma(t)\right] \text{ for } Q \text{ even} \tag{2.5}$$

$$H_Q\left[-\Gamma(t)\right] = -H_Q\left[\Gamma(t)\right] \text{ for } Q \text{ odd} \tag{2.6}$$

A nonlinear scatterer insonified by the pulse $p(t)$ shown in Eq. (2.1) thus produces a signal:

$$\begin{aligned} p_{nl}(t) &= H_1\left[\Gamma(t)\right] - H_1\left[\Gamma(t-\Delta_d)\right] \\ &+ H_2\left[\Gamma(t)\right] + H_2\left[\Gamma(t-\Delta_d)\right] + H_3\left[\Gamma(t)\right] - H_3\left[\Gamma(t-\Delta_d)\right] .... \end{aligned} \tag{2.7}$$

The basis of TWIPS processing is to form linear combinations of delayed versions of the received signal. Specifically, one creates $p_-(t)$ and $p_+(t)$ defined as:

$$p_-(t) = p_{Rx}(t) - p_{Rx}(t+\Delta_d) \quad \text{for} \quad 0 \le t \le \Delta_d \tag{2.8}$$

$$\text{and} \quad p_+(t) = p_{Rx}(t) + p_{Rx}(t+\Delta_d) \quad \text{for} \quad 0 \le t \le \Delta_d \tag{2.9}$$

For linear scatterers, such processing leads to

$$p_-(t) = 2H_{lin}\left[\Gamma(t)\right] \quad \text{for} \quad 0 \le t \le \Delta_d \tag{2.10}$$

$$\text{and} \quad p_+(t) = 0 \quad \text{for} \quad 0 \le t \le \Delta_d \tag{2.11}$$

whereas for nonlinear scatterers, based on a Volterra representation, the equivalent expressions are:

$$p_-(t) = 2H_1\left[\Gamma(t)\right] + 2H_3\left[\Gamma(t)\right] + \ldots \quad \text{for} \quad 0 \le t \le \Delta_d \tag{2.12}$$

$$\text{and} \quad p_+(t) = 2H_2\left[\Gamma(t)\right] + \ldots \quad \text{for} \quad 0 \le t \le \Delta_d \tag{2.13}$$

Eq. (2.10) to (2.13) shows that by computing $p_-(t)$, one can enhance the returns from linear scatterers and suppresses some nonlinear effects whilst enhancing others, whereas with $p_+(t)$, one suppresses the returns from linear scatterers.

2.3. Enhancing target discrimination in bubbly water using TWIPS

TWIPS has received extensive testing through simulation, tank and field experiments which indicate it holds possibilities for detection and classification of objects through clutter reduction for oceanic applications [2-6]. The ability to calculate the two variables, $p_+(t)$ and $p_-(t)$, from a single echo pair, provides a classification capability that is absent in standard sonar system. Comparison of the outputs of the two functions provides a tool to distinguish clutter from targets if their respective scattering can be forced into different harmonic bands.

In general, the effectiveness of TWIPS increases as a greater proportion of the bubble population scatter nonlinearly. Hence if the bubble population is monodisperse or near-monodisperse, then the greatest degree of nonlinearity (and hence the potential of TWIPS to work most effectively) tends to occur when the bubbles are driven at a frequency which is close to the main pulsation resonance of the population, or to some harmonic, subharmonic etc. For oceanic bubble clouds, where there is a wide distribution of bubble sizes, optimizing the effectiveness of TWIPS generally means a lower frequency needs to be used as the driving frequency. This is because the frequency of the pulse must be sufficiently low so as to give the bubble time to pulsate to a large amplitude, and the characteristic response time of a bubble is determined by its own natural frequency.

If the insonifying pulse is of high amplitude but high frequency (compared to the bubble pulsation resonance), then by the time the bubble has begun to respond to the first half cycle of the pulse (which, say, causes it to expand), it encounters the subsequent half cycle of the driving pulse (which in this example will tend to cause the bubble to contract). Therefore, the bubble simply does not respond fast enough to generate a highly nonlinear response if the driving sound field has a frequency much greater than its resonance. If however, the bubble is sufficiently small that its natural frequency is much greater than the insonifying frequency, it responds rapidly to the compressive or expansive half cycles and undergoes high amplitude nonlinear pulsation. On this basis, together with transducer constraints, which restricted the transmitter to a single type of waveform, TWIPS has only been tested using low frequency narrowband pulses. Based on the same argument, the use of a broadband signal would result in a greater degree of nonlinearity to occur in the bubble cloud as a higher number of bubbles are driven at frequencies which are close to the resonant frequencies of the population.

A practical problem associated with a wide bubble-size distribution is $p_-(t)$ does not completely remove the influence of the nonlinear bubbles as it also enhances the linear and odd-powered nonlinearity. To provide further enhancement in the contrast between the linear and nonlinear scatterers, the ratio $p_-(t)/p_+(t)$ can be formed. The use of $p_+(t)$ in the denominator further suppresses the scatters from the nonlinear bubbles. A particular important feature of this ratio is that it does not require range correction since it self-corrects for range, as both the denominator and numerator fall off with range at the same rate [38]. Thus, the ratio is immune to the requirement of *a priori* knowledge of the beam and environment. The use of such ratios has been independently noted in biomedical field for use of contrast agents [39]. One disadvantage of using ratios is that they are prone to instability. Small change in the denominator may result in large fluctuation in the outputs, for example, when the denominator consists of very small values. This instability is mitigated by averaging the value of $p_+(t)$ over sets of adjacent returns [3].

However, a more debilitating disadvantage of using this ratio is that target close to or within the bubble cloud cannot be easily discerned as the use of $p_+(t)$ in the denominator would also suppress the linear backscattered contribution of the target. The performance of TWIPS and the use of the TWIPS ratio, will be demonstrated in Chapter 5 with a linear frequency modulated (LFM) waveform.

While the use of two-pulse techniques in sonar to mitigate the challenge of target detection in bubbly water is not common, different types of two-pulse techniques for imaging of UCAs in blood vessels are increasingly being proposed in the biomedical imaging.

2.4. Biomedical imaging techniques with microbubbles

In biomedical imaging, microbubbles known as ultrasonic contrast agents (UCAs) are artificially inserted into the blood stream to improve the detection and visualisation of blood vessels in a variety of organs to aid clinical diagnosis. Detecting the nonlinear harmonic responses from these UCAs and differentiating them from the echoes that result from the tissue has formed the basis of UCAs imaging research. For oceanic applications, TWIPS aims to enhance the detection of the linear scatterer (the ‘target’); the opposite is true for biomedical imaging which seeks to enhance the presence of UCAs.

Harmonic imaging [40, 41] was one of the first methods proposed in biomedical imaging field to detect the harmonics returned by the contrast agents from each pulse. Harmonic imaging exploits the nonlinear bubble response around the second harmonic component by linearly filtering the received signal around twice the fundamental frequency of the transmitted pulse.

For harmonic imaging, axial resolution is a major issue. To obtain satisfactory axial resolution, a large transmitted signal bandwidth is generally favoured but this will potentially cause an overlap in frequency band between the second harmonic of the microbubble echo and the fundamental component. Such overlap means that a simple high-pass filter cannot completely remove the linear component without removing portion of the nonlinear component, consequently reducing contrast. Narrowing both transmit and receive bandwidths reduce this effect, but at the expense of the axial resolution. To overcome this key drawback, techniques based on two- or more pulse techniques were proposed.

2.4.1. Pulse Inversion imaging

One of the first two-pulse techniques proposed was the pulse inversion imaging [40, 42]. Pulse inversion imaging overcomes the limitations of harmonic imaging by detecting nonlinear echoes over the entire transducer bandwidth. Similar to TWIPS, it exploits the fact that when two ultrasound pulses are transmitted, with the phase of the second pulse inverted, adding the corresponding echoes together cancels the linear component and reinforces the nonlinear components. This provides a contrast between the region where nonlinear scatterers (microbubbles) dominates and the region where linear scatterers (tissue) are. Through addition of the corresponding echoes, the fundamental (linear) component is removed even when the fundamental and second harmonics overlap, thus overcoming the limitations of harmonic imaging.

This technique was then modified by Simpson *et al.* [41] with the incorporation of Doppler processing. Doppler schemes like harmonic power Doppler and harmonic color Doppler were found to be extremely sensitive in detecting and imaging microbubbles in tissues because they suppressed echoes from moving tissues better. In this context, it would be the flow of microbubbles in blood streams. Using *in vitro* measurements, Simpson *et al.* [41] demonstrated that pulse inversion Doppler could provide 3 to 10 dB more agent to tissue contrast than harmonic imaging with similar pulses. Using broadband pulse inversion Doppler was also shown to provide up to 16 dB more contrast than broadband conventional Doppler.

2.4.2. Amplitude-modulated signals

To increase the sensitivity in nonlinear biomedical imaging, other multi-pulse approaches were also adopted. One approach proposed by Brocker-Fisher *et al.* [43] used a pair of amplitude-modulated or power-modulated pulses rather than a pair of inverted pulses. Similar to the pulse inversion scheme, cancellation of linear component and reinforcement of the nonlinear components of the echoes are achieved by adding the corresponding echoes with an appropriate scaling. Note the use of a pair of inverted pulses can be considered to be amplitude modulation of a kind with the scaling having a value of -1.

The principle by which this technique operates can be described by first considering the insonifying field $p(t)$ in a manner similar to Section 2.2. Pairs of identical pulses of finite length, having different amplitudes with a pulse interval of Δ_d, are emitted by the transmitter. The magnitude of the second pulse is assumed to be greater than the magnitude of the first pulse by a factor of G.

A mathematical description of such a pair is:

$$p(t) = \Gamma(t) + G\Gamma(t - \Delta_d) \tag{2.14}$$

Hence Eq. (2.3) becomes:

$$p_{lin}(t) = \int_{-\infty}^{t} h_{lin}(t-\tau)p(\tau)d\tau = H_{lin}\left[p(t)\right] = H_{lin}\left[\Gamma(t)\right] + GH_{lin}\left[\Gamma(t-\Delta_d)\right] \tag{2.15}$$

and Eq. (2.7) becomes:

$$\begin{aligned} p_{nl}(t) &= H_1\left[\Gamma(t)\right] + H_1\left[G\Gamma(t-\Delta_d)\right] + H_2\left[\Gamma(t)\right] \\ &+ H_2\left[G\Gamma(t-\Delta_d)\right] + H_3\left[\Gamma(t)\right] + H_3\left[G\Gamma(t-\Delta_d)\right].... \end{aligned} \tag{2.16}$$

The basis of amplitude-modulated processing is to form linear combinations of delayed versions of the received signal with the delayed version appropriately-scaled. Specifically, one creates $p_-(t)$ and $p_+(t)$ which are defined as:

$$p_-(t) = p_{Rx}(t) - \frac{1}{G}p_{Rx}(t+\Delta_d) \quad \text{for} \quad 0 \le t \le \Delta_d \tag{2.17}$$

$$\text{and} \quad p_+(t) = p_{Rx}(t) + \frac{1}{G}p_{Rx}(t+\Delta_d) \quad \text{for} \quad 0 \le t \le \Delta_d \tag{2.18}$$

For linear scatterers, such processing leads to

$$p_+(t) = 2H_{lin}\left[\Gamma(t)\right] \quad \text{for} \quad 0 \le t \le \Delta_d \tag{2.19}$$

$$\text{and} \quad p_-(t) = 0 \quad \text{for} \quad 0 \le t \le \Delta_d \tag{2.20}$$

Similar to Section 2.2, the Volterra kernels can also be related to harmonic generation in the nonlinear system. In particular if $\Gamma(t)$ is scaled by *G*, the *Q*th-order functional will be scaled by G^Q.

Hence:

$$H_Q\left[G\Gamma(t)\right]=G^Q H_Q\left[\Gamma(t)\right] \tag{2.21}$$

whereas for nonlinear scatterers, based on a Volterra representation, the equivalent expressions are:

$$\begin{aligned}p_-(t)&=H_2\left[\Gamma(t)\right]+H_3\left[\Gamma(t)\right]+...\\&-\frac{1}{G}\left\{H_2\left[G\Gamma(t)\right]+H_3\left[G\Gamma(t)\right]+...\right\}\\&\text{for}\quad 0\le t\le\Delta_d\end{aligned} \tag{2.22}$$

$$\begin{aligned}p_+(t)&=H_1\left[\Gamma(t)\right]+H_2\left[\Gamma(t)\right]+H_3\left[\Gamma(t)\right]+...\\&+\frac{1}{G}\left\{H_1\left[G\Gamma(t)\right]+H_2\left[G\Gamma(t)\right]+H_3\left[G\Gamma(t)\right]+...\right\}\\&\text{for}\quad 0\le t\le\Delta_d\end{aligned} \tag{2.23}$$

For a nonlinear scatterer like a bubble, both $p_-(t)$ and $p_+(t)$ will be non-zero. By comparing $p_-(t)$ and $p_+(t)$, linear and nonlinear scatterers can be differentiated. The use of amplitude-modulated signals to enhance UCAs were demonstrated clinically by Mor-Avi [44]. Using in vitro experiments, Eckersley *et al.* [45] found that the UCA enhancement for both pulse inversion with amplitude-modulated schemes were comparable.

2.4.3. Using pair of time-reversed signals

Another proposed approach is the use of a pair of time-reversed chirp signal [46-49]. This technique exploits the responses of the microbubbles to a wideband chirped excitation where the first pulse is a linear frequency-modulated (LFM) signal with instantaneous rate of change of frequency that is increasing (termed ‘up-chirp’ or ‘increasing chirp’) and the second is a LFM signal with a instantaneous rate of change of frequency that is decreasing (termed ‘down-chirp’ or ‘decreasing chirp’). The second pulse can thus be considered a time-reversed replica of the first pulse.

The microbubble has been found to respond differently when excited by an up-chirp or a down-chirp. Both Sun *et al.* [48, 49] and Novell *et al.* [47] have shown in a series of simulations, optical, and acoustical measurements that the matched filtered responses of the microbubbles were different when excited by a increasing chirp and a decreasing chirp. A linear scatterer, like a tissue, will have the same matched filtered responses. Cancellation of linear component and reinforcement of the nonlinear components of the echoes can thus be achieved by a combination of the corresponding matched filtered echoes as described. A mathematical description of a pair of identical time-reversed pulses of finite length emitted by the transmitter is:

$$p(t) = \Gamma(t) + \Gamma(-t - \Delta_d) \tag{2.24}$$

Hence Eq. (2.3) becomes:

$$p_{lin}(t) = \int_{-\infty}^{t} h_{lin}(t-\tau)p(\tau)d\tau = H_{lin}\left[p(t)\right] = H_{lin}\left[\Gamma(t)\right] + H_{lin}\left[\Gamma(-t-\Delta_d)\right] \tag{2.25}$$

$$\begin{aligned} p_{nl}(t) = {} & H_1\left[\Gamma(t)\right] + H_1\left[\Gamma(-t-\Delta_d)\right] + H_2\left[\Gamma(t)\right] \\ & + H_2\left[\Gamma(-t-\Delta_d)\right] + H_3\left[\Gamma(t)\right] + H_3\left[\Gamma(-t-\Delta_d)\right] .... \end{aligned} \tag{2.26}$$

If $P_{Rx}(t)$ is the matched filtered version of the received signal, $p_{Rx}(t)$, with the matched filter used having a gain of unity, the basis of time-reversed chirp processing is to form linear combinations of matched filtered versions of the received signal with the delayed version defined as:

$$P_{-}(t) = \Gamma(-t) * p_{Rx}(t) - \Gamma(t) * p_{Rx}(t + \Delta_d) \quad \text{for} \quad 0 \le t \le \Delta_d \tag{2.27}$$

$$P_{-}(t) = P_{Rx}(t) - P_{Rx}(t + \Delta_d) \quad \text{for} \quad 0 \le t \le \Delta_d \tag{2.28}$$

and $$P_{+}(t) = \Gamma(-t) * p_{Rx}(t) + \Gamma(t) * p_{Rx}(t + \Delta_d) \quad \text{for} \quad 0 \le t \le \Delta_d \tag{2.29}$$

$$P_{+}(t) = P_{Rx}(t) + P_{Rx}(t + \Delta_d) \quad \text{for} \quad 0 \le t \le \Delta_d \tag{2.30}$$

where $*$ denotes convolution.

Using the property:

$$\Gamma(t) * \Gamma(-t) = \Gamma(-t) * \Gamma(t) \tag{2.31}$$

For linear scatterers, such processing leads to

$$P_{-}(t) = 0 \quad \text{for} \quad 0 \le t \le \Delta_d \tag{2.32}$$

and $P_{+}(t)$ will be non-zero. For nonlinear scatterers, both $P_{-}(t)$ and $P_{+}(t)$ will be non-zero. From Eq. (2.32), $P_{-}(t)$ can be utilized for the purpose of imaging nonlinear entities like microbubbles, since complete cancellation of linear scatterers (in this case, tissues) will occur with $P_{-}(t)$.

2.5. Summary

Reviews from field of ocean acoustics and biomedical field have yielded several ideas that will be investigated in this thesis.

While there has been a number of studies on enhancing target detection by minimizing the degradation of acoustic signal by bubbles for oceanic applications, only the Twin Inverted Pulse Sonar (TWIPS) has been used to great effect in discrimination of linear scatterers from nonlinear scatterers by Leighton *et al.* [3, 6] for sonar applications in bubbly water. TWIPS has been tested in tank tests and limited sea trial using narrowband pulses. The efficacy of TWIPS will be demonstrated in Chapter 5 using LFM waveforms.

Bearing in mind that the wider ocean bubble population (compared to the narrower artificially inserted UCAs population) will made it more challenging for sonar applications, reviews of biomedical imaging techniques have yielded several methods that could possibly form the basis of new sonar solutions for improved detection of solid objects in bubbly water. They are the amplitude-modulated technique and the use of a pair of time-reversed pulses. However, the exploitation of Doppler effects by Simpson *et al.* [41] cannot be similarly implemented for sonar applications. This is because the terminal rise speed of the smallest oceanic bubbles (which make the vast majority of oceanic bubbles) is on the order of 10000 lower than the speed of sound in the ocean.

The techniques and ideas proposed in this thesis will be investigated theoretically using a sonar simulation model and experimentally with controlled tank experiments. Both the sonar simulation model and the experimental set-up will be described next.

Chapter 3. Methods

3.1. Sonar simulation model

This section describes the sonar simulation model developed to test the viability of various sonar enhancement techniques and ideas which arose from the literature review. The sonar simulation model consists of several parts. The bubble responses of individual bubble radii are first computed. Separately, the distribution of the bubble radius in the cloud will be obtained. Depending on the aim of investigation required, attenuation because of geometric losses, bubble cloud and seawater absorption can be included. The bubble cloud attenuation incorporated in the sonar simulation model is a linear bubble attenuation model after Commander and Prosperetti [50].

The sonar simulation model uses the theoretical responses of representative bubbles, characterising a bubble size bin encompassing bubbles of similar radii. The three-dimensional volume of liquid is divided into spatial cells into which the bubble population, and the target, may be placed. The responses of all the bubbles from that volume are then calculated by convolving the bin-representative bubble response with the bubble population for that volume. Each part of the model will now be elaborated.

3.1.1. Nonlinear single bubble model

The nonlinear response of a single bubble of different bubble radius is calculated in the sonar simulation model using the Keller-Miksis model [29] shown in Eq. (1.35). This model assumes spherical oscillations of a single bubble in water and extends the Rayleigh-Plesset model by considering a compressible medium with a constant speed of sound.

After defining the excitation pressure, Eq. (1.35) is solved using a variable step length Runge-Kutta method implemented in MATLAB®. The radiated pressure at a given distance from each bubble is then calculated from the radius and velocity of the bubble surface for each time point.

It should be recalled that, the Keller-Miksis equation includes viscous damping (as does the Rayleigh-Plesset) arising from the term involving η, radiation damping from the term of c, up to the first order of $\frac{\dot{R}}{c}$ and does not include thermal loss. Damping reduces the resonance frequency of a system [51], causes decay in time and introduces phase shift [52]. Since the Keller-Miksis equation does not include thermal damping, it is noted there may be underestimates of overall damping in some instances. Hence, it is important to compare the contribution of the different types of damping to the overall damping based on the derivations of Eller [20] for a range of frequency of representative bubble radii so as to obtain a generalised trend of underestimation of the total damping.

Figure 3.1 shows the damping constant, *d*, and its separation contributions as a function of frequency for three representative bubble radii of 10, 100 and 1000 μm. The overall damping (denoted as 'total' in Figures 3.1 and 3.2) is the sum of thermal, radiation and viscous damping. For a bubble of radius of 10 μm, Figure 3.1(a) shows that neglecting thermal losses would result in an under-estimation of the overall damping losses as thermal losses dominates at such small bubble sizes. For a bigger bubble radius of 100 μm, the thermal contribution to the overall damping dominates below 10 kHz as shown in Figure 3.1(b). As the insonifying frequency increases beyond 10 kHz, the contribution from radiation damping relative to the other two types of damping (thermal and viscous) increases. For larger bubble sizes (of order of 1000 μm), the main contribution to the damping constant is radiation damping (Figure 3.1(c)). Thermal damping is only significant at low frequency of less than 2 kHz for such large bubbles.

For a frequency of 80 kHz, Figure 3.2 shows the range of bubble radii (< 60 μm) for which the overall damping will be under-estimated if thermal damping is neglected. As the radius of the bubble radius increases beyond 60 μm, radiation damping dominates. Viscous damping remains constant across the bubble radius.

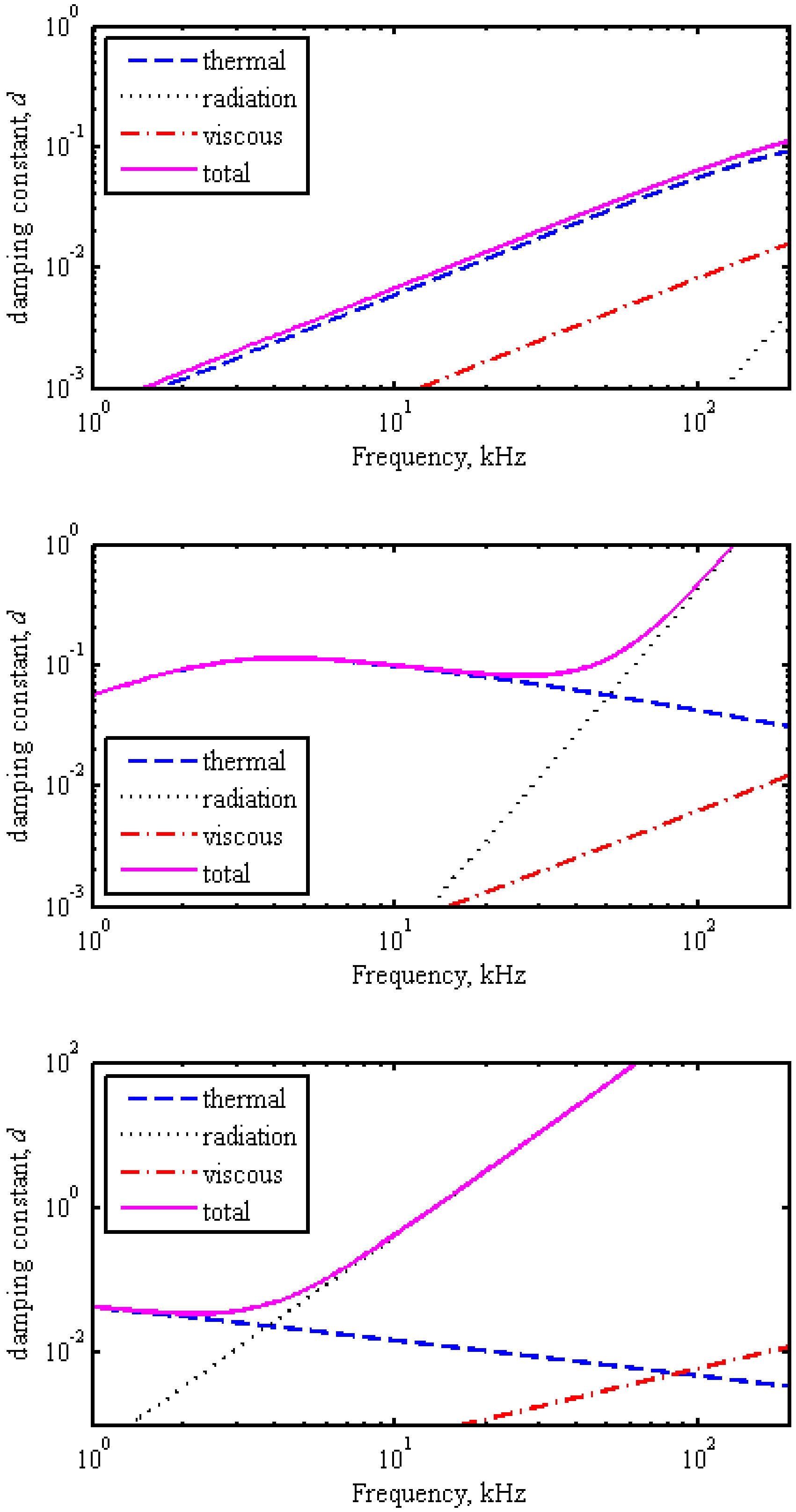

(a) R_o=10μm

(b) R_o=100μm

(c) R_o=1000μm

Figure 3.1. Dimensionless damping constant and its separate contributions as a function of frequency for an air bubble of equilibrium radius, R_o (a) 10 μm (b) 100 μm and (c) 1000 μm. The thermal, radiation, viscous and total damping constant are denoted by dashed, dotted, dot-dashed, and solid lines respectively.

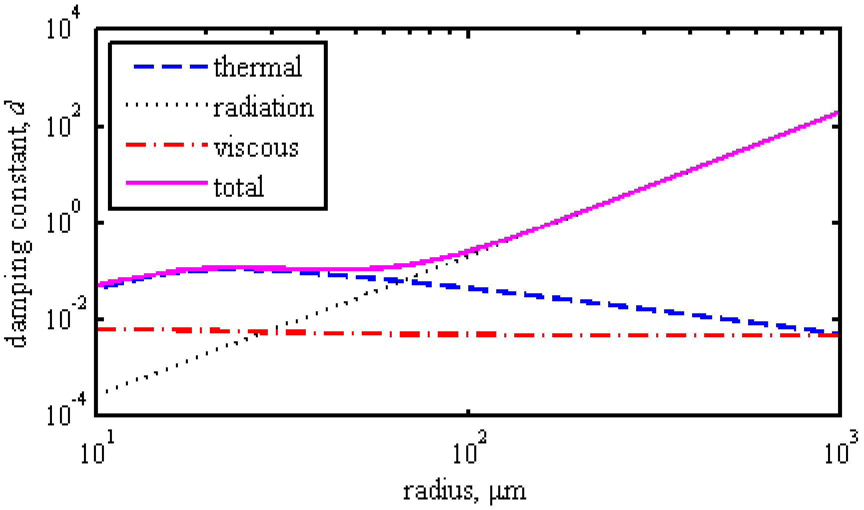

Figure 3.2. Dimensionless damping constant and its separate contributions as a function of bubble radius for a frequency of 80 kHz. The thermal, radiation, viscous and total damping constant are denoted by dashed, dotted, dot-dashed, and solid lines respectively.

Figures 3.1 and 3.2 reaffirm the following generalized conclusions of Eller [20]:

- For driving frequencies less than the bubble resonance, thermal damping dominates.
- For driving frequencies greater than the bubble resonance, the radiation damping dominates.
- The damping tends to undergo a local minimum in the transition region between the dominance of thermal and radiation damping. This local minimum occurs at a driving frequency close to, but not exactly on, the bubble resonance.

A generalized trend is thus clear. Radiation damping can be taken to be negligible at low frequencies whilst thermal damping is negligible at high frequencies.

It is thus noted that without introduction of thermal damping in the nonlinear Keller-Miksis equation, the overall damping will be under-estimated for the smaller bubbles present in a typical oceanic bubble cloud. Based on historical measurement data, a typical oceanic bubble cloud is known to contain mainly bubble sizes ranging from 15 to 700 μm (see Figure 3.4 later). This under-estimation of damping will be more significant when the driving pulse is of a low frequency A full discussion of the neglect of thermal damping in a nonlinear model can be found in Leighton *et al.* [26]. The next section will describe the transmission loss model incorporated in the bubble cloud model.

3.1.2. Transmission loss model

As a pulse propagates through seawater, transmission losses result. The main types of transmission losses defined in the bubble cloud model are geometric losses, bubble cloud attenuation and seawater absorption. For geometric losses, spherical spreading is assumed. The cloud attenuation model and seawater absorption model are described in Section 3.1.2.1 and 3.1.2.2 respectively. Both seawater absorption and bubble cloud attenuation are assumed to be frequency-dependent.

3.1.2.1. Cloud attenuation model

In the cloud attenuation model, the propagation of pressure waves in bubbly liquids is predicted using the model proposed by Commander and Prosperetti [50] with typographic errors corrected as described by Ainslie and Leighton [18].

$$\frac{c^2}{c_m^2} = 1 + \frac{4\pi c^2 n R_o}{\omega_o^2 - \omega^2 + 2ib_c\omega} \tag{3.1}$$

where

$$\omega_o^2 = \frac{p_{i,e}}{\rho R_o^2}\left(\operatorname{Re}\Phi - \frac{2\sigma}{R_o p_{i,e}}\right) \tag{3.2}$$

$$b_c = \frac{2\mu}{\rho R_o^2} + \frac{p_{i,e}}{2\rho\omega R_o^2}\operatorname{Im}\Phi + \frac{\omega^2 R_o}{2c} \tag{3.3}$$

$$\Phi = \frac{3\gamma}{1 - 3(\gamma - 1)i\chi\left[\left(\frac{i}{\chi}\right)^{\frac{1}{2}}\coth\left(\frac{i}{\chi}\right)^{\frac{1}{2}} - 1\right]} \tag{3.4}$$

and

$$\chi = \frac{D_g}{\omega R_o^2} \tag{3.5}$$

In the cloud attenuation model proposed, Eq. (3.1) is first solved for a mono-dispersed bubble population with equal equilibrium radius R_o. The variables, c_m, is the complex speed of sound of the mixture, n is the number of bubbles per unit volume, $p_{i,e}$ is the pressure within the bubble at equilibrium, and D_g is the thermal diffusivity of the gas. The variables, b_c, Φ and χ are defined as above. The variable, c_m, is expressed as a complex variable to represent the dissipative nature of the mixture. For a discrete bubble distribution containing a range of bubble sizes, Eq. (3.1) is found using a summation over the range of bubble sizes present. The attenuation coefficient in dB per unit length is then computed using Eq. (3.6).

$$\text{Attenuation coefficient for bubble distribution} = 20(\log_{10} e)(\frac{\omega Z}{c}) \simeq 8.68589(\frac{\omega Z}{c}) \tag{3.6}$$

The variable Z is the imaginary component of $-\frac{c}{c_m}$. It is noted that this model is for small-amplitude cases and hence a linearised approximation. A number of nonlinear model for pressure waves in bubbly liquids have been proposed which can include effects such as Reynolds stresses [50]. As the primary motivation of a cloud attenuation model in the sonar simulation model is to give a more realistic model to investigate and assess the performance of various sonar enhancement techniques, a balance between the sophistication of the treatments and the numerical efforts required (in terms of computation cost) has to be struck. A linear cloud attenuation model has thus been implemented in view of the higher computational cost associated with a nonlinear cloud attenuation model.

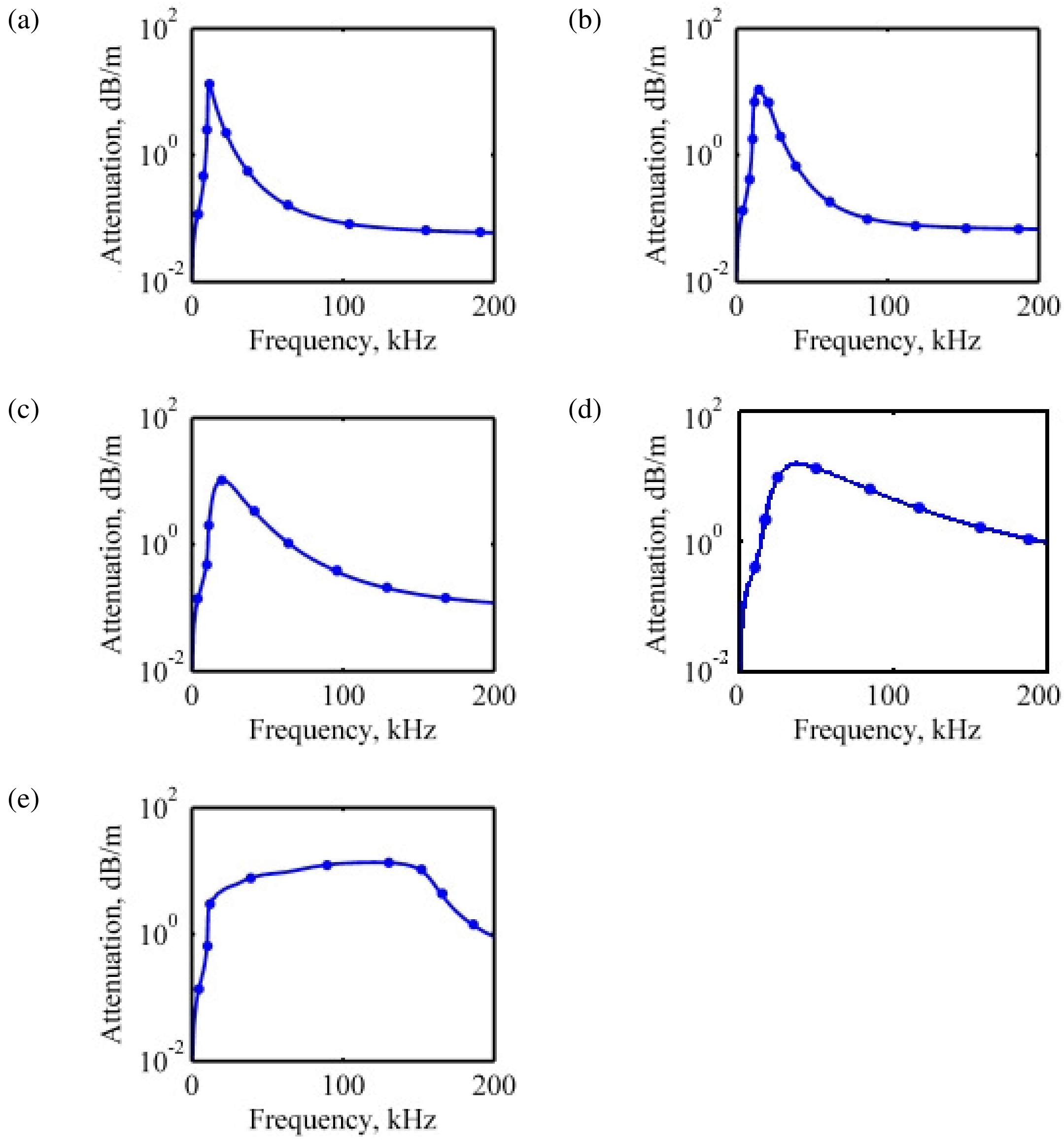

Figure 3.3. Comparison of the attenuation functions for synthetic bubble population (a) uniform (b) triangular (c) Gaussian (d) exponential (e) power law with the computed attenuation functions (denoted by solid line with circle marker) and the attenuation functions in Commander & MacDonald [53] (denoted by solid line).

The attenuation cloud model developed was verified with the synthetic cloud distributions used by Commander and MacDonald [53]. These bubble populations were generated to verify the computed attenuation of the developed cloud model. The computed attenuation functions are observed to overlap with those in Commander and MacDonald in Figure 3.3. The sets of bubble distributions generated range from uniform to Gaussian distributions. In each case, a volume fraction of 10^{-4} % was used.

3.1.2.2. Seawater absorption model

The Francois-Garrison equation shown in Eq. (3.7) for sound absorption in seawater (dB km^{-1}) is used in the absorption model [54, 55].

$$\text{Total sound absorption in seawater} = \frac{A_1 B_1 f_1 \omega^2}{\omega^2 + f_1^2} + \frac{A_2 B_2 f_2 \omega^2}{\omega^2 + f_2^2} + A_3 B_3 \omega^2 \qquad (3.7)$$

In Eq. (3.7), A_1, A_2, A_3, B_1, B_2, B_3, f_1, and f_2 are empirical constants obtained from Francois and Garrison [54, 55]. The absorption of sound in seawater is considered as the sum of three contributions: those from pure water, magnesium sulphate, and boric acid. In the equation, contributions from other reactions have not included [54, 55].

3.1.3. Modelled bubble cloud population

The bubble population measured in the water tank at the A. B. Wood Underwater Acoustic Laboratory, in Institute of Sound Vibration Research (ISVR), University of Southampton, is shown in Figure 3.4. This bubble population is used in the sonar simulation model. The bubble-size distribution produced was confirmed as resembling historical at-sea bubble-size distribution using the technique of Leighton *et al.* [26]. A detailed description of how the bubble-size distribution resembling historical at-sea data was generated in the water tank will be given in Section 3.2.2.

In the sonar simulation model, for the pulses within the same pulse pair, the bubble cloud is assumed unchanged. Between runs, the bubble cloud is allowed to evolve, with the restriction that the overall bubble population does not change. The largest bubble in the bubble population used in the sonar simulation model has a radius of 1000 μm. This bubble has a resonant frequency of approximately 3 kHz at the sea surface.

The simulation of the environment will largely consider a low frequency LFM waveform, which has a frequency range of 2 to 8 kHz. The bubble-size distribution used in the model is extrapolated to include bubbles of radius up to 1500 μm when a waveform of this frequency range is used. This is to ensure the bubbles, whose resonant frequencies are within the frequency range of the driving waveform, are included in the model. While there are very few bubbles with radius of 1000 to 1500 μm in the bubble population used, these bubbles have resonances in the band of the LFM pulse and so are strong scatterers of sound [14].

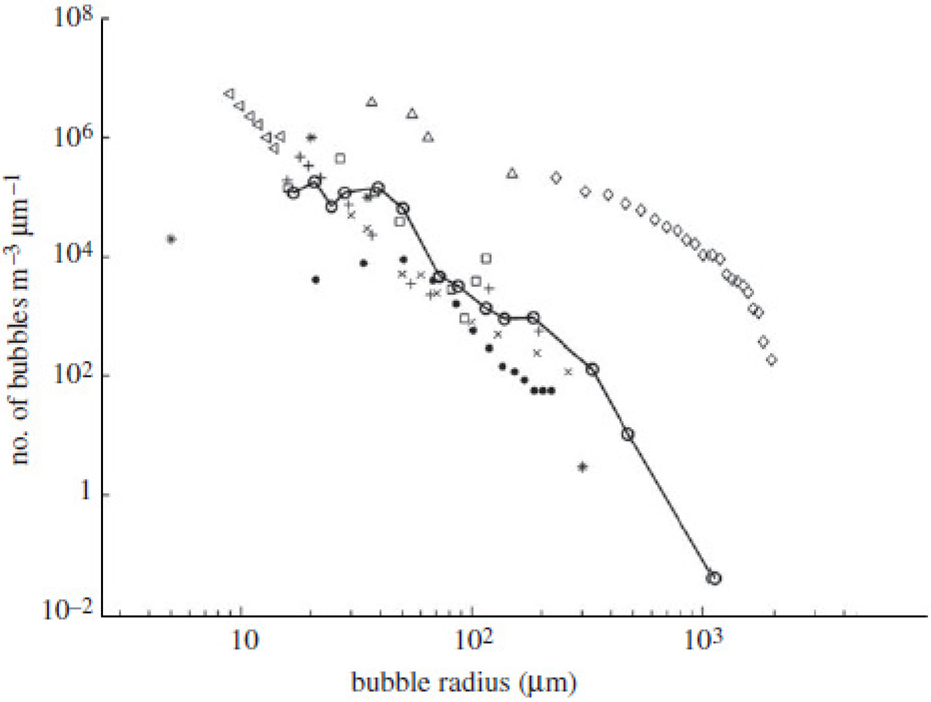

Figure 3.4. Measured bubble-size distributions expressed in number of bubbles per cubic metre per micrometer increment in bubble radius. The line connecting the open-circle data points is the average of six measurements taken approximately 1 second apart in the water tank. Historic measurements are included for comparison (noting that the environmental conditions such as wind speed, measurement depth, etc. reported in the original sources vary). Open symbols are used to indicate open ocean measurements, specifically of Phelps and Leighton [56] (+); Breitz and Medwin [57] (x); Farmer and Vagle [58] (*); Johnson and Cooke [59] (•) (noting that the photographic technique of the latter might have undercounted the smaller bubbles). Close symbols are used to indicate the four surf zone datasets of Leighton *et al.* [26] (□); Deane and Stokes [60] (◊); Phelps *et al.* [61] (Δ); Meers *et al.* [35](◁).

The spatial distribution of the bubble cloud is also included in the sonar simulation model based on the best fit bubble cloud proposed by Culver *et al.* [62]. They carried out several sets of bubble density measurements at various locations using the bubble generator at the A. B. Wood tank. From these measurements, a best fit bubble cloud was found which was orientated by a distribution vent or bubble diffuser placed at the bottom of the tank. The location of the centre of the best fit bubble cloud centre was found to be below the centre of the bubble diffuser. This was marked by a star with the position (x≈ -0.29 m, y≈ -0.24 m) shown in Figure 3.5. The standard deviations of bubble density were estimated to be $\sigma_{x'} \approx 0.38$ m and

$\sigma_{y'} \approx 0.37$ m in the direction of the dashed lines (Figure 3.5). The bubble population shown in Figure 3.4 was measured approximately at the centre of the bubble cloud.

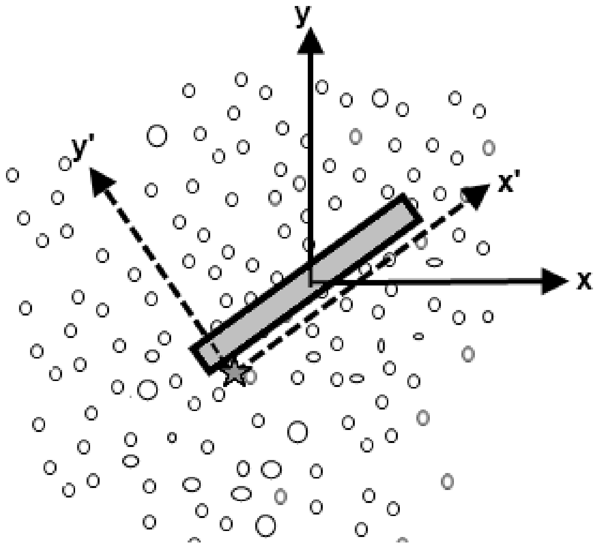

Figure 3.5. Schematics of the bubble cloud produced by the bubble diffuser. The diffuser sits at the bottom of the tank and is approximately 2 m in length. The dashed lines are the axes of the bubble cloud which are assumed to be oriented by the diffuser[1] (diagram drawn not to scale).

3.2. Experimental set-up

Tank experiments were conducted to test the efficacy of the various sonar enhancement techniques for both target detection and classification in presence of a bubble cloud. The setup of the experiments to test the efficacy of the various two-pulse techniques will be described here.

3.2.1. Geometric layout

The experiments were performed in the water tank at A. B. Wood tank. The water tank is a rectangular freshwater tank measuring 8 m x 8 m x 5 m, as shown in Figure 3.6 below. The body of fresh water has a water temperature of approximately 11 °C and a sound speed (in bubble-free conditions) of approximately 1450 ms^{-1}.

---

[1] See Section 3.2.2 for a detailed description of the mechanism of the bubble cloud diffuser.

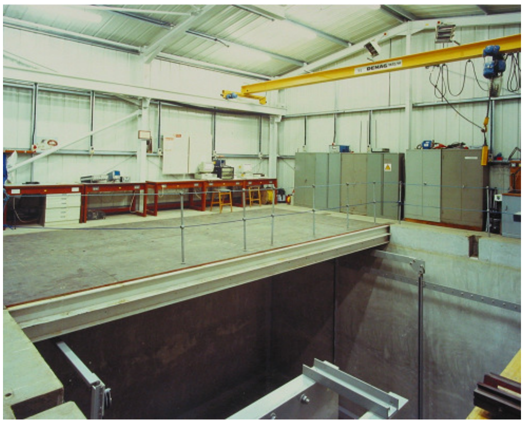

Figure 3.6. A photograph of the A B Wood Underwater Acoustics Laboratory. The tank is shown here as being empty.

The geometric layout of the experiments conducted is shown in Figure 3.7. The centre of the target was on the acoustic axis of the transmitter. The target was placed at two different depths of 2.0 m and 2.6 m, depending on the transducers used. As bubble cloud attenuation varies with frequency, the positions of the bubble diffuser (where the bubbly water is pumped into the main tank; see Figure 3.8) and target has to be placed at different distances from the source when transducers of different frequency bands are used.

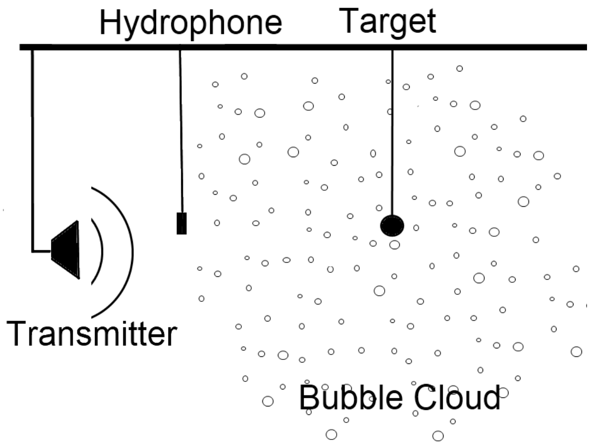

Figure 3.7. Schematic of the tank set-up during tests.

For the low frequency (LF) transducer, the position of the target used was placed at a distance of 2.5 m in front of the source with the bubble diffuser placed at 1.5 m. For the high frequency (HF) transducer, the bubble diffuser was placed at approximately 1 m in front of the source. The target was placed at a distance of 0.65 m in the investigation of the effects of pulse duration on sonar performance, while in the study of the proposed two-pulse techniques, the target was placed further from the source at a distance of 0.85 m. In the latter, pulses of longer pulse duration were used. Hence, the target was placed further from the source to reduce the backscattered contribution of the target. This allowed for more meaningful comparisons of the examined techniques. The near-field to far-field transition of the transducers will be considered in Section 3.2.4.

3.2.2. Generation of the bubble cloud

To facilitate the testing of any technique for detection of linear scatterers in bubbly water in a controlled environment like the A. B. Wood water tank, it will be necessary to produce ocean-like bubble cloud so that the tank bubble cloud is as close to the ocean's as possible. In a typical oceanic bubble-size distribution, the number of large bubbles (with radii in order of 100 μm) present is relatively small, but is not insignificant. Direct injection of gas to the base of a tank does not result in an ocean-like bubble distribution because this method tends to generate large bubbles at the base of the water column, an occurrence which buoyancy opposes under breaking waves.

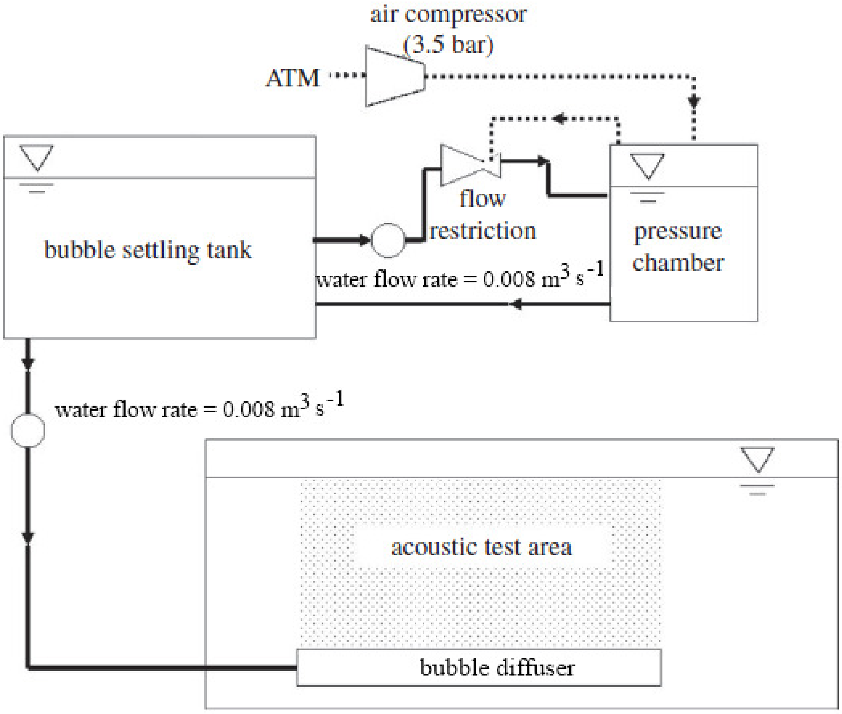

Figure 3.8. The apparatus used to generate the bubble population in the A. B. Wood water tank.

Leighton *et al.* [63] tried a range of candidate techniques (e.g. electrolysis, catalytic conversion of hydrogen peroxide) and found the use of a settling or mixing tank with a Venturi system to be most effective in generating such a bubble cloud. For this technique, the bubble cloud is generated by first producing a ‘milk’ of small bubbles in a settling tank using a Venturi system, and then pumping this 'milk' to the base of the A. B. Wood tank using a bubble diffuser (Figure 3.8). The diffuser is approximately 2 m in length. The bubble-size distribution so produced (shown in Figure 3.4) was confirmed as resembling historical at-sea distribution by applying the techniques of Leighton *et al*. [26] to invert the attenuation of a train of 14 pulses, repeated every second.

3.2.3. Signal acquisition

For the tank tests described in this dissertation, a single hydrophone (Blacknor Technology D140 with built-in preamplifier, calibrated by National Physical Laboratory) was used. The hydrophone used was an omnidirectional receiver with a flat frequency response (±3 dB) between 1 kHz and 150 kHz [64] with a reported frequency range up to 250 kHz [64, 65]. It was mounted approximately 0.1 m in front of the source and 0.2 m above its acoustic axis to reduce reception of the backscatter of the target echoes from the source. Hydrophone data were acquired onto a computer using a National Instruments sound card (DAQ/PXI-2010). Depending on the frequency of the pulse transmitted, the data was acquired either at 200 kHz or 500 kHz. One channel acquired a trigger signal from a trigger box and the second channel acquired the acoustic data. Data were taken with and without the target in position, and with a bubble cloud present.

3.2.4. Signal generation

Experiments were performed over two distinct frequency bands (2 to 8 kHz and 30 to 110 kHz). Two transducers were used. The low frequency (LF) band (2 to 8 kHz) were produced using the 3D-Chirp source [66] from the National Oceanography Centre, Southampton. The high frequency (HF) band of 30 to 110 kHz was transmitted using a custom designed and built transducer.

3.2.4.1. Low frequency transducer

The 3D-chirp source consists of four separate high power transducers, the GeoAcoustics T135D transducers, powered by a matched amplifier, which is controlled by a trigger box and, in turn, a personal computer. The transducers can operate within a bandwidth of between 2 to 8 kHz with an approximate zero-to-peak sound pressure level (SPL) of 212 dB re 1 μPa m. The source characteristics have been documented by previous investigators [5, 67].

Bull *et al*. [67] showed that, by mounting the four transducers in a Maltese Cross (as shown in Figure 3.9), the far-field level would be maximized. The near-field to far-field transition has also been measured to be less than 1.0 m for the frequency range of 2 to 8 kHz during field testing. Each transmitted pulse in the LF experiments used a Blackmann-Harris [68] envelope function and a chirp waveform, over a frequency range of 2 to 8 kHz. For the 3D-chirp sonar system, a Blackmann-Harris envelope function is used because of its very low side-lobe level [66, 69].

In the experiments performed, the transducers were mounted so that they would be side-firing. Figure 3.10 shows the mounting rig that was built for the experiments. The rig was designed to ensure that it could support the acoustic transducers within the A. B. Wood tank. The complete transducer stand measured approximately 3.3 m high.

The desired outgoing sound pulses must be first written as ASCII files before they can be downloaded into the matched amplifier (the 'bottle'). After the pulses have been downloaded into the bottle, they can then be produced acoustically via a trigger box which tells the bottle when to power the transducers with the desired pulse. Hence, there are only a limited number of waveforms in the bottle at any one time.

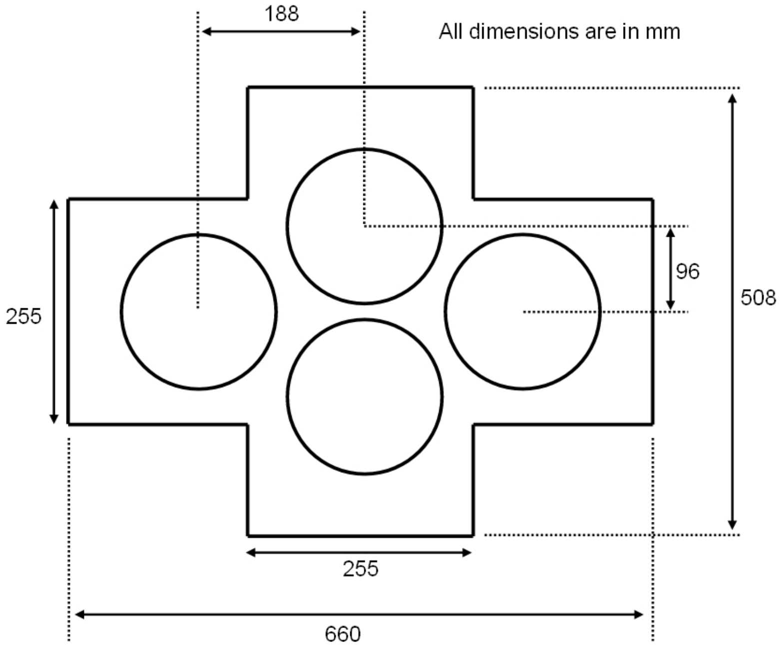

Figure 3.9. The Maltese cross configuration in which the acoustic transducers were arranged for the tests. The transducers were held in place by a steel frame having the dimension shown in the sketch.

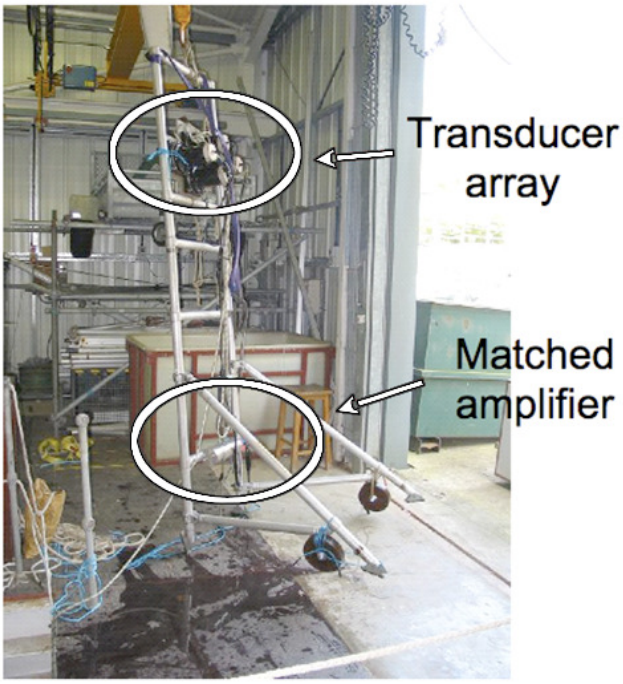

Figure 3.10. Photograph of the scaffolding used to support the acoustic transducers within the A B Wood tank.

3.2.4.2. High frequency transducer

The high frequency (HF) transducer used was a custom made transducer, supplied by Neptune Sonar. This transducer operates within a bandwidth between 30 to 120 kHz, powered by a wideband amplifier. The wideband power amplifier is designed and built by Paul Doust.

The amplifier has an input and output equaliser to improve the fidelity of the waveform generated. The output equaliser consists of a number of passive electrical components such as inductors, transformers and capacitors. Together with the transducer, it forms a bandpass filter [70-72]. The output equaliser has the effect of significantly improving the efficiency of power transfer between the transducer and amplifier over a much broader band of frequencies. The fidelity of the acoustic waveform in the water is further improved using an input equaliser, which corrects for the poor nonlinear phase response of the transducer and its associated output equaliser [73, 74].

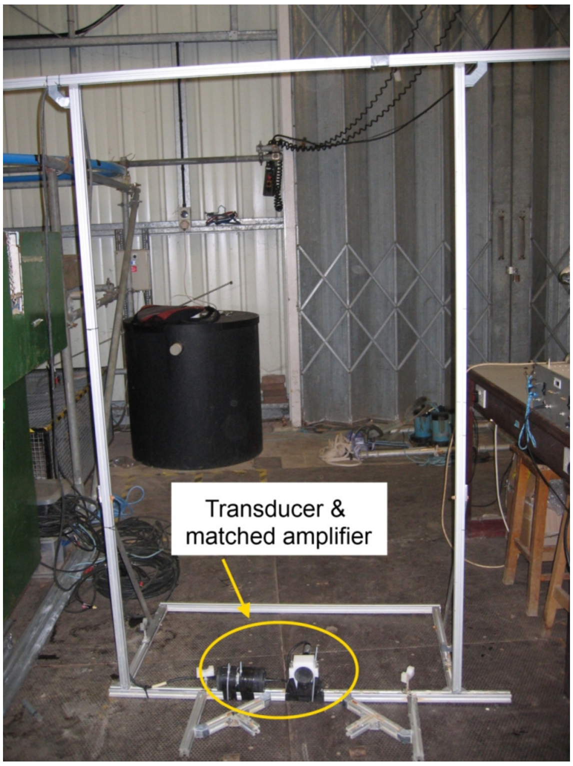

Figure 3.11. Photograph of the frame used to support the high frequency transducer within the water tank in A. B. Wood laboratory.

The HF transducer can transmit a maximum zero-to-peak SPL of between 207.5 and 215.5 dB re 1 μPa m in the frequency range of 30 to 110 kHz, with a maximum zero-to-peak SPL of between 212.5 and 215.5 dB re 1 μPa m for frequencies between 45 and 105 kHz. The beamwidth of the source has been measured in the range of 40 to 100 kHz, where the 3 dB beamwidth is reported as 10° to 30° [75].

$$N = \frac{D^2}{4\lambda} \tag{3.8}$$

From the geometry of the transducer, the extent of the near-field of the source is estimated to be less than 0.3 m for frequencies up to 120 kHz. This estimate is based on Eq. (3.8) obtained from Kinsler *et al.* [76]. Here, N is the extent of near-field, D is the greatest dimension of the source, taken to be the diameter here, and λ is the wavelength of the acoustic wave. The diameter of the transducer used is approximately 114 mm. In the experiments described here, the target and bubble cloud were placed at a distance well above this theoretical near-field limit at a distance of at least 0.65 m.

In tank tests, the transmitted pulse was generated using a universal arbitrary waveform generator (Aim & Thurlby Thandar Instruments TGA 1244) at a transmit sampling frequency of 500 kHz. To evaluate the effects of the pulse duration on sonar performance, the set of driving pulses tested has pulse durations of 70 to 240 μs. Each pulse used a Gaussian envelope function and a linear frequency modulated (LFM) function, over a frequency range of approximately 40 to 110 kHz.

In the investigation of the two-pulse techniques proposed, each pulse has pulse duration of 300 μs with a Tukey [68] envelope function with ratio of taper to constant section set to 0.4. A ratio of zero gives a rectangular envelope while a ratio of 1 gives a Hanning [68] envelope function. A Tukey envelope function was used to increase the amplitude of the driving pulse over a larger frequency bandwidth. Each pulse used has a linear instantaneous frequency function over a frequency of 30 to 110 kHz.

3.2.4.3. Inter-pulse delay

In the experiments, a train of pulse is emitted such that the interval between each pulse pair is 0.5 s. The separation between the pulses in each pulse pair or the inter-pulse delay, Δ_d, is set at 50 ms and 15 ms for the LF and HF experiments respectively. The upper limit for the inter-pulse delay strongly depends on prevailing environmental conditions while the lower limit is determined by considering the reverberation time of the tank used.

For the upper limit of the inter-pulse, important factors that need to be considered include the motion of the scatterer, for example, bubbles rising through buoyancy, motion of the sonar platform and motion of the surrounding medium, for example, through turbulence. For the tank experiments conducted, the motion of the bubbles is thus the crucial factor since there is little turbulence in the test environment and the sensor system is rigidly mounted.

A series of simulations was conducted using a bubble cloud by Finfer [77] in which the individual bubbles were allowed to move. In these simulations, the performance of TWIPS was reduced by 50% when the path-length differences corresponded to 0.37 λ, where λ was the acoustic wavelength. In the LF experiments, a pulse with a centre frequency of 5 kHz is used. The 0.37 λ allowable path-length difference corresponds to about 0.10 m for a frequency of 5 kHz. In general, it can be assumed that the largest bubble in tank will rise fastest (and assuming the largest bubble in the tank has a diameter of order of 2 mm), an upper bound speed can be taken approximately to be 30 cm s^{-1}. This can be inferred from Figure 3.12. For a distance of 0.10 m, this translated to an upper limit of 330 ms. Finfer [77] has also found that, for the A. B. Wood tank, the reverberation time, measured at the location of the hydrophone used, was 240 ms for a frequency of approximately 6 kHz, and correspondingly the reverberation was found to take 65 ms to decay by 15 dB. In practice, a minimum inter-pulse time of 50 ms is found to produce acceptable results [3, 6] and this is used for the LF experiments performed here.

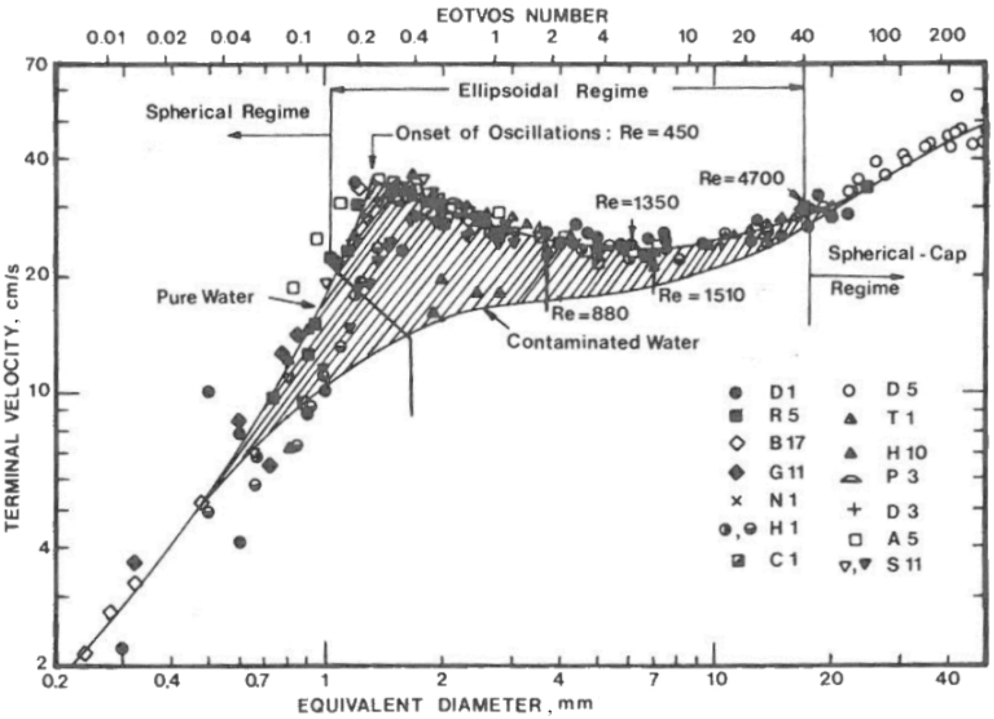

Figure 3.12. Terminal velocity of air bubbles in water at 20° C from Clift *et al.* [78].

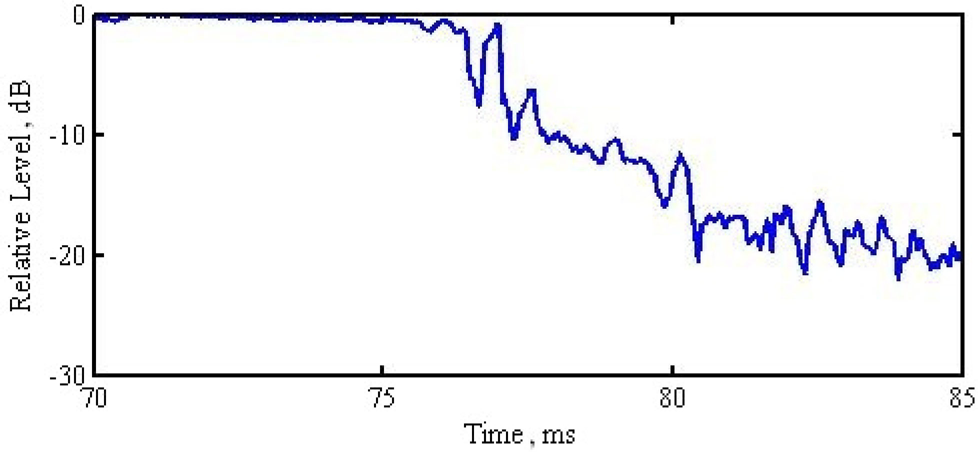

Figure 3.13. Reverberation curve for the A. B. Wood tank for frequency of 60 kHz.

Similarly for the HF experiment, to determine the lower limit, the reverberation of the A. B. Wood tank was measured at several frequencies from 40 to 100 kHz, of which only the measurement at frequency of 60 kHz is shown in Figure 3.13. The reverberation of the tank was found to take less than 10 ms to decay by approximately 15 dB. Figure 3.13 shows the reverberation of the A. B. Wood tank measured at frequency of 60 kHz took approximately 5 ms to decay by approximately 15 dB.

To determine the upper limit of the inter-pulse delay for the HF experiment, the 0.37 λ allowable path-length difference proposed by Finfer [77] is first used. For a centre frequency of 70 kHz, this corresponds to an allowable path-length of approximately 0.008 m. Using an upper bound speed of 30 cm s^{-1}, inferred from Figure 3.12, this translates to an upper limit of 26 ms for a distance of 0.008 m.

This upper limit would appear to be an extremely conservative estimate as the beamwidth of the transmitted beam at the bubble cloud has not been considered. In addition, the bulk of the bubble cloud used contains bubbles with diameter between 40 to 500 µm. These bubbles have rising velocities, which are considerably less than 30 cm s^{-1}. For example, a bubble diameter of 1000 µm will have a terminal velocity of approximately 20 cm s^{-1} (see Figure 3.12). To obtain an estimate of the upper limit, the insonified width can be compared to the motion of the bubbles in the two-dimensional case. Using a sonar beamwidth of 10°, this translates to an insonified width of approximately 0.18 m at a distance of 1 m. Using a rising speed of 30 cm s^{-1} (this being the upper bound speed for the range of bubble sizes present in the tank bubble population [78]), a conservative estimate of 60 ms is obtained for a 10% change in the insonified cloud. The value of 15 ms used for the inter-pulse delay is well within this maximum value. The inter-pulse delay, Δ_d, can also be regarded as defining the maximum range of the two-pulse system. Using $c\Delta_d/2$, this corresponds roughly to maximum range of 10 m (rounded to nearest 10 m) for Δ_d of 15 ms.

3.2.5. Targets used

Two targets were used in the experiments so as to have targets with several values of target strength (TS). The targets employed included a steel disc of diameter 0.46 m and thickness 0.05 m, and a solid sphere of diameter of 0.12 m. The steel disc is rotated by an angle of 10° to give a TS value of -15 dB while the sphere gives a TS value of -30 dB.

Figure 3.14. Two of the targets used from the tests with (a) a miscellaneous steel weight of diameter 0.46 m and thickness 0.05 m and (b) spherical weight of diameter of 0.12 m.

3.2.6. Measurement procedures

Measurements were performed in two configurations. All measurements were performed with the target in and out of water. This was necessary for the computation of a Receiver Operating Characteristics (ROC) curve which will be described in Section 3.3. "Target in" measurements and their respective "Target out" measurements were never performed at intervals greater than 5 minutes. This was done to ensure the bubble cloud conditions for the two data sets remain fairly consistent.

There was limited control of the bubble cloud void fraction via the valve controlling air flow from the air compressor into the pressurisation tank, and this control was not calibrated. Whilst ideally, the bubble size distribution would be measured during each experiment, this was not practical because such measurements are extremely time-consuming and require equipment not frequently available in this unfunded project (which substantially relied on borrowed equipment).

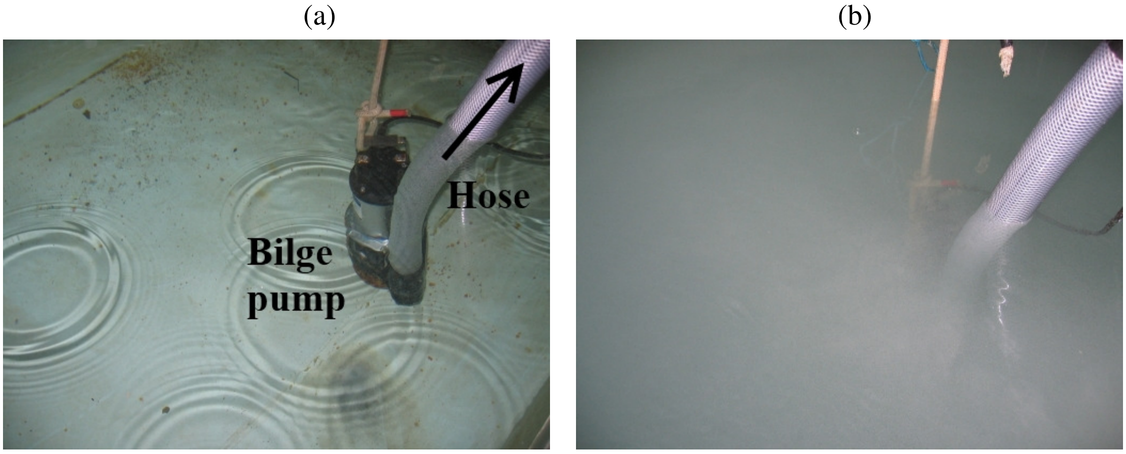

Figure 3.15. The visibility within the bubble settling tank in (a) when the Venturi system first started and (b) after 5 minutes.

Instead, once a bubble population had been measured, protocols were placed to ensure the conditions that produced it (and hence the bubble population generated) were replicated as follows. Firstly, the air tank pressure was always kept at a constant level of 2.5 bar. Secondly, the water level in the bubble settling tank was always at the same level when measurements were taken. Thirdly, the flow rate through the Venturi system was always fixed at the same level. Fourthly, the water flow rates in and out of the bubble settling tank were adjusted such that they were the same. Lastly, the measurements were always carried out at the same time interval, approximately 5 minutes after the Venturi system was switched on and for a further twenty minutes. Throughout the measurements, checks would also be made at regular intervals to ensure that there is no significant difference in visibility throughout the water within the bubble settling tank (see Figure 3.15). The visibility within the bubble settling tank when the Venturi system first started and after 5 minutes is illustrated in Figure 3.15. The bilge pump placed at a depth of approximately 1 m took the water from the settling tank via the hose to the base of A. B. Wood tank. Both the pump and the hose within the settling tank can be observed in Figure 3.15 to be no longer visible 5 minutes after the Venturi system was switched on.

3.3. Notations and criteria for determining performance

3.3.1. Notation used

Throughout the thesis, the study of the two-pulse techniques like TWIPS will require the uses of terms like $p(t)$, $p_{-}(t)$ and $p_{+}(t)$ defined in Chapter 2. The smoothed envelope of the processed versions of $p(t)$, $p_-(t)$ and $p_+(t)$ are denoted by P, P_- and P_+ respectively. In certain instances, filter is used to enhance particular harmonics. When such processing is performed, then the notation is augmented so that P_{m+} denotes the envelope of $p_+(t)$ after applying a filter whose centre frequency is *m* times the centre frequency of the driving pulse. Hence, P_{1-} will denote the envelope of $p_-(t)$ after applying a filter matched to the frequency of the driving pulse and P_{2+} will denote the envelope of $p_+(t)$ after a filter matched to twice the frequency of the driving pulse is applied.

3.3.2. Standard sonar processing

There is currently no established baseline to compare the performance of a sonar for the detection of solid objects in bubbly water for techniques like TWIPS [3]. As such, a baseline, referred to as 'standard sonar processing' is established here to facilitate comparison with the other techniques proposed. The standard sonar processing uses the filtered responses of the returned signals. As the linear target enhancement techniques introduced are dependent on the returns from more than one pulse, an averaging of this standard sonar processing is carried out for each pair or sequence to ensure fair comparison between these techniques and the standard sonar processing defined here. Henceforth, the standard sonar processing technique consists of averaging the smoothed envelopes of the filtered responses from the pulse pair or sequence.

3.3.3. Classification of linear and nonlinear scatterers

To determine the efficacy of the various techniques in distinguishing linear scatterers from nonlinear scatterers, image plots are used to compare the processed outputs of the techniques introduced and that of standard sonar processing.

The returned signals (over consecutive runs) are processed and for display purposes are then stacked (with output values represented by colour, as defined in the colour bar), forming the image plots for comparison. These image plots (displayed in a linear colour scale) show the repeatability of the test as the bubble cloud evolves.

3.3.4. Detection of linear scatterers

The performance of each technique in the detection of linear scatterers within a bubble cloud is determined by comparing its ROC curve with one another. ROC curves were first applied to assess how well a radar in World War II can distinguish between the random interference (noise) from signals of enemy planes [79] and are used widely to depict the trade-off between probability of detection (a true positive) and probability of false alarm (a false positive) of signal detection theory [80, 81].

The ROC curves presented are generated using the distribution of the backscattered responses in a region containing the backscattered reverberation of the bubble cloud and target in the target absent and target present cases. In the LF experiments, where the target was placed at 2.5 m from the transducer and the bubble cloud placed at 1.5 m from the transducer, this region was taken to span from 1.5 to 4 ms so as to encompass the backscattered reverberation of the bubble cloud and target.

In the HF experiments, the target was placed close to the bubble diffuser such that the target could be taken to be close to or within the bubble cloud, dependent on the natural evolution of the bubble cloud. The region selected corresponded to approximately 0.15 ms centred on the target position. A region of 0.15 ms was chosen so that only the first echo return from the target and the backscattered reverberation of the bubble cloud were included. The backscattered characteristics of a solid sphere submerged in water will generally appear in the form of multiple echoes of the original pulse, caused by the excitation of a number of elastic waves [82-85]. For a steel sphere of diameter of 0.12 m (and circumference of 0.375 m), and a Rayleigh wave speed of approximately 3000 m s^{-1} [86], the second echo return would arrive approximately 0.125 ms after the first echo return.

To summarise the performance of a technique, two parameters will be inferred from its ROC curve. These are the probability of detection before giving a single false alarm and the area under the ROC curve. The former gives the probability a technique will give a correct decision (detection) before giving a wrong decision (false alarm). For the latter, an indication of the average performance of a technique is obtained with the area under the ROC curve. A bigger area under a ROC curve will indicate a better average performance [87]. In many instances, this can often be inferred from the ROC curves visually. In sonar applications, it is important to have an idea of the performance of a particular technique from its ROC curve. Depending on the scenario, even small levels of false alarm can be costly (for example, a false alarm in mine detection could entail closure of a sea route and deployment of divers).

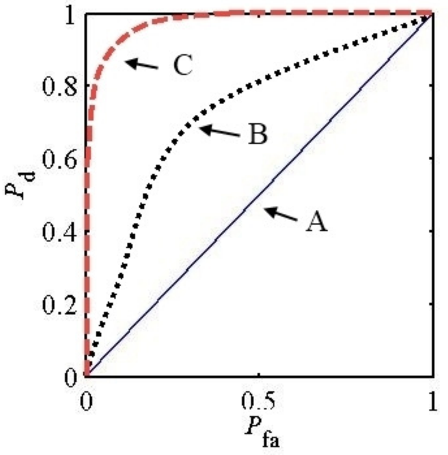

Figure 3.16. Illustrative figure comparing three ROC curves with curve A, B and C denoted by solid, dotted and dashed lines respectively where P_d denotes probability of detection and P_{fa} denotes probability of false alarm.

Figure 3.16 shows three ROC curves representing those of a poor, medicore, and good technique as depicted by curve A, B and C respectively. ROC curve A shows a technique, which is extremely poor, with 50/50 odds of making a correct decision. This is no better than flipping a coin to decide whether a sonar contact is a genuine target or clutter. Curve A covers an area of 0.5. Curve A is also sometimes known as the 50/50 line. As the curve moves more to the top left (curve B), it indicates better average performance as represented by a greater area under the ROC curve compare to curve A. Curve C indicates that it has the best average performance amongst the three, since it has the greatest area under its curve. While it may not be always the case, the probability of true positive before giving a single false alarm is also highest for Curve C. By inferring the two parameters from its ROC curve, the detection performance of each technique developed in this thesis can thus be summarised quantitatively.

3.4. Summary

The review of current sonar enhancement work in ocean acoustics and biomedical imaging in Chapter 2 has introduced several techniques and ideas. These techniques and ideas will subsequently be investigated theoretically and experimentally.

For the theoretical work, a sonar simulation model has been developed based on the non-linear Keller-Miksis model. While the Keller-Miksis model is highly sophisticated, thermal damping is not included in this model. Hence, the conditions under which under-estimation of the total damping can occur were described. Damping can reduce the resonant frequency of a system, causes decay of response in time and phase change. In the sonar simulation model, bubble cloud attenuation has been incorporated using the linear attenuation model of Commander and Prosperetti [50]. This cloud attenuation model was then verified with the work of Commander and McDonald [53].

All the sonar experimental works were carried out in the A. B. Wood water tank at ISVR, University of Southampton. The set-up of the experiment conducted has been described. Two different transducers were used so that pulses in different frequency bands can be studied. One is termed the low frequency (LF) pulse with a frequency band of 2 to 8 kHz while the other is termed the high frequency (HF) pulse with a frequency band of 30 to 110 kHz. A section was devoted to how the bubble cloud was produced in the water tank to ensure the produced bubble population would be close to that of a typical oceanic population. The steps taken to ensure the conditions used to produce the bubble cloud (and hence the population produced) were replicated were also described. These steps were necessary because measuring the bubble size distribution in each experiment is an expensive and time-consuming task which relied on borrowed equipment not frequently available. Hence, the measurements of the bubble size distribution were not done frequently in this thesis.

The chapter concluded with a description of the notations to be used in subsequent chapters as well as the criteria of performance which are adopted throughout the thesis. These criteria are used to assess the performances of the techniques and ideas proposed in this thesis.

Chapter 4. Single bubble model

4.1. Introduction

This chapter will describe the theoretical response of a single bubble when excited by an incident plane wave using the single bubble model described in Section 3.1.1. Here, two types of signals will be studied – a narrowband and a wideband signal. Following Leighton *et al.* [3, 6], the narrowband signal consists of a Gaussian-modulated single frequency pulse of finite duration. The wideband signal is a linear frequency modulated (LFM) waveform, also known as a LFM chirp. For each type of signal, three key pulse characteristics are investigated. They are their frequency, amplitude and duration. The effects of these parameters on the pressure radiated by a bubble when excited by an incident plane wave and their implications on the sonar enhancement will be discussed where appropriate. For the study of the pulse frequency, two representative frequencies are used. A frequency of 6 kHz is used to represent a 'low' frequency (LF) pulse. This frequency has been extensively tested by Leighton *et al.* [3, 6] for TWIPS. For the 'high' frequency (HF) pulse, a frequency of 80 kHz is used.

Here, the linear and nonlinear response of a bubble will be presented. The linear response of a bubble will be represented by its response at the fundamental frequency while the nonlinear bubble response will be represented by its response at its second harmonic. While the nonlinear response of a bubble, especially at large amplitude of excitation, will contain harmonics of higher order, the higher harmonics can often be neglected as the second harmonic tends to be the most prominent. This is especially so in the context of sonar applications where the source level of the transducer is often not sufficient to drive the whole oceanic bubble cloud to generate higher harmonics. The detection of higher harmonics will often be masked by the high ambient noise. Hence, the linear response of the bubble will be represented here by its response at its fundamental frequency while its nonlinear response will be represented by its second harmonic response.

In the analysis that follows, the theoretical model involves the simulation of the radial motion of the bubble and the pressure waves radiated by it, after applying acoustic pressure signal as the forcing or excitation function. This is the nonlinear Keller-Miksis bubble model described in Chapter 3. In the plots showing the response of a bubble as a function of the radius of that bubble, the peak pressure radiated by a bubble at 1 m from the bubble is presented. This peak pressure of the bubble at the fundamental frequency (the linear response) is obtained by applying a filter that is matched to the instantaneous frequency and bandwidth parameter of the driving pulse to the returned signal. The second harmonic response of the bubble (the nonlinear response) is obtained by applying a filter that is matched to twice the instantaneous frequency and bandwidth parameter of the driving pulse to the returned signal [88, 89].

The analysis here is limited to only bubble radii up to only 1000 μm. This is because historical measurements have shown that oceanic bubble populations contain mostly bubbles with radii less than 1000 μm (see Figure 3.4). It is noted, as bubble size increases, it will reach a point where the long acoustic wavelength assumption (i.e. $kR_o \ll 1$, where k is the wavenumber and R_o is the equilibrium bubble radius) which underpins the theoretical model will break down. In such a limit of the bubble size being much larger than the acoustic wavelength, the process is geometric, with the bubbles generating acoustic shadows [27].

This chapter concludes with a discussion of the implications of the findings of the single bubble model on sonar enhancement in bubbly water.

4.2. Narrowband signal

4.2.1. Frequency

Two sets of comparison can be made to compare the effects of using pulses of different frequencies (6 kHz and 80 kHz). Either pulses of the same number of cycles or same duration can be used for this comparison. As the bubble pulsation takes a finite time to ring-up [30-32, 34, 35, 90, 91] and ring-down [26], and because the bubble can pulsate nonlinearly [92, 93], the number of cycles within a pulse which is related to pulse duration can be crucial parameters.

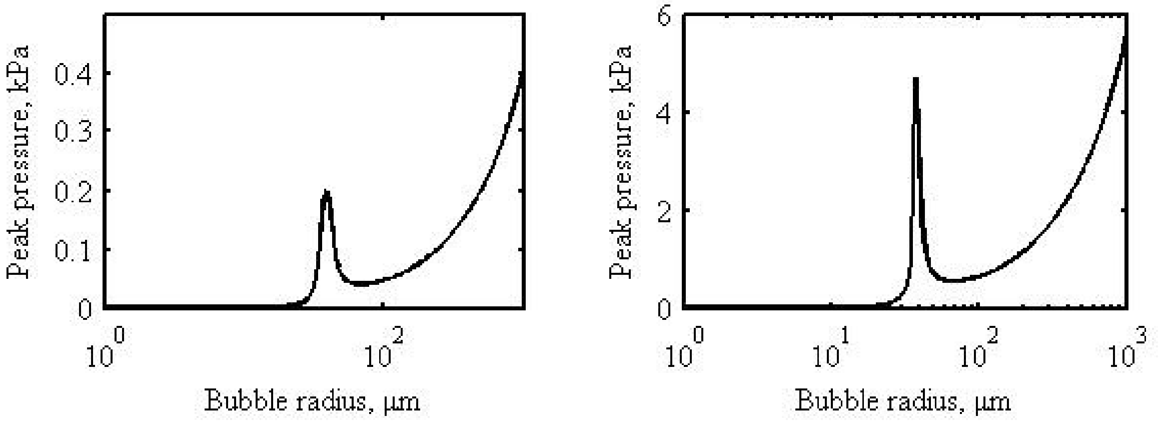
(a) Eight-cycle long - Fundamental response

(b) 1.3 ms - Fundamental response

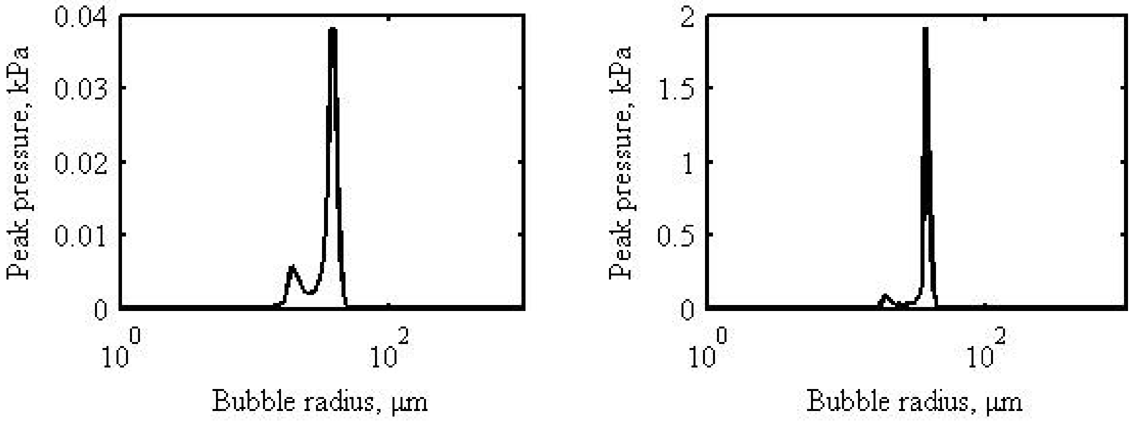
(c) Eight-cycle long - Second harmonic response

(d) 1.3 ms - Second harmonic response

Figure 4.1. The peak pressure radiated by a single bubble at 1 m as a function of the radius of that bubble after applying a matched filter at the driving frequency and second harmonic are shown in (a) and (c) respectively when driven by a 10 kPa Gaussian-modulated eight-cycle pulse of center frequency of 80 kHz. In (b) and (d), the peak bubble pressure radiated after applying a matched filter at the driving frequency and second harmonic respectively when driven by the same pulse with a higher duration of 1.3 ms are shown.

In Figure 4.1, the peak pressure radiated by a single bubble at 1 m after applying a matched filter at the fundamental frequency and second harmonic of the driving pulse as a function of the radius of that bubble when excited by two pulses of different durations are shown. For the same amplitude of 10 kPa, an eight-cycle long pulse gives similar trends as a 1.3 ms pulse with a frequency of 80 kHz for the linear and nonlinear responses of a bubble across the range of bubble radii studied. However, there are two notable differences. Firstly, the range of bubbles excited to high pulsations for the eight-cycle pulse is larger than that of the

1.3 ms pulse as shown in Figure 4.1. This is the result of the narrower bandwidth associated with a longer pulse [94]. Secondly, the level of nonlinear response for the longer pulse of 1.3 ms is significantly higher than that of the shorter eight-cycle pulse. The total energy associated with the 1.3 ms pulse is higher because the pulse duration is increased with the amplitude kept constant. A longer pulse (which has more energy) can drive a bubble to a higher amplitude of pulsation. This consequently results in a higher peak pressure radiated by the bubble. In general, nonlinear effects are associated with high amplitude of bubble pulsation [92]. For the subsequent comparisons of pulse parameters here, other than that of pulse duration, the analysis will be restricted to pulses of same number of cycles.

To investigate the effects of varying frequency on the behaviour of a single bubble, pulses of two different frequencies (6 and 80 kHz) of eight cycles each are used. Figure 4.2 shows the peak pressure radiated by a bubble at 1 m as a function of the bubble radius after applying a matched filter at the fundamental frequency and second harmonic of the driving pulse. Gaussian-modulated eight-cycle pulses of different centre frequencies have been applied as the forcing function. In each pulse, an amplitude of 10 kPa has been used.

Figures 4.2(a) and (b) shows the peak pressure radiated by a bubble as a function of the bubble radius when driven by a pulse of 6 kHz and 80 kHz respectively when applied with a matched filter at the fundamental frequency of the driving pulse. The peak pressure across the range of bubble radii studied has a local maximum at the bubble radius resonant with the driving frequency, and then slowly increases with bubble size. While this is not obvious for Figure 4.2(a) because of the frequency used with respect to the range of bubble size studied, it can be clearly observed in Figure 4.2(b) where the frequency used is higher. At the other extreme, as the bubble size becomes much less than resonance, the peak pressure radiated by the bubble tends to zero. This trend is observed in both Figures 4.2(a) and (b).

For the peak pressure radiated by a bubble after applying a matched filter at the fundamental frequency of the driving pulse, both Figures 4.2(a) and (b) show peaks at the bubble radius resonant with the driving frequency. At resonance, the greater bubble response is due to the strong coupling with the incident acoustic waves, as manifested by the large amplitude of wall pulsation. A much larger bubble with a lower resonant frequency, in contrast, pulsates to a negligible degree. This is because a larger bubble cannot respond rapidly enough. As the bubble size tends towards being larger than the acoustic wavelength of the driving pulse, the backscattering from these bubbles are mainly geometric in nature and increase with size [95]. The bubble starts to behave as a linear scatterer. For a higher frequency of 80 kHz, bubbles much larger than the bubble resonant radius are observed to give greater responses than the bubble at resonance (Figure 4.2(b)). The peak at the bubble radius resonant with the driving frequency for the lower frequency pulse, on the other hand, has the greatest response for the range of bubble size studied (Figure 4.2(a)).

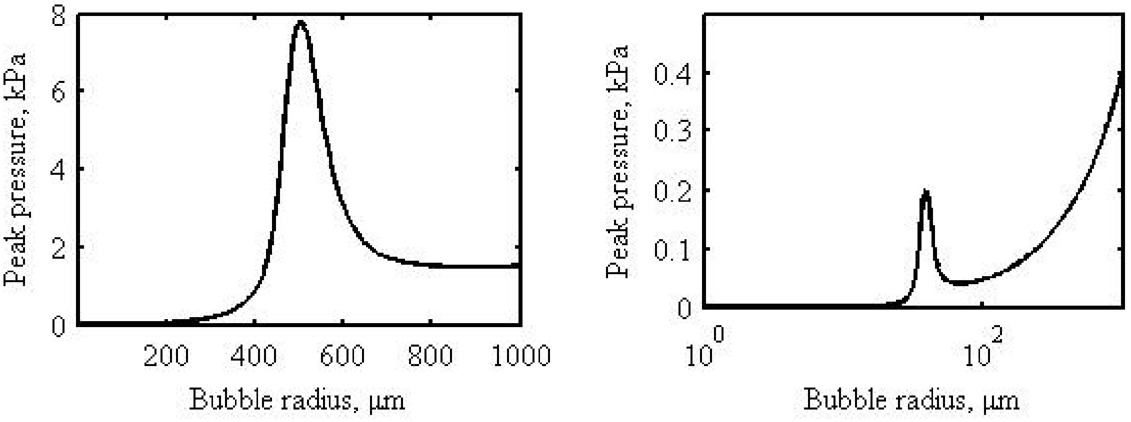
(a) 6 kHz - Fundamental response

(b) 80 kHz - Fundamental response

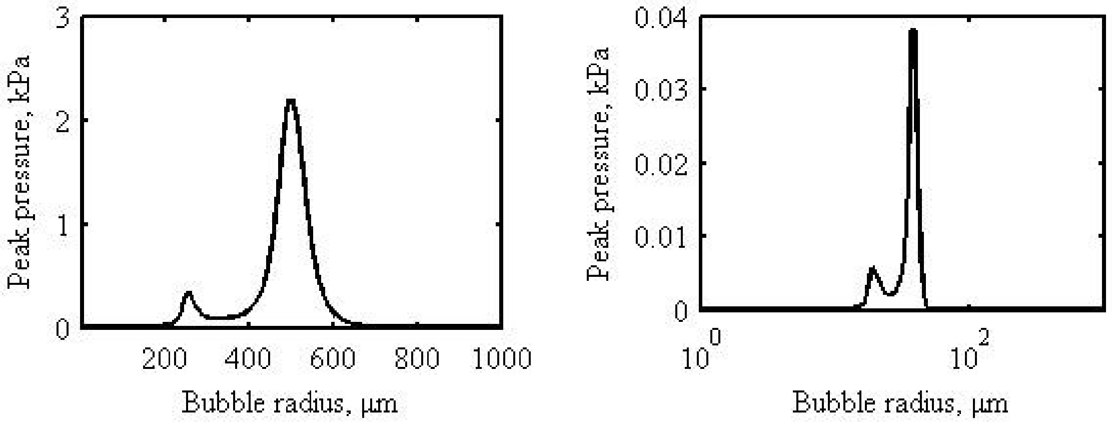
(c) 6 kHz - Second harmonic response

(d) 80 kHz - Second harmonic response

Figure 4.2. The peak pressure radiated by a single bubble at 1 m as a function of the radius of that bubble after applying a matched filter at the driving frequency and second harmonic are shown in (a) and (c) respectively when driven by a Gaussian-modulated eight-cycle pulse of center frequency of 6 kHz. In (b) and (d), the peak bubble pressure radiated after applying a matched filter at the driving frequency and second harmonic respectively when driven by a Gaussian-modulated eight-cycle pulse of center frequency of 80 kHz are shown. Both pulses have amplitude of 10 kPa.

For a bubble, a large amplitude of pulsation near resonance leads to a nonlinear pulsation as shown by the higher second harmonics bubble response at the radius resonant with the driving frequency (Figures 4.2(c) and (d)). The x-axes of Figures 4.2(b) and (d) have been presented on a logarithmic scale to better emphasize the peak pressure radiated by a bubble as a function of the bubble radius when excited at different frequencies. Bubbles, which are sufficiently small that their resonant frequencies are higher than the frequency of the driving pulse, can still respond rapidly to the compressive or expansive cycles, and hence can still undergo nonlinear pulsations, albeit to a lesser extent than the bubble radius resonant with the driving frequency [95]. Compared to the linear response of a bubble, the nonlinear response of a bubble at its resonant bubble radius will be a global maximum [1]. In Figures 4.2(c) and (d), the smaller bubbles (relative to the resonant bubble radius) are shown to have higher nonlinear responses than larger bubbles with bubbles whose pulsation resonances are multiples of the insonifying frequency having a corresponding increase in nonlinear responses.

In Figure 4.2(a), the peak pressure radiated by the resonant bubble at 1 m is observed to be higher for a lower frequency of 6 kHz compared to a higher frequency of 80 kHz (Figure 4.2(b)). This is because when the driving frequency is lower, a larger bubble is driven to resonance. A larger bubble will have larger amplitude of wall pulsation.

The implications for sonar applications will thus seem obvious. Historical measurement data has shown a typical oceanic bubble cloud to contain mostly bubbles whose size ranges from microns to millimetres over several order of magnitude [35, 56-60, 96, 97] with the majority of bubble radii below 1 mm. For any technique which exploits the nonlinearity of bubbles to enhance target detection and classification, it will appear a pulse of lower frequency will be preferred to ensure a wider distribution of bubble radii can pulsate to a nonlinear state. More importantly, with a lower frequency pulse, the range of the larger bubbles in a bubble cloud, which will behave as mainly linear scatterers, will be reduced.

4.2.2. Amplitude

The peak pressure radiated by a bubble as a function of the bubble radius when driven by a Gaussian-modulated eight-cycle pulse of centre frequency of 80 kHz for two representative amplitudes of 1 kPa and 100 kPa are shown in Figure 4.3. As the amplitude of the driving signal becomes higher, the nonlinear response of a bubble becomes increasingly apparent. This is represented by a higher maximum (for the peak pressure radiated) at the bubble radius resonant with the driving frequency as can be seen in Figure 4.3(d) when compared to Figure 4.3(c).

At lower amplitudes, for example, an amplitude of 1 kPa, the response of a bubble is approximately linear [27] and the response at the second harmonic is low as represented by a lower peak pressure radiated (see Figure 4.3(c)). In Figure 4.3(d), when the amplitude of the pulse is 100 kPa, the nonlinearities are apparent. The presence of ambient noise will mask the low level of nonlinear responses.

(a) 1 kPa - Fundamental response (b) 100 kPa - Fundamental response

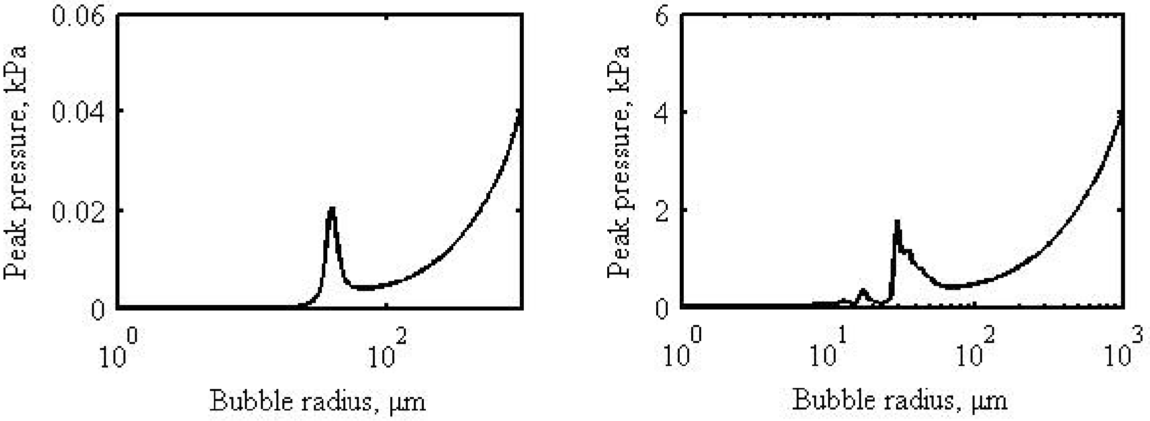

(c) 1 kPa - Second harmonic response (d) 100 kPa - Second harmonic response

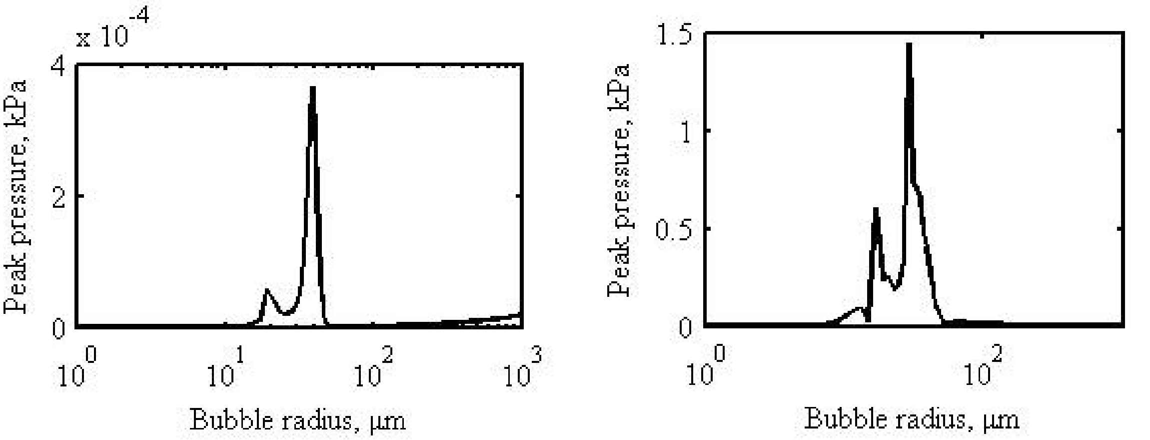

Figure 4.3. The peak pressure radiated by a single bubble at 1 m as a function of the radius of that bubble after applying a matched filter at the driving frequency and second harmonic are shown in (a) and (c) respectively when driven by a 1 kPa Gaussian-modulated eight-cycle pulse of center frequency of 80 kHz. In (b) and (d), the peak bubble pressure radiated after applying a matched filter at the driving frequency and second harmonic respectively when driven by the same pulse with a higher amplitude of 100 kPa are shown.

Comparing Figures 4.3(c) to (d), the bubble response at its second harmonic is also more apparent across a wider range of bubble sizes for the higher amplitude case of 100 kPa. With an increase in the amplitude of the driving pulse, there is a corresponding energy increase in the frequency band around the driving frequency. The bubble radii resonant with these frequencies will be excited and if the amplitude of excitation is high enough, high nonlinear pulsations result with harmonic responses occurring at these bubble radii.

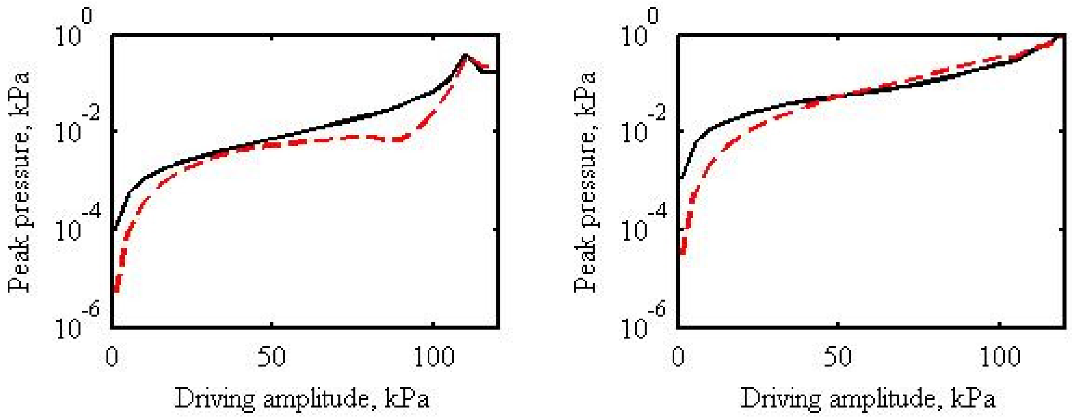
(a) 15 μm

(b) 27 μm

(c) 225 μm

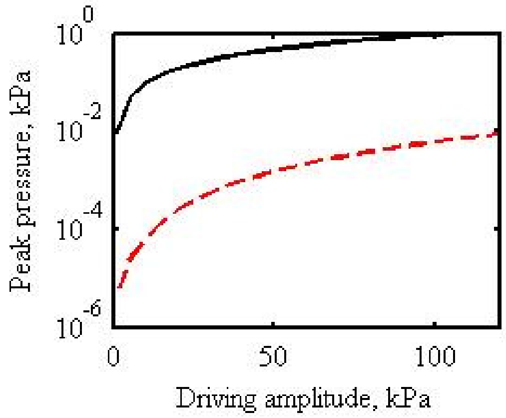

Figure 4.4. The peak pressure radiated by a single bubble at 1 m of radius (a) 15 μm (b) 27 μm and (c) 225 μm when excited by Gaussian-modulated eight-cycle pulse of center frequency of 80 kHz as a function of the amplitude of the driving signal. The solid line denotes the peak bubble pressure after applying a matched filter at the fundamental frequency while the dotted line denotes the peak bubble pressure after applying a matched filter at the second harmonic of the driving pulse.

The peak pressure radiated by a bubble at 1 m for a range of amplitudes is shown in Figure 4.4 for three representative bubble radii when a Gaussian-modulated eight-cycle pulse of center frequency of 80 kHz is used as a driving pulse. When the amplitude of the driving pulse is low, a bubble is commonly treated as a linear scatterer because of its low nonlinear response. As the amplitude of the driving pulse increases, the nonlinear pulsation of the bubble becomes more apparent and harmonics are emitted at integer multiples of the driving frequency up to higher orders. This nonlinear behaviour of a bubble here is represented by the peak pressure radiated by the bubble at 1 m from the bubble matched filtered at its second harmonic as shown in Figure 4.4.

One factor which influences the degree of nonlinearity of a bubble is the bubble resonant frequency relative to the frequency of the driving pulse. Figure 4.4(a) shows the bubble response when excited by a range of amplitudes for a bubble radius with a resonant frequency higher than the driving frequency of 80 kHz. Figures 4.4(b) and (c) show the bubble response when excited by a range of amplitudes for a bubble radius close to and lower than the driving frequency respectively.

For a bubble radius with resonant frequency close to the driving frequency, high linear and nonlinear bubble responses result. In Figure 4.4(b), the high linear and nonlinear responses are represented by the high peak pressure radiated by the bubble at the fundamental frequency and second harmonic respectively. The level of the nonlinear response is high relative to the linear response of the bubble as some of the energy which will reside at the fundamental frequency will be “pumped” up to the higher order harmonics as the amplitude of the driving pulse increases. This effect is two-fold. It reduces the linear response (at the fundamental frequency) and increases the nonlinear response (at the higher harmonics).

For bubbles with resonant frequencies higher than the driving frequency, these bubbles can still respond rapidly to the compressive or expansive half cycles, and hence can still undergo nonlinear pulsations, albeit to a lesser extent than those bubbles with resonant frequencies close to the frequency of the driving pulse [95]. These nonlinear pulsations also increase with increasing amplitude of the driving pulse as exemplified by an increase in the peak pressure radiated by the bubble in its second harmonics (Figure 4.4(a)). The larger bubbles (with resonant frequencies lower than the driving frequencies) cannot respond rapidly enough to generate a high nonlinear response even at high amplitudes, and thus can only be considered as linear scatterers. In Figure 4.4(c), the pressure waves radiated by a bubble at 1 m from the bubble contain frequency components which resided mainly in the fundamental frequency.

This discussion highlights the importance of using a sufficiently high amplitude driving pulse if a bubble is to be excited to a nonlinear state. For oceanic applications, a source of sufficiently high amplitude will thus have to be used. Figure 4.4 appears to suggest this amplitude will have to be at least in the order of tens of kilopascals. For a bubble with resonant frequency close to the frequency of the driving pulse, it can be estimated from Figure 4.4(b) that proportion of second harmonic responses relative to the responses in the fundamental frequency increases from approximately 2% to 40% when the driving amplitude is increased from 1 to 20 kPa. This implies at low amplitudes, even for bubbles close to resonance, bubbles will tend to behave as linear scatterers. For practical applications, in the case of an absence of a source of sufficiently high amplitude, the effective range of the sonar will be compromised after taking losses like bubble cloud attenuation and propagation loss into account. The above discussion also inadvertently highlights the debilitating effect of large bubbles. Figure 4.4(c) suggests that, if the bubble cloud contains mainly large bubbles, it will be difficult to drive the bubble cloud to a nonlinear state. This indicates the choice of a lower frequency driving pulse.

4.2.3. Pulse duration

In Figure 4.5, the effect of varying duration of the driving pulse is shown for two different amplitudes. Three representative bubble radii are presented. For bubble radii of 15 μm and 27 μm, the bubble resonant frequencies are higher than or close to the driving frequency while a bubble radius of 225 μm has a resonant frequency lower than the driving frequency. For the pulse used here, Figure 4.5 shows that with increasing the pulse duration while keeping the amplitude of the pulse constant, the peak pressure radiated by a bubble at both the fundamental frequency and second harmonic increase. This is because it is the matched-filtered responses which are presented in Figure 4.5. Without matched-filtering, the peak pressure radiated by a bubble typically reaches steady state within a few tens of cycles of the driving pulse [30],

In Figure 4.5, the increase in nonlinear responses of bubbles with resonant frequencies close to, or higher than, the driving frequency is observed to be more significant at a higher amplitude of 100 kPa than 10 kPa. In addition, when the duration of pulse is less than a few cycles, transient effects prior to reaching steady-state oscillation are observed, which is related to the ring-up time of a bubble [30]. This is more prominent in Figures 4.5(a), (c) and (e) where the amplitude of the driving pulse is lower. This transient effects prior to reaching steady-state oscillation suggests that use of very short-duration pulses can result in less backscatter from the bubbles if certain conditions like amplitude and bubble sizes are met [30]. This potentially can be exploited in enhancement of target detection in bubbly water. This transient effect will be studied in Chapter 6.

(a) 15 µm (10 kPa) (b) 15 µm (100 kPa)

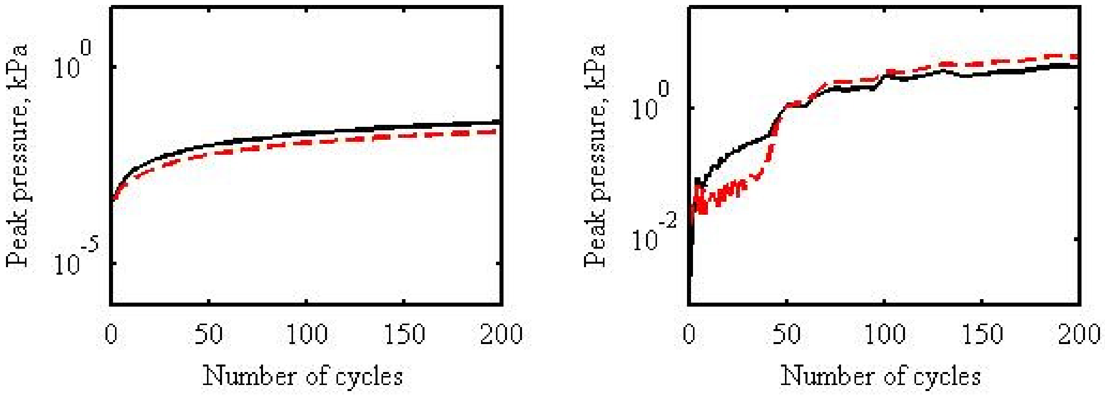

(c) 27 µm (10 kPa) (d) 27 µm (100 kPa)

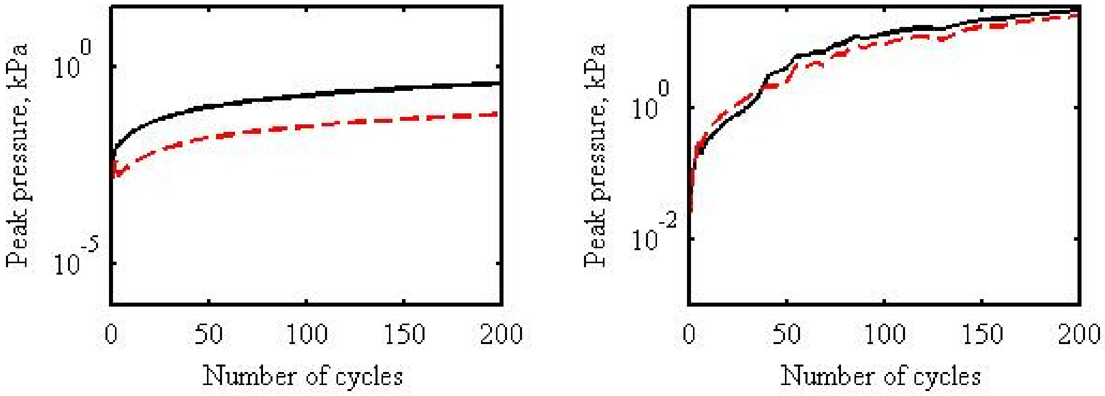

(e) 225 µm (10 kPa) (f) 225 µm (100 kPa)

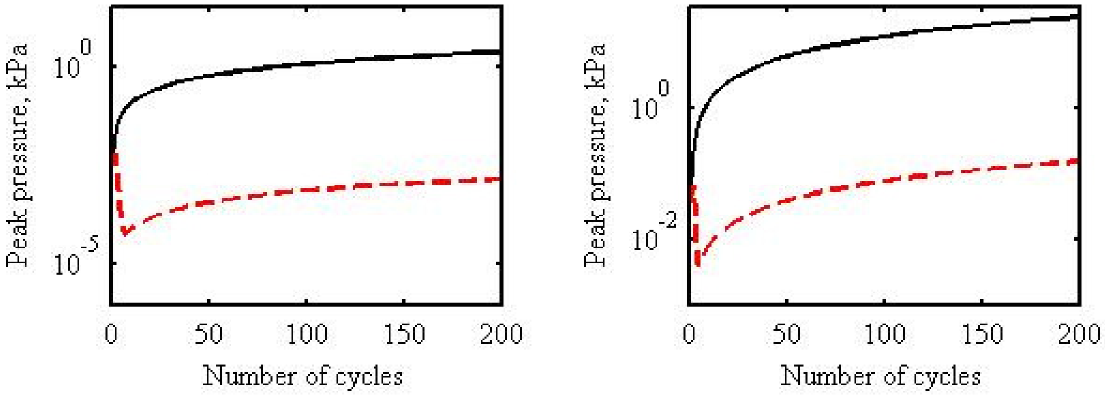

Figure 4.5. The peak pressure radiated by a single bubble at 1 m of radius of 15 µm, 27 µm and 225 µm as a function of the number of cycles of the pulse when driven by a 10 kPa Gaussian-modulated pulse of centre frequency of 80 kHz are shown in (a), (c) and (e) respectively. The case with a higher amplitude of 100 kPa are shown in (b), (d) and (f) respectively. The solid line denotes the peak bubble pressure after applying a matched filter at the fundamental frequency while the dotted line denotes the peak bubble pressure after applying a matched filter at the second harmonic of the driving pulse.

For sonar applications, if the high amplitude of the driving pulse is limited by practical considerations such as hardware, it will be advantageous to use driving pulses of longer duration so as more energy can be used to insonify the bubble cloud at the driving frequency. However, the use of a long pulse, especially for a narrowband pulse, will compromise the range resolution of the sonar [98, 99]. To overcome this, an appropriate wideband signal can be used. In the next section, the theoretical response of a single bubble when excited by a wideband signal will be studied.

4.3. Wideband signal

So far in this chapter, the effects of parameters like frequency, amplitude and pulse duration of a narrowband pulse on the response of a single bubble has been discussed. The importance of parameters like frequency, amplitude and pulse duration has been highlighted with respect to the dynamics of a single bubble.

In both man-made active sonar systems and biosonar systems of dolphin, it is common to observe wideband pulses being used as the emitted pulse. In man-made active sonar systems, a wideband signal is usually used because it can provide better range resolution than narrowband signals through pulse compression [98-100]. Pulse compression can occur when an appropriate waveform is chosen and matched filtered. The matched filter is central to active sonar processing [98, 99]. Fundamentally, the matched filter is a correlator which compares the received signal with a set of signals. With better range resolution, good range accuracy and better target discrimination follows.

Target detection range can also be increased with the use of a wideband signal. In general, target detection range is influenced by the peak power of the pulse. With a narrowband pulse, it is extremely difficult to transmit pulses of very short duration and high peak power. Increasing the duration of such a pulse, on the other hand, will compromise the range resolution. Hence, one solution is to use an appropriate wideband waveform with pulse compression so as to transmit the necessary average power at a reasonable level of peak power.

One of the most basic pulse compression waveform is the LFM waveform. With pulse compression, a LFM waveform with a pulse length T is compressed to a pulse whose length is $1/B$ where B is the bandwidth of the pulse [98, 99]. Another commonly used waveform is the linear period modulated (LPM) waveform. The LPM waveform has the additional property of being Doppler-tolerant [99, 101].

The use of wideband signals has also been proposed for active sonar applications because of the possibility of better target classification using such signals. The use of wideband dolphin pulses for discrimination of cylinders of different materials and composition as well as different fish species have been studied [102-104]. The discrimination of buried and partially buried underwater targets using bio-inspired wideband signals has also been proposed [105-109]. From the analysis of biological signals, including dolphin clicks, Brown *et al*. [105] demonstrated that a bio-inspired wideband sonar can offer greater capability for tracking cables on the seafloor in several sets of experiments.

For techniques which exploit the nonlinearities of bubbles, the use of a wideband signal has the additional advantage of exciting a larger range of bubbles to resonance due to the wider range of driving frequencies present. A LFM chirp is commonly used. The theoretical peak pressure radiated by a single bubble at 1 m when excited by such an incident pulse is compared with that of a narrowband pulse of centre frequency of 6 kHz in Figure 4.6.

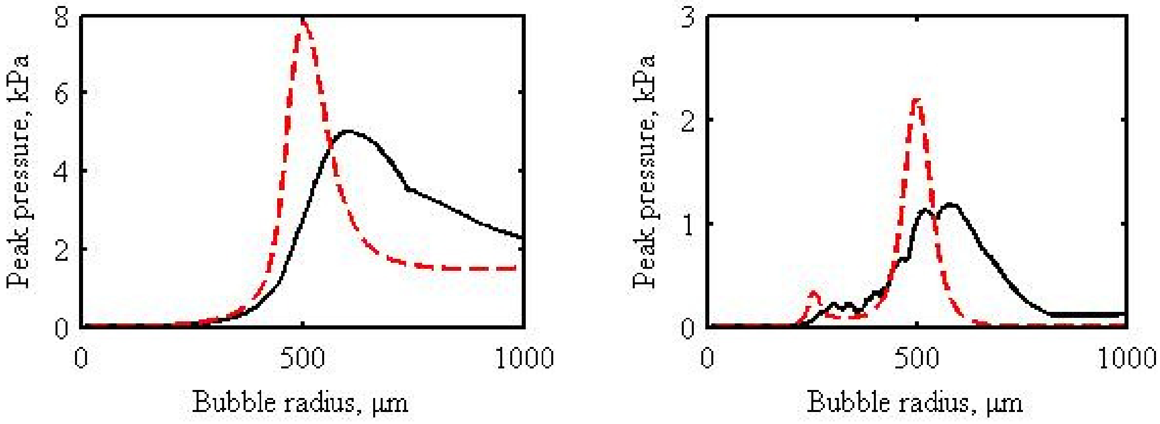
(a) Fundamental response (b) Second harmonic response

Figure 4.6. The peak pressure radiated by a single bubble at 1 m as a function of the radius of that bubble when applied a matched filter at (a) fundamental frequency and (b) second harmonic of the driving pulse. Two driving pulses are shown: the Gaussian-modulated eight-cycle pulse of center frequency of 6 kHz (denoted by dashed line) and the Gaussian-modulated LFM chirp of frequency of 2 to 8 kHz (denoted by solid line). Both driving signals have amplitudes of 10 kPa.

Compared to the narrowband pulse of centre frequency of 6 kHz, the 2 to 8 kHz LFM pulse of approximately the same number of cycles (giving pulse duration of 1.6 ms) has a wider range of bubble radii radiating a higher peak pressure (Figure 4.6). For the narrowband pulse of 6 kHz, a narrower range of bubble radii is found to radiate at higher peak pressure as seen in Figure 4.6. As the energy of the wideband signal is distributed over a wider range of frequencies compared to the narrowband signal, the bubbles are also driven to a lower pulsation compared to the resonant bubbles driven by the narrowband pulse. The centre frequency of the LFM chirp (approximately 5 kHz) is also lower than that of the narrowband pulse used to generate Figure 4.6. Hence, for the LFM chirp, the maximum of the fundamental and second harmonic bubble responses occur at a larger radius compared to that of the 6 kHz narrowband pulse.

A 30 to 130 kHz LFM chirp of 100 μs, termed the HF chirp, is compared with that of a 2 to 8 kHz LFM chirp of approximately 1.6 ms, termed the LF chirp. For the two pulses, the pulse duration is chosen such that both chirps have approximately the same number of cycles.

Figure 4.7 shows the peak pressure radiated by a bubble at 1 m as a function of the radius of that bubble when two types of LFM signals (of different frequencies) are used as the driving signals. When bubble pulsations are high enough, nonlinear bubble responses become apparent. Figure 4.7 highlights another notable difference between the use of a high and low frequency pulses. When a HF chirp is used, the bandwidth will have to be significantly larger (compared to a LF chirp) to excite a larger range of bubble sizes to high bubble pulsations. Using the rough guideline for bubble resonance [23]:

$$v_o R_r \approx 3 \text{ m s}^{-1} \qquad (4.1)$$

the resonant frequency, v_o, of air bubble in water under one atmosphere can be related to its resonant radius, R_r. While this relationship may be used for a large bubble with low resonance frequency, a small bubble (of radius approximately less than 20 μm) with high resonance frequency will necessitate a correction factor as effects of heat conduction and surface tension become important [23, 110]. However, for purpose of the discussion here, it is sufficient to use this rough guideline for bubble resonance. Using Eq. (4.1), it can be shown that frequencies of 30 to 130 kHz will approximately correspond to resonant bubble radii of 20 to 100 μm while frequencies of 2 to 8 kHz will approximately correspond to resonant bubble radii of 375 to 1500 μm. The above analysis showed that the frequency band of the HF chirp will have to be significantly wider than that of the LF chirp so as to correspond to a larger range of resonant bubble radii.

(a) 30 to 130 kHz- Fundamental response

(b) 2 to 8 kHz - Fndamental response

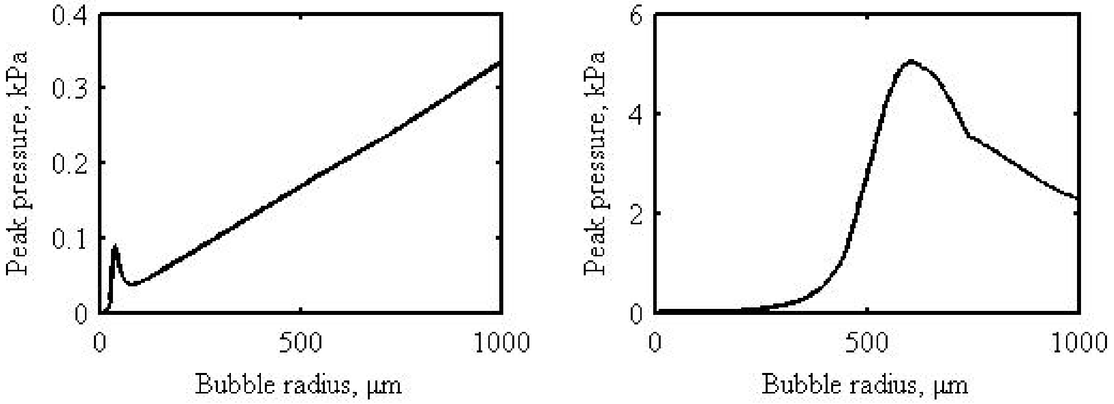

(c) 30 to 130 kHz- Second harmonic response

(d) 2 to 8 kHz - Second harmonic response

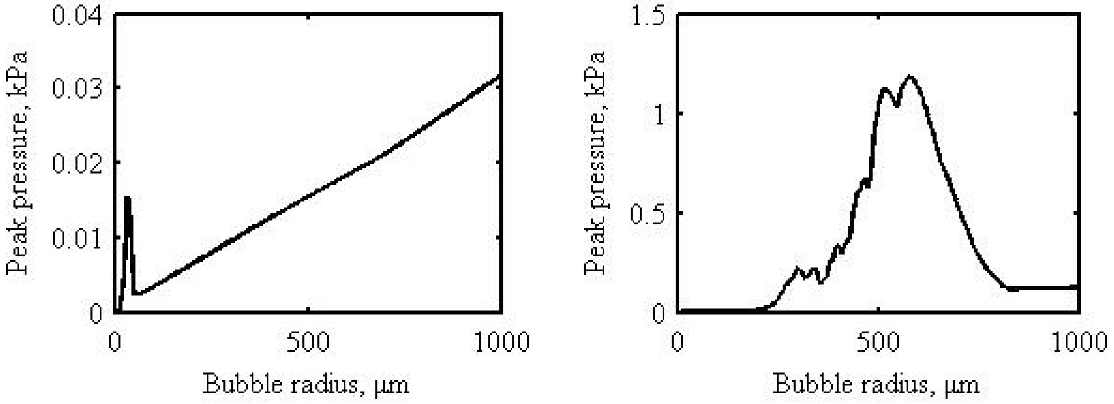

Figure 4.7. The peak pressure radiated by a single bubble at 1 m as a function of the radius of that bubble after applying a matched filter at the fundamental frequency and second harmonic are shown in (a) and (c) respectively when driven by a Gaussian-modulated eight-cycle LFM chirp of frequencies 30 to 130 kHz. In (b) and (d), the peak bubble pressure radiated after applying a matched filter at the driving frequency and second harmonic respectively when driven by a Gaussian-modulated eight-cycle LFM chirp of lower frequencies of 2 to 8 kHz are shown. Both pulses have amplitude of 10 kPa.

In the case of driving a typical oceanic bubble cloud to a nonlinear state, this will not be the only consideration. As historical oceanic bubble cloud measurements have shown in Figure 3.4, the bubble size distribution of an oceanic bubble cloud roughly follows a power-law distribution [95, 111]. With a power-law distribution, the number of smaller bubbles can be several orders of magnitude higher than the number of bigger bubbles. This means that the contributions of bigger bubbles to the overall response of the bubble cloud will be much less significant than those of smaller bubbles, than say, if the bubble size distribution of the bubble cloud follows an uniform distribution. While a wideband HF pulse with a wider frequency bandwidth will be desirable, the performance (in term of driving an oceanic bubble population to a high level of nonlinear state) of the HF chirp, may not necessarily be worse than that of wideband LF pulse. This is, despite, having a frequency band that corresponds to a narrower range of resonant bubble radii.

It has already been shown in Section 4.2.1 that a lower frequency pulse elicits greater bubble responses than a higher frequency pulse. Comparing Figures 4.7(a) and (c) to (b) and (d) respectively, a low frequency chirp also results in the resonant bubbles undergoing higher state of linear and nonlinear responses when both driving pulses have the same amplitude. For example, in Figure 4.7(a), the highest peak pressure radiated by its resonant bubbles for the HF chirp is approximately 0.1 kPa while in Figure 4.7(b), for the LF chirp, the highest peak pressure radiated by its resonant bubbles is approximately 5 kPa.

An observation similar to that made in Section 4.2.3 is seen in Figure 4.8 when the pulse duration increases. As the total energy of the pulse increases with increases in the pulse duration, higher bubble responses in both fundamental frequency and second harmonic result. However, the degree of second harmonic bubble response relative to the bubble response at its driving frequency band stays fairly constant as both pulses have the same amplitude. In both cases shown in Figure 4.8, the peak pressure radiated by a bubble at its driving frequency is approximately an order of magnitude higher than its peak pressure radiated by the bubble at its second harmonic.

Figures 4.7(c) and (d) also highlight one disadvantage of using a wideband signal as the transmitted signal if the higher harmonics of the received signal are important. Being wideband, the overlap in the frequency domain between frequency of the transmitted signal and, in this case, its second harmonics may be substantial. The second harmonic component in the resonant bubble response is no longer a global maximum within the range of the bubble size studied. The second harmonic component of the bubble responses will also contain linear bubble responses of other bubbles. Bubbles much larger than the resonant bubble radius, cannot respond rapidly enough to generate nonlinear responses. The larger bubbles pulsate to a lesser degree, and behave like linear scatterers. This linear response slowly increases with bubble size. This effect can be made less pronounced when using a wideband signal with higher amplitude or lower frequency. The latter can be clearly observed by comparing Figures 4.7(c) and (d). In Figure 4.7(c), when a HF chirp is used, the second harmonic component of the resonant bubble response is no longer a global maximum within the range of bubble radii up to 1000 μm whilst in Figure 4.7(d), when a LF chirp is used, the second harmonic component of the resonant bubble response remains a global maximum for bubble radii up to 1000 μm. While the use of an efficient filter, in this case a matched filter, has reduced this frequency overlap effect for the HF chirp, it does not eliminate this effect completely. For this particular case of HF chirp, the second harmonic component of the resonant bubble is not sufficiently high to reduce the effect of frequency overlap.

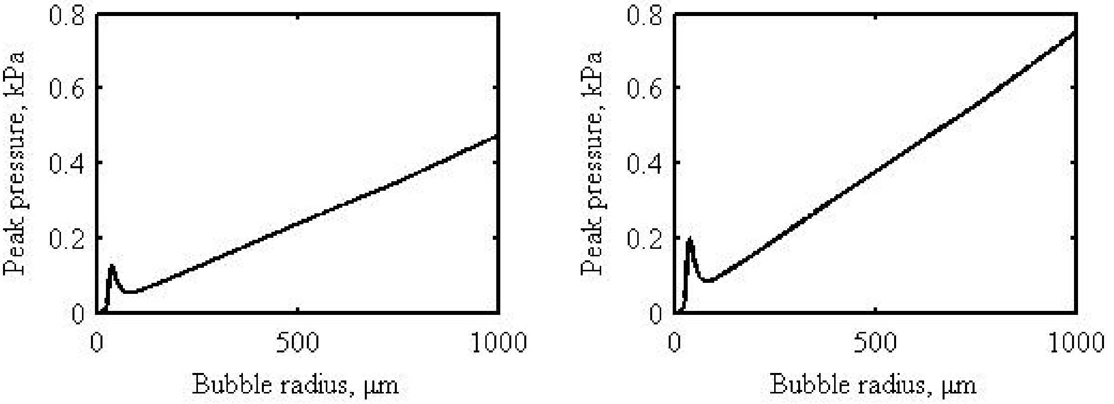

(a) Duration of 0.2 ms- Fundamental response (b) Duration of 0.5 ms- Fundamental response

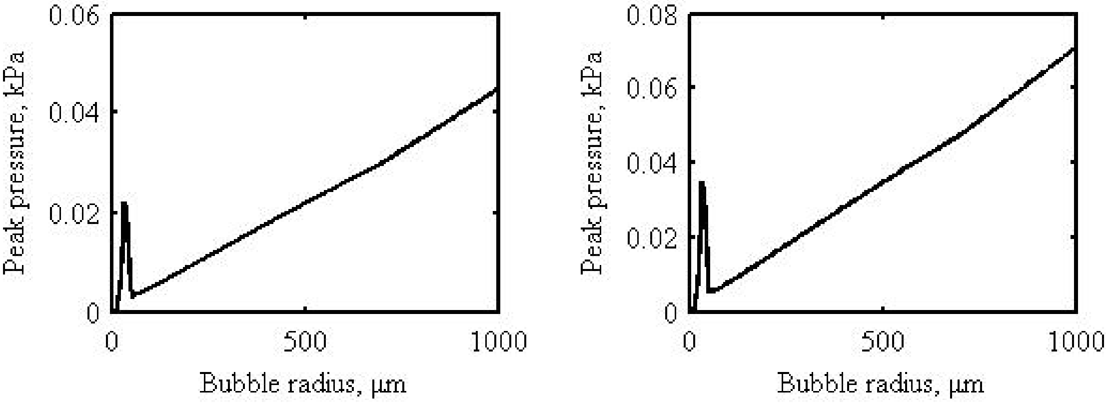

(c) Duration of 0.2 ms-
Second harmonic response

(d) Duration of 0.5 ms-
Second harmonic response

Figure 4.8. The peak pressure radiated by a single bubble at 1 m as a function of the radius of that bubble when excited by a Gaussian-modulated LFM 30 to 130 kHz chirp of amplitude of 10 kPa with duration of 0.2 ms and 0.5 ms with a matched filter applied at fundamental frequency depicted in (a) and (b) respectively and with a matched filter applied at the second harmonic depicted in (c) and (d) respectively.

One way to mitigate the frequency overlap effect is by using a higher amplitude HF chirp. Figure 4.9 compares the effect on bubbles of different radii when pulses of different amplitude are used. Both Figures 4.9(a) and (b) show the peak pressure radiated by a bubble at 1 m at the driving frequency (the linear response) is a maximum at the bubble radius resonant with the driving frequency. This maximum is a local maximum with the linear response of the larger bubbles increasing with size. In both cases, that bubbles at much larger than resonance can give a response to a greater degree than those at resonance.

(a) Fundamental response (1 kPa) (b) Fundamental response (100 kPa)

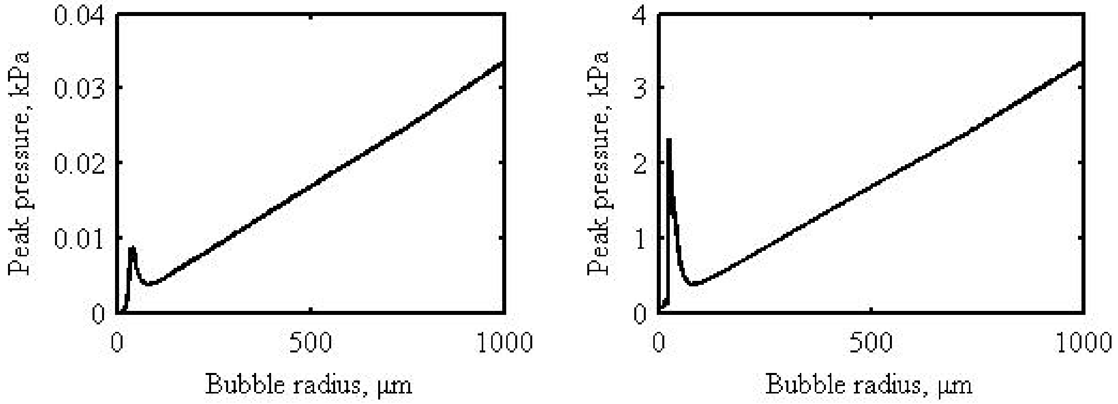

(c) Second harmonic response (1 kPa) (d) Second harmonic response (100 kPa)

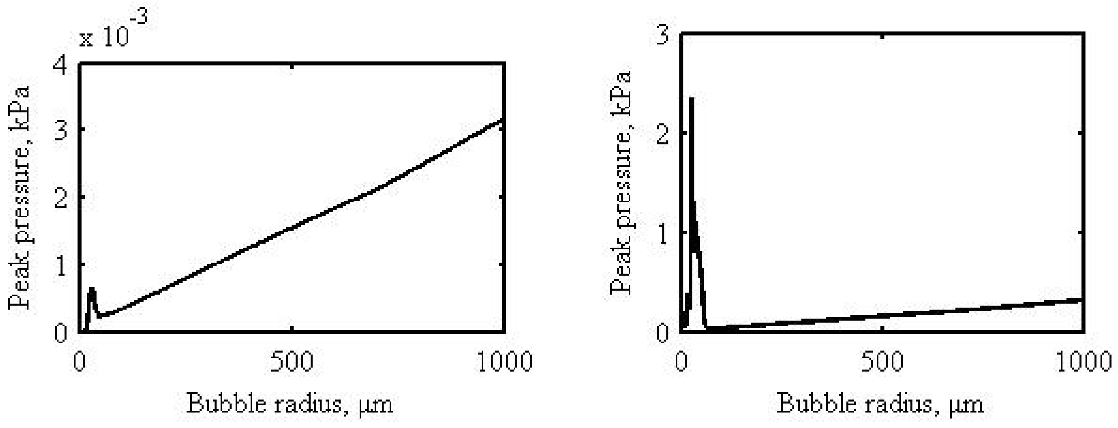

Figure 4.9. The peak pressure radiated by a single bubble at 1 m as a function of the radius of that bubble when driven by a eight-cycle Gaussian-modulated LFM 30 to 130 kHz chirp of amplitude of 1 kPa and 100 kPa with a matched filter applied at the fundamental frequency depicted in (a) and (b) respectively and a matched filter applied at the second harmonic depicted in (c) and (d) respectively.

From the second harmonic component of the peak pressure radiated by a bubble as a function of bubble radius (Figures 4.9(c) and (d)), it can be surmised that the second harmonic response of a bubble increases with amplitude. When the amplitude of the pulse is low (1 kPa), the second harmonic bubble response at the bubble radius resonant with the driving frequency is a local maximum as a larger bubble (with resonant frequency lower than the driving frequency) continues to give a high response in the second harmonics. This high second harmonic response from a larger bubble is geometric in nature. The linear scattering by a larger bubble contributes to the bubble response in the second harmonic because of an overlap in frequency domain between the driving pulse and its second harmonic.

However, as the amplitude increases, bubble nonlinearity becomes more apparent (Figure 4.9 (d)). A higher nonlinear pulsation of the bubbles resonant with the driving frequency means the second harmonic response of the resonant bubble remains a maximum (up to bubble radii of 1000 μm) as shown in Figure 4.9(d). The effect of the frequency overlap thus diminishes as the high nonlinear responses of the resonant and smaller bubbles dominate. With a higher amplitude of 100 kPa, the linear responses of larger bubbles become proportionally smaller relative to the nonlinear responses of the resonant and smaller bubbles with an increase in the amplitude of the driving pulse. This reduces the frequency overlap effect.

For sonar applications, historical data has shown that a typical oceanic bubble cloud contains mostly bubbles less than 1 mm and the bubble size distribution of the bubble cloud follows roughly a power-law distribution [95, 111]. With the former, using a LF pulse like a 2 to 8 kHz LFM waveform will result in this frequency overlap effect being less pronounced. With the latter, as a typical oceanic bubble cloud follows roughly a power-law distribution, the contributions of the larger bubbles will not be as significant as those of the smaller bubbles. This characteristic of the oceanic bubble cloud implies the frequency overlap effect will be less pronounced for a HF wideband pulse in oceanic conditions. In other applications like biomedical imaging, where satisfactory axial resolution is desired, this frequency overlap effect can be significant with a large transmitted signal bandwidth and simple band-pass filter. Two-pulse techniques have been implemented to overcome this limitation [41].

4.4. Implication on sonar enhancement

Using the single bubble model, the variation of bubble responses with size for several key parameters of the driving pulse has been shown. The results of using narrowband and wideband signals have also been presented in previous sections. The implications of these results on sonar enhancement to improve detection and classification of target in bubbly water will be discussed here.

For techniques like TWIPS, it is important that the bubbles can be driven to high amplitudes of pulsation so that nonlinear responses result. The single bubble model has shown that a low frequency pulse will be preferred to ensure a wider distribution of bubble radii can pulsate to a nonlinear state.

In a sonar system, a higher frequency is sometimes preferred because of its characteristics of high spatial resolution, wide bandwidth, small size and relatively low cost [98, 100, 112]. These attractive characteristics sometimes override the severe range limitation imposed by attenuation. A higher frequency pulse will typically result in higher cloud attenuation and absorption. For the bubble distribution used, with a void fraction of order of 10^{-5} %, the linear cloud attenuation, calculated using Eq. (3.1) to (3.6), will be approximately 0.3 dB/m and 1 dB/m and the seawater absorption, approximately 0.0004 dB/m and 0.03 dB/m, for frequencies of 6 kHz and 80 kHz respectively. A higher driving frequency will thus have higher cloud attenuation and absorption. This will have a debilitating effect on the range of the sonar. From this perspective, a lower frequency might be preferred.

The above discussion suggests the use of a higher frequency pulse may be attractive in scenarios where pulse attenuation is not a key consideration, for example, the target of interest is within a short range and a high power source is available. A higher source level will somehow mitigate, to a certain extent, against the lower amplitude of pulsation in a bubble cloud, when a higher frequency pulse is used, by driving the bubbles close to resonance to a higher levels of pulsation, even though bigger bubbles will behave mostly like linear scatterers.

It is thus interesting to note that the frequencies of pulses emitted by some species of odontocetes are similarly high (of order of tens of kilohertz) and of high amplitude (with peak-to-peak sound pressure level (SPL) as high as 230 dB re 1µPa m) [113-115] . They inhabit shallow water and are sometimes observed to generate bubble nets [3, 113, 114, 116, 117], making interesting points of discussion the benefits of using such pulses in a bubble-filled environment [116-119]. The characteristics of pulses emitted by odontocetes will be reviewed and studied in Chapter 6.

The comparison of a narrowband signal with a wideband signal has shown that a larger range of bubble size can be excited by the wideband signal. However, when both the narrowband and wideband signal are set to the same amplitude level and comparable pulse length, the wider range of bubbles are driven to a lower pulsation state by the wideband signal as its energy is distributed over a wider range of frequencies. Depending on the bubble population of the cloud, the overall backscatter of the bubble cloud may be lower when the bubble cloud is excited by a wideband signal compared to being excited by a narrowband signal.

One disadvantage of using a wideband signal is the overlap between the driving frequency band and the harmonics of the signal. This frequency overlap means that the response of the bubble cloud filtered at the harmonics will also contain linear responses. However, this frequency overlap effect can be made less pronounced with the use of a pulse of an appropriate characteristic (a LF pulse as in Figure 4.6 or a high amplitude HF pulse as in Figure 4.9). In addition, the use of an efficient filter like a matched filter will also reduce this frequency overlap effect.

In sonar applications, this frequency overlap effect is probably less pronounced in an oceanic bubbly environment for a HF pulse. This is because, while the use of a LFM pulse of a higher frequency range has the frequency overlap effects shown in Figure 4.7, the two characteristics of an oceanic bubble cloud (where the bubble population consists of mostly bubbles of radii less than 1 mm and the size distribution roughly follows a power-law distribution) suggests that the use of a HF chirp will have a less pronounced frequency overlap effect because the number of larger bubbles will be proportionately less than the number of small bubbles. Besides, it is common to use a matched filter in sonar systems [98]. Use of an efficient filter like a matched filter reduces this frequency overlap effect.

4.5. Summary

In this chapter, the nonlinear Keller-Miksis model described in chapter 3 was used to study the effects of several key parameters of a signal on the response of a single bubble. The bubble response was represented by the peak pressure radiated by a bubble at 1 m from a bubble. These parameters included frequency, amplitude and pulse duration. For any technique which exploits the nonlinearity of bubbles, a lower frequency driving pulse will be preferred to ensure a wider distribution of bubble radii can pulsate to a nonlinear state. As larger bubbles (relative to the bubble radius resonant with the frequency of the driving pulse) will mainly behaves as linear scatterers, a lower frequency driving pulse will reduce the range of larger bubbles in a bubble population. Similarly, a pulse of sufficiently high amplitude will also be preferred to excite a bubble to a nonlinear state. A longer pulse duration will also be desirable so that more energy can be transmitted to insonify the bubble to a nonlinear state. Similar observations have been made for the LFM chirp studied.

While the wideband LFM chirp was shown to excite a wider range of bubble size, there can be frequency overlap between the fundamental frequency and second harmonic of the driving pulse, especially when a HF LFM chirp is used. This frequency overlap between the fundamental frequency and second harmonic of the driving pulse is one key disadvantage of using a wideband signal when the backscattered contribution in the harmonics from nonlinear scatterers is important. Two-pulse techniques like TWIPS does not have this limitation.

The implications on sonar enhancement of these findings were discussed in the concluding section of this chapter. Taking the bubble population typically present in an oceanic cloud into consideration, a low frequency and high amplitude pulse will be preferred to ensure high degree of nonlinear pulsation in the bubble cloud. However, it was also discussed that if pulse attenuation was not a key consideration (like in a short-range system), the use of a higher frequency pulse can be considered. Use of higher frequency pulses is common in man-made sonar systems because of the high spatial resolution, wide bandwidth, small size and relative low cost associated with such pulses.

In nature, pulses emitted by some species of odontocetes are of similar high frequencies (in order of tens of kilohertz). In the single bubble analysis, the use of a higher frequency pulse was also shown to have a more pronounced frequency overlap effect than a lower frequency pulse. Characteristics of oceanic bubble clouds, however, suggest this effect may not be as pronounced for sonar applications in oceanic bubbly water. In biomedical imaging, this effect may be significant and the two-pulse techniques like pulse inversion technique have been proposed. In the next chapter, another two-pulse technique proposed for sonar applications, TWIPS, will be described and demonstrated. Using a LFM waveform, TWIPS will be demonstrated in distinguishing between a solid target (a linear scatterer) and bubble cloud (nonlinear scatterers). This will be the primary advantage. A secondary advantage of improving detection performance (compared against standard sonar) will also be studied.

Chapter 5. TWIPS using LFM waveforms

Two-pulse techniques have been proposed in biomedical imaging to enhance the contrast between the backscattered contribution of the tissues and the nonlinear UCAs [39-43, 45, 46, 48, 49]. In sonar, the use of a two-pulse technique, TWIPS, has been suggested as a viable engineering solution to enhance targets in bubbly water. TWIPS has been tested in tank tests and sea trials using a pair of eight-cycle 6 kHz signal by Leighton *et al.* [3, 6]. Using this waveform, it has been shown to provide classification ability absent in standard sonar system. It can also improve detection performance of linear targets in some manifestations. Here, the efficacy of TWIPS in target discrimination in bubbly water will be demonstrated with a LFM waveform theoretically and experimentally.

In Chapter 4, the single bubble model has been used to investigate the effects of several parameters, like amplitude and frequency, of a signal on the linear and nonlinear responses of a bubble. Comparisons have also been made between narrowband and wideband signals. The implications on sonar enhancement of these findings were also discussed.

The single bubble model will first be used to show how TWIPS with a LFM waveform can differentiate between the even and odd harmonics of a scatterer like a bubble, through linear combinations of the returned signals from the TWIPS pulse pair. A 2 to 8 kHz LFM chirp will be used as the driving pulse. This is followed by a series of tank tests in the ISVR water tank at the A. B. Wood laboratory with a solid target placed behind a bubble cloud. The results of the tank tests are then corroborated by the sonar simulation model using a similar bubble population. In conclusion, the performance of TWIPS in target enhancement in bubbly water will be discussed.

5.1. Single bubble model

Here, the single bubble model is used to demonstrate ability to distinguish between the even and odd harmonics of a single scatterer using the 2 to 8 kHz LFM chirp of approximately 1.6 ms as the driving pulse. A brief re-cap of the TWIPS theory is shown in Eq. (5.1) - (5.3). From Eq. (2.1), (2.8) and (2.9), we get:

$$p_i(t) = \Gamma(t) - \Gamma(t - \Delta_d) \tag{5.1}$$

which shows a TWIPS pulse pair consists of a pulse, $\Gamma(t)$, and a second pair, $-\Gamma(t - \Delta_d)$, which is of the opposite polarity of $\Gamma(t)$.

$$p_-(t) = p_{Rx}(t) - p_{Rx}(t + \Delta_d) \quad \text{for} \quad 0 \le t \le \Delta_d \tag{5.2}$$

$$\text{and} \quad p_+(t) = p_{Rx}(t) + p_{Rx}(t + \Delta_d) \quad \text{for} \quad 0 \le t \le \Delta_d \tag{5.3}$$

Figures 5.1(a) and (b) shows the typical response of a bubble whose resonant frequency is close to or higher than the driving frequency when the bubble is excited by a TWIPS pulse pair. The responses of a bubble to the two pulses are observed to be different from each other. When the responses of the bubble to these two pulses are subtracted from each other as in $p_-(t)$ (Eq. (5.2)) or added to each other as in $p_+(t)$ (Eq. (5.3)), complete cancellation of the bubble responses do not occur. For a nonlinear scatterer like a bubble, $p_-(t)$ does not always result in a doubling of its responses (Figure 5.1(c)). This occurs when the resonant frequency of the bubble is close to or higher than the driving frequency. In such a scenario, using $p_-(t)$ processing of a pair of TWIPS pulse would result in reduced backscattered contribution from the nonlinear scatterer.

On the other hand, a larger bubble whose resonant frequency is lower than that of the driving frequency can often be approximated as a linear scatterer. The responses to this pulse pair (Figures 5.2(a) and (b)) are of comparable magnitude but of opposite polarity. Subtracting these responses from each other results in a doubling of these responses, while the summation results in a complete cancellation of the responses of the linear scatterer.

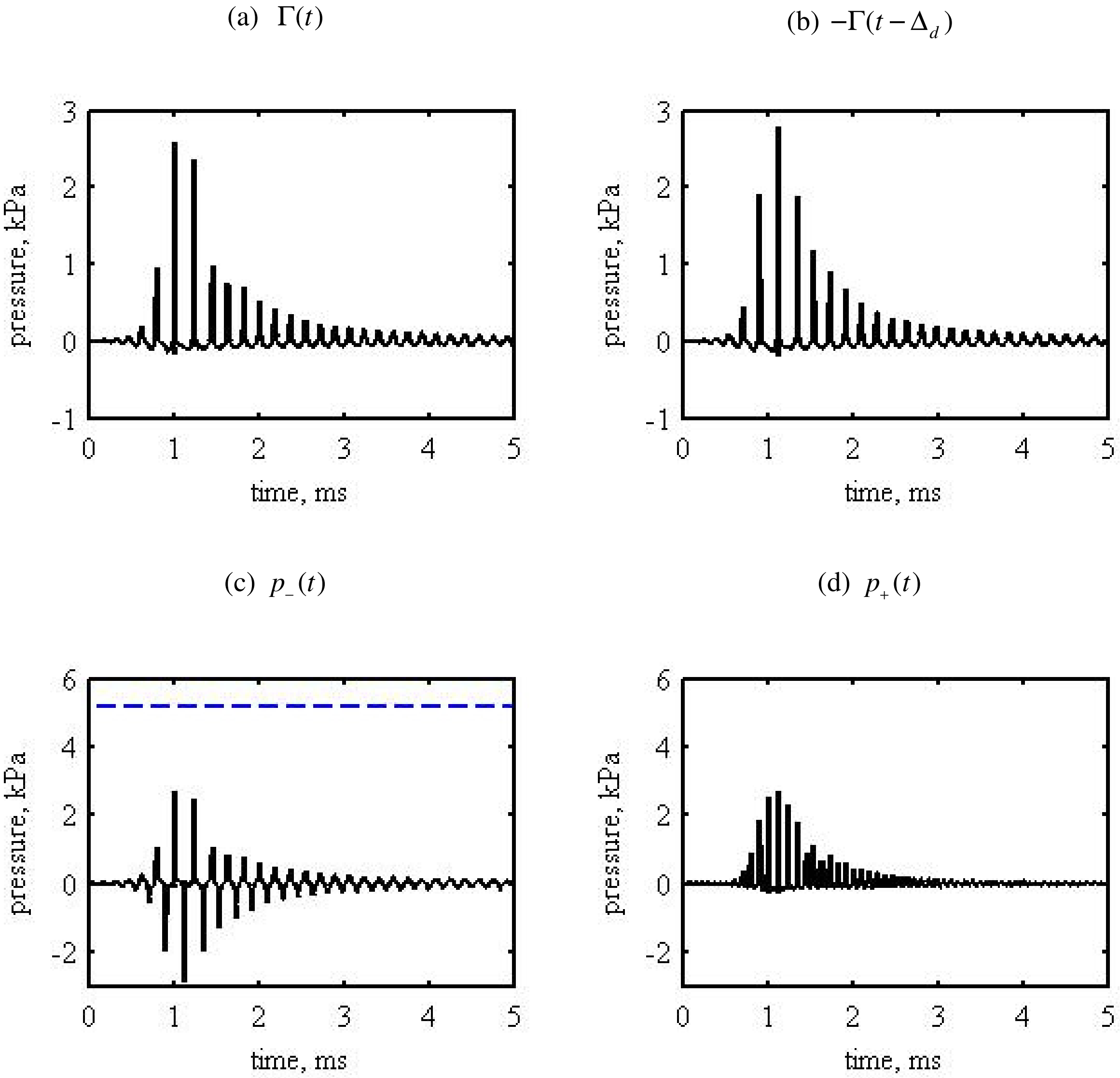
(a) $\Gamma(t)$

(b) $-\Gamma(t-\Delta_d)$

(c) $p_-(t)$

(d) $p_+(t)$

Figure 5.1. Time series of acoustic pressure emitted by the bubble at 1 m from the bubble due to (a) the first pulse $\Gamma(t)$, and (b) second pulse $-\Gamma(t-\Delta_d)$, with (c) $p_-(t)$ and (d) $p_+(t)$ for bubble radius of 500 μm when excited by Gaussian-modulated 2 to 8 kHz LFM chirp pulse with amplitude of 50 kPa. The horizontal dashed line in (c) shows the 200 % mark of the peak amplitude of the first pulse $\Gamma(t)$.

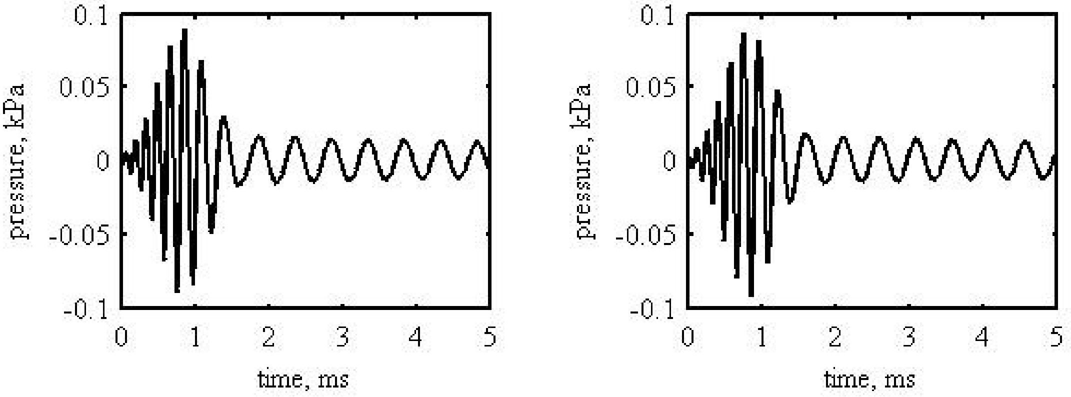
(a) $\Gamma(t)$ (b) $-\Gamma(t-\Delta_d)$

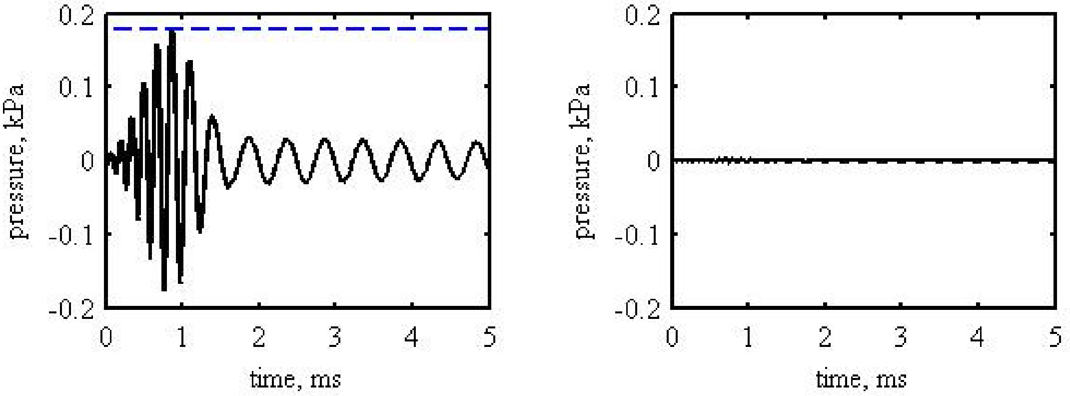
(c) $p_-(t)$ (d) $p_+(t)$

Figure 5.2. Bubble response to (a) the first pulse $\Gamma(t)$, and (b) second pulse $-\Gamma(t-\Delta_d)$, with (c) $p_-(t)$ and (d) $p_+(t)$ for bubble radius of 1500 μm when excited by Gaussian-modulated 2 to 8 kHz LFM chirp pulse with amplitude of 50 kPa. The horizontal dashed line in (c) shows the 200 % mark of the peak amplitude of the first pulse, $\Gamma(t)$.

Using the single bubble model, both the TWIPS functions, $P_{1-}(t)$ and $P_{2+}(t)$, are obtained for a range of bubble radii when a 2 to 8 kHz LFM chirp is the driving pulse (Figure 5.3). Results using a higher frequency chirp (30 to 130 kHz) are presented in Figures 5.4 and 5.5. The pulse duration for each pulse is chosen such that both pulses have approximately the same number of cycles. The HF chirp has pulse duration of 0.1 ms while the LF chirp has pulse duration of approximately 1.6 ms. The TWIPS functions, $P_{1-}(t)$ and $P_{2+}(t)$ are compared with the peak pressure emitted by a bubble at 1 m after a matched filter is applied at the fundamental frequency and the second harmonic in Figure 5.3. For a fair comparison, the average peak bubble pressure shown is taken to be the average of the peak pressures emitted by a bubble when excited by the TWIPS pulse pair.

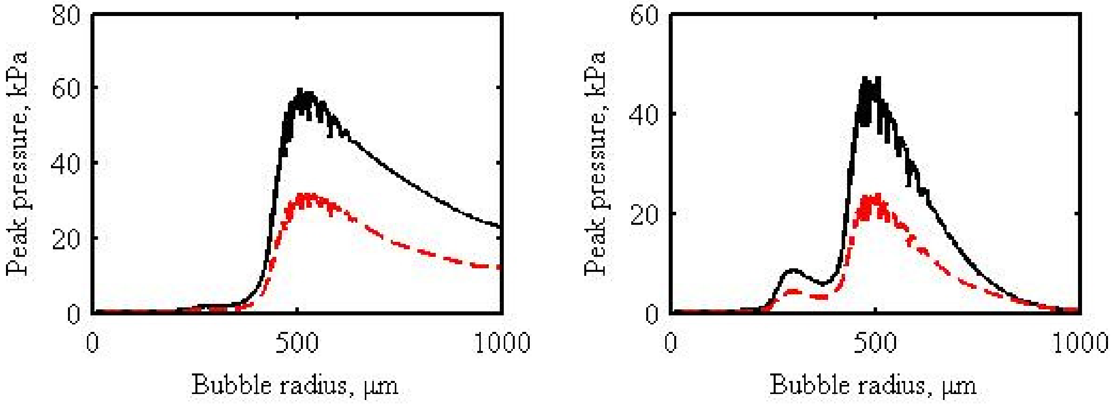
(a) $P_{1-}(t)$ (b) $P_{2+}(t)$

Figure 5.3. The TWIPS functions, $P_{1-}(t)$ and $P_{2+}(t)$, when excited by a LFM chirp (2 to 8 kHz) at amplitude of 50 kPa as a function of the bubble radius are shown as solid lines in (a) and (b). The average peak pressure emitted by a single bubble at 1 m when matched filtered at the driving frequency and the second harmonic from the TWIPS pulse pair are denoted as dotted lines in (a) and (b) respectively.

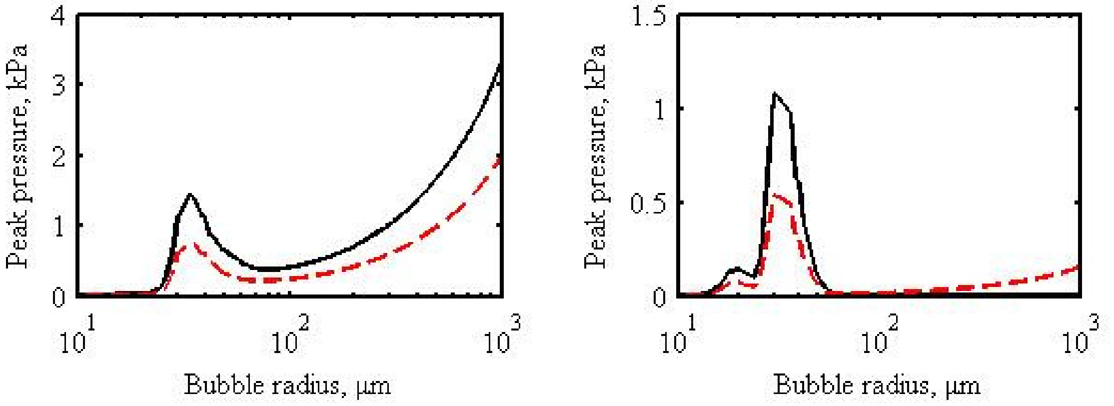
(a) $P_{1-}(t)$ (b) $P_{2+}(t)$

Figure 5.4. The TWIPS functions, $P_{1-}(t)$ and $P_{2+}(t)$, when excited by a LFM chirp (30 to 130 kHz) at amplitude of 50 kPa as a function of the bubble radius are shown as solid lines in (a) and (b). The average peak pressure emitted by a single bubble at 1 m when matched filtered at the driving frequency and the second harmonic from the TWIPS pulse pair are denoted as dotted lines in (a) and (b) respectively.

Figure 5.3 shows that, whilst using TWIPS can remove the frequency overlap effect, the use of a low frequency pulse will also make this frequency overlap effect less pronounced. When a chirp of higher frequency is used, this is more pronounced (Figures 5.4 (b) and 5.5 (b)). The frequency overlap effect can be mitigated with a high amplitude pulse as the bubbles are driven to high level of pulsation (Figure 5.4 (b)) as described in Section 4.2.2. In Figure 5.5, a lower amplitude of 10 kPa has been used. With $P_{2+}(t)$ processing, the more pronounced frequency overlap effects can be removed (Figure 5.5 (b)). This overcomes one key disadvantage of using a wideband signal while preserving the higher range resolution associated with such a signal [98-100].

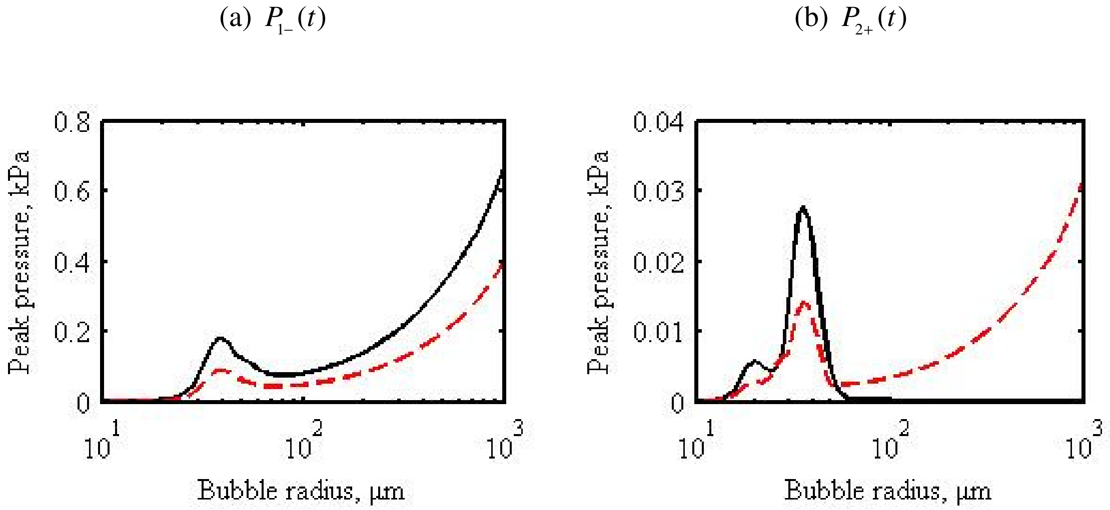
(a) $P_{1-}(t)$ (b) $P_{2+}(t)$

Figure 5.5. The TWIPS function, $P_{1-}(t)$ and $P_{2+}(t)$, when excited by a LFM chirp (30 to 130 kHz) at amplitude of 10 kPa as a function of the bubble radius are shown as solid lines in (a) and (b). The average peak pressure emitted by a single bubble at 1 m matched filtered at the driving frequency and the second harmonic from the TWIPS pulse pair are denoted as dotted lines in (a) and (b) respectively.

While $P_{2+}(t)$ is shown to cancel completely the linear components of the backscatter from the bubbles, $P_{1-}(t)$ enhances the backscattered contribution of the linear scatterer (for example, a solid target) and suppresses the nonlinear backscatters of the nonlinear scatterers (bubbles). It is noted that the linear responses of the bubbles at the driving frequency are enhanced with $P_{1-}(t)$ processing. These include the linear pulsations of the resonant bubbles. For a bubble, the pulsations at resonance can be very strong, with scattering cross sections typically 1000 times their geometric cross sections [14]. In Figure 5.4(a), the peak pressure radiated by a bubble at 1 m from the bubble when applied a matched filter at the driving frequency for a resonant bubble (with radius around 40 μm) is shown to be higher than that of a bubble with radius up to approximately 600 μm. From this, it can be inferred that the linear responses from a bubble with radius larger than 600 μm, if present in sufficient number, will be higher than that of the resonant bubbles. These large bubbles behave mainly as linear scatters and $P_{1-}(t)$ processing may not result in reduced backscattered contribution from these bubbles. This will affect the detection performance of $P_{1-}(t)$ compared to standard sonar processing which will be elaborated later in Section 5.4.

The results of the single bubble model suggest that, by using two wideband pulses, one of which is of opposite polarity to another, it is possible to carry out some form of classification between a linear and nonlinear scatterer as shown in Figures 5.1 and 5.2. The results from the tank tests and simulations of TWIPS using a LFM waveform will be described next.

5.2. Results from tank tests and simulations

5.2.1. Test set-up

A linear frequency modulated (LFM) waveform was used as the transmitted pulse in the tank tests. Figure 5.6 shows the pair of transmitted pulse measured in the ISVR water tank at 1 m from the source. The second pulse (Figure 5.6 (b)) of the TWIPS pulse pair is of opposite polarity to the first pulse (Figure 5.6 (a)). The pulse used has a zero-to-peak SPL of 212 dB re 1 μPa m with pulse duration of approximately 1 ms. The same pulses were then used in the sonar simulation model.

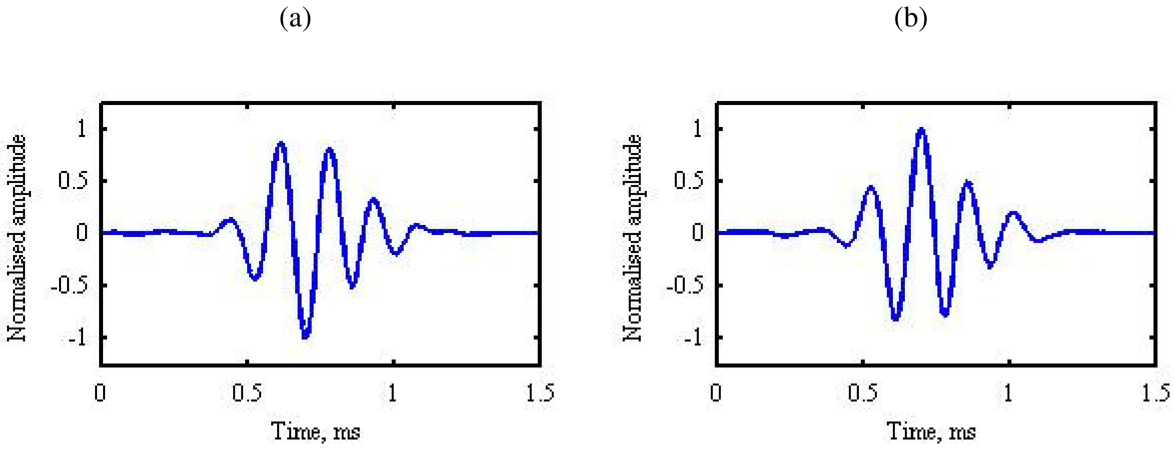

Figure 5.6. The LFM 2 to 8 kHz chirp used in tank tests with (a) being the first pulse and (b) the inverted pulse with a zero-to-peak SPL of 212 dB re 1 μPa m.

In both measurements and simulation model results, the target was placed at approximately 2.5 m behind the bubble cloud as described in Chapter 3. The returned signals from each pulse are processed as follows. The returned signal from each pulse is first matched filtered, then their envelope computed (by exploiting the Hilbert transform) and finally smoothing the result by averaging over the duration of the outgoing pulse. As explained in Section 3.3.1, the smoothed envelopes of $p(t)$, $p_-(t)$ and $p_+(t)$ are denoted here by P, P_- and P_+ respectively. The TWIPS functions, P_{1-} and P_{2+}, denote the functions, P_- and P_+, with a matched filter applied at the fundamental and second harmonic respectively.

Besides the TWIPS functions, P_{1-} and P_{2+}, a TWIPS ratio, P_{1-} / P_{2+}, is also used to further enhance the contrast between the linear target and bubble cloud. One disadvantage of using ratios is that they can be prone to instability. Small change in the denominator of the ratio can lead to large fluctuations in the output. The fluctuations in the denominator are reduced through averaging of values of P_{2+} over sets of adjacent returns. Here, geometrical averaging of ten adjacent returns is used. This use of geometrical averaging will be discussed in Section 5.5.

The ROC curves presented are generated using the distribution of the backscattered responses in the region containing the backscattered reverberation of the bubble cloud and target in the target absent and target present cases. Here, this region is taken to span from 1.5 to 4 ms so as to encompass the backscatter of the target and bubble cloud.

5.2.2. Measurement results

Figure 5.7 shows the measurement results when the LFM chirp waveform was used with a solid disc (shown in Section 3.2.5) placed at 2.5 m from the source. The solid disc was rotated by an angle of approximately 10° to give a target strength (TS) of -15 dB. The bubble cloud was placed in between the source and the solid target, with the bubble diffuser placed at approximately 1.5 m from the source. An image plot is formed by stacking the processed returned signal with the amplitude represented by colour, as defined in the colour scale bar. Each image plot shows the repeatability of each test as the environment changes with bubble cloud evolution.

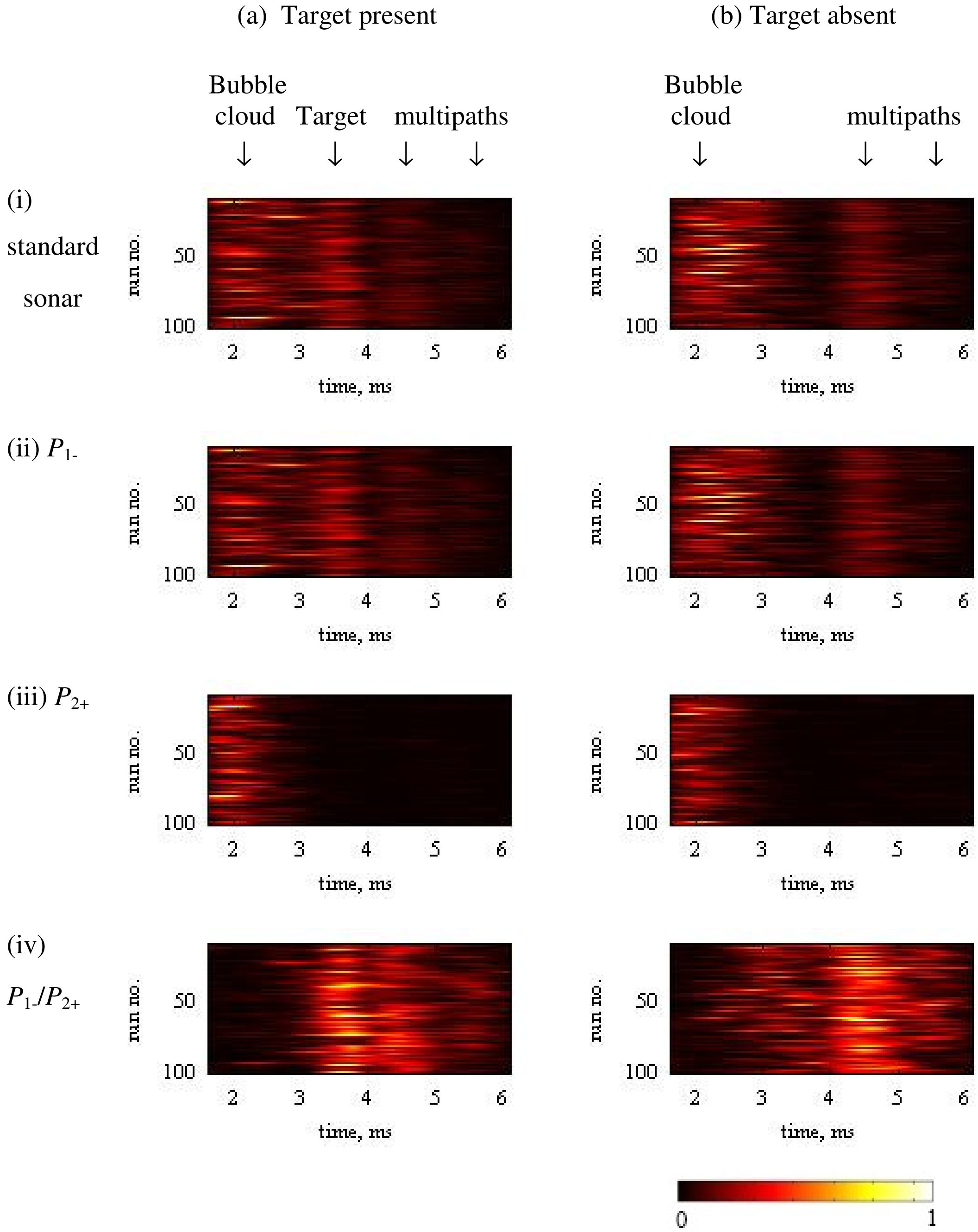

Figure 5.7. Plots of measurements using LFM chirp waveform with target (TS= -15 dB) placed at 2.5 m to compare the processing operators: (i) standard sonar (ii) P_{1-} (iii) P_{2+} (iv) P_{1-}/P_{2+}. In (a) target is present and located between 3 and 4 ms, and in (b) the target is absent. Each colour scale is normalised to the maximum value within each plot, which for (a) is (i) 4.9×10^4, (ii) 1.9×10^5, (iii) 2.0×10^3, and (iv) 4.5×10^3 and for (b) is (i) 3.7×10^4, (ii) 1.5×10^5, (iii) 1.7×10^3, and (iv) 2.7×10^3.

Figure 5.7 shows the plots of the various TWIPS functions with and without target. The colour scale of each plot has been normalised to the maximum value within the plot. Both standard sonar and P_{1-} processing show the presence of the bubble cloud (between approximately 1.5 to 2.5 ms), the target between 3 to 4 ms and wall reverberations between 4 and 6 ms. In Figures 5.7(a)(ii) and (b)(ii), using P_{1-} alone does not completely suppress the backscattered contribution of the bubble cloud. With P_{2+} processing, the presence of the bubble cloud is enhanced while the presence of the linear scatterer, in this case, the solid target, is suppressed (Figure 5.7(a)(iii)). Figure 5.7(a)(iv) shows P_{1-} / P_{2+} can enhance the presence of the target and suppress the backscatters of the bubble cloud, resulting in improved target detection. Wall reverberation is observed between 4 and 6 ms.

The improved target detection is represented by a better ROC curve for P_{1-} / P_{2+} as illustrated in Figure 5.8(b). The ROC curve for the TWIPS function of P_{1-} / P_{2+} gives a probability of detection of 16% before giving a single false alarm while the ROC curve for the standard sonar processing has a probability of detection of only 1% before giving a single false alarm. The area under the ROC curve for P_{1-} / P_{2+} is 0.85 against an area of 0.66 for standard sonar processing. An area of 1 represents the area under the ROC curve of a perfect detector.

By comparing the results of P_{1-} and P_{2+} (Figures 5.7(a)(ii) and (iii)), an operator can easily distinguish between the backscattered contribution of the linear scatterer (target) and backscattered reverberation of the nonlinear scatterers (bubble cloud), resulting in effective classification of these two types of scatterers. This classification ability is absent in standard sonar technique. However, in target detection performance, the use of P_{1-} is not as effective as using the ratio, P_{1-} / P_{2+} as seen in Figure 5.8. Instead, the detection performance of P_{1-} is only comparable to that of standard sonar processing with comparable ROC curves. In this case, the detection performance of the TWIPS ratio, P_{1-} / P_{2+}, is better than those of standard sonar technique and TWIPS function P_{1-}, as measured by the ROC curves.

The above discussion has shown that TWIPS is able to differentiate between the backscattered contribution of a linear scatterer (the solid target) and the backscattered reverberation of the nonlinear scatterers (bubble cloud). This ability to differentiate between linear and nonlinear scatterers may also help in improving the "visibility" of the linear scatterer. This improvement in target detection capability of the solid target in a bubble-filled environment is demonstrated in the measurement results as quantified using ROC curves.

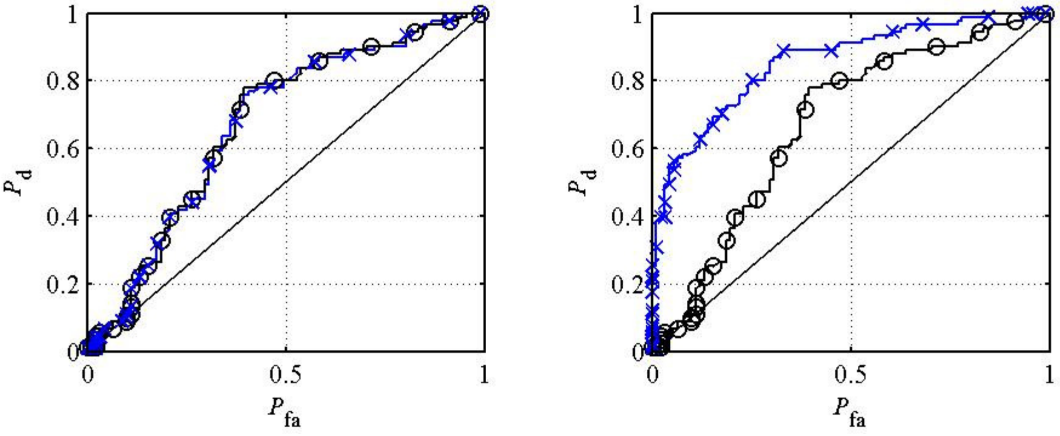
(a) P_{1-}

(b) P_{1-} / P_{2+}

Figure 5.8. Comparison of the ROC curves of standard sonar processing and TWIPS functions computed from the measurements of LFM chirp waveform with target placed at 2.5 m where the open circles are the ROC curve of standard sonar processing and the crosses represent the ROC curve of the TWIPS functions, P_{1-} and P_{1-}/P_{2+} in (a) and (b) respectively. P_d is the probability of detection while P_{fa} is the probability of false alarm.

5.2.3. Sonar simulation model results

Results from the sonar simulation model for a set-up similar to that of tank tests are shown in Figure 5.9. Similar to the tank tests, the standard sonar processing is unable to differentiate the linear scatterer (solid target) from nonlinear scatterers (the bubble cloud). In contrast, Figures 5.9(a)(ii), (a)(iii) and (a)(iv) show the two types of scatterers (solid target and the bubble cloud) can be distinguished from each other by comparing the results of P_{1-} and P_{2+} or the results of the TWIPS ratio and P_{2+}. The primary advantage of using TWIPS in distinguishing between a solid target and bubble cloud is thus demonstrated.

By suppressing the backscatter from the bubble cloud through the use of P_{2+} in the denominator, the backscatter from the linear target is enhanced with the TWIPS ratio (Figure 5.9(a)(iv)). This provides the secondary advantage of improving the target detection performance. A quantitative measure of the improvement in target detection performance compared to standard sonar processing can be obtained from the ROC curves.

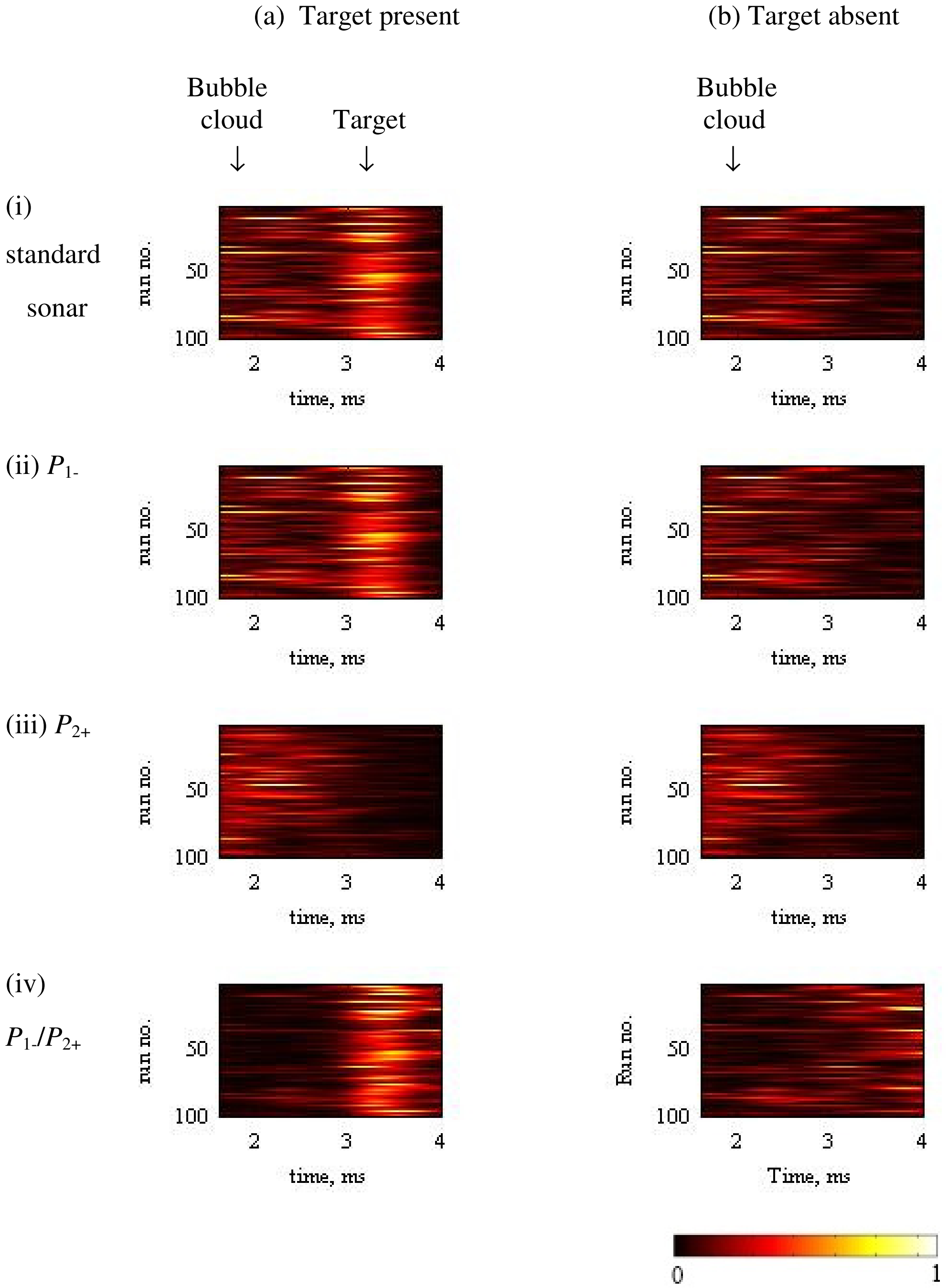

Figure 5.9. Plots of simulations using LFM chirp waveform with target (TS= -15 dB) placed at 2.5 m to compare the processing operators: (i) standard sonar (ii) P_{1-} (iii) P_{2+} (iv) P_{1-}/P_{2+}. In (a) target is present and located between 3 and 4 ms, and in (b) the target is absent. Each colour scale is normalised to the maximum value within each plot, which for (a) are (i) 1.2×10^8, (ii) 4.9×10^8, (iii) 2.8×10^8, and (iv) 3.3×10 and (b) are (a) are (i) 1.2×10^8, (ii) 4.7×10^8, (iii) 2.8×10^8, and (iv) 1.6×10.

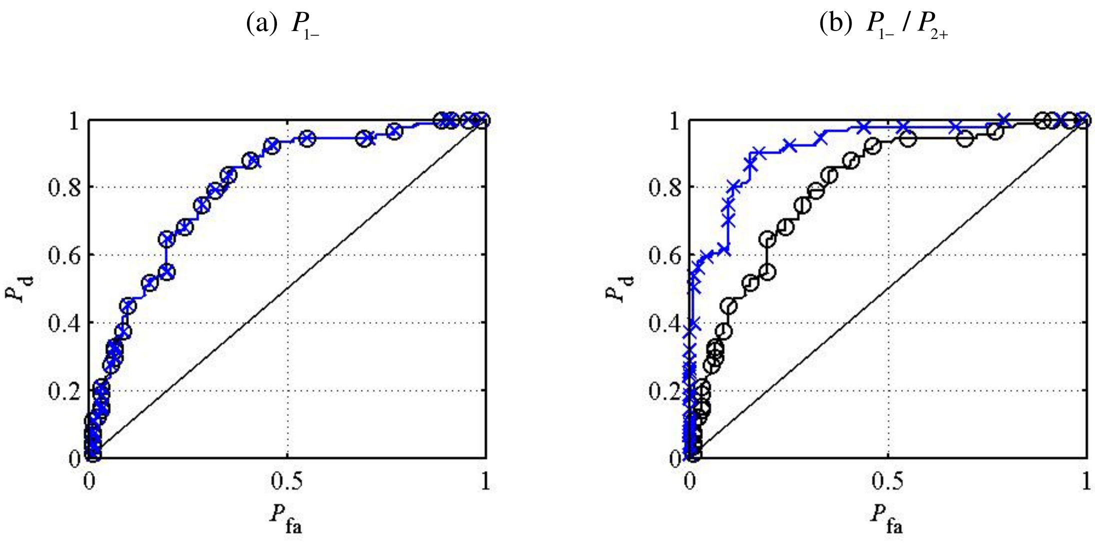

Figure 5.10. ROC curves of standard sonar processing and TWIPS functions computed from the simulation results of LFM chirp waveform with target placed at 2.5 m where the open circles are the ROC curve of standard sonar processing and the crosses represent the ROC curve of the TWIPS functions, P_{1-} and P_{1-}/P_{2+} in (a) and (b) respectively.

Figure 5.10 shows the ROC curves computed from results in Figure 5.9. Both ROC curves show the same trend as the corresponding ROC curves of the tank measurements. The ROC curves in Figure 5.10(b) shows the detection performance of TWIPS function, P_{1-}, is comparable to that of standard sonar processing while detection of the linear target can be improved with the TWIPS ratio, P_{1-} / P_{2+}. While the same trends are observed in the ROC curves for the sonar simulation model (Figure 5.10) and measurements (Figure 5.8), the difference between these curves for the experiment and simulation is explained by the fact that the model fails to reproduce certain aspects of the specific bubble cloud in the tank. In particular, the cloud formed in an experiment will exhibit spatial and temporal heterogeneity which the model is unable to replicate precisely. The absolute performance, as measured by the ROC curves, of the model relative to the experiment suggests that this environmental feature is not perfectly modelled.

5.3. Classification of linear and nonlinear scatterers

The results of both tank tests and sonar simulation model have shown that by visually comparing the plots of P_{1-} and P_{2+}, the backscattered reverberation of the bubble cloud can be distinguished from the backscattering of the solid target. In the tank tests and simulations,

P_{1-} processing enhances the linear backscattered contributions from the linear scatterers, while P_{2+} processing results in the complete cancellation of the returned signals of the linear scatterers. This capability is inherently absent from standard sonar processing.

In both tank tests and sonar simulation model, the bubble cloud used has a wide bubble size distribution which is typical of an oceanic bubble cloud. The backscattered reverberation from the bubble cloud will contain linear backscattered contributions of the larger bubbles, which behave mainly as linear scatterers. Hence, P_{1-} processing may not necessarily result in reduced backscattered contribution from the bubble cloud, and consequently better detection performance compared to standard sonar processing. This will be discussed in greater detail in the next section.

5.4. Efficacy of P_{1-} processing

The results of both tank tests and sonar simulation model have shown that the target detection performance of P_{1-} processing is only comparable to that of standard sonar. They have the same area under their ROC curves, giving a value of 0.66 (Figure 5.8(a)) and 0.79 (Figure 5.10(a)) for the tank tests and simulations respectively. A value of 1 will represent the area under a ROC curve of a perfect detector. The TWIPS function, P_{1-} processing will only outperform standard sonar processing in linear target detection if P_{1-} processing can reduce the backscattered reverberation of the bubble cloud more than standard sonar processing. This reduction of bubble cloud backscatter has to be significant such that the returned signals from the linear target will be higher relative to that of the bubble cloud.

The TWIPS function, P_{1-} and standard sonar are computed as follows. The TWIPS function, P_{1-}, is the smoothed envelope of the responses of $p_-(t)$ computed after application of a filter matched to the frequency of the driving pulse while the standard sonar processing technique consists of averaging the smoothed envelopes of the same matched filtered responses of the pulse pair.

In Section 5.1, it has been shown that $p_-(t)$ does not completely eliminate the scattering of the bubble cloud as $p_-(t)$ gives a doubling of the responses of bubbles larger than the resonant bubble radius (which can be taken as linear scatterers) while giving a reduced response for bubbles with resonant frequencies close to or higher than the frequency of the driving pulses (which can be taken as nonlinear scatterers). Hence, one contributing factor is the wide size distribution of the bubble cloud studied as such bubble cloud will contain large bubbles with resonant frequencies lower than the frequency of the driving pulse.

(a) 150 μm (b) 150 μm (expanded)

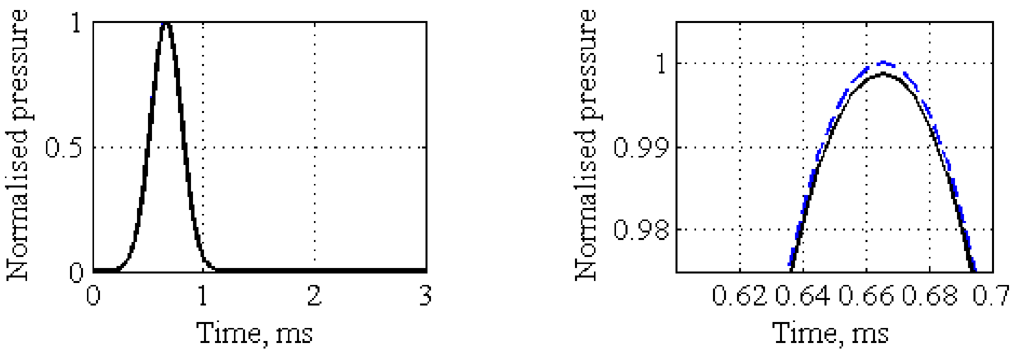

(c) 750 μm (d) 750 μm (expanded)

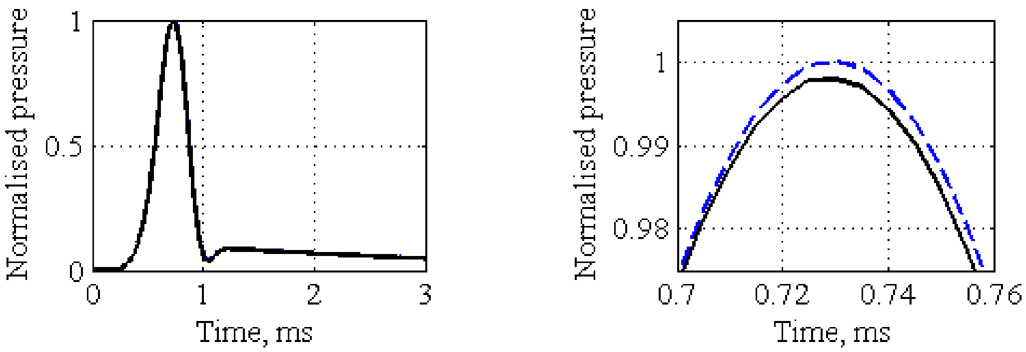

(e) 1600 μm (f) 1600 (expanded)

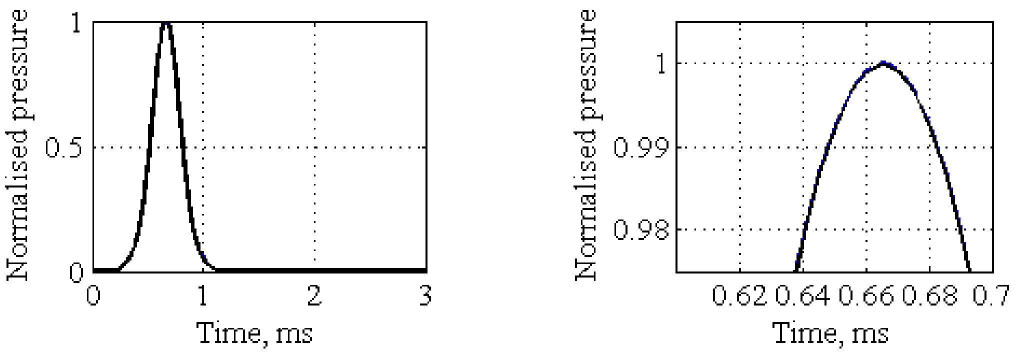

Figure 5.11. Standard sonar processing (denoted by the dotted line) and TWIPS P_{1-} processing (denoted by the solid line) of the bubble response normalized by values of standard sonar processing for pulse used in Section 5.2.1. The bubble radius in (a) is 150 μm, (b) 150 μm (expanded), (c) 750 μm, (d) 750 μm (expanded), (e) 1600 μm, (f) 1600 μm (expanded),

The efficacy of TWIPS P_{1-} can be discussed in greater detail by examining the bubble responses at several representative radii using the nonlinear single bubble model described in Chapter 3 with the LFM chirp used in Section 5.2.1. To prevent simple gains in TWIPS P_{1-} and standard sonar processing, the TWIPS P_{1-} and standard sonar processing have been normalised such that both processing schemes give the same value for the backscattered response of a linear target. In Figure 5.11, the normalised P_{1-} and standard sonar processing values for three representative bubble radii are shown. Figures 5.11(a) and (b) show the processed bubble response for a bubble whose resonant frequency is higher than the driving frequency, or in another word, a smaller bubble. Figures 5.11(c) and (d) show the results for a bubble whose resonant frequency is within the frequency band of the driving pulse and Figures 5.11(e) and (f) for a larger bubble whose resonant frequency is lower than the frequency band of the driving pulse. For the larger bubble, it behaves like a linear scatterer.

For large bubbles (whose resonant frequency are lower than the driving frequencies), the TWIPS P_{1-} processing is only comparable to standard sonar processing as the large bubbles behave mostly like linear scatterers as described in Section 5.1. For bubbles whose resonant frequencies are within (Figure 5.11(b)) or higher (Figure 5.11(d)) than the frequency band of the driving pulse, the TWIPS P_{1-} processing results in lower backscattering compared to standard sonar processing. However, for this particular driving pulse, these differences between TWIPS P_{1-} and standard sonar processing for these bubble sizes are not significant enough for TWIPS P_{1-} processing to have any performance advantage compared to standard sonar processing based on the ROC curve analysis. The ROC curves show the detection performance of TWIPS P_{1-} processing is only comparable to that of standard sonar processing. For this particular pulse, one way to improve the performance advantage of TWIPS P_{1-} processing is by increasing the amplitude of the pulse.

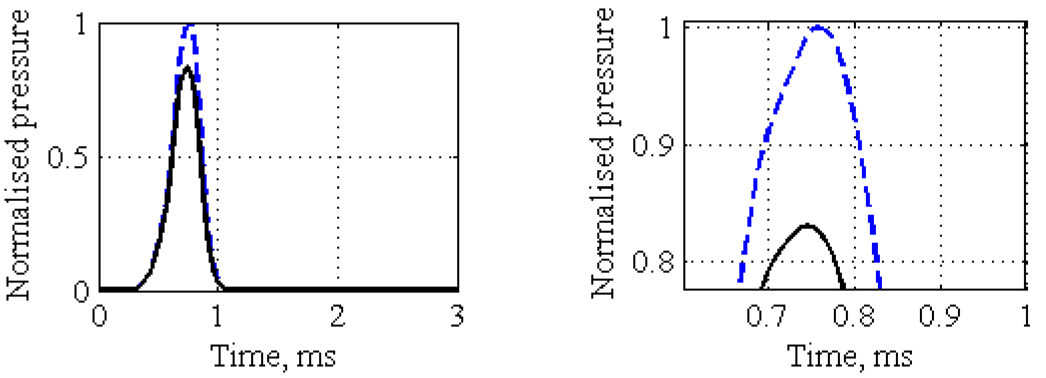
(a) 150 μm (b) 150 μm (expanded)

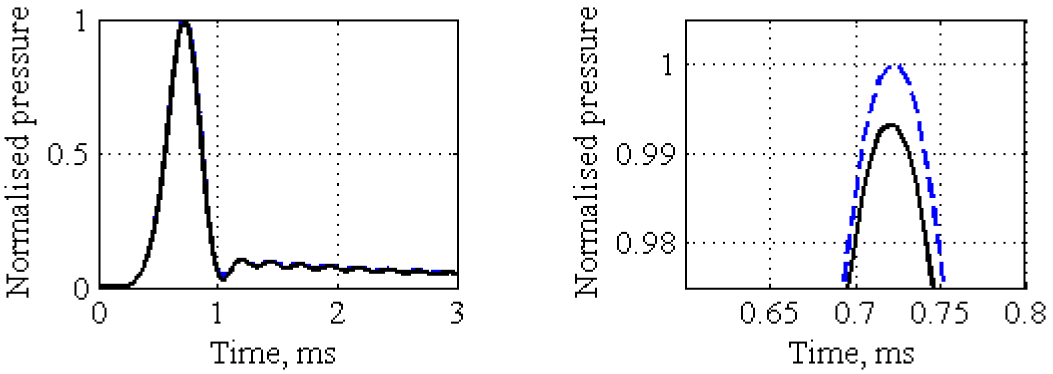
(c) 750 μm (d) 750 μm (expanded)

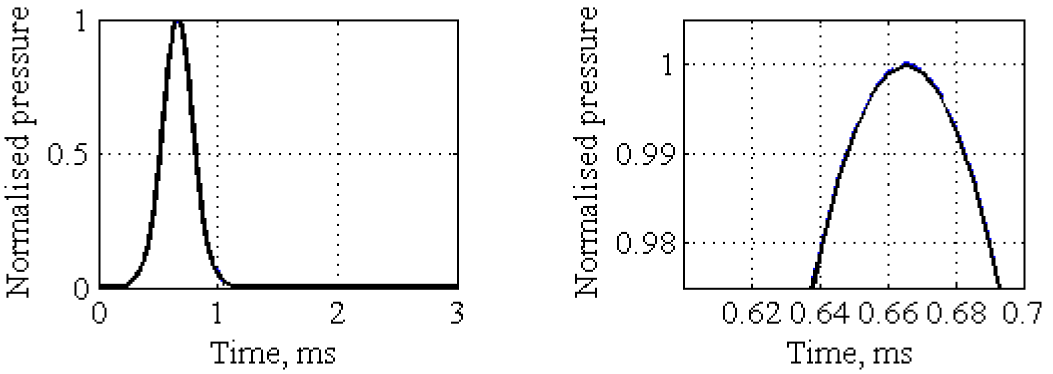
(e) 1600 μm (f) 1600 (expanded)

Figure 5.12. Standard sonar processing (denoted by the dotted line) and TWIPS P_{1-} processing (denoted by the solid line) of the bubble response normalized by values of standard sonar processing for pulse used in Section 5.2.1 with amplitude increased by 6 dB. The bubble radius in (a) is 150 μm, (b) 150 μm (expanded), (c) 750 μm, (d) 750 μm (expanded), (e) 1600 μm, (f) 1600 μm (expanded).

When the amplitude of the pulse used in Section 5.2.1 is increased by 6 dB, Figure 5.12 shows the TWIPS P_{1-} processing results in a lower backscattering compared to standard sonar processing for resonant and smaller bubbles (Figures 5.12(b) and (d) respectively). The differences between TWIPS P_{1-} processing and standard sonar becomes more significant for these bubble sizes at higher amplitudes, suggesting that, if the bubble population contain only bubbles of similar sizes, the detection performance of the TWIPS P_{1-} processing can outperform that of standard sonar processing. However, for the bubble cloud of a wide bubble size distribution studied, larger bubbles will be present. Figure 5.12(e) shows the TWIPS P_{1-} processing is only comparable to standard sonar processing for a large bubble. While the use of a low frequency pulse can decrease the number of larger bubbles (relative to the acoustic wavelength of the driving pulse), and a high amplitude can improve the performance of TWIPS P_{1-} processing relative to standard sonar processing, there are practical constraints in producing a very high amplitude and low frequency signal in oceans [98-100].

To improve the detection performance of TWIPS, a combination of the functions, P_{1-} and P_{2+}, has been proposed by Leighton *et al.* [3, 6] to improve the detection of solid target in bubbly water. This combination of TWIPS functions is commonly referred to as the TWIPS ratio and will be discussed next.

5.5. TWIPS ratio processing

For the LFM waveform used, both tank tests and simulations have shown that the TWIPS ratio, P_{1-} / P_{2+}, can improve the detection of a linear target behind a bubble cloud by enhancing the linear backscattered contribution from the linear target with P_{1-} suppression of the nonlinear backscattered reverberation of the bubble cloud with P_{2+} in the denominator. This improved detection performance can be quantified using the ROC curves shown in Figures 5.8(b) and 5.10(b) for the tank and simulation results respectively.

While the TWIPS ratio, P_{1-} / P_{2+}, obviates the need for time varying gain, this comes with the disadvantage of instability [3, 119]. One way to mitigate this instability is by averaging the values of P_{2+} over sets of adjacent returns. In the results of the TWIPS ratio presented in Figures 5.7 and 5.8, geometrical averaging over ten sets of adjacent returns have been carried out following after Leighton *et al.*[3, 6]. Geometrical averaging is preferred because the natural evolution of the cloud means that the values of P_{2+} over sets of returns can fluctuate and sometimes give rise to very large values. Geometrical averaging reduces large changes to ratios equal to the smaller relative changes by giving each change equal weight without overemphasizing these large values by treating them as absolute numbers [120, 121]. While geometrical averaging is preferred here, arithmetic and reciprocal averaging have all been found effective [3].

One limitation of using the TWIPS ratio is its inability to improve the detection of a linear target in bubbly water if the target is placed close to or within a bubble cloud. This deficiency is the result of its dependence on the suppression of the linear backscatters of the bubble cloud through the use of P_{2+} in the denominator. While the use of P_{2+} in the denominator greatly improves the contrast between the scatters from the linear target and the bubble cloud by suppressing the linear scatters of the bubble cloud, it will also suppress the linear scatters from the target if the target is close to or within the main scatter of the bubble cloud. Use of P_{1-} does not have this limitation. However, the ROC curve (Figures 5.8(a) and 5.10(a)) has shown the TWIPS function, P_{1-} is only comparable to standard sonar processing for the particular pulse used.

The TWIPS function, P_{1-} / P_{2+} together with P_{2+}, like P_{1-} and P_{2+}, allows the nonlinear backscattered reverberation of the bubble to be easily distinguished from the linear backscatters of the solid target, which is the primary advantage of using TWIPS. By visually comparing the plots of P_{1-} / P_{2+} and P_{2+}, the backscatters of the linear target in bubbly environment can be separated from those of the bubble cloud. Here, the detection performance also improves with P_{1-} / P_{2+} outperforming standard sonar processing as measured by the ROC curves.

5.6. TWIPS in nature

From the earliest days of the study of TWIPS, the impetus in finding a sonar solution for shallow bubbly water had come from the dilemma that species of odontocetes, which rely so heavily on echolocation, not only inhabit shallow coastal waters but some species also occasionally at times also make bubble nets, begging the question of whether any odontocete uses TWIPS [1, 7]. While there is no evidence that odontocetes use TWIPS, a major part of this issue is the lack of data in the open literature taken in ways appropriate for answering this question, for example, tank tests of appropriate species subjected to bubbly environments. The paucity of data thus makes it impossible to be categorical about the use of TWIPS by odontocetes while making it interesting points of discussion. Such speculation is justified given that TWIPS has been made to work in sea trials [3, 6].

Multiple pulses with nearly constant amplitude and separation times have been reported from Commerson's dolphin (*Cephalorhynchus commersonii*) [122-124] and Hector's dolphin (*Cephalorhynchus hectori*) [125, 126]. Like all the *Cephalorhychus* species, these are creatures whose primary habitats are shallow waters. For example, the Hector's dolphin is found in coastal waters of New Zealand while the Commerson's dolphin is found in coastal waters of Argentina and Chile. In addition, multiple pulses have also been reported from members of the genus *Phocoena*. Pulses of equal amplitude and in anti-phase have also been reported from the Finless porpoise (*Neophocoena phocoena*) in coastal Asia. While Li *et al*. [127] have attributed these pulses to reflections from the air/water interface, which is a distinct possibility, Dawson and Thorpe [126] have outline evidence for the deliberate generation of multiple pulses by some species. Multiple hydrophones should thus be used to confirm these surface reflections since Medwin [128] found significant fall-off with amplitude of even normal incidence reflections from an upward-looking sonar directed at the air/water interface and significant variation in these reflections attributed to surface waves was also found by Tindle *et al*. [129]. In addition, a study of the propagation loss of porpoise-like clicks by DeRuiter *et al.* [130] also found large variability in transmission loss which can be partly attributed to surface waves.

One of the key ingredients for TWIPS to work is the ability to hear the second harmonic of the echolocation emission. Study of the audiogram of individual animals of various species like the harbour porpoise (*Phocoena phocoena*) [131] has shown that these animals will have difficulty hearing the second harmonic of their echolocation emission. However, the dataset from those species which emit multiple pulses is sparse.

Whilst the above discussion justifies the question of what adaptations shallow-water odontocetes have made for their environment, the pulses measured to date are also ill-suited to generating nonlinearity from oceanic bubble clouds. Firstly, their amplitudes are too low. Some species of odontocetes have been observed transmitting at very high source level [113]. For example, peak-to-peak source levels of 230 dB re 1 μPa m have been recorded from species like the Atlantic bottlenose dolphin, Pacific bottlenose dolphin (*Tursiop gilli*) and false killer whale (*Pseudorca crassidens*) [113, 115]. However, these are not the species that are suspected of transmitting double pulses of opposite polarity. Secondly, the frequencies of echolocation emission of odontocetes tend to be above 100 kHz. This frequency is not optimal for generating nonlinearities from a wide bubble size distribution of oceanic bubble clouds [5]. Bubbles respond to sudden pressure changes on timescale determined by their natural frequencies, which are roughly inversely proportional to their bubble radii. While a nonlinear response can be readily obtained from a resonant bubble, the wide bubble size distribution of an oceanic cloud means that there will be bubbles which will be off-resonant. With a high frequency pulse, the proportion of larger off-resonant bubbles will be higher and larger bubbles will respond approximately linearly whereas a low frequency pulse will be able to excite nonlinearity even from the small bubbles [95]. This has also been discussed in details in Section 4.2.1. While a high frequency pulse is not ideal, it may not as debilitating as initially thought. This is because the bubble size distribution of an oceanic bubble cloud roughly follows a power-law distribution with an exponent ranging from -2.0 to -6.4 (depending on environmental conditions) [95, 111]. Specifically, a high frequency pulse may still operate in an environment with a bubble size distribution which obeys a power-law with a large exponent. In such an environment, the proportion of larger off-resonant bubbles will be significantly lower.

Beside the possibility of TWIPS-like processing with the use of double pulses, Finfer *et al.* [118] also described several scenarios where there might be other competitive advantages of using multiple pulses. For example, if the second pulse insonified the target at an angle which differed from the direct path, it could possibly provide information as to the directional nature of the scatter from the target. Multiple pulses emitted in succession might allow for coherent averaging. This coherent averaging could mitigate the effects of ambient noise or interferences from clutter such as those of oceanic bubble clouds.

5.7. Summary

The efficacy of TWIPS has been demonstrated using a pair of LFM chirp of opposite polarity in this chapter. TWIPS was first demonstrated using a single bubble model. This was then followed by the tank tests at ISVR water tank. Similar observations were obtained using a similar set-up in the sonar simulation model. From the subtraction and addition of the pair of inverted pulses, denoted as $p_-(t)$ and $p_+(t)$ respectively, TWIPS differentiates between the returned signals of a solid target and a bubble cloud, distinguishing between the solid target (linear scatterer) from the bubble cloud (nonlinear scatterers). This capability to distinguish between linear and nonlinear scatterers is absent in the standard sonar technique. Using the TWIPS ratio, P_{1-} / P_{2+}, the secondary advantage of TWIPS was demonstrated. Here, the TWIPS ratio is able to detect the linear target behind the bubble cloud better than that of standard sonar technique. This performance advantage of the TWIPS ratio will be important in a number of applications where the targets are not expected to be close to or within the bubble cloud. For example, given the bubbly nature of the near-surface ocean layer, the performance of a hull-mounted sonar for the detection of naval mines laid on seabeds in shallow water regions could be improved using the TWIPS ratio.

One limitation of the TWIPS ratio is also raised in Section 5.5. Specifically, the TWIPS ratio, while effective in scenarios where the solid target is placed away from the main scatter of the bubble cloud, is not as effective if the solid target is placed close to or within the bubble cloud. While the use of P_{1-} is not constrained by this limitation as it does not depend on the suppression of the bubble cloud through the use of P_{2+} in the denominator, its detection performance was found to be only comparable to that of standard sonar processing for the particular pulse used. For the particular scenario studied, the detection performance of the TWIPS ratio, P_{1-} / P_{2+}, on the other hand, was shown to be outperform the detection performance of standard sonar.

The theoretical and experimental testings of TWIPS have demonstrated that a pair of high amplitude and low frequency pulses will ideally be required. Such conditions appeared to be absent in the available evidence of echolocating odontocetes, which have been observed to give out multiple pulses, some of which have been recorded to be of opposite polarity to each other. While a high frequency pulse is not ideal, it may not as debilitating because of the bubble size distribution present in an oceanic bubble cloud but none of the evidence to date of these odontocetes emit amplitude high enough to suggest the possibility of TWIPS-like processing but. The paucity of data for these odontocetes, however, means that the possibility of TWIPS, in one form or another, cannot be ruled out categorically. Compared to these odontocetes, other echo-locating species like the Atlantic bottlenose dolphin (*Tursiops truncatus*) is known to emit high amplitude pulses. These pulses are also of high frequency, which is not optimal for generating nonlinearity from a wide bubble size distribution. However, they have biosonar that are widely acknowledged to outperform man-made sonar in target echolocation tasks in demanding environments [113, 114]. The next chapter will thus review the current understanding of the echolocation ability of mainly this species of odontocetes for possible insights into potential sonar enhancement solutions. In particular, emphasis will be on sonar enhancement techniques that can allow for capability to distinguish solid targets from bubble clouds and, if possible, improve the detection of such targets.

Chapter 6. Echolocation ability of dolphins

6.1. Literature survey

6.1.1. Introduction

Odontocetes routinely produce pulsed sounds, which many studies have shown to be used for echolocation [106, 113, 115, 132, 133]. The previous chapter described reports of double or multiple pulses of equal amplitudes which were commonly recorded from odontocetes such as from the genus *Cephalorhynchus* [122, 124, 125, 134] and the *Phocoenidae* family [122, 135]. However, it is not clear if these multi-pulses were from surface and bottom reflections [127] or if they were directly generated at source by the animals [134, 136]. The animals could make use of the second pulse of a pair even if they did not generate it, like if they were the source, and purpose of these multiple pulses has not been determined.

However, it has been established that animals like the Atlantic bottlenose dolphin (*Tursiops truncatus*) use many pulses to interrogate a target [113, 115]. Their performance in detecting and classifying targets, particularly in a shallow water environment where the returned signal is dominated by the scatter from the wave-generated bubble clouds in the vicinity of targets, is widely accepted to be superior to man-made sonar [114]. This widely acknowledged fact is why military-trained bottlenose dolphins often represent the only viable sonar option for certain tasks.

The majority of the studies published on odontocete echolocation are on the Atlantic bottlenose dolphin. One reason is because they are the most commonly held odontocetes in zoological parks, research facilities and military compounds. This stems largely from the fact that they can be found close to shore and can be captured relatively easily, easy to train, and they survive in captivity better than most other odontocetes. Hence, the term dolphin used in this chapter will mainly refer to the Atlantic bottlenose dolphin.

This section will review the echolocation ability of the dolphin. It starts with a description of the pulse emitted by the dolphin. This will be followed by a review of the current work on the possible strategies adopted by a dolphin to detect and identify objects in an underwater environment. Based on these understanding, a study on how certain aspects of these findings can possibly be used to enhance target detection and classification in bubbly water is carried out at the end of this chapter.

6.1.2. Characteristics of dolphin signals

A dolphin echolocates by emitting acoustic pulses commonly called ‘clicks’ [113]. These clicks are typically wideband (-3 dB bandwidth potentially exceeding 85 kHz) [113, 137, 138] and short duration (50 to 80 μs) [113, 137, 138]. Peak-to-peak source level as high as 230 dB re 1μPa m has been measured [113, 115, 132]. The dolphin sonar beam has also been characterized as highly directional with past measurements showing a transmission beamwidth of approximately 10^{o} in both horizontal and vertical planes [139-141] with a later study of Moore *et al.* [142], showing the dolphin’s ability to steer and modify the width of its echolocation beam. When searching for targets, the dolphin also transmits a number of clicks normally referred to as a click train. They have been observed to emit 5 to 150 clicks to interrogate a target over a period of a few seconds [143]. The inter-click interval can be as low as tens of millisecond, depending on the distance to the target.

A number of click types have been observed and one click taxonomy was proposed by Houser *et al.* [137] as shown in Figure 6.1. While the clicks are typically wideband and short duration, the echolocation clicks used have been found to vary across individual dolphins with clicks produced by individual dolphins clustering around different peak frequencies [137, 138].

This variation in click types of a dolphin may be caused by age. Ibsen *et al.* [144] studied the characteristics of a female dolphin’s signals and found that the peak frequency, average source level and spectrum shape of the signals emitted by the dolphin changed significantly over a period of five years. Despite these differences, the dolphin was able to perform the same discrimination task at nearly the same level of success.

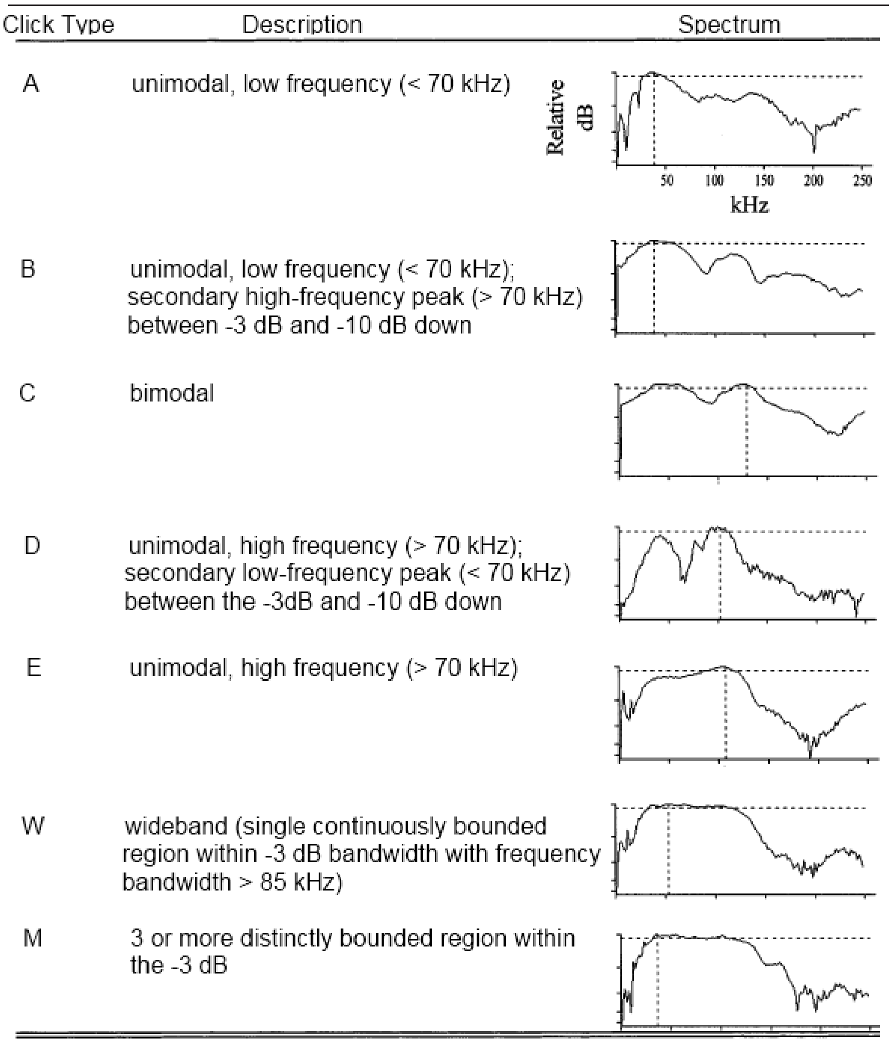

Click Type	Description	Spectrum
A	unimodal, low frequency (< 70 kHz)	
B	unimodal, low frequency (< 70 kHz); secondary high-frequency peak (> 70 kHz) between -3 dB and -10 dB down	
C	bimodal	
D	unimodal, high frequency (> 70 kHz); secondary low-frequency peak (< 70 kHz) between the -3dB and -10 dB down	
E	unimodal, high frequency (> 70 kHz)	
W	wideband (single continuously bounded region within -3 dB bandwidth with frequency bandwidth > 85 kHz)	
M	3 or more distinctly bounded region within the -3 dB	

Figure 6.1. Categories of click types, click type description and a representative spectrum for each. The horizontal dotted line represents -3 dB regions and the vertical dotted line represents peak frequency. (Figure reproduced from Houser *et al.* [137].)

Another possible factor is the task at hand. Capus *et al.* [133] used the experimental data collected from dolphins in both open water testing pens [145] and free-swimming [138] during target echolocation tasks. They found systematic variations in the click types while the dolphins were echolocating a target. This systematic variation will be discussed in greater detail in Section 6.1.3.

The characteristic of the clicks emitted by a dolphin is also known to change with the environment. The earlier measurements of dolphin signals were all carried out in water tanks where the animals were housed until Au *et al.* [146] measured the dolphin signals in open water. Earlier tank measurements reviewed by Evans [139] reported a typical source level of 170 dB re 1 μPa m for peak frequencies that varied between 30 to 60 kHz. The open sea measurements by Au *et al.* [146], on the other hand, obtained signals that have an average peak-to-peak source level of 220 dB re 1 μPa m with peak frequencies that increase to 120 to 130 kHz. Subsequently, peak-to-peak source level as high as 230 dB re 1 μPa m has been measured [132]. The measurements in open water revealed that the dolphin sonar can be highly flexible. One factor affecting the performance of the dolphin sonar is the operating environment. In noisy environments, dolphins have been found to produce louder clicks that have higher frequencies [146] and to produce a greater number of clicks when performing the same task [147].

Past experiments have also suggested that a relationship between centre frequency of the signals and the source level might exist. This relationship between centre frequency and the source level in dolphins was further examined by Thomas *et al.* [148, 149] and Au *et al.* [150] in a series of experiments using other species of odontocetes. With a false killer whale (*Pseudorca crassidens*), their results suggested that there was a relationship between the frequency content of echolocation signals and source level. Au and Nachtigall [132] also compared data of a beluga or white whale (*Delphinapterus leucas*) of Turl *et al.* [151] with the measurements of Au *et al.* [152]. Turl *et al.* [151] measured the sonar signals of a beluga in a clutter detection task in San Diego Bay and these were compared to the low amplitude signals emitted by a beluga in the experiments conducted by Au *et al.* [152]. The peak frequency of the signal was found to be lower when the amplitude was lower, suggesting a relationship between the peak frequency of the signals and source level. Au *et al.* [150] postulated that there could be a physiological reason for the relationship between the frequency and source level of the signal emitted, meaning the species of odontocetes studied could only emit high level clicks if they use higher frequencies.

While it has not been categorically proved that there is a physiological reason for the relationship between centre frequency and source level, what is clear is the adaptability of a dolphin sonar to external factors like age (which probably affects hearing abilities [153, 154]), task types [133, 138, 155, 156], and environment [139, 146, 147, 151, 152]. This flexibility is probably one of the main factors that contribute to the overall performance of the dolphin sonar in object detection and identification, and possibly the reason why it is often difficult to understand fully how a dolphin uses its sonar in target echolocation. The work investigating the possible strategies of a target-hunting dolphin is now reviewed.

6.1.3. Object detection and identification by dolphins

There have been numerous works undertaken to improve the understanding of how a dolphin detects and identifies underwater objects. In the course of the review, it is noted that the practical constraints of an experiment involving dolphins as well as the adaptive nature of the dolphin sonar system mean it is often difficult to devise experiments that can categorically pin-point how a dolphin uses its sonar to detect and identify underwater objects. Instead, many studies seek to test a particular hypothesis of how dolphin sonar operates so as to aid in the design of an analogous biomimetic system. While there have been many studies that seek to understand the dolphin sonar system in the last few decades, there is none which specifically address the issue of target detection and classification in bubbly water. For these reasons, it is of little surprise that many aspects of how the dolphin operates its sonar remain a mystery [115].

One of the factors that can possibly contribute to the good detection performance of the dolphin sonar appears to be the characteristics of their clicks. As stated earlier, a dolphin click is typically broadband, short duration pulse [114]. Based on the bandwidth and duration of a typical dolphin click, Au [113] pointed out the temporal resolution of such a click would be approximately 15 to 20 μs which translated to a distance resolution of 15 cm.

In addition, studies have also found that a dolphin auditory system is able to differentiate the duration, frequency, and intensity of a return echo. For example, a dolphin has been shown to separate broadband sounds that are only 264 μs apart as separate sounds [157, 158]. Discriminating intensities in broadband sound that vary by a small amount (about 1 dB for signal 36 dB above threshold) was shown by Evans [139]. They can also discriminate between a 114.0 kHz tone and a 114.2 kHz tone [159]. Another study has also found dolphins detecting broadband signals slightly better than a pure-tone signal [160]. Evidence presented by Au and Turl [104] also suggested that dolphins can discriminate echoes based on their frequency content. In their experiments, a dolphin was able to discriminate between cylinders, presented two at a time, which varied in material (aluminium versus stainless steel and aluminium versus coral rock). A later study by DeLong *et al.* [161] used a wider array of objects which also suggests the use of the frequency content of the echo returns in the discrimination of the objects.

When performing target detection task, a dolphin will produce click trains to interrogate the target. When faced with a difficult target, the dolphin has been observed to use a greater number of clicks [155, 156]. Hence, many studies focused on the use of click trains by dolphins during target echolocation. In a sonar system, one obvious reason for using multiple pulses would be in improving signal-noise ratio (SNR) when the multiple echoes are combined [118, 162].

Other potential benefits of emitting multiple pulses at fixed interval would include ability to track targets, range of target and to form acoustic images. Altes *et al.* [162] demonstrated that SNR required for target detection decreased in a series of experiments conducted with dolphins as the number of available of echoes increased. Dankiewicz *et al.* [163] further explored this idea of multi-echo processing by artificially manipulating the echoes received by a dolphin. Echoes with varying amplitude modulation rate were created. In their experiments, they found that the dolphin was able to discriminate amplitude-modulated echo trains from those that are not modulated. However, as the echoes used in the experiments were designed to vary in amplitude specifically, it is not clear if an echolocating dolphin actually use amplitude-modulated information for object recognition. The possibility of producing synthetic sonar-like images by combining echoes from objects insonified at multiple orientations was also demonstrated using the short, broadband dolphin clicks [164].

Based on the physics of acoustic scattering, it can be shown that the acoustic scattering of an object will vary at different aspects [82, 83]. With an understanding of the scattering characteristic of an object, it is thus possible to detect and classify an object based on its scattering patterns. Using wideband signals inspired from dolphin clicks, Brown *et al.* [105] showed that shape and material information of an underwater object can be elicited from the responses of the object over different frequencies. This can improve current detection, identification and tracking of underwater objects like buried and partially buried cables [105, 107, 108].

The strategy of the dolphin to use multiple pulses to interrogate a target at different orientations (using body or head movements as observed by Herzing [165]) would seem to be another effective way to improve target classification. The possibility of using multiple pulses to improve sonar performance by odontocetes like the Hector's dolphin and porpoises was also raised by Finfer *et al*. [118]. Use of multiple pulses akin to a dolphin's click train to obtain echoes from different orientation of an object was also investigated and shown to be a strong possibility for better target classification [161, 166]. Using synthetic signals of the dolphin, different acoustic cues were found to be present for different species of fish at different orientation, suggesting that these might be used by the dolphin for prey discrimination [102, 167].

Based on the data of Moore *et al.* [145] and Houser *et al.* [138, 168] collected as part of the Navy Marine Mammal Program, Capus *et al.* [133] hypothesized that the dolphin could obtain additional target information by varying the transmit pulses. From the two sets of data, they observed individual dolphins vary their clicks from uni-modal to bi-modal clicks and back over the course of a target discrimination trial. For one individual, it was observed that the lower frequency component (Click type A in Figure 6.1) was relatively stable but the higher frequency component showed marked variation, varying between Click type B to E as illustrated in Figure 6.1. For another dolphin, the variation in types of clicks was somewhat different but still involved fluctuating between the different click types while keeping the high frequency component relatively steady. From these observations, Capus *et al.* [133] proposed the use of a double down-chirp model to represent a typical dolphin click. In this model, the total duration of the dolphin click is modelled as two down-chirp components having the same chirp rate but with one at a higher frequency than the other. In each case, the high frequency component is delayed by a specified time delay relative to the low frequency component. They suggested that the systemic variation of the click patterns can be represented by varying the amplitude of each component in the model. The 'dolphin' or dolphin-like click used in the sonar simulation model in this thesis is based on this model of Capus *et al.* [133], which can be taken to be an appropriate representation of a real dolphin pulse for engineering purpose.

Houser *et al*. [138] also observed dolphins either varied the source level of the echolocation clicks or moved closer to the targets as the target was interrogated in their experiments. The variation in source level of these clicks during these experiments was found to be as high as 6 dB. Others have reported these echolocation clicks varied from 10% to 70% in a click trains of dolphins compared to the peak during target echolocation [113, 132, 169].

This review of the dolphin echolocation has highlighted the adaptive nature of the dolphin sonar system and give an overview of the possible strategies dolphins may adopt to increase their success rate in an echolocation task. Potentially, these same strategies can aid in enhancing target detection and classification in bubbly water.

6.2. Solution Inspiration

Reviews of the field of ocean acoustics, biomedical imaging techniques to dolphin echolocation studies have yielded hypotheses that merit further investigation in this thesis.

TWIPS has been used to great effect in distinguishing linear scatterers from nonlinear scatterers by Leighton *et al.* [3, 6] for sonar applications. In Chapter 5, the performance of TWIPS in 'classifying' a solid target (a linear scatterer) and bubble clouds (nonlinear scatterers) has been demonstrated using a pair of LFM chirp of approximately 2 to 8 kHz. In some manifestations, TWIPS also improves the detection performance compared to standard sonar processing.

Review of biomedical imaging techniques and dolphin echolocation studies have also yielded several techniques that can form the basis of new sonar solutions for the detection of solid objects in bubbly water.

One technique involves using pulse pair which consists of pulses with different frequencies, referred here as a pair of alternate pulses. The source of inspiration is from the observation of dolphins varying their click types as they investigate a target during target echolocation experiments.

Another technique exploits the use of a pulse pair of different amplitudes which will form the basis of a new sonar solution, the Biased Pulse Summation Sonar (BiaPSS). In biomedical imaging, an amplitude-modulated technique based on a similar principle has also been proposed, albeit to improve detection of the nonlinear UCAs. This is in contrast to the aim of enhancing the detection of linear target while reducing the clutter from bubble clouds for sonar applications. While there is no firm evidence presently to state categorically that dolphins use the same technique to improve target discrimination, the fact that they have been observed to use train of clicks with varying amplitude [113, 115, 138], coupled with the work of Dankiewicz *et al.* [163] on amplitude-modulated echoes, suggest a distinct possibility this may also be applied in biosonar. This argument increases its possibility as a viable engineering solution for distinguishing solid target from bubbles and better target detection in bubbly water.

In biomedical imaging field, a pair of time-reversed pulses has also been proposed to better highlight the presence of nonlinear UCAs for tissue imaging purposes, exploiting the nonlinearity of bubbles. This technique will also be investigated for potential use for sonar applications here.

Before proceeding to investigate these three techniques, it will be appropriate to analyse the characteristics of the dolphin-like pulses. With a better understanding of the performance of such pulses in a bubble-filled environment, certain pulse characteristics may potentially be exploited to enhance target detection and classification in bubbly water.

6.3. Pulse characteristics and sonar enhancement

There has been much work done on the way bubbles might degrade acoustic signals by attenuating the signal and reducing clutter. Most of this concentrated on the steady state response of bubbles, such that with a few exceptions [26, 30, 31, 34] the scattering and extinction cross sections were formulated for the steady state [33]. These studies also focus on the pulse duration of the driving pulse, as the pulsing of the sound field can cause the effect of bubbles to depart significantly from the steady-state behaviour. None of them has focused specifically on dolphin-like pulses. Whist in some circumstances pulsing may increase the bubble-generated effects [90, 91, 170-172], simple growth model, based on an exponential time constant, for the growth of the bubble acoustic cross-sections were mostly used [31, 34] with the exception of Clarke and Leighton [30] who used appropriate time-dependent acoustic cross-sections. For the period after the pulse ended, Leighton *et al.* [26] proposed a strategy to enhance the detection and classification of target in bubbly water. This strategy exploited bubble nonlinearity that might be generated with the use of a pair of inverted pulses (TWIPS) [3, 6]. The investigation of the pulse characteristic seeks to produce similar enhancements from the same basis [26] with the pulse in question being chosen to resemble dolphin echolocation emissions.

For the study carried out here, a chirp signal with characteristics close to the dolphin frequency will be used. Before investigating the effect of the different pulsing of a dolphin-like signal on possible sonar enhancement, which will build on the findings of Clarke and Leighton [30], the influences of two other pulse parameters (pulse amplitude and chirp structure) on possible sonar enhancement will be described in this chapter.

6.3.1. Amplitude of pulse

Odontocetes, like the Atlantic bottlenose dolphin (*Tursiops truncatus*), emit sequences of pulses (a click train) when interrogating a target. Each pulse can have high peak-to-peak source level (up to 230 dB re 1 μPa m) [113, 115, 132] which implies that it has an amplitude which is sufficient to scatter nonlinearly from nearby oceanic bubble populations (the issue here being not the ability to scatter nonlinearly from one specific bubble size, the resonant one, but from a sufficient proportion of the population to give sonar enhancement). During echolocation, the dolphin has been observed to vary the amplitude of each pulse, adapting the characteristics according to the task at hand.

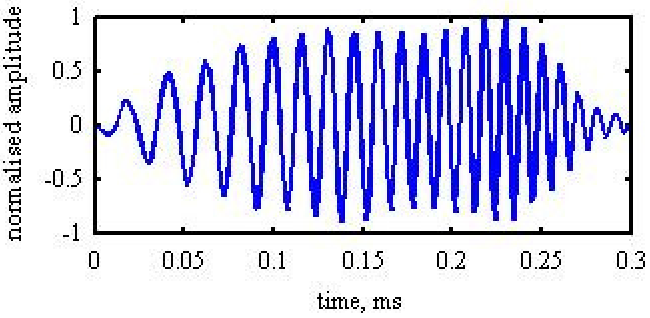

Figure 6.2. The pulse used in the sonar simulation model and tank tests with a zero-to-peak SPL of approximately 212 dB re 1 μPa m.

The consequences of varying the amplitude of the transmitted pulse is illustrated here with a set of results from the tank tests and the sonar simulation model presented in Chapter 3. Figure 6.2 shows the waveform used in the sonar simulation model and tank tests. The pulse used has a LFM waveform whose frequency increased from 30 to 110 kHz over a pulse duration of approximately 300 μs. This will be denoted as Pulse 1 here. A second pulse with amplitude approximately 15% of the amplitude of the first pulse was then used to represent a pulse of lower amplitude, this will be referred to as Pulse 2 here.

The frequency bandwidth of the pulse used is not as wide as that of some reported dolphin pulses [137] so as to keep within the capabilities of the available transducer. To reduce demand on the transducer, the characteristics of the pulses used in the tank tests also deviate from reported dolphin pulses in other ways. Firstly, the duration of the pulse is several factors longer than that of a dolphin pulse. Secondly, the chirp structure of the pulse is different. It is a single up-chirp. rather than the double-chirp structure observed in some dolphin clicks [133, 137].

Figure 6.3 shows the results of the simulation and experiment when the driving pulse was Pulse 1 (Figures 6.3(a)(i) and (a)(ii)) and Pulse 2 (Figures 6.3(b)(i) and (b)(ii)). They were obtained by applying a matched filter to the returned signals from the driving pulse and the processed results over 100 runs are shown. Each plot in Figure 6.3 has been normalised to the maximum value within each plot.

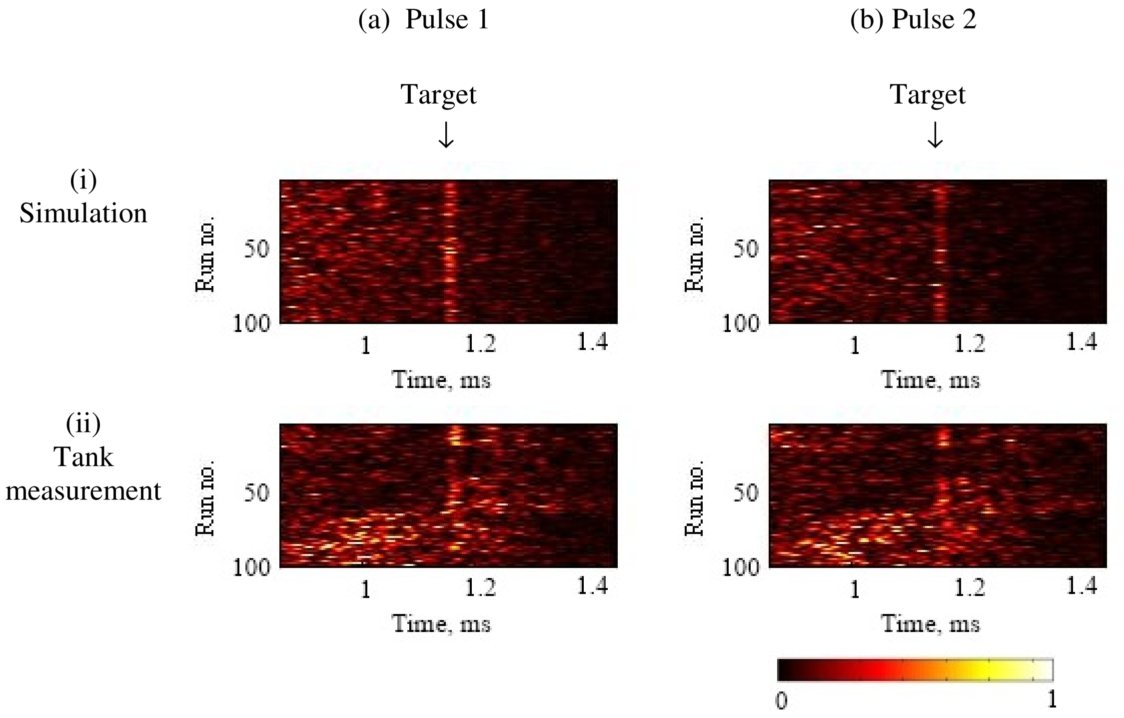
(a) Pulse 1

(b) Pulse 2

Figure 6.3. Use of pulses of different amplitude for a target (TS= -30 dB) placed in a bubbly water with the matched filter applied to the returned signals from Pulse 1 shown in (a) and from Pulse 2 (with amplitude 15% of Pulse 1) in (b). The simulation and measurement results are shown in (i) and (ii) respectively. Each plot has been normalised to the maximum value within each plot. The plots in (a)(i), (b)(i), (a)(ii) and (b)(ii) are normalised by values of 4.8×10^{10}, 2.9×10^{9}, 78 and 1.9 respectively.

Both simulation and measurement results show that there are only marginal differences in the detection performance when amplitude of the pulse is varied. The ROC curve (Figure 6.4) computed from the measurement and simulation results supports this conclusion. Exact agreement between measurements and sonar simulation model are not expected even though the ROC curves follow the same trend. This is mainly because of the spatial and temporal heterogeneity in the bubble clouds of the experiments as explained in Section 5.2.3. Another contributing factor is the linear bubble cloud attenuation model described in Section 3.1.2.1. In practice, a decrease in nonlinear bubble backscatter will commensurate with a decrease in the nonlinear bubble attenuation [173]. This phenomenon has not been adequately represented in the model as only linear bubble cloud attenuation has been incorporated into the sonar simulation model. Only the nonlinear backscattered response of the bubble cloud is described in the sonar model. Hence as the amplitude of the pulse varies, the sonar model only accounts for the nonlinear backscattered response of the bubble cloud and not the nonlinear bubble attenuation.

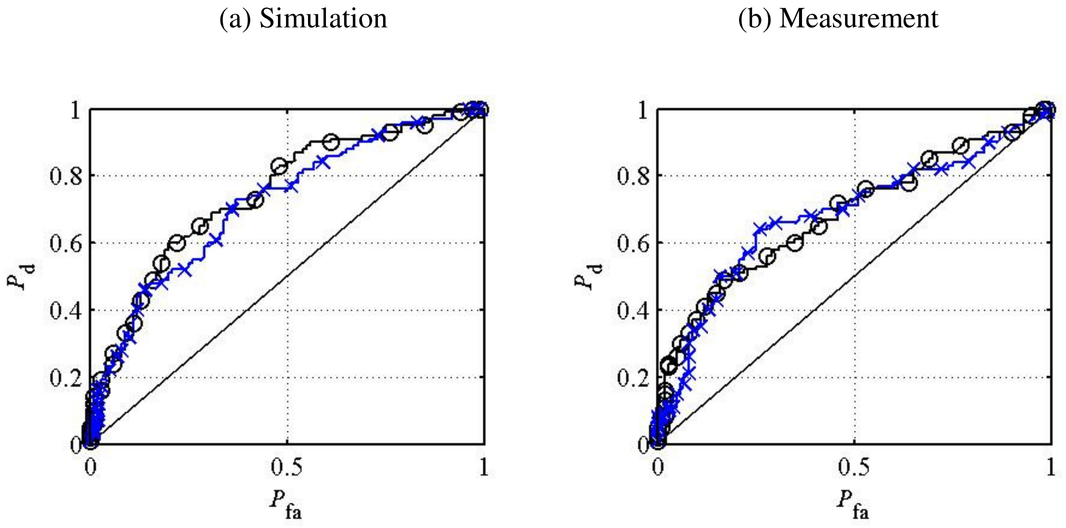

Figure 6.4. ROC curves computed from (a) simulation (shown in Figure 6.3(a)(i) and (b)(i)) and (b) measurements (shown in Figure 6.3(a)(ii) and (b)(ii)). The ROC curve of Pulse 1 is denoted by solid line with open circles and that of Pulse 2 is denoted by solid line with crosses. The solid line indicates the 50:50 line.

When the amplitude of a pulse is reduced, both the backscattered responses of the bubble cloud and target decrease. A target enhancement ratio, $10\log_{10}(E_{\text{target}}/E_{\text{cloud}})$, is calculated where E_{target} is the "energy" associated with the backscatters from the target, taken to be between 1.1 to 1.2 ms and E_{cloud} is the "energy" associated with scatters from the bubble cloud, taken to be between 0.8 to 1.1 ms. This target enhancement ratio compares the relative backscattered energy from the target to that of the bubble cloud. It is found to decrease by 0.7 dB as the amplitude decreases to 15% of the initial amplitude in the measurements.

6.3.2. Chirp structure of pulse

Here, the backscattered responses of a target in a bubble-filled environment to a pulse (up-chirp) and its time-reversed replica (down-chirp) are studied. The up-chirp used is shown in Figure 6.2. The returned signals of the measurements are applied filters matched to the fundamental frequency and second harmonic of the driving signal to obtain the responses shown in Figure 6.5. This is similarly implemented in the sonar simulation results shown in Figure 6.6.

In Figure 6.5(i), the first echo return from the solid sphere can be observed between 1.1 and 1.2 ms. As explained in Section 3.3.4, the size of the spherical target used and the time of arrival of this second echo return suggest that Rayleigh waves resulted in a second echo return around 1.3 ms. The Rayleigh waves are observed between the twentieth and fortieth runs. This is only observed at these times, because then, the main bulk of the cloud was behind the target, reducing the overall attenuation of the driving pulse. Figure 6.5(a)(i) also shows the bubble cloud reverberation for a up-chirp is lower than that of a down-chirp (Figure 6.5(b)(i)). This phenomenon inadvertently affects the identification of the target as the target cannot be easily observed in an environment with increased bubble cloud clutter. This is especially so in the last fifty runs where the main backscattered reverberation of the bubble cloud is observed to be in front of the target.

The detection performance of the up-chirp, as measured by the ROC curves in both simulation and measurements (Figure 6.7), is found to be better than that of the down-chirp. While the ROC curves in both simulations and measurements (Figure 6.7) follows the same trend of the up-chirp having performance advantage in detection compared to the down-chirp, it is noted that the performance advantage of the up-chirp is larger than the down-chirp in the simulations compared to the measurements. In the ROC curves computed from the simulated data (Figure 6.7(a)), the area under the ROC curve increases by 41% for up-chirp against down-chirp. In the measurements, the area under the ROC curve (Figure 6.7(b)), however, increases only by 26%. This difference between measurement and simulation observed in the ROC curves are mainly because of the spatial and temporal heterogeneity in the bubble clouds of the measurements which are not precisely modelled (see Section 5.2.3). In Section 6.3.1, the absence of a nonlinear bubble cloud attenuation model is also cited as another contributing factor.

Another consequent effect of the increased pulsations of a bubble cloud from a down-chirp is the resultant higher second harmonic backscattered reverberation from the bubble cloud. This is observed in measurement results (Figures 6.5(a)(ii) and (b)(ii)) and similarly observed in simulation results (Figures 6.6(a)(ii) and (b)(ii)). Before the second harmonic backscattering results obtained in the measurements are discussed, it is noted that the hydrophone has a reported receive frequency range up to 250 kHz but this response is not flat (> ±5 dB) after 150 kHz [64, 65]. Hence, it will be misleading to obtain a precise level of the second harmonic emission from these tank tests. Instead, only qualitative comparison of the second harmonic emission in the measurements will be made.

In Figure 6.5(b), the second harmonic backscattered reverberation of the bubble cloud is observed to be higher when the driving pulse is a down-chirp. While the use of an efficient filter like a matched filter here will reduce the effects of frequency overlap, it will not be possible to determine if this second harmonic backscatter is entirely nonlinear backscatter without the use of two-pulse techniques like TWIPS.

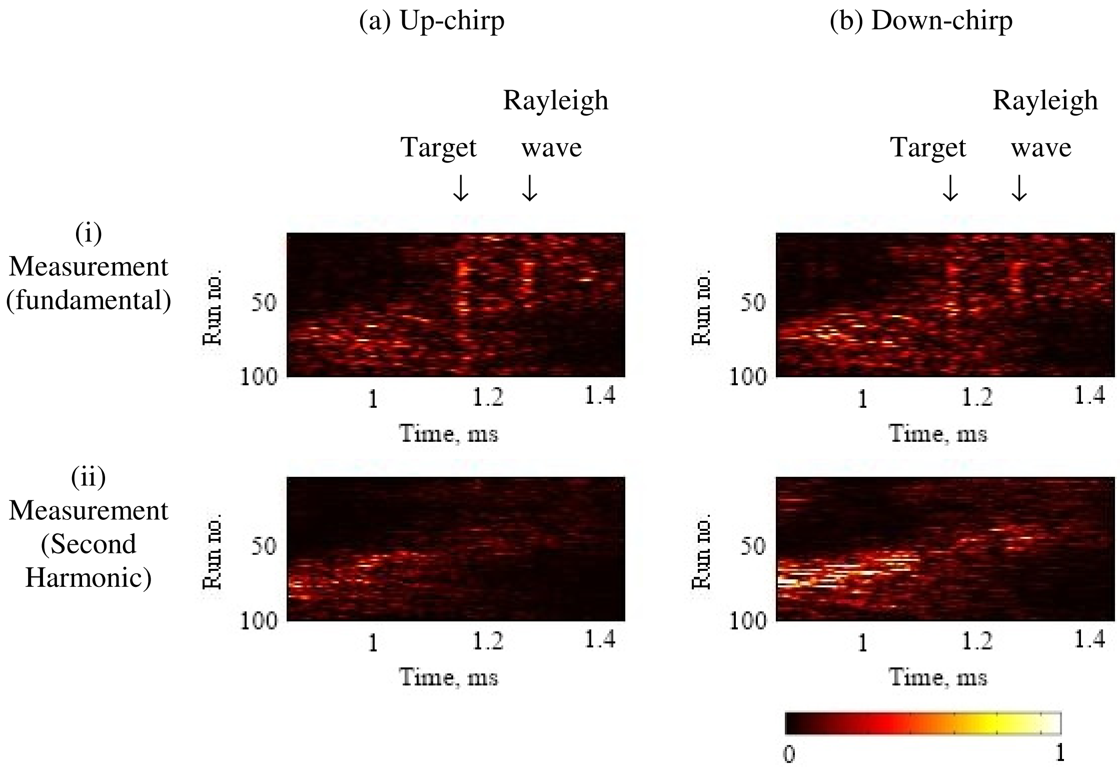

Figure 6.5. Measured backscattered responses of a target (TS= -30 dB) placed in a bubble-filled environment when (a) up-chirp and (b) down-chirp pulse was used. The responses with matched filter applied in the fundamental frequency and second harmonic are shown in (i) and (ii) respectively. The plots in (i), and (ii) are normalised by values of 1.5×10^2 and 1.0×10^2 respectively.

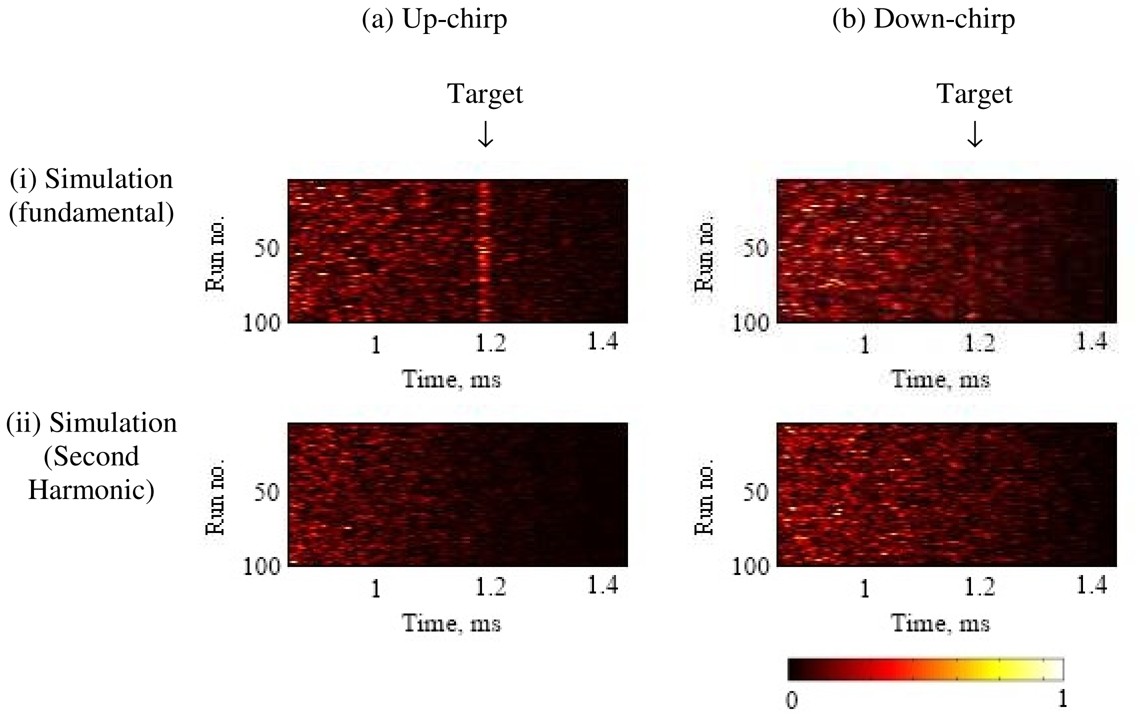
(a) Up-chirp

(b) Down-chirp

(i) Simulation (fundamental)

(ii) Simulation (Second Harmonic)

Figure 6.6. Theoretical backscattered responses of a target (TS= -30 dB) placed in a bubble-filled environment when (a) up-chirp and (b) down-chirp pulse was used. The responses with matched filter applied in the driving frequency and second harmonic are shown in (i) and (ii) respectively. The plots in (a)(i), (b)(i), (a)(ii) and (b)(ii) are normalised by values of 5.5×10^{10}, 4.1×10^{11}, 2.8×10^{10} and 2.3×10^{11} respectively.

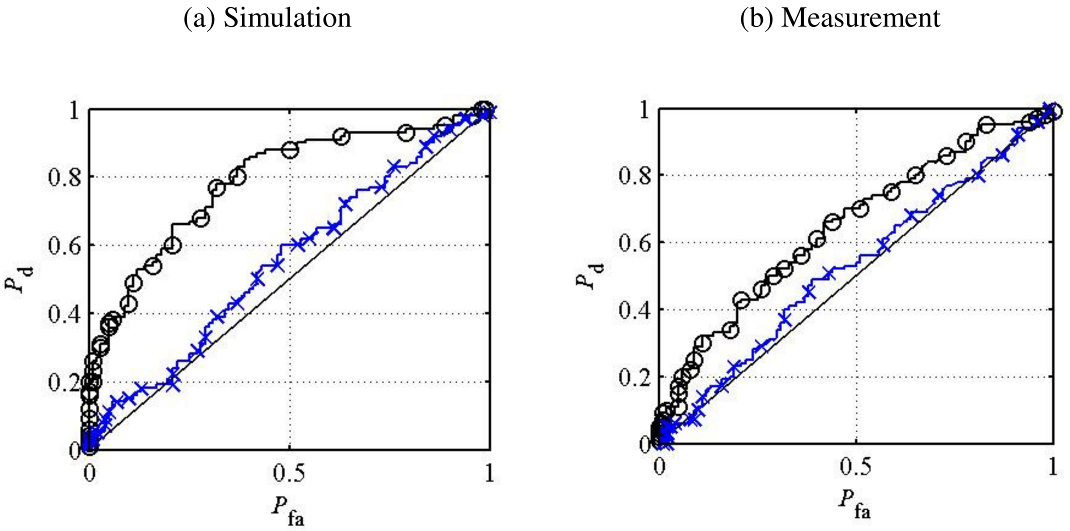
(a) Simulation

(b) Measurement

Figure 6.7. ROC curves computed from 100 runs shown in Fig 6.6 with (a) simulation and (b) measurement. The solid line with circle markers denotes the case with an up-chirp and the solid line with crosses denotes the case with down-chirp.

6.4. Duration of pulse

6.4.1. Using pulses of equal amplitude

Pulses of different duration but of equal amplitude were first used to investigate the effects of varying pulse duration on the detection of target in bubbly water. Figure 6.8 shows two of the pulses used in both sonar simulation model and tank measurements presented in the time domain.

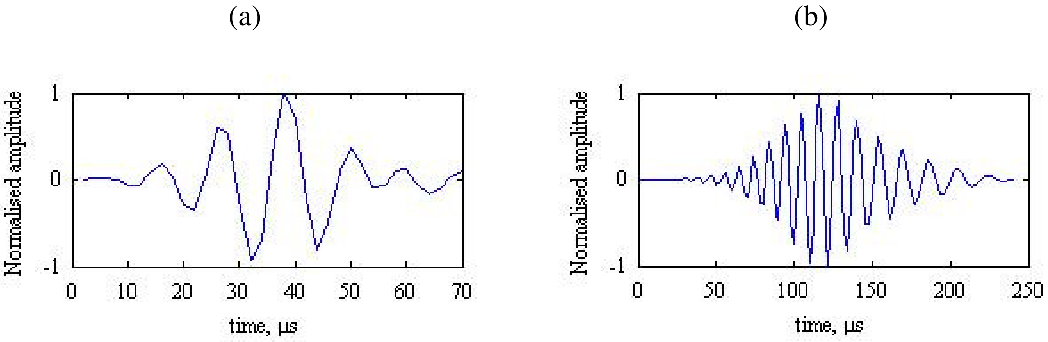

Figure 6.8. The two pulses of duration of (a) 70 μs and (b) 240 μs but of same amplitude used in both the tank tests and sonar simulation models presented in the time domain.

The pulses used have pulse durations ranging from 70 to 240 μs with a zero-to-peak SPL of approximately 213 dB re 1 μPa m. A LFM chirp of the same bandwidth was used for each pulse so that their results would have the same range resolution. The pulses used have frequencies that decreased from approximately 110 to 40 kHz. The normalised amplitude of the pulses used is presented in the frequency domain in Figure 6.9. The pulses used are shown to have similar amplitudes in the frequency domain, and hence very similar bandwidth.

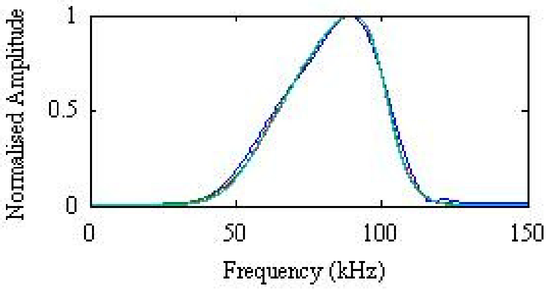

Figure 6.9. The normalised amplitude of the pulses of different durations used in both the tank tests and sonar simulation model presented in the frequency domain.

Figure 6.10 shows the measurement results (from 100 runs) for a target placed in a bubble-filled environment when pulses of different duration were used. The three plots have been normalised to a common value so that meaningful comparison can be made between them. Comparing Figure 6.10(a), where the pulse duration is 70 µs, to Figure 6.10(c), where the pulse duration used is 240 µs, the backscattered reverberation of the bubble cloud relative to the backscattered contribution from the target appears to be higher when a longer pulse is used. This observation is confirmed by the results of the ROC curves shown in Figure 6.11. The ROC curves suggest an improvement in the detection of the linear target when a shorter pulse is used. This improvement is exemplified by a bigger area under the curve as well as a higher probability of detection before giving a single false alarm. Relative to the area under the ROC curve of the longest pulse, the areas under the ROC curve for pulse duration of 70 µs and 180 µs are 16% and 6% higher respectively. The probability of detection before giving a single false alarm are 41%, 17% and 14% for pulse duration of 70 µs, 180 µs, and 240 µs respectively.

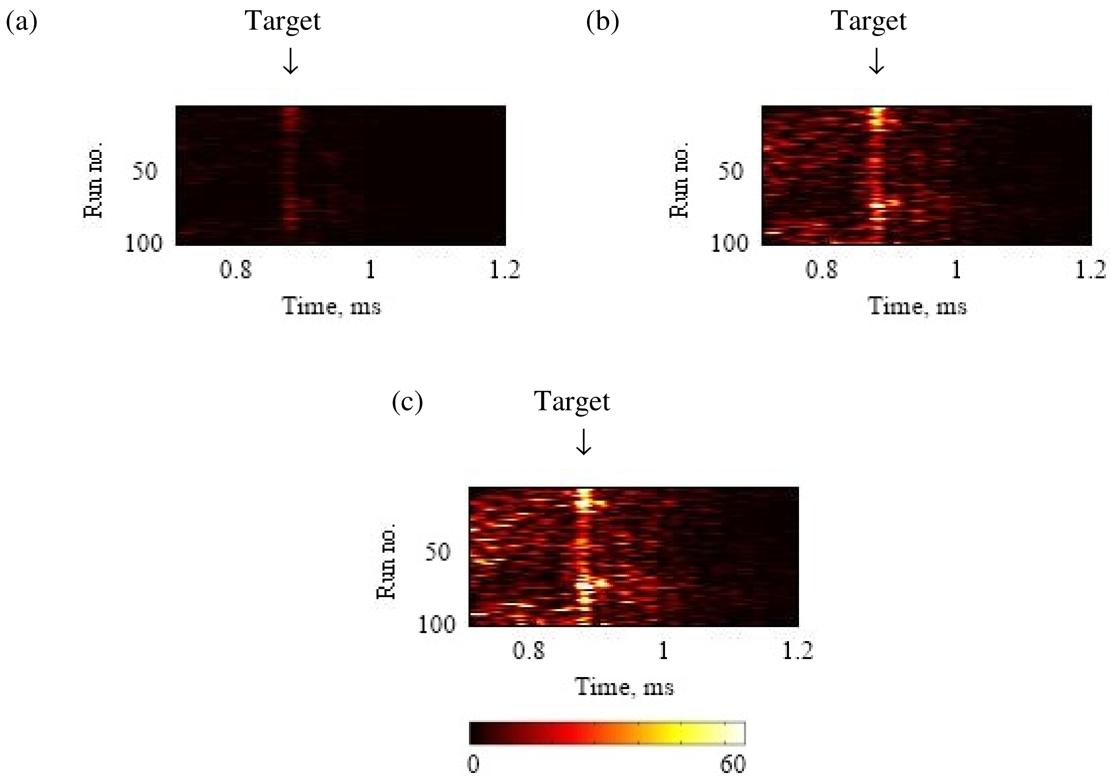

Figure 6.10. Measured backscatter of a target of TS= -30 dB placed in a bubble-filled environment for pulses having a pulse duration of (a) 70 µs (b) 180 µs (c) 240 µs but of same amplitude. The plots are normalised to a common value of 60.

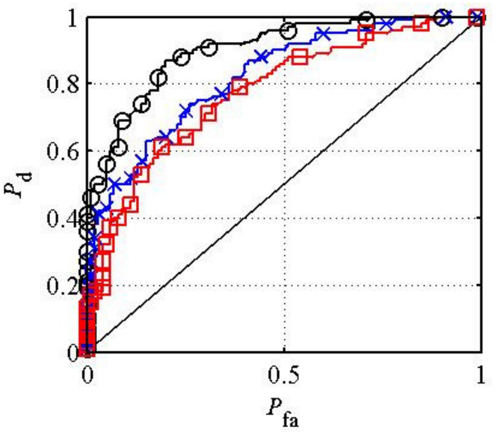

Figure 6.11. ROC curves computed from measurements shown in Figure 6.10. The ROC curve of the pulse with duration of 70 μs, 180 μs and 240 μs are denoted by solid line with circular markers, solid line with cross markers and solid line with square markers respectively. The solid line indicates the 50:50 line.

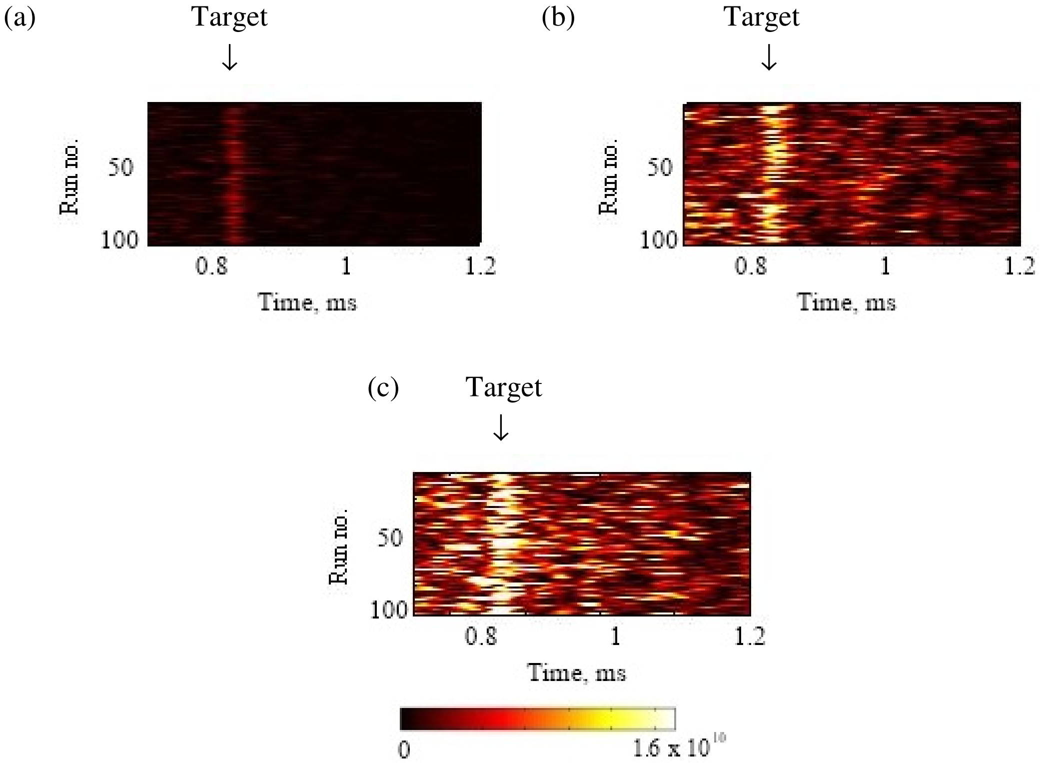

Figure 6.12. Backscatter of a target of TS= -30 dB placed in a bubble-filled environment for pulses having a pulse duration of (a) 70 μs (b) 180 μs (c) 240 μs but of same amplitude from simulations. The plots are normalised to a common value of 1.6×10^{10}.

The sonar simulation model was also used to compute the returned signals of a target placed in the bubble cloud in a set-up similar to the tank test. Using the same pulses used in the tank tests, the observations made in the sonar simulation model (Figure 6.12) follow similar trends seen in measurements. Based on the ROC curves (Figure 6.13), the shortest pulse is shown to have the best detection performance compared to the other longer pulses.

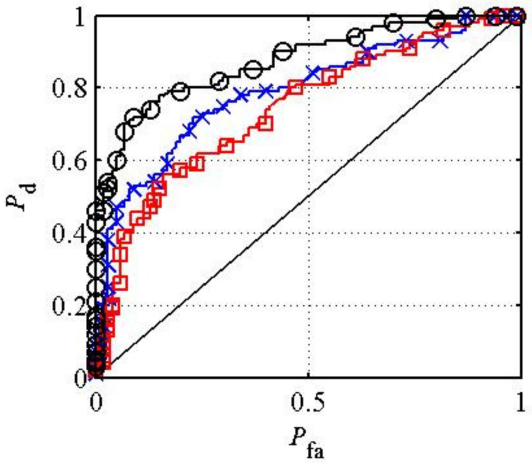

Figure 6.13. ROC curves computed from sonar simulation results shown in Figure 6.12. The ROC curve of the pulse with duration of 70 μs, 180 μs and 240 μs are denoted by solid line with circular markers, solid line with cross markers and solid line with square markers respectively. The solid line indicates the 50:50 line.

6.4.2. Using pulses of equal energy

The effects of pulse duration on the detection performance of a target in a bubbly environment were then investigated using pulses of different duration but of equal energy. By adjusting the amplitude of each pulse, the integral of the square of the pressure waveform for each pulse was made equal. Figure 6.14 shows two pulses of different durations, with Figure 6.14(a) showing a pulse of 70 μs and Figure 6.14(b) showing a pulse of 240 μs.

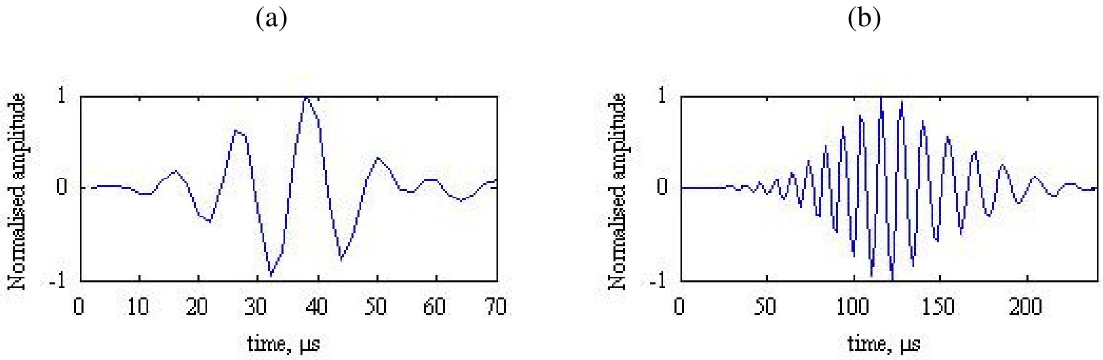

Figure 6.14. The normalised amplitude of two pulses of duration of (a) 70 μs and (b) 240 μs but of same energy used in both the tank tests and sonar simulation models presented in the time domain.

The shortest pulse has a zero-to-peak SPL of approximately 213 dB re 1μPa m with the longest pulse having a zero-to-peak SPL of approximately 209 dB re 1μPa m. The amplitude of each pulse was scaled such that the pulses used could be considered to have the same energy.

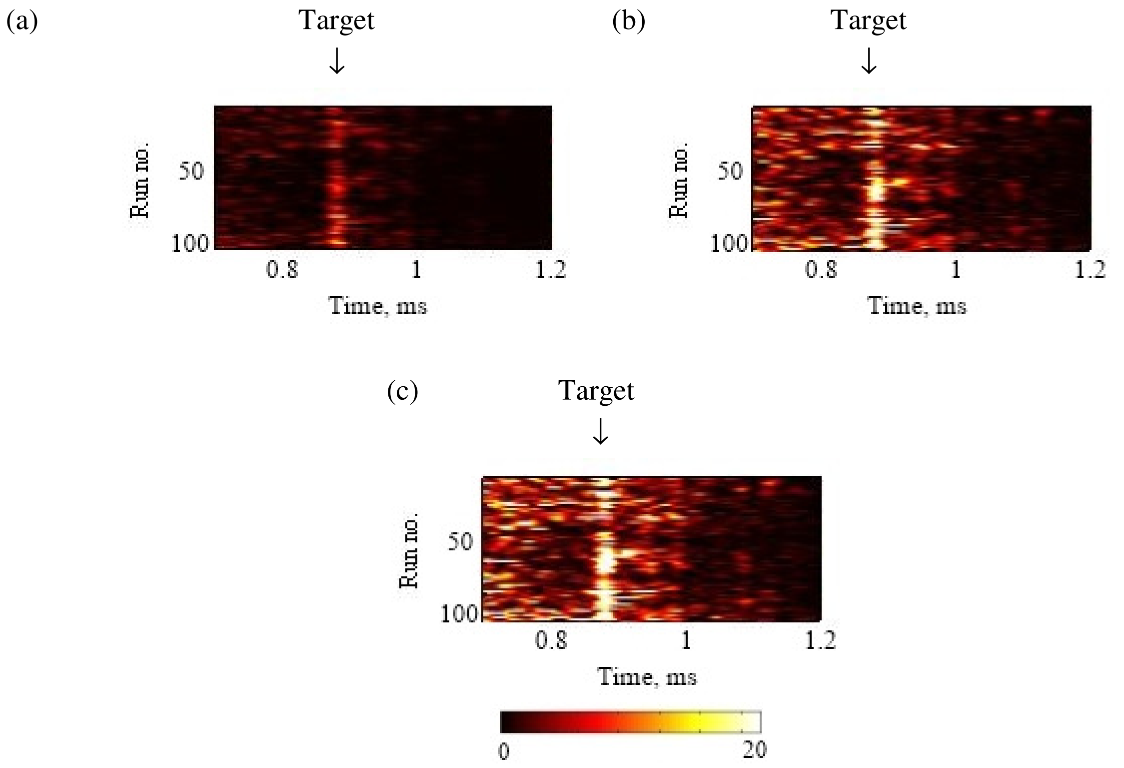

Figure 6.15. Measured backscatter of a target of TS= -30 dB placed in a bubble-filled environment for pulses having a pulse duration of (a) 70 μs (b) 180 μs (c) 240 μs but of same energy. The three plots are normalised to a common value of 20.

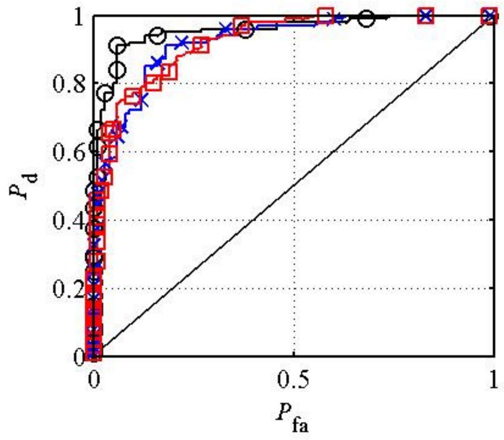

Figure 6.16. ROC curves computed from measurements in Figure 6.15. The ROC curve of the pulse with duration of 70 μs, 180 μs and 240 μs are denoted by solid line with circular markers, solid line with crosses and solid line with square markers respectively. The solid line indicates the 50:50 line.

Figure 6.15 shows the measurement results as the duration of the signal increases from 70 μs to 240 μs. The returned signals from the bubble cloud (relative to that of the solid target) are marginally higher for the longer pulses.

Figure 6.16 presents the ROC curves generated from the tank measurements shown in Figure 6.15. Amongst the pulses studied, the ROC curves suggest the shortest pulse (duration of 70 μs) gives the best detection performance. The probability of detection of the shortest pulse (of 70 μs) is 49% before giving a single false alarm. For the longer pulses, the 180 μs and 240 μs pulse has a probability of detection (before giving a single false alarm) of 33% and 22 % respectively. While similar trends are observed in the ROC curves for the sonar simulation model (Figure 6.18) and measurements (Figure 6.16) with poorer detection performance for longer pulses, the absolute performance as measured by the ROC curves for the experiments and simulations are not the same. This is because the model does not replicate certain spatial and temporal aspects of the specific bubble cloud in the tank and the bubble cloud attenuation model used is linear which does not represent the bubble cloud attenuation in the tank tests precisely. These have been explained in Sections 5.2.3 and 6.3.1.

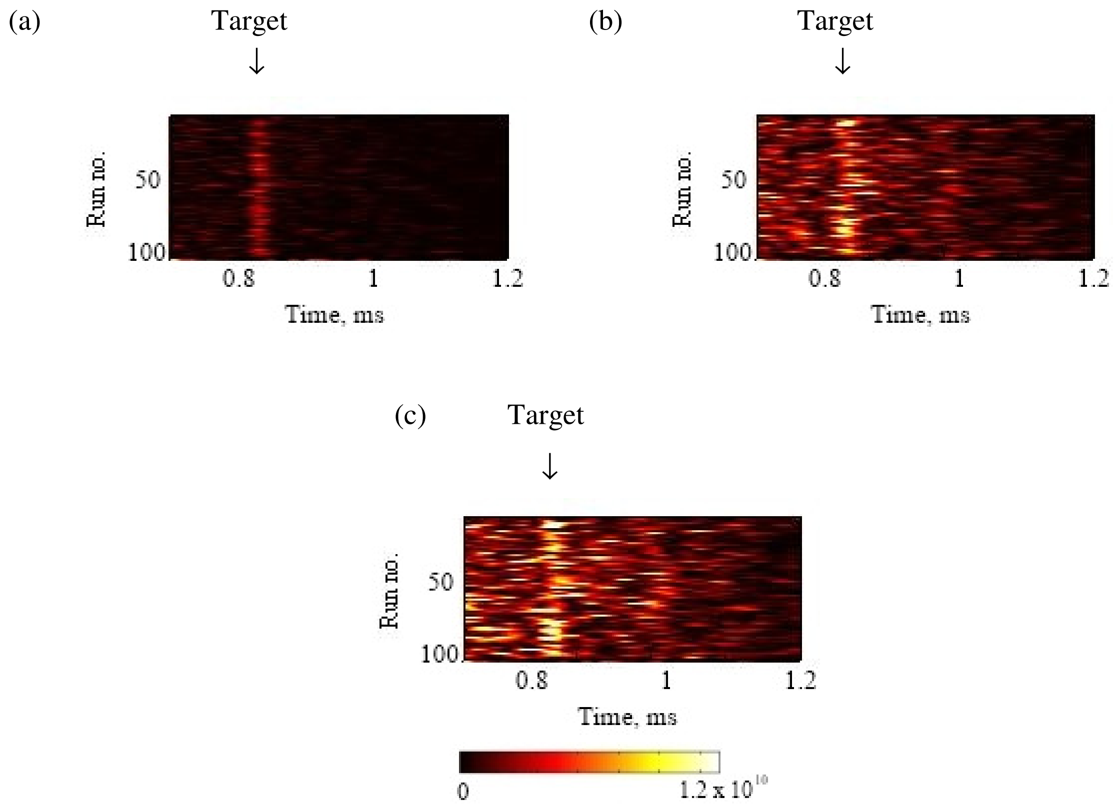

Figure 6.17. Backscatter of a target of TS= -30 dB placed in a bubble-filled environment for pulses having a pulse duration of (a) 70 μs (b) 180 μs (c) 240 μs but of same energy from simulations. The plots are normalised to a common value of 1.2×10^{10}.

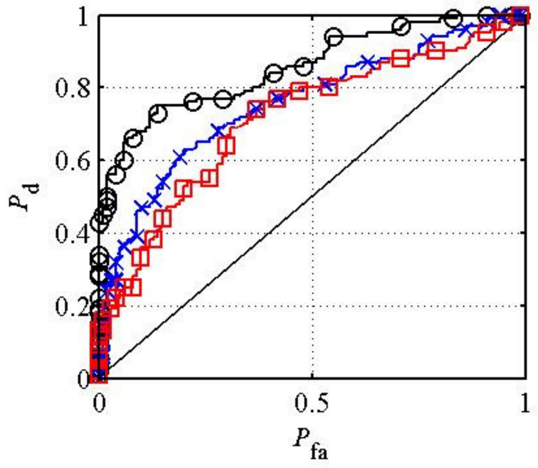

Figure 6.18. ROC curves computed from sonar simulation model in Figure 6.17. The ROC curve of the pulse with duration of 70 μs, 180 μs and 240 μs are denoted by solid line with circular markers, solid line with crosses and solid line with square markers respectively. The solid line indicates the 50:50 line.

6.5. Discussion

6.5.1. Amplitude of pulse

Both the measurements and the sonar simulation model have demonstrated a not unexpected effect in the response of the bubble cloud as the amplitude of the pulse is decreased. In this instance, the amplitude is reduced to approximately 15% of that of the initial pulse and the target enhancement ratio, $10\log_{10}(E_{\text{target}}/E_{\text{cloud}})$, decreases by 0.7 dB. This ratio gives a quantitative measure of the level of backscattered contribution from the target relative to the clutter of the bubble cloud. The small decrease in target enhancement ratio results in only a marginal change in the ROC curve, without any significant difference in the detection performance.

The decrease in the target enhancement ratio when the amplitude is decreased can be explained by considering the bubble pulsation as the driving amplitude changes. The nonlinear response of the bubble increases as the driving amplitude increases and we see an increase in the ratio of the power scattered and absorbed by the bubble in the higher harmonics, to the intensity of the driving field (the acoustic scatter and absorption cross-section, respectively). For a linear scatterer, like a solid target, the acoustic scatter and attenuation scale with the amplitude of the driving pulse. In both measurements and the sonar simulation model, the returned signal was applied a filter matched to the frequency of the driving pulse. As the amplitude increases, nonlinearity of the bubbles results in more backscattered energies in the higher harmonics, resulting in a corresponding lower backscattered energy in the fundamental from the bubbles as observed in Figure 6.3. Hence, with an increase in amplitude, the target enhancement ratio may actually increases.

In the scenario studied, the decrease in target enhancement ratio with a corresponding decrease in amplitude suggests the overall cloud response might be dominated by resonance bubbles and, for the population in question, it is the fundamental of the pulsation resonance (rather than, say, geometrical scattering from the large bubbles) which is causing the scatter and attenuation.

While the population used here suggests the dominant effects of the resonant bubbles, the number of bubbles responding at the second harmonics is also not insignificant. If the population is biased such that there is insufficient number of these bubbles, the decrease in target enhancement ratio will be higher and consequently the detection performance as measured by the ROC curves will be significant. With such a bubble population, a decrease in the fundamental resonance peak in the acoustic extinction cross-section will be accompanied by increase in the contribution from bubbles having radii which are integer multiples of the driving frequency. The driving pulse used was a chirp waveform that increased from 30 to 110 kHz. Using the centre frequency of 70 kHz as an illustration and Eq. (4.1) as a rough guideline for bubble resonance, there would be increases in the cross-section of bubbles having radii of about 20 μm and 14 μm, corresponding to resonant frequencies of 140 and 210 kHz respectively. However, a decrease of 0.7 dB in the target enhancement ratio in the scenario studied here suggests that these bubbles were not present in sufficient number to outweigh the effects of the resonant bubbles.

The decrease in target enhancement ratio observed should also not be taken as a general rule the backscattered contribution of a bubble cloud at the driving frequency will not always decrease with an increase in amplitude of the driving pulse. Leighton *et al.* [173] have illustrated the complexity of this issue by comparing the change in attenuation (from which backscatter can be inferred) with driving amplitude for a range of bubble populations and pulse amplitudes. For bubble populations with certain power law exponents, they have shown increasing the driving amplitude can first decrease and then (at even higher amplitude) increase the attenuation and such behaviour can possibly be leveraged upon to gain some information on the bubble size distribution.

6.5.2. Up-chirp and down-chirp

Significant differences between the responses to an up-chirp or down-chirp signal in the same frequency band have been observed. In nature, it is common to find signals similar to chirps produced by animals using echolocation, like bats and dolphin. Some of these signals have been reported to be down-chirp [113, 174].

Both the tank measurements and the sonar simulation model have shown that the overall backscattered reverberation of the bubble cloud increases when a down-chirp signal is used. The responses of the bubble cloud when applied a matched filter in the second harmonics of the driving pulse is also found to be higher when a down-chirp signal is used.

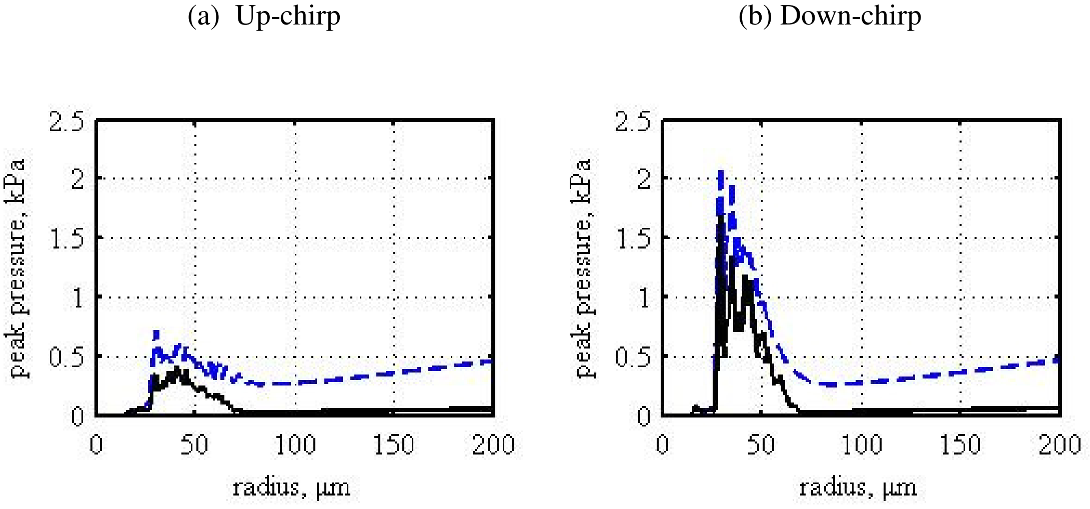
(a) Up-chirp

(b) Down-chirp

Figure 6.19. Simulation results of the peak pressure radiated by a single bubble at 1 m as a function of the radius of that bubble when applied a matched filter at fundamental frequency (dotted line) and second harmonic (solid line) of the driving pulse. The two driving pulses used in Section 6.3.2 are shown: (a) the up-chirp and (b) the down-chirp.

This increase in the overall backscattering response of the bubble cloud can be better understood by considering the theoretical response of a single bubble for a range of bubble size when excited by the same up-chirp and down-chirp used in the experiments. In Figure 6.19, the down-chirp is shown to give both higher fundamental and second harmonic bubble responses compared to the up-chirp for the resonant bubbles. The level of second harmonic response as a percentage of the fundamental response is also observed higher for the down-chirp compared to the up-chirp, implying a higher state of nonlinearity. For a bubble radius of 50 µm, this percentage is 49% for the up-chirp against 67% for the down-chirp. Figure 6.19 also shows that for larger bubbles, they begin to behave more like linear scatterers. The match-filtered responses of the larger bubbles (~ > 100 μm for this case) are the same whether driven by an up-chirp or down-chirp. It is likely a nonlinear mechanism is responsible for the increased overall backscattering response of the bubble cloud by a down-chirp (against an up-chirp), and consequently its poorer detection performance, as measured by the ROC curve (Figure 6.7). From the theoretical response of a single bubble (Figure 6.19), the increase in the overall backscattering response of the bubble cloud for a down-chirp is attributed to the increased backscattering of the bubbles in the range of bubble sizes with resonant frequencies within or close to the frequency of the driving pulse.

While it is not intuitive the exact mechanism which accounts for different bubble cloud behaviour when a down-chirp is used against an up-chirp of the same frequency band and amplitude, the results shown in both Figures 6.19 and 6.20 suggest the down-chirp is able to drive the bubble to a higher state of nonlinearity compared to an up-chirp. Comparing the local maximum of the peak pressure radiated by a bubble as a function of its radius when applied a matched filter at the fundamental frequency for a down-chirp (Figure 6.20(b)) against an up-chirp at a lower amplitude of 10 kPa (Figure 6.20(a)), it can be estimated the use of a down-chirp increased the fundamental response of the bubble by approximately 3% against an up-chirp when the pulse duration is 50 μs. As the pulse duration increases to 300 μs (Figures 6.20(c) and (d)) and 1 ms (Figures 6.20(e) and (f)), the increases for a down-chirp against an up-chirp are 23% and 141% respectively. It is thus clear that for a short-duration chirp signal of 50 μs, the bubble responses (after applied a matched filter) when driven by a down-chirp is only marginally higher than that of the up-chirp at amplitude of 10 kPa. As the pulse duration increases (with the amplitude kept constant), the pulse will contain greater energy and therefore able to excite a greater degree of nonlinearity. Hence, for the three pulses of different durations studied (Figure 6.20), the greatest difference between the responses to an up-chirp or down-chirp signal in the same frequency band has been observed when the pulse duration is 1 ms.

(a) 50 µs up-chirp (b) 50 µs down-chirp

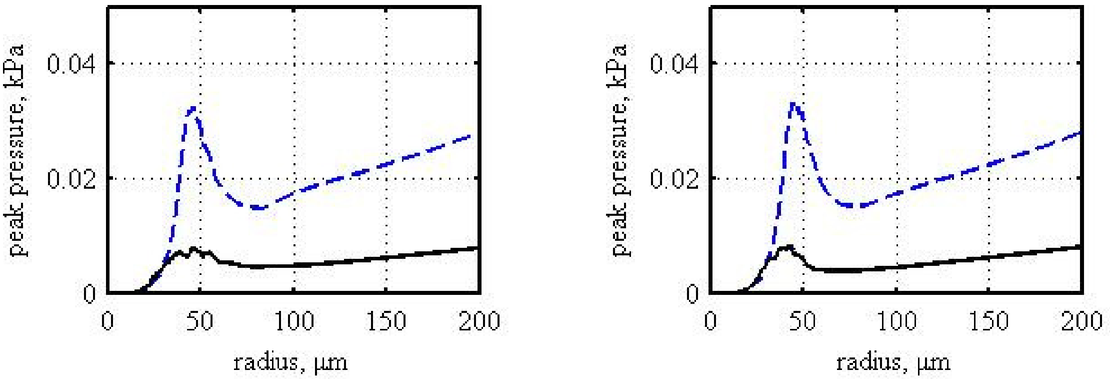

(c) 300 µs up -chirp (d) 300 µs down -chirp

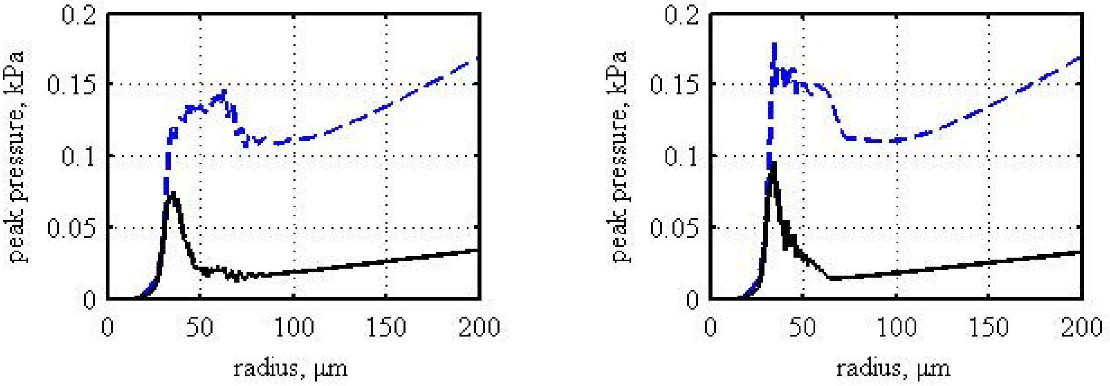

(e) 1 ms up-chirp (f) 1 ms down-chirp

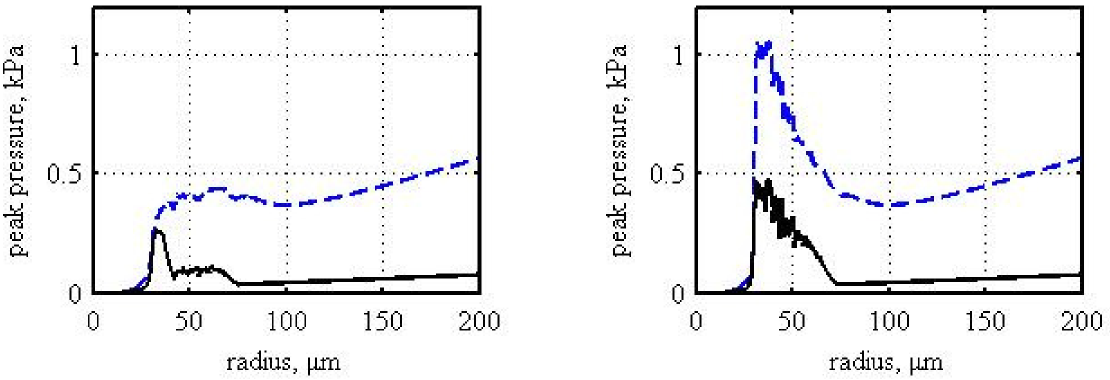

Figure 6.20. Simulation results of the peak pressure radiated by a single bubble at 1 m as a function of the radius of that bubble when applied a matched filter at fundamental frequency (dotted line) and second harmonic (solid line) of the driving pulse. A 30 to 110 kHz LFM chirp of amplitude of 10 kPa with different pulse duration are shown with: (a) 50 µs up-chirp, (b) 50 µs down-chirp, (c) 300 µs up-chirp, (d) 300 µs down-chirp, (e) 1 ms up-chirp, and (f) 1 ms down-chirp.

Whilst the study of the single bubble response to an up-chirp and a down-chirp of different pulse durations show a shorter pulse (with duration of the order reported in dolphin clicks [113, 115, 138]) will reduce the difference in bubble responses between an up-chirp and down-chirp, the difference between an up-chirp and a down-chirp begs question why dolphins like the Atlantic bottlenose dolphin use down-chirps, sometimes with amplitude as high as 230 dB re 1 μPa m, in their echolocation. In coastal waters where the water may be bubbly, a high-amplitude down-chirp (against an up-chirp) will result in a poorer target detection performance, even though nonlinear scatterers like bubble clouds can be driven to a higher degree of nonlinearity with such pulse, making it easier to implement some form of nonlinear processing. Currently, there is no evidence to suggest dolphins can use any form of nonlinear processing and hence, this raises question which can only be answered with more data from dolphins.

6.5.3. Pulses of different duration

The ROC curves for pulses of equal amplitude and energy are computed from both measurements and simulations showing the effects of varying pulse duration on the detection performance of a solid target in a bubbly environment. The better detection performance of the shorter pulses appears to be the result of decreased backscattered response of the bubble cloud.

Test configuration	**Pulse duration**	
	180 μs	**240 μs**
Equal amplitude	-0.9 dB	-1.4 dB
Equal energy	-0.8 dB	-1.0 dB

Table 6.1. The differences in measured target enhancement ratio of different pulse durations with respect to the shortest pulse (duration of 70 μs) in decibels.

The target enhancement ratio, which compares the total energy associated with the backscattered responses of the target to that of the backscattered responses of the bubble cloud, is computed for the tank measurements. Results are summarised in Table 6.1. When pulses of different durations are compared, the target enhancement ratio of the longer pulses are found to be between -0.8 to -1.4 dB lower than that of the shortest pulse used. This is related to the dynamic and nonlinear nature of the bubble cloud before it reaches steady state.

The importance of nonlinearity of the bubbles cannot be downplayed. It has been shown that the time taken to reach steady state is the longest for a resonant bubble in a low amplitude sound field [30]. Therefore, in a low-amplitude condition, unless the driving pulse is much longer than the resonant bubble ring up time (or unless the number of resonant bubble ring up present is insignificant), then the actual scatter attained by the bubble during the pulse would be less than in the steady state [30]. This increase in bubble ring up time with a lower amplitude driving signal is observed in the 'equal energy' measurements. The decrease in target enhancement ratio is less significant in the 'equal energy' than the 'equal amplitude' configuration as the pulse duration increased from 70 μs to 240 μs (see Table 6.1). The amplitude of the driving pulse is lower for the 'equal energy' than 'equal amplitude' configuration for a pulse of the same duration as the total energy of the pulse is kept constant in the former. With lower amplitude, the driving pulse will have to be longer for the resonant bubble to reach steady state as the ring-up time of the bubble increases.

The picture is more complicated for a bubble cloud if the bubble population is not dominated by resonant bubbles. Clarke and Leighton [30] has shown that the simple correspondence between the pulse duration and scattered power may not hold true in the presence of a number of off-resonant bubbles, especially with the geometrical effects of the large bubbles and/or high amplitude. For non-resonant bubbles, a reduced dependence on sound pressure level and a rapid rise time with subsequent reduction and oscillation have been observed using bubble wall displacement plots. In addition, the time taken to reach steady state has been established to be the longest for a resonant bubble when excited by a low amplitude acoustic field [30].

From the ROC curves of the tank measurements (Figures 6.11 and 6.16) and that of the sonar simulations (Figures 6.13 and 6.18), the detection performance of the pulse is shown to improve as the pulse duration is reduced. Based on the understanding of the nonlinear and time-dependent characteristic of the bubble cloud, there may be several factors which will contributed to the better performance of the short pulses investigated here.

One factor will be the bubble distribution present. The tank population used has a bubble distribution typical of an oceanic environment. The number of resonant bubbles has a significant effect on the response of the cloud as a whole. This is probably because the bubble distribution approximately follows a power-law relationship and the number of the off-resonant and larger bubbles were present in much smaller numbers [111]. It is also noted that the frequency of the LFM pulse used decreased approximately from 110 to 40 kHz which translates to bubble resonant radii ranging from approximately 25 to 75 μm. For the bubble distribution used, the number of bubbles larger than 75 μm accounted for less than 5% of the total number of bubbles. The weighted response of the bubble population was thus dominated by the bubbles with radii less than 75 μm.

One aim of using a high frequency band (40 to 110 kHz) is to obtain a driving pulse as close to the frequencies emitted by a dolphin as practically possible with the available transducer. One disadvantage of such a pulse is its higher attenuation. The high attenuation is the result of a higher absorption [54, 55] and bubble cloud attenuation [50]. While the former scales roughly with frequency, the latter depends on the bubble size distribution. For a bubble cloud where the number of resonant bubbles dominates, the attenuation will be high. As the sonar simulation model incorporates only a linear attenuation model [50], it is noted that in the tank tests, the bubble cloud attenuation of the shorter pulses may be lower compared to the longer pulses because of the time-dependency effect [30]. Nonetheless, the decrease in amplitude as the driving pulse propagates through the bubble cloud means that the ring-up time of the cloud will tend to increase, owing to the relationship between the ring-up time and driving amplitude. The ring-up time of a bubble has been shown to decrease with increasing driving amplitude [30]. This is observed in the measurement results where the decrease in target enhancement ratio in the 'equal amplitude' configuration is larger compared to the 'equal energy' configuration.

In addition, the number of cycles varied from approximately 6 to 20 for pulse duration of 70 to 240 μs in this study. The presence of off-resonant and large bubbles, even in relatively small number, has been known to have a significant effect on the response of the cloud as a whole. This has been shown to be particularly significant during the first few cycles of the driving pulse [30]. For the scenario investigated, the number of cycles resided in the regimes beyond the first few cycles. As the pulse duration increased beyond 180 μs, it appears the improvement in detection performance became less significant as the ring-up times tend towards steady state (Figures 6.11 and 6.16).

6.6. Summary

This chapter began with a review on the current understanding of the echolocation ability of dolphins, specifically the Atlantic bottlenose dolphin. Particular attention was paid to the characteristics of pulses used and the strategies adopted by this animal in target discrimination tasks. The pulses, commonly called 'clicks', used are generally wideband, short duration and of high amplitude. During target echolocation, the dolphin emits a train of clicks and these clicks are observed to vary in both frequency (producing different click types) and amplitude.

The characteristics of dolphin-like pulses like amplitude, chirp structure and pulse duration were investigated for possible sonar performance in bubbly water. There is no simple correspondence between amplitude and backscattered response of a bubble cloud as explained by Leighton *et al.* [173]. Changing the amplitude of the pulse appeared to have only a marginal effect on target enhancement ratio in the scenario considered. The marginal improvement in target enhancement ratio was not sufficient to result in a better ROC curves for the detection of the solid target in a bubble-filled environment.

The performance of an up-chirp and down-chirp signals were compared. A down-chirp signal caused a higher overall bubble cloud response compared to an up-chirp signal, and consequently poorer detection performance.

By changing the duration of a signal, the attenuation and backscattered power of a bubble cloud was also affected. Using a ROC curve, short pulse duration, of the order comparable to that of a dolphin click, gave the best detection performance. The better detection performance could be attributed to the nonlinear time-dependent characteristic of bubbles and bubble clouds prior to steady state.

By studying the strategies adopted by dolphins during echolocation, several potential two-pulse techniques to enhance sonar performance in bubbly water have been proposed. One of these strategies, the change in amplitude of dolphin clicks within a pulse train, formed the basis of BiaPSS. This technique depends on the use of two pulses of the same waveform but of different amplitudes to distinguish between linear and nonlinear scatterers. This technique, together with the other two-pulse techniques discussed in the literature review, will now be investigated in the next chapter.

Chapter 7. Two-pulse techniques for sonar enhancement in bubbly water

7.1. Introduction

The review of the pulses and strategies adopted by dolphins during echolocation experiments has inspired several two-pulse techniques for sonar enhancement. The previous chapter has shown that using pulses with characteristics similar to those of the dolphin may have potential in enhancing sonar performance in bubbly water.

In this chapter, particular attention will be paid to the strategies used by a dolphin during echolocation. It has been shown that in echolocation tasks, the dolphin is observed to use a click train. The clicks within the train are observed to vary in both frequency and amplitude [113, 133, 137, 138]. These observations have given credence to the belief that the superior performance of the dolphin sonar compared to man-made sonar may be partly because of the adoption of one or both of these strategies [133]. These strategies are thus investigated for potential sonar solution to distinguish between the backscatter of a solid target (linear scatterer) and that of bubbles (nonlinear scatterers). While the dolphin uses many pulses within a click train, only a pair of pulse will be examined here as a form of simplification. The dolphin's strategy of varying the frequency and amplitude of its click is first examined using ‘dolphin’ or dolphin-like pulses in the sonar simulation model.

These strategies give rise to several two-pulse techniques, which will be studied here. Following this, a general processing framework for a two-pulse technique will be described. Section 7.3 will study one of the proposed two-pulse techniques, the Alternate Pulse (AP) technique theoretically using a pair of dolphin-like pulses. In the AP technique, two pulses of different frequencies make up the pulse pair. This will be followed by the variation of amplitude of a pair of dolphin-like pulses. The variation of amplitude in a pulse pair forms the basis of Biased Pulse Summation Sonar (BiaPSS) [175, 176].

It will be shown that both the AP technique and BiaPSS (using a pair of dolphin-like pulses) allow for the linear and nonlinear scatterers to be easily distinguished, demonstrating a form of classification ability absent in standard sonar technique. However, the detection performance of the AP method, unlike BiaPSS, is only comparable to standard sonar performance. Hence only BiaPSS was subsequently tested experimentally. The tank tests of BiaPSS will be described in Section 7.5.

Although probably unrelated to the dolphin schemes for detection, the proposed use of a pair of time-reversed (TR) pulses [46, 48, 49] in biomedical imaging will also be investigated for their potential enhancement of sonar performance. This chapter concludes by comparing the three techniques (TWIPS, BiaPSS, and TR pulse technique) in the ISVR water tank. In these tank tests, the three different types of pulses were placed consecutively at intervals of 15 ms within the same train so that the natural evolution of bubble cloud between the pulses (within each train) would be kept to a minimum.

7.2. Generalised pulse pair processing framework

Consider a pulse pair of the form:

$$p_i(t) = \Gamma_1(t) + \Gamma_2(t - \Delta_d) \tag{7.1}$$

where the delay, Δ_d, is sufficiently large that the received waveform does not overlap. The signal scattered from a linear target will be:

$$p_{Rx}(t) = h(t) * \Gamma_1(t) + h(t) * \Gamma_2(t - \Delta_d) \tag{7.2}$$

forming the sum and difference signals:

$$P_-(t) = \psi_1(t) * p_{Rx}(t) - \psi_2(t) * p_{Rx}(t + \Delta_d) \tag{7.3}$$

$$P_+(t) = \psi_1(t) * p_{Rx}(t) + \psi_2(t) * p_{Rx}(t + \Delta_d) \tag{7.4}$$

where $h(t)$ is the impulse response of the system, while $\psi_1(t)$ and $\psi_2(t)$ are filters.

In the interval $0 \le t \le \Delta_d$, then

$$P_-(t) = \psi_1(t) * h(t) * \Gamma_1(t) - \psi_2(t) * h(t) * \Gamma_2(t)$$

$$P_-(t) = h(t) * \left(\psi_1(t) * \Gamma_1(t) - \psi_2(t) * \Gamma_2(t)\right) \tag{7.5}$$

$$P_+(t) = h(t) * \left(\psi_1(t) * \Gamma_1(t) + \psi_2(t) * \Gamma_2(t)\right) \tag{7.6}$$

If one selects ψ_1, ψ_2, Γ_1, and Γ_2 such that

$$\psi_1(t) * \Gamma_1(t) - \psi_2(t) * \Gamma_2(t) = 0 \tag{7.7}$$

then the linear response is absent from $P_-(t)$.

Basic TWIPS framework will corresponds to the choice of:

$$\Gamma_1(t) = \Gamma_2(t) \tag{7.8}$$

$$\psi_1(t) = \psi_2(t) \tag{7.9}$$

Or, equivalently,

$$\Gamma_1(t) = -\Gamma_2(t) \tag{7.10}$$

$$\psi_1(t) = -\psi_2(t) \tag{7.11}$$

In this thesis, TWIPS has been used with a matched filter, in which case

$$\psi_1(t) = \Gamma_1(-t),\ \psi_2(t) = -\Gamma_2(-t) \text{ and } \Gamma_1(t) = -\Gamma_2(t) \tag{7.12}$$

then,

$$\psi_1(t) * \Gamma_1(t) + \psi_2(t) * \Gamma_2(t) = 0 \tag{7.13}$$

giving the converse case of the linear response being absent from $P_+(t)$ and not $P_-(t)$.

The technique, BiaPSS, corresponds to the choice of

$$\Gamma_1(t) = G\Gamma_2(t) \tag{7.14}$$

$$\psi_1(t) = \frac{1}{G}\psi_2(t) \tag{7.15}$$

Assuming the use of a matched filter means that one chooses $\psi_1(t) = \psi_2(t) = \Gamma_1(-t)$ and the magnitude of the first pulse is assumed to be a factor of *G* of the magnitude of the second pulse.

The AP technique is equivalent to choosing

$$\psi_1(t) = \Gamma_2(t) \tag{7.16}$$

$$\psi_2(t) = \Gamma_1(t) \tag{7.17}$$

The TR pulse technique will be equivalent to

$$\Gamma_2(t) = \Gamma_1(-t) \tag{7.18}$$

$$\psi_1(t) = \Gamma_1(-t) \tag{7.19}$$

$$\psi_2(t) = \Gamma_2(-t) = \Gamma_1(t) \tag{7.20}$$

It is trivial to show that all the choices satisfy Eq. (7.7) (with the exception of the TWIPS case where the roles of $P_-(t)$ and $P_+(t)$ are reversed) and so removes the linear scattering component. When a matched filter is included in the processing, in which case, one also requires that:

$$\psi_1(t) = \alpha_1\Gamma_1(-t) \tag{7.21}$$

$$\psi_2(t) = \alpha_2\Gamma_2(-t) \tag{7.22}$$

where α_1 and α_2 are variables such that the condition in Eq. (7.7) will be satisfied.

7.3. Alternate Pulse (AP) technique using dolphin-like pulses

The Alternate Pulse (AP) technique uses the linear combination of the delayed versions of the received signal from two different pulses as described in Section 7.2 (with the conditions described in Eq. (7.16) and (7.17)). For linear scatters, complete cancellation occurs with $P_{-}(t)$ while enhancement of the linear scatters from the scatterers occurs with $P_{+}(t)$.

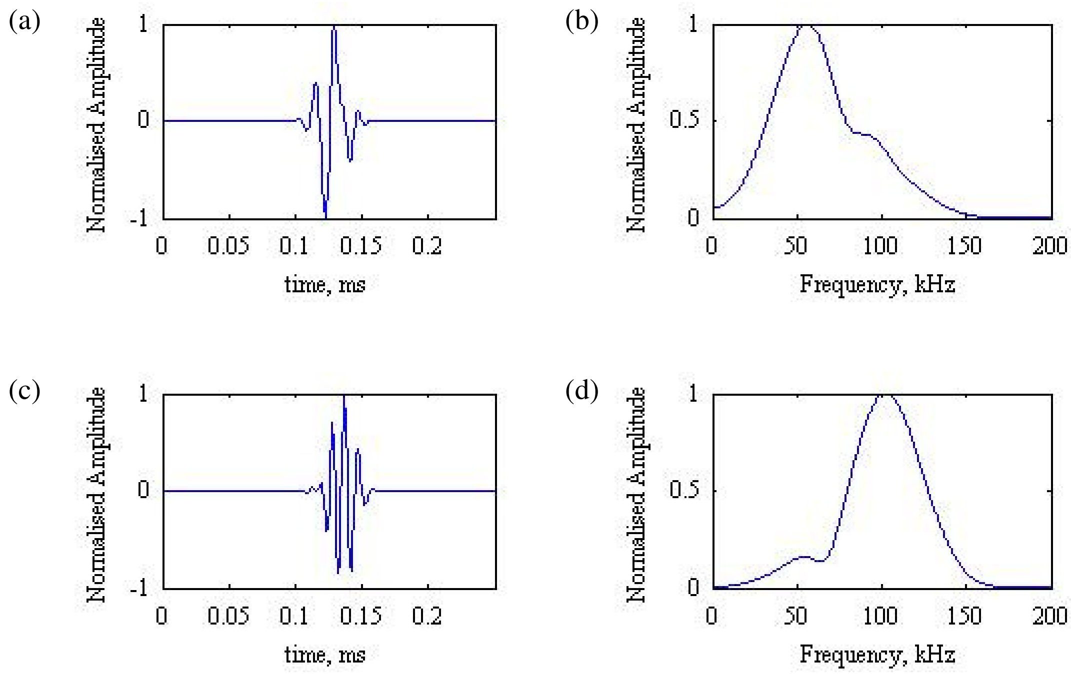

Figure 7.1. The low frequency pulse (Click type A) used in the simulation presented in (a) time-domain (b) frequency-domain with peak-to-peak SPL of approximately 217 dB re 1 µPa m and the high frequency pulse (Click type E) of peak-to-peak SPL of 223 dB re 1 µPa m presented in (c) time-domain and (d) frequency-domain.

The 'dolphin' pulse, or dolphin-like pulse, used here is based on the double chirp model proposed by Capus *et al.* [133], which can be taken to be an appropriate representation of a dolphin pulse for engineering purposes. Two different dolphin-like signals with approximately the same bandwidth are used. Each pulse used is 60 µs in duration and consists of two chirps with nominal frequency band of 30 to 84 kHz and 76 to 130 kHz. The higher frequency chirp is delayed by 10 µs relative to the lower frequency chirp. The SPL of the low frequency pulse (Click type A) used is about 6 dB lower than that of the higher frequency pulse (Click type E). The click types are based on the click taxonomy proposed by Houser *et al.* [137] (Figure 6.1). A lower SPL is used for the lower frequency pulse here as there are suggestions of physiological constraints that coarsely couple both source level and frequency content in animals like the bottlenose dolphin and false killer whale (*Pseudorca crassidens*) [150]. The time and frequency domain representations of the dolphin-like pulses used are shown in Figure 7.1.

7.3.1. Frequency of pulse

Before examining the performance of the alternate pulse (AP) method in target detection and classification performance, the effects of using two different frequency pulses are compared in Figure 7.2. Here, the linear target is represented by an instantaneous linear scatterer with TS of -40 dB. This value of -40 dB is within the typical range of target strength of some species of fish (for fish length of approximately 15 to 30 cm) [177]. The bubble-filled environment will be represented by a bubble population (with size distribution similar to that in the tank tests but with a void fraction in the order of 10^{-5} %) with an uniform spatial distribution.

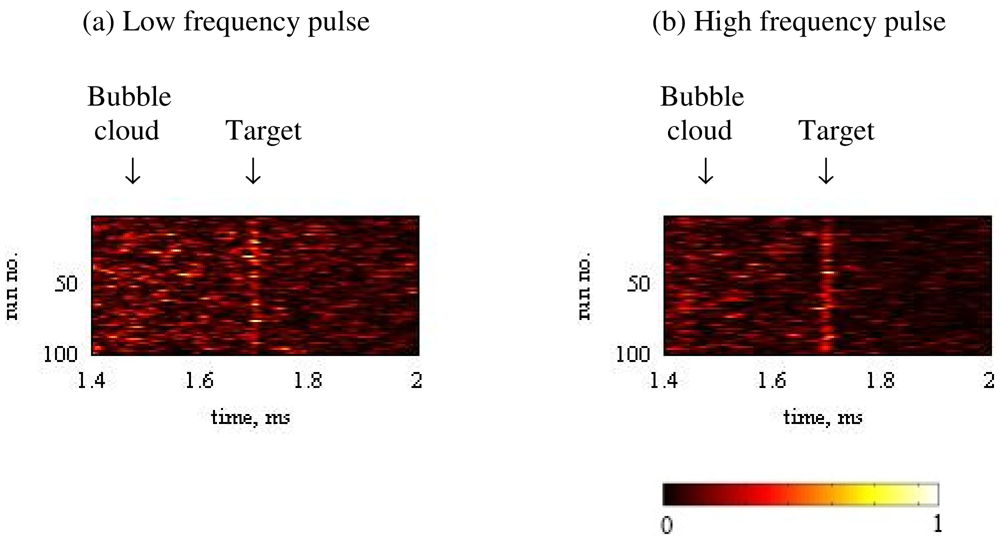

Figure 7.2. Backscatter of a target (TS= -40 dB) placed in a bubble-filled environment with the smoothed envelope of the matched filtered responses of (a) the low frequency pulse (Click type A) and (b) the high frequency pulse (Click type E) of 100 separate runs from simulations with (a) and (b) normalised to values of 5.9×10^8 and 2.3×10^9 respectively.

In Figure 7.2, the smoothed envelopes of the matched filtered responses from each pulse are shown. The plot in Figure 7.2(a) shows the presence of the target (around 1.7 ms for a distance of 1.25 m) is not easily seen in the bubble-filled environment. In contrast, the target is more easily observed in Figure 7.2(b) when a higher frequency click is used. A target enhancement ratio, which compares the total energy associated with the backscattered responses of the bubble cloud in the region, 1.2 ms to 1.6 ms, to that of the backscattered responses of the target in the region 1.6 ms to 1.8 ms, is computed for each case. The target enhancement ratio of a higher amplitude and higher frequency click is approximately 3 dB higher than the target enhancement ratio of a lower amplitude, and lower frequency click.

ROC curves are also computed from the results as shown in Figure 7.2. From the areas under the two ROC curves (as shown in Figure 7.3), the average detection performance of the lower frequency click (area under the ROC curve = 0.7) is determined to be poorer than that of the higher frequency click (area under the ROC curve = 0.86). A value of 1 for the area under the ROC curve represents a perfect detector. The poorer detection performance is mainly attributed to the higher backscattered reverberation of the bubble cloud associated with a lower frequency pulse, despite a lower amplitude.

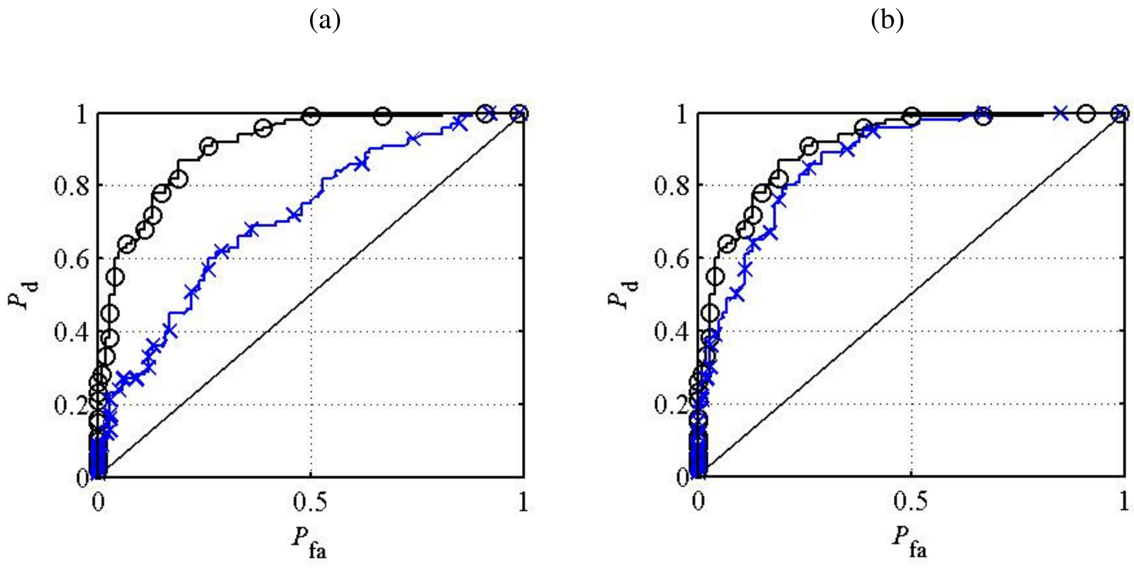

Figure 7.3. ROC curves of (a) low frequency click (Click type A) and (b) high frequency click (Click type E) both denoted by solid line with crosses computed from simulated data. The ROC curve of standard sonar processing using this pair of clicks is denoted by solid line with open circles.

As in the comparison of the other two-pulse techniques throughout this thesis, the average responses of the two pulses used is taken to represent standard sonar processing. In Figure 7.3, the ROC curves of both click types are compared to the ROC curve of standard sonar processing. The ROC curves show the detection performance of the standard sonar processing is comparable to that of the higher frequency click. The area under the ROC curve for standard sonar is 0.9 while the area under the ROC curve for the higher frequency click is 0.86. This is because the backscattered responses of the higher amplitude higher frequency click dominate and hence the detection performance of the standard sonar processing is closer to that of the higher frequency click as measured by the ROC curves.

7.3.2. Simulated results of the Alternate Pulse (AP) technique

Figure 7.4 shows that, by using a pair of dolphin-like signals of different click types, the linear and nonlinear scatterers can be distinguished from each another by a linear combination of the delayed versions of the received signal from the two different pulses as described for the AP technique in Section 7.2.

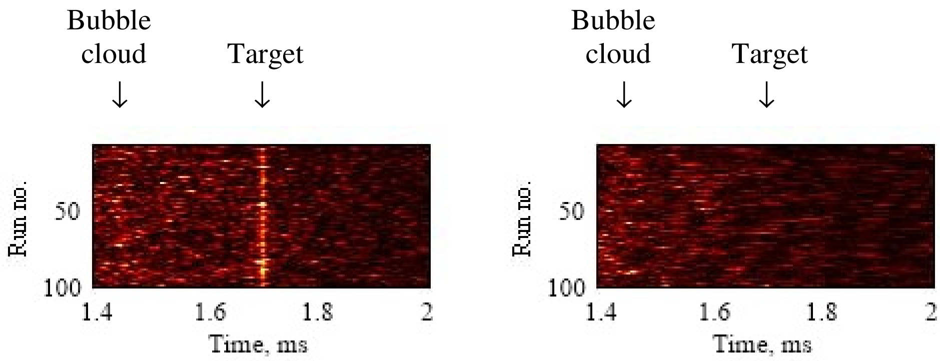
(a) AP P_+

(b) AP P_-

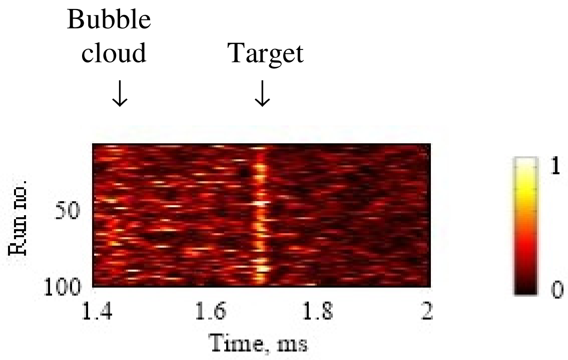
(c) standard sonar processing

Figure 7.4. Plots showing (a) P_+ and (b) P_- using the alternate pulse (AP) method and (c) standard sonar processing of 100 separate runs of the backscatter of a target (TS= -40 dB) placed in a bubble-filled environment from simulations with (a), (b) and (c) normalised to values of 2.2×10^{17}, 1.9×10^{17} and 6.6×10^{8} respectively.

In Figure 7.4(a), the function P_+ shows the presence of the bubbles and the linear target. These bubbles are mostly larger bubbles which are not excited to high amplitude for nonlinear pulsations to occur. In Figure 7.4(b), the corresponding result for P_- shows only the nonlinear backscattered reverberation from the bubble cloud as the backscattered contributions of the linear target are completely cancelled. Hence, by comparing results of P_+ and P_-, classification of linear and nonlinear backscattered contributions can occur. The standard sonar processing technique does not have this capability. The normalised values of P_+ and P_- in Figure 7.4 are noted to be several orders of magnitude higher than the standard sonar processing because in the AP technique processing, the filter used has a filter gain.

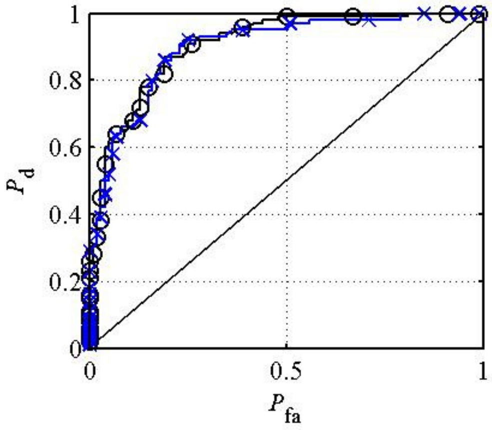

Figure 7.5. ROC curves of standard sonar processing compared with P_+ for the simulated data show in Figure 7.4 where the solid line with open circles represent the ROC curve of the former and the solid line with crosses represent the ROC curve of the latter.

Compared to standard sonar technique, the ROC curves in Figure 7.5 show that P_+ does not necessarily give a significantly better detection performance. Figures 7.4(a) and (c) also show that, while the detection performance does not improve with P_+ processing compared to standard sonar processing, there appears to be improvement in the range resolution with linear combinations of the AP pulse pair. This is surprising because AP processing does not involve the use of a matched filter. One advantage of using a matched filter in sonar systems is to increase the pulse length without compromising range resolution [98, 99]. The convolution of the responses with the 'other' pulses (as described in Eq. (7.16) and (7.17)) is expected to result in lower resolution than matched filtering. However, it is noted the two pulses used, while having different peak frequency spectrums, occupied roughly the same frequency band. The use of a short duration wideband dolphin-like pulse appears to suggest that the advantage of using matched filtering (for better range resolution with a longer pulse length) will be less significant [114]. In addition, the use of a pulse with a double down-chirp structure (with the higher frequency chirp delayed by 10 μs relative to the lower frequency chirp) is probably another contributing factor.

7.4. Biased Pulse Summation Sonar (BiaPSS) using dolphin-like pulses

It is common for a dolphin to emit multiple pulses during target interrogation. This may be for the orthodox purpose of monitoring changes in a target, assessing their relative motion between target and source, or for insonifying different aspects of a target. Here, the focus will be to investigate if the variation of amplitude in the multiple pulses can further be used in clutter reduction or target discrimination. This change in amplitude forms the basis of Biased Pulse Summation Sonar (BiaPSS). BiaPSS uses two pulses of the same form but of different amplitude. The BiaPSS processing has been described in Section 7.2 (with the conditions described by Eq. (7.14) and (7.15)), where the magnitude of the first pulse is assumed to be a factor of *G* greater than that of the second pulse. A re-cap of the BiaPSS processing scheme is described in Figure 7.6.

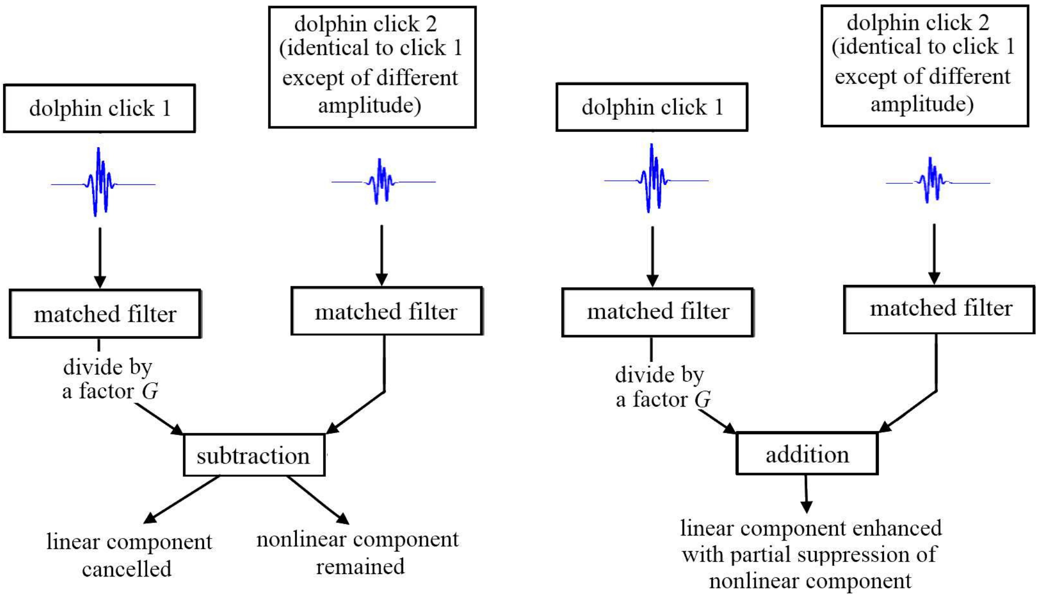

Figure 7.6. Processing scheme by which the echoes from a pair of dolphin-like pulses of differentamplitude are processed to enhance/cancel the nonlinear/linear components of the scattering through weighted subtraction and addition of the scattering. The magnitude of the first pulse is greater than that of the second pulse by a factor of *G*.

A factor of half has been used for the dolphin-like BiaPSS pulse pair here since a dolphin has been reported to vary the amplitude of its click by 10% to 70% during target echolocation [113, 132, 138, 169]. Similar to Section 7.3, the dolphin-like click used here is based on the model proposed by Capus *et al.* [133]. The pulse used is shown in Figure 7.7. The higher amplitude dolphin-like pulse has a peak-to-peak SPL of 226 dB re 1 μPa m.

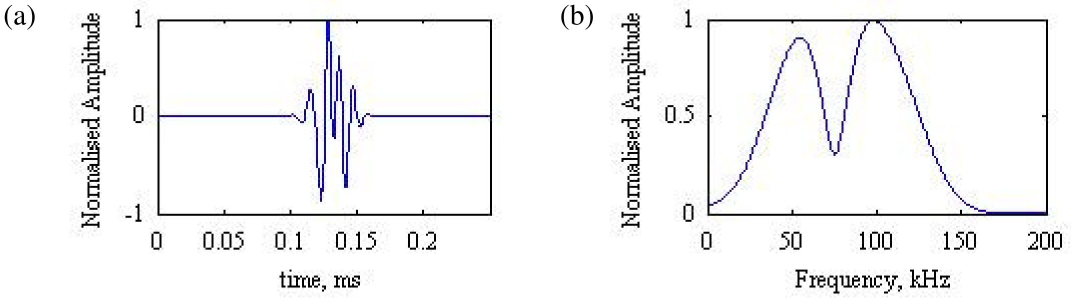

Figure 7.7. The dolphin-like signals used here is the double-chirp structure (peak-to-peak SPL of 226 dB re 1 μPa m) is presented in (a) time domain and (b) frequency domain.

As the amplitude of the driving pulse is decreased by a factor of two, the response of a nonlinear system like a bubble does not scale proportionately. For a linear scatterer, its response would scale with the amplitude of the driving pulse. The next section will discuss this in detail. This scaling in responses of the linear scatterer suggests that the linear combination of the responses of a pulse pair of different amplitude can be used to discriminate between a linear and a nonlinear scatterer. By appropriately scaling the responses of the scatterers from the second pulse, linear combination of these responses can result in the complete cancellation and enhancement of the returned signals from these linear scatterers. This approach can be regarded as a generalisation of the TWIPS principle [3, 6], with TWIPS corresponding to the choice of $G = -1$, albeit that in that instance the roles of P_+ and P_- are reversed (see Section 7.2).

7.4.1. Results from sonar simulation model

From the results of P_{1+} and P_{1-} shown in Figure 7.8, the linear backscattered contribution of a target and the nonlinear backscattered reverberation of the bubble cloud can be distinguished from each another. In Figure 7.8(a), the results of P_{1+} are shown to enhance the backscattered contribution of the linear target while partially suppressing the nonlinear backscattered reverberation of the bubble cloud. The backscattered reverberation of the bubble cloud observed is contributed by the larger bubbles which behave mainly as linear scatterers.

In Figure 7.8(b), the results of P_{1-} show there is complete cancellation of the backscattered responses from the linear target with the nonlinear backscattered reverberation from the bubble cloud remaining. By comparing the results of P_{1+} and P_{1-}, it is thus possible to distinguish a linear target placed in a bubble-filled environment from the bubble cloud.

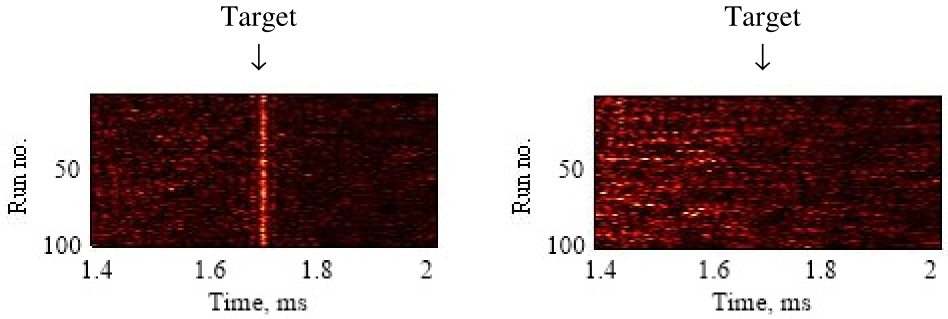

(a) P_{1+} (b) P_{1-}

(c) Standard sonar processing

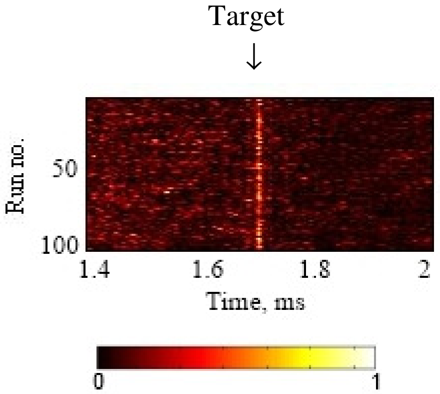

Figure 7.8. Plots of 100 separate runs of simulated data showing BiaPSS processing of (a) P_{1+} and (b) P_{1-} and (c) standard sonar processing of the backscatter of a target (TS= -40 dB) placed in a bubble-filled environment with (a), (b) and (c) normalised to values of 5.2×10^9, 2.0×10^9 and 9.0×10^8 respectively.

Figure 7.8(c) show the backscattered responses of the target and bubble cloud when processed using standard sonar processing. Figure 7.8(a) suggests BiaPSS enhances backscattered contribution of the target with P_{1+} more than standard sonar processing (Figure 7.8(c)) and partially suppresses the backscattered reverberation of the bubble cloud. This is corroborated by the ROC curves in Figure 7.9. The area under its ROC curve implies the average performance of P_{1+} is better than that of standard sonar. This area increases by approximately 3% for BiaPSS P_{1+} against the equivalent area for standard sonar processing. The probability of detection of P_{1+} before giving a single false alarm is 85% for P_{1+}. This is higher than the equivalent value for standard sonar technique, which is 63%. A higher probability of detection of P_{1+} (relative to standard sonar processing) suggests there is reduced backscattered reverberation from the bubble cloud when the returned signals are processed using BiaPSS P_{1+}, implying a degree of incoherent scattering in the bubble cloud.

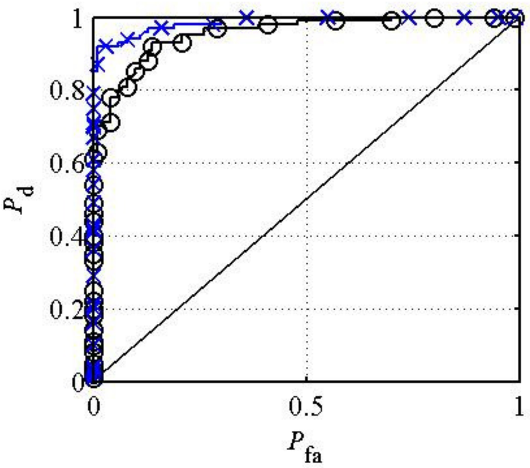

Figure 7.9. ROC curves of standard sonar processing compared with BiaPSS P_{1+} for simulated data shown in Figure 7.8 where the solid line with open circles markers represents the ROC curve of the former and the solid line with crosses represents the ROC curve of the latter.

The above example illustrates the ability of BiaPSS to distinguish between the solid target (a linear scatterer) and the bubble cloud (nonlinear scatterers). As with TWIPS [3, 6], such effectiveness at distinguishing between a linear target and nonlinear scatterers is seen as its primary advantage, an enhancement of the ability to detect the target in the first place (prior to classifying it) being a secondary, lesser advantage.

7.4.2. Theoretical response of a single bubble

To understand the reduced backscattered reverberation of the bubble cloud in P_{1+} processing, the theoretical responses for bubbles of different radii when subjected to a pair of pulses of different amplitude are examined. The frequency bandwidth of the dolphin-like pulses used corresponds to a bubble resonant radius of approximately 25 to 110 μm at the sea surface.

Figure 7.10 shows the normalised response of a bubble of different radius when excited by two pulses with identical waveforms but different amplitudes. In Figures 7.10(a) and (c), the resonant frequency of the bubble is outside of the frequency bandwidth of the pulse. The resonant frequency of the bubble is lower than the frequency bandwidth of the input pulse in Figure 7.10(a), whereas in Figure 7.10(c), the resonant frequency is above the frequency bandwidth of the pulse.

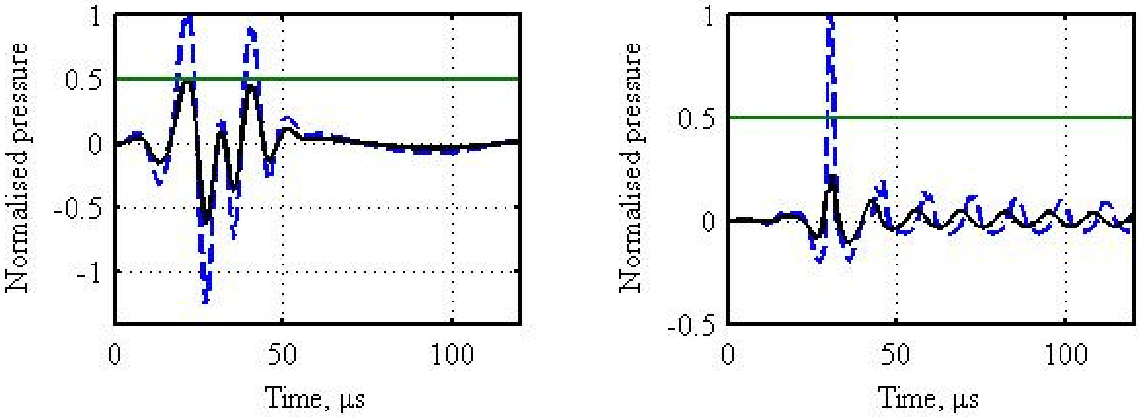

(a) 250 µm

(b) 40 µm

(c) 20 µm

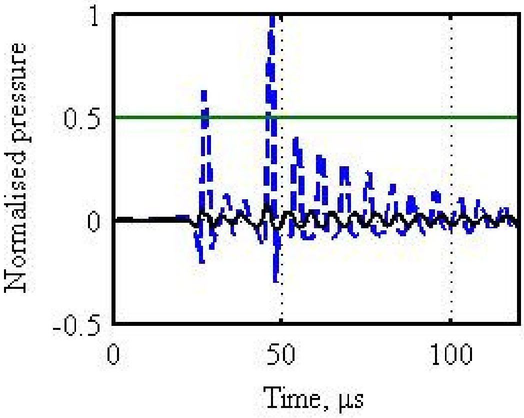

Figure 7.10. Bubble response to the first pulse (denoted by the dotted line) and the second pulse (denoted by the solid line) normalised by the maximum positive pressure of the bubble response due to the first pulse. The horizontal line shows the level representing 50% of the peak amplitude of the first pulse. The bubble radius in (a) is 250 µm, (b) 40 µm and (c) 20 µm.

In Figure 7.10(a), the bubble cannot respond rapidly enough to generate a nonlinear response and behaves like a linear scatterer. Bubbles which are sufficiently small that their resonant frequencies are higher than the frequency of the driving pulse (Figure 7.10(c)), can still respond rapidly to the compressive or expansive half cycles, and hence undergoes nonlinear pulsations, albeit to a lesser extent than those bubbles within the frequency of the driving pulse [95]. This means the responses of these bubbles will not scale with the amplitude of the input pulse. Likewise, when the resonant frequency of the bubble is within the frequency bandwidth of the pulse (as in Figure 7.10(b)), the amplitude of the response of the bubble does not scale with the amplitude of the input pulse.

When a bubble undergoes nonlinear oscillations as in Figures 7.10(b) and (c), there is a shift in the phase of the bubble oscillation when the amplitude of the input pulse varies. This is absent in a linear scatterer (as in Figure 7.10(a)) which has a constant phase relation as the amplitude of the input pulse varies. This shift in phase, as the amplitude of the input pulse varies, accounts for the reduced backscattered reverberation of the bubble cloud in P_{1+} processing.

7.5. Biased Pulse Summation Sonar (BiaPSS): tank tests and simulations

7.5.1. Experiment set-up

The efficacy of BiaPSS is subsequently tested with a pair of pulses which can be produced using the available transducers. The two pulses used in the tank tests are shown in Figure 7.11. Like the pulses used in Section 6.3.1, the transmitted BiaPSS pulse pair used was a chirp which varied within a frequency band of 30 to 110 kHz over duration of 300 μs. The first pulse has a zero-to-peak SPL of approximately 212 dB re 1 μPa m. The second pulse has amplitude which was approximately 15% of the amplitude of the first pulse. A solid sphere of TS = -30 dB was placed at a distance of 0.85 m from the source such that it was close to the centre of the bubble cloud.

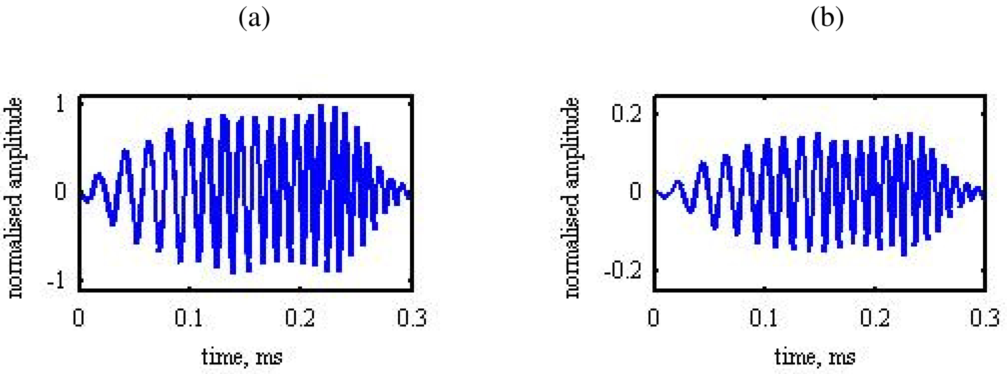

Figure 7.11. The pulse pair used in the sonar simulation model and tank tests measured at 1 m from the source. The amplitude of the second pulse was approximately 15% of the first pulse. The first pulse has a zero-to-peak SPL of approximately 212 dB re 1 μPa m.

7.5.2. Results

Figure 7.12 shows how a linear and nonlinear scatterer can be distinguish from each another using a pair of pulses of different amplitude when a linear target is placed within a bubble-filled environment. The linear backscatters of the solid sphere are observed between 1.1 and 1.2 ms while the backscattered reverberation of the bubble cloud can be observed throughout the plots, depending on the natural evolution of the cloud.

The results of the BiaPSS function, P_{1+} are shown in Figure 7.12(ii), presented on a linear colour scale. They are obtained by adding the returned signals of a pulse pair (of which the second pulse has amplitude that was approximately 15% of the first), processed using the BiaPSS processing scheme described in Figure 7.6. The linear backscattered contributions of the solid target are enhanced with P_{1+}. By subtracting the responses from the first pulse with appropriately-scaled responses from the second pulse, the backscattered contribution of the linear scatterers can be cancelled (Figure 7.12(a)(iii)). By comparing the results of the sum and difference of the responses (P_{1+} and P_{1-}) of the returned signals of the BiaPSS pulse pair, linear and nonlinear scatterers can thus be distinguished from each another. This cannot be achieved using standard sonar processing.

From the ROC curves (computed from the results shown in Figure 7.12), the detection performances of P_{1+} and standard sonar processing can be compared. Figure 7.13 shows the function, P_{1+}, gives a probability of detection of 32% before giving a single false alarm, compared to an equivalent value of 5% for standard sonar processing. The average performance of BiaPSS P_{1+} is also better than that of standard sonar processing as represented by a larger area under the ROC curve of BiaPSS. The area under the ROC curve of BiaPSS is approximately 16% larger than equivalent area for standard sonar processing.

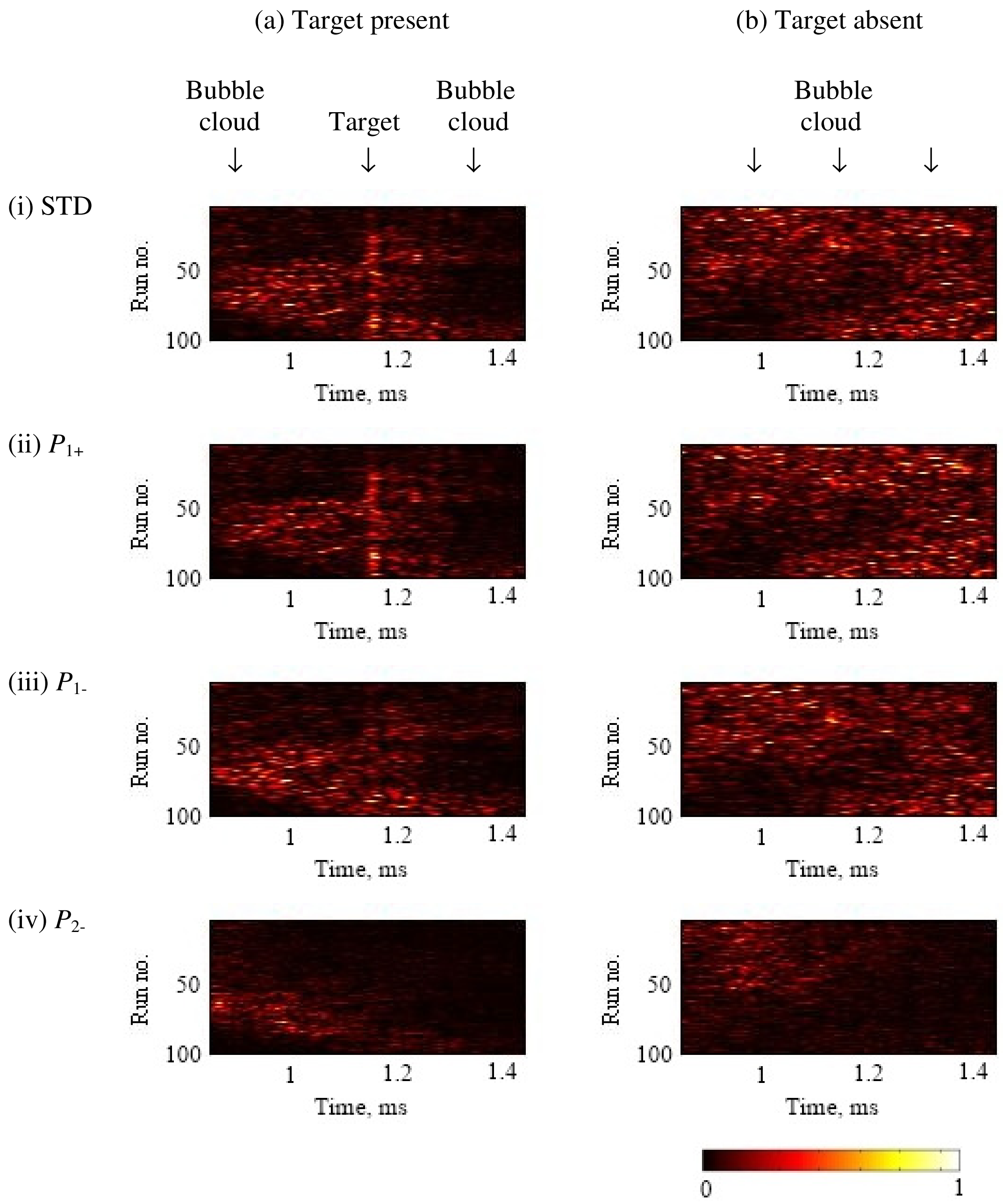

Figure 7.12. Plots of 100 runs of measurement data to compare the processing operators: (i) standard sonar, (ii) BiaPSS P_{1+}, (iii) BiaPSS P_{1-} , (iv) BiaPSS P_{2-} for tank tests with a solid sphere (TS= -30 dB) placed in a bubble-filled environment. In (a), the target is located between 1.1 and 1.2 ms and in (b), the target is absent. Each colour scale is normalised to a maximum value, which for (a) is (i) 65, (ii) 4.2×10^2, (iii) 2.3×10^2, and (iv) 1.6×10^2 and (b) is (i) 38, (ii) 1.7×10^2, (iii) 1.7×10^2, and (iv) 1.2×10^2.

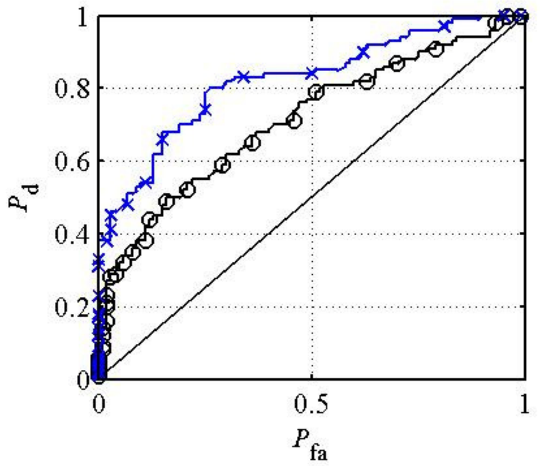

Figure 7.13. ROC curves of standard sonar processing technique compared with BiaPSS P_{1+} for the measurement data shown in Figure 7.12 where the solid line with open circles is the ROC curve of the former and the solid line with crosses represents the ROC curve of the latter.

The results of sonar simulation models show the same trends as the results of the tank tests. Figure 7.14(a) shows the results for the case when a target is present, while Figure 7.14(b) shows the results for the case when the target is absent. The function, P_{1+} (Figure 7.14(ii)) enhances the presence of the target while the functions, P_{1-} and P_{2-} (Figures 7.14(iii) and (iv)) highlight the presence of the bubble cloud with cancellation of the linear backscattered contribution of the linear scatterers. The linear and nonlinear backscattered contributions can thus be classified using the results of P_+ and P_-.

From the results shown in Figure 7.14, the ROC curves are computed and presented in Figure 7.15. The ROC curve of the standard sonar processing is compared with that of BiaPSS processing. The BiaPSS function, P_{1+}, gives a probability of detection before giving a single false alarm of 38%, compared to an equivalent value of 7% for standard sonar. The average performance of BiaPSS P_{1+} is also better than that of standard sonar as represented by a bigger area under the ROC curve of BiaPSS P_{1+}.

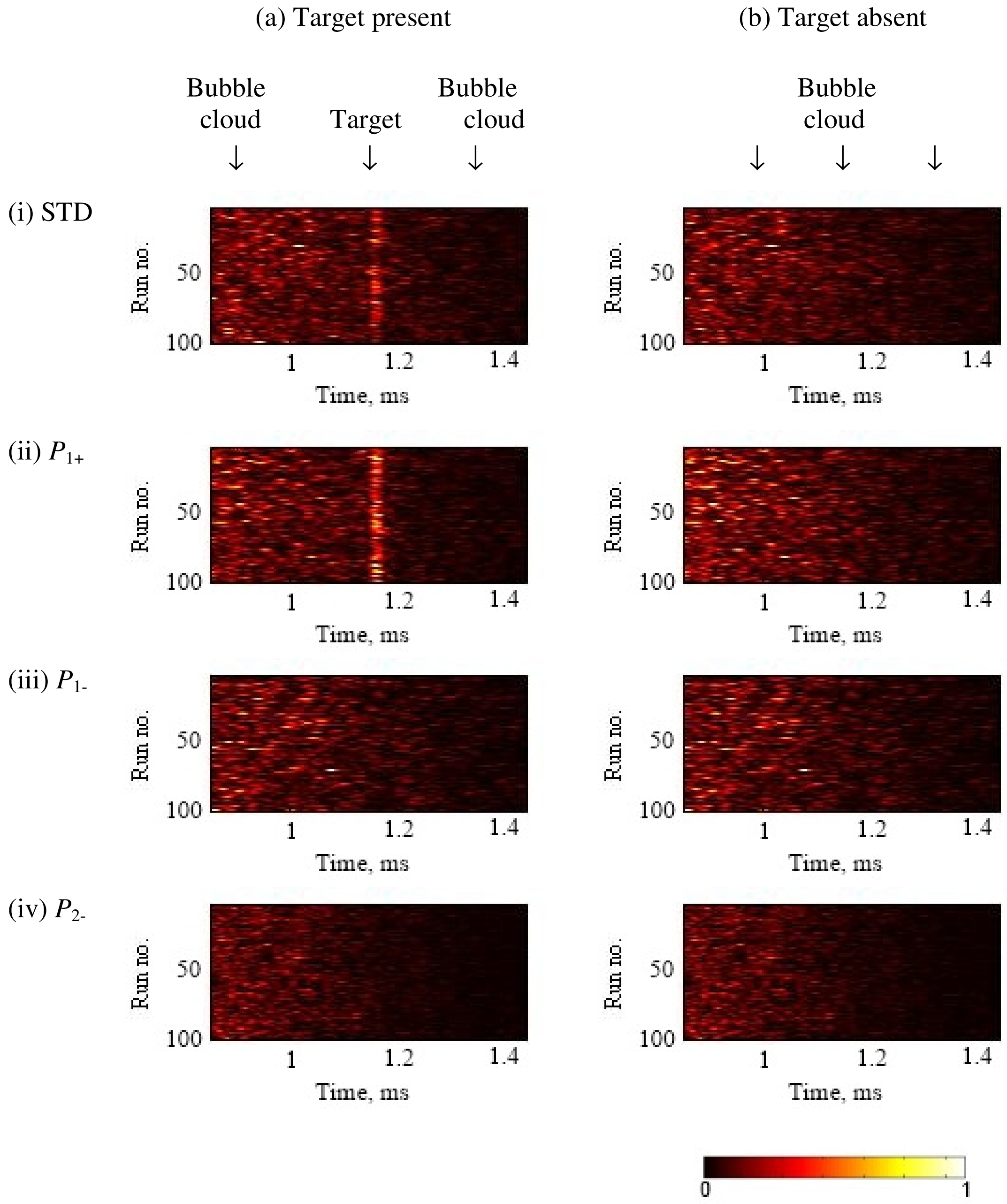

Figure 7.14. Plots of 100 runs of simulated data to compare the processing operators: (i) standard sonar, (ii) BiaPSS P_{1+}, (iii) BiaPSS P_{1-} , (iv) BiaPSS P_{2-} for simulations with a target (TS= -30 dB) placed in a bubble-filled environment. In (a), the target is located between 1.1 and 1.2 ms and in (b), the target is absent. Each colour scale has been normalized to a maximum value in each plot, which for (a) is (i) 4.8×10^{10}, (ii) 2.3×10^{11}, (iii) 2.0×10^{11}, and (iv) 4.6×10^{10} and (b) is (i) 4.8×10^{10}, (ii) 1.9×10^{11}, (iii) 2.0×10^{11}, and (iv) 4.6×10^{10}.

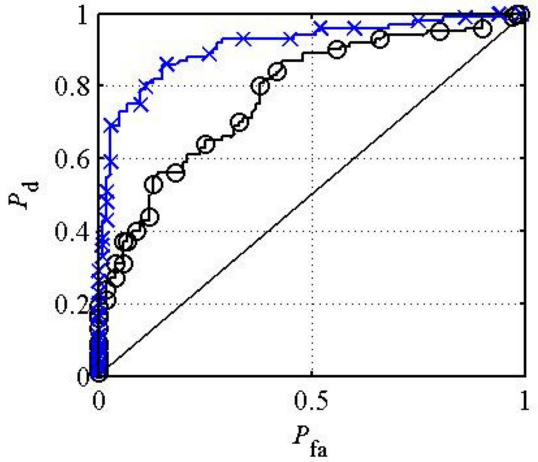

Figure 7.15. ROC curves of standard sonar processing compared with BiaPSS P_{1+} computed from the simulated data shown in Figure 7.14 where the solid line with open circles is the ROC curve of the former and the solid line with crosses represents the ROC curve of the latter.

7.5.3. Discussion

Both tank tests and simulations (Figures 7.12 and 7.14) show the backscattered contributions of linear and nonlinear scatterers can be effectively distinguished using BiaPSS by comparing the plots of P_{1+} and P_{1-} visually. The BiaPSS functions of P_{1-} and P_{2-} can be taken to be the resulting difference between the returned signals from the pair of BiaPSS pulses when a filter matched to the fundamental and second harmonic of the driving pulse respectively is applied. It represents the energy which has leaked out into the higher harmonics when the amplitude of the driving pulse changes. This energy leakage will only occur for a nonlinear scatterer like a bubble.

On the other hand, the BiaPSS P_{1+} represents the total amount of energy associated with the backscattered contributions of the target and the bubble cloud. Figures 7.13 and 7.15 show the ROC curves computed from the plots in Figures 7.12 and 7.14 respectively. Both the ROC curves (from measurements and simulations) show that the sum of the responses, the function P_{1+}, in BiaPSS processing gives a higher probability of detection before giving a single false alarm when compared to the standard sonar processing. The enhancement in linear target scattering suggests that the scattering from the bubbles tend to be incoherent. This is a result of the nonlinear response of the individual bubbles which will not scale linearly with amplitude and the phase shift when the amplitude of input pulse varies. Hence, the linear sum of the signal responses results in a decreased level of scatters from the bubble, and an increased level of backscatter from the linear target. This translates to a higher detection rate in the ROC curve.

The BiaPSS results thus raise the possibility similar BiaPSS-like processing technique may also be implemented by dolphins. The pulses used here are high frequency (in the order of tens of kilohertz) and high amplitude. These two ingredients are commonly found in the pulses emitted by odontocetes like the Atlantic bottlenose dolphin. The use of the results for P_{1-} (with P_{1+}) for the purpose of distinguishing between a solid target and bubble cloud also removes the requirement to hear the second harmonic of the echolocation emission. In addition, these dolphins have been reported to give out trains of pulses (which vary in both amplitude and frequency) during echolocation experiments in both controlled environments (such as dolphin pens) and open seas [133, 137, 138, 168]. These reported behaviours further raise the possibility that similar BiaPSS-like processing techniques may have contributed to the performance of their biosonar.

For BiaPSS to work efficiently in a dolphin, the receiver of a dolphin would ideally have an upper frequency limit of twice the centre frequency of the pulse used. The audiogram of the Atlantic bottlenose dolphin is reported to have an upper frequency limit of 150 kHz and a large number of the dolphin's echolocation clicks reported have peak frequency between 100 and 130 kHz [113, 146]. Such values suggest that a dolphin cannot access the majority of the information in the signals necessary to exploit such strategies. It is noted that dolphins adapt their echolocation pulses to suit their environment [113, 138, 155, 157]. To exploit nonlinear processing, such as BiaPSS, dolphins would be expected to use pulses with lower peak frequencies, below 75 kHz, a value which is well within the range observed in absence of bubble production [113, 138]. If future tests were to show dolphins do not adjust their clicks to transmit significant energy below half of their upper frequency hearing limit when echolocating in bubbly water, the possibility that they are using nonlinearities in the way similar to BiaPSS would be remote.

For practical implementation of a BiaPSS system, it will be interesting to discuss the effective range of such a system since BiaPSS, like TWIPS, will require the bubble cloud to be driven to high amplitude of pulsations so that nonlinear responses result. This suggests a sonar source of sufficient power is required. Given a source of SPL of 230 dB re 1 μPa m, and assuming a linear cloud attenuation of 1 dB/m, the effective range of such a system will be approximately up to 10 m. To improve the range, bistatic arrangements can be used that placed the source close to the potentially nonlinear scatterers while the observer remain distant [178].

While unrelated to the dolphin, the proposed use of a pair of time-reversed pulses in biomedical imaging of tissues using UCAs is investigated here for possible enhancement of sonar performance. This technique will then be compared with TWIPS and BiaPSS processing using the LFM waveform in the same set-up.

7.6. Time-reversed (TR) pulse technique

7.6.1. Single bubble model

In the absence of both target and bubble cloud, the transmitted time-reversed (TR) pulse pair used in the experiment was measured at 1 m. The first pulse shown in Figure 7.16(a) is identical to the pulse used in BiaPSS. The time-reversed replica of the first pulse is shown in Figure 7.16(b). The time-reversed replica of the first pulse was then transposed and overlapped on the first pulse. The result is presented in Figure 7.16(c) and they are found to differ slightly from each other. The difference between the two pulses is probably because of the finite reaction time of the transducer during transmission. To compensate for this difference, a factor of 1.02 has been added to the response of the first pulse to ensure that the two matched filtered responses cancel out perfectly when the scatterer is a linear one.

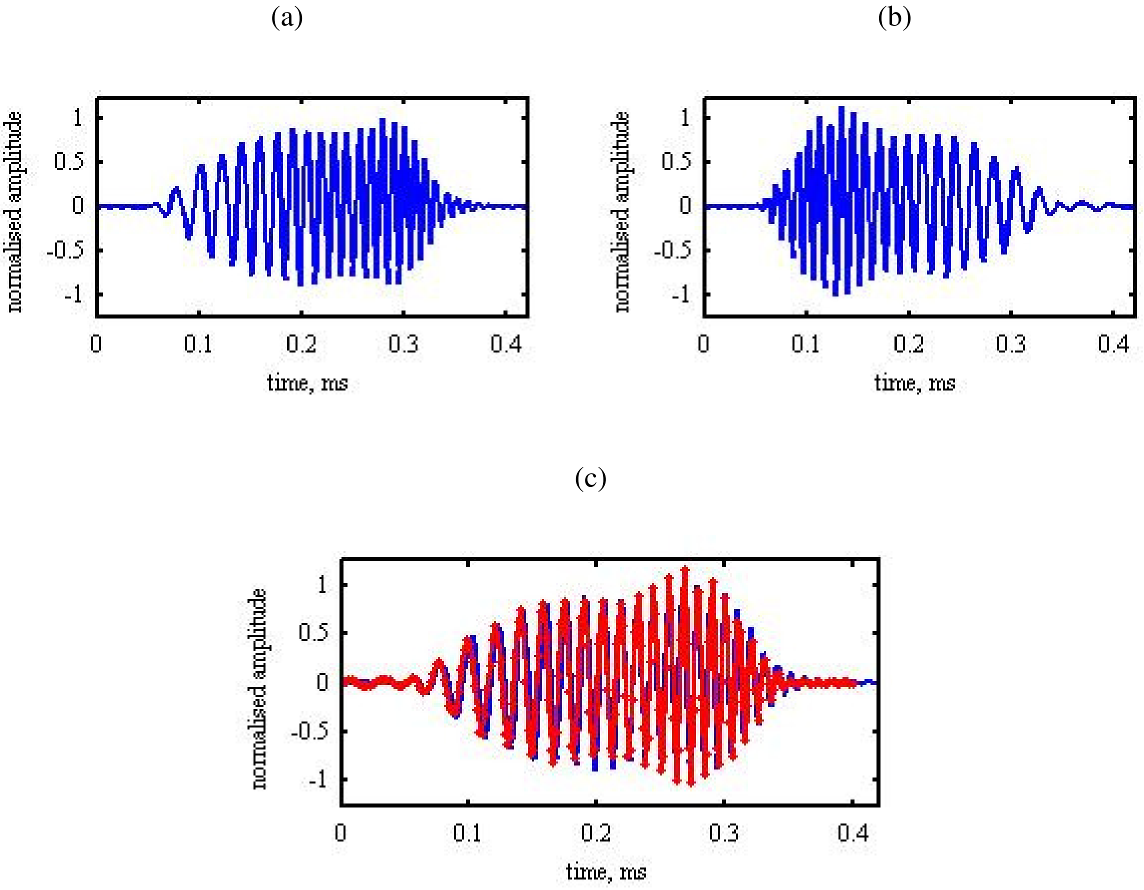

Figure 7.16. The pulse pair used in the sonar simulation model and tank tests measured at 1 m from the source is shown in (a) with the second pulse is the time-reversed replica of the first pulse shown in (b). The time-reversed replica of the second pulse is overlapped with the first pulse in (c). All the amplitude of the pulses shown have been normalised by the amplitude of the first pulse. The first pulse has a zero-to-peak SPL of approximately 212 dB re 1 μPa m.

Using the pulse pair in Figure 7.16, it is shown, for a linear scatterer which is represented here by a large bubble (whose resonant frequency is much lower than the frequency of the pulse), perfect cancellation of the matched filtered responses of the two pulses can occur as in Figure 7.17(a). The matched filtered response of the returned signal from the first pulse and its time-reversed replica overlap perfectly (Figure 7.17(a)). For bubbles whose resonant frequencies are within or higher than the frequency of the pulse (Figures 7.17(b) and (c)), the bubbles can still undergo nonlinear pulsations, and the subtraction of the matched filtered responses of the bubble response of the time-reversed pulse pair, P_{1-}, will not cancel completely. Through the linear combination of the matched filtered responses of the returned signal of the TR pulse pair, this can be exploited for classification of linear and nonlinear scatterers. The TR processing scheme has been described in Section 7.2 (with the conditions described by Eq. (7.18) to (7.20)).

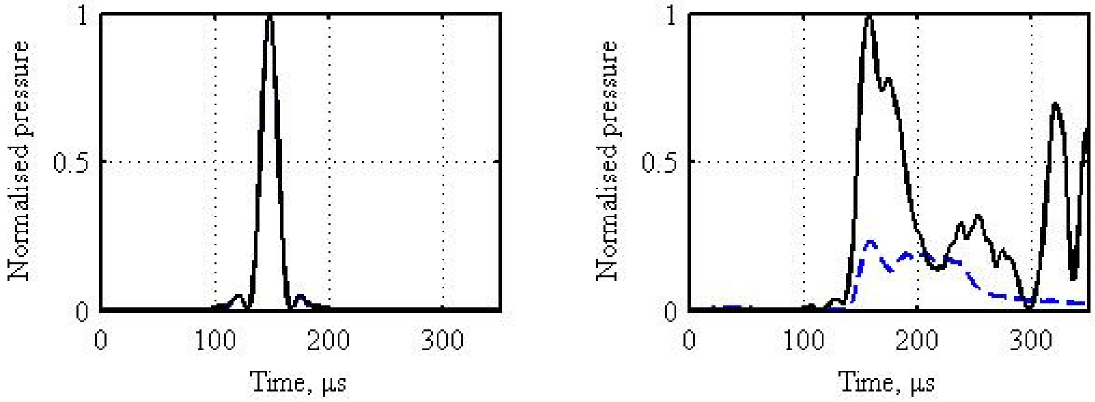
(a) 250 µm

(b) 50 µm

(c) 15 µm

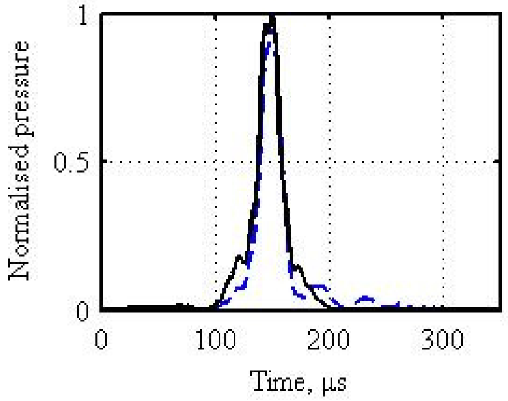

Figure 7.17. Matched filtered bubble response to the first pulse (dotted line) and the second pulse (solid line) normalised by the maximum positive pressure of the matched filtered bubble response due to the second pulse. The bubble radius in (a) is 250 µm, (b) 50 µm and (c) 15 µm.

7.6.2. Results

The pair of time-reversed signal was investigated at ISVR water tank with a solid sphere of TS = -30 dB placed at a distance 0.85 m away from the source in the bubbly water. The position of the target was placed such that the target would be close to or within the cloud, depending on the natural evolution of the cloud.

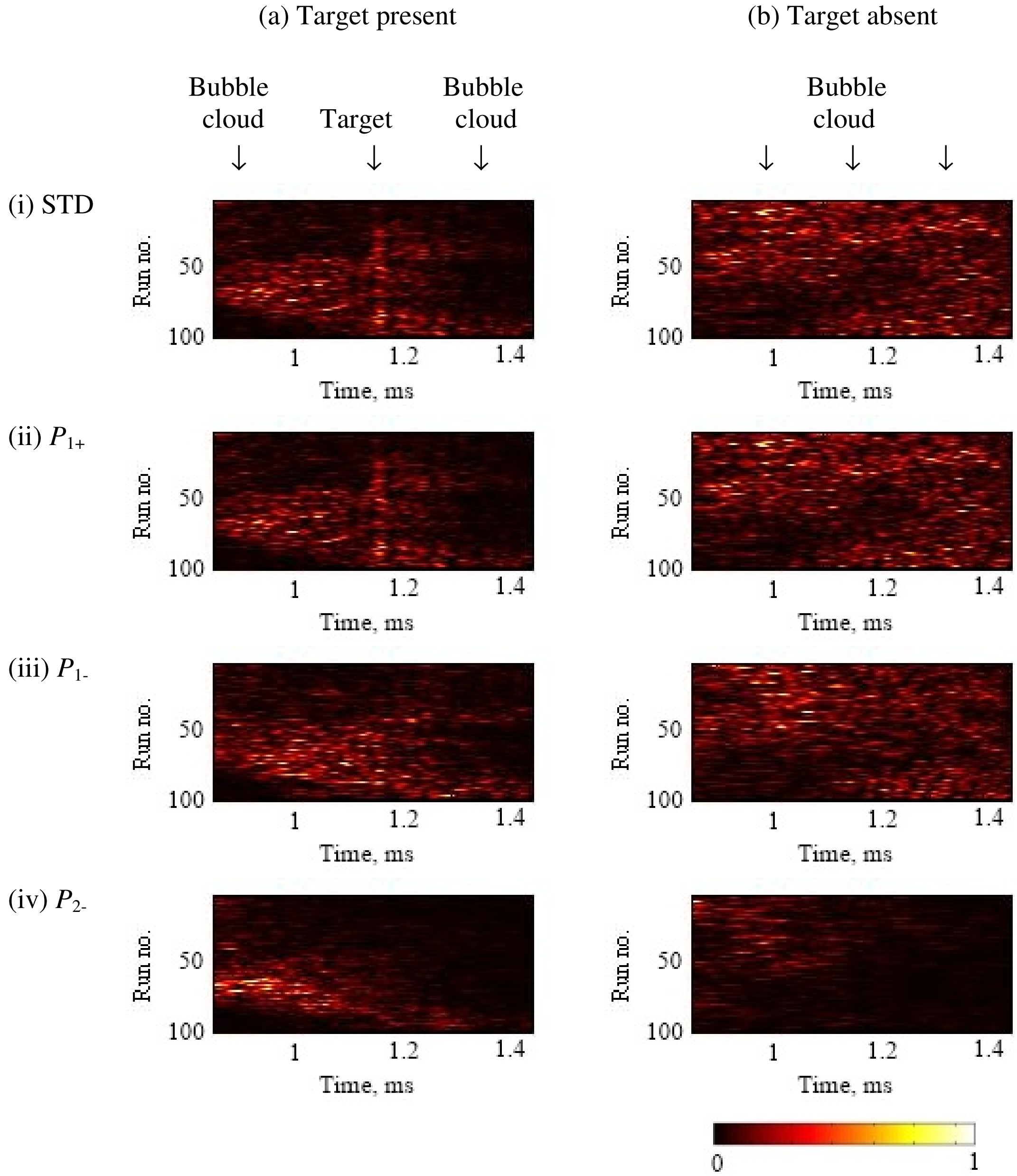

Figure 7.18. Plots of 100 runs to compare the variable processing operators: (i) standard sonar, (ii) TR P_{1+}, (iii) TR P_{1-} , (iv) TR P_{2-} for tank tests with a solid sphere (TS= -30 dB) placed in a bubble-filled environment. In (a), the target is located between 1.1 and 1.2 ms and in (b), the target is absent. Each colour scale is normalised to a maximum value, which for (a) is (i) 1.5×10^2, (ii) 5.9×10^2, (iii) 50, and (iv) 1.8×10^2 and for (b) is (i) 84, (ii) 3.2×10^2, (iii) 38, and (iv) 2.4×10^2.

With a TR signal pair, classification of linear and nonlinear scatterers is achieved from comparison of the results of P_{1+} and P_{1-}. Figure 7.18(ii) shows the measurement results of P_{1+} where the backscattered contributions of both bubble cloud and target can be observed. In the measurement results of P_{1-} (Figure 7.18(iii)), the linear backscattered contribution from the target has been completely eliminated, leaving only the nonlinear backscattered reverberation of the bubble cloud. Using the functions, P_{1+} and P_{1-}, the solid spherical target can thus be distinguished from the bubble cloud, allowing for effective classification of the linear and nonlinear scatterers.

Figure 7.18(iv) shows the results of P_{2-} can also be exploited to enhance the presence of the nonlinear scatterers (in this case, the reverberation of the bubble cloud) as the linear backscattered contributions of the solid target are suppressed. Similar observations can be found in the plots generated using the results of the sonar simulation model in Figure 7.20.

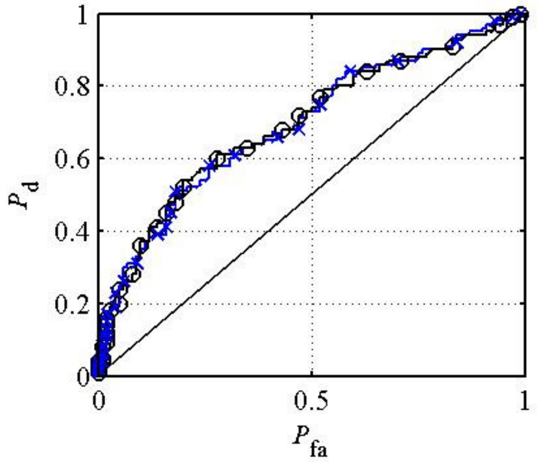

Figure 7.19. ROC curves of standard sonar processing compared with TR P_{1+} for measurement data shown in Figure 7.18 where the solid line with open circles is the ROC curve of the former and the solid line with crosses represents the ROC curve of the latter.

The results of P_{1+} in Figure 7.18(ii) show its performance in enhancing the linear backscatters from the solid target to be comparable to that of standard sonar processing (Figure 7.18(i)). This observation is consistent with that of the ROC curves shown in Figure 7.19. The ROC curves have similar areas under the curves, implying their average performance is comparable. Both P_{1+} and standard sonar processing have very poor probability of detection (before giving a single false alarm) with only values of 4%.

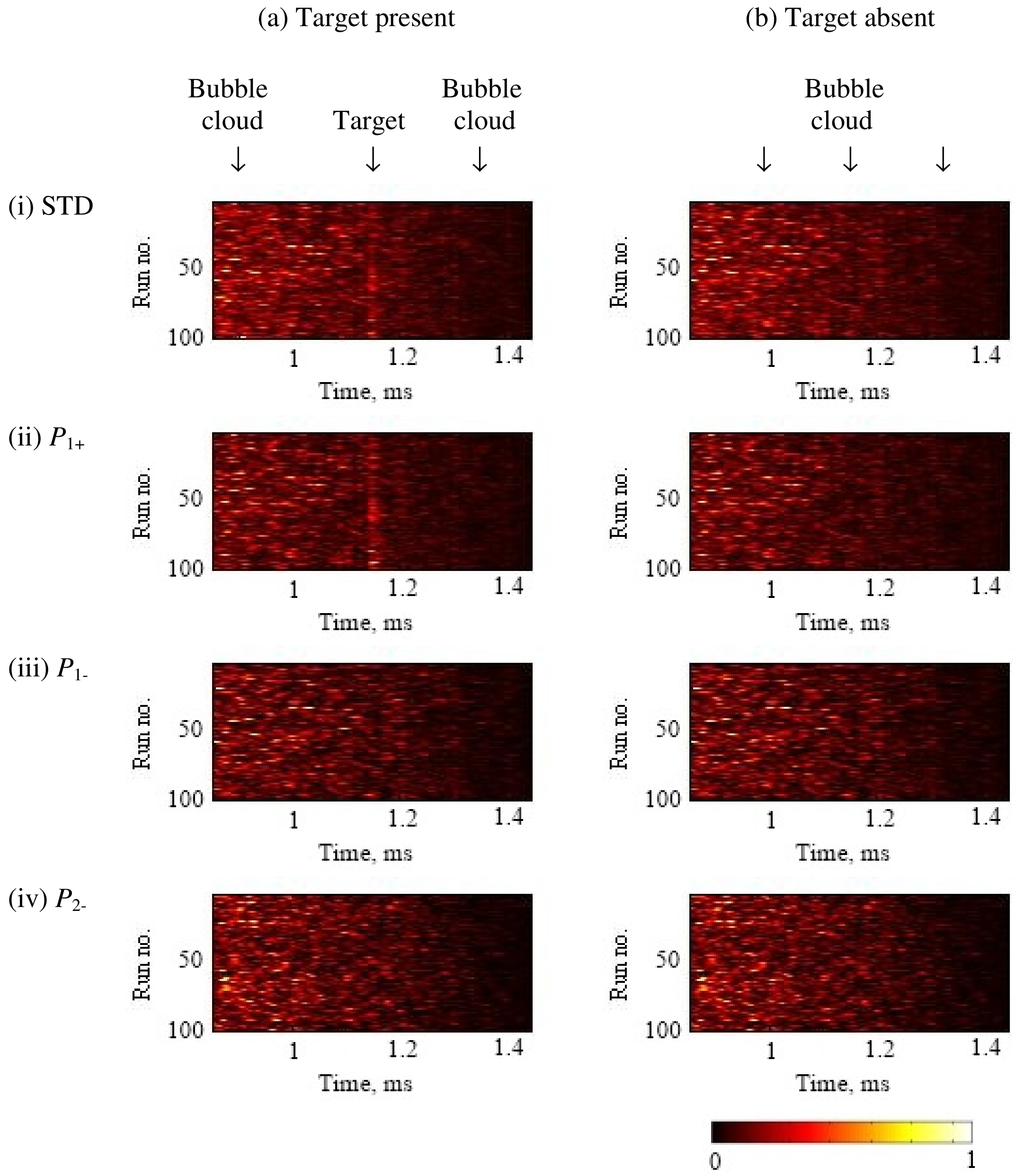

Figure 7.20. Plots of 100 runs to compare the variable processing operators: (i) standard sonar, (ii) TR P_{1+}, (iii) TR P_{1-}, (iv) TR P_{2-} for simulations with a solid sphere (TS= -30 dB) placed in a bubble-filled environment. In (a), the target is located between 1.1 and 1.2 ms and in (b), the target is absent. Each colour scale is normalised to a maximum value, which for (a) is (i) 2.1×10^{11}, (ii) 6.2×10^{11}, (iii) 4.1×10^{11}, and (iv) 2.0×10^{11} and (b) is (i) 2.1×10^{11}, (ii) 6.2×10^{11}, (iii) 4.1×10^{11}, and (iv) 2.0×10^{11}.

Compared to the measurements, the ROC curves computed from the sonar simulation model results show a similar trend of poor detection performance (Figures 7.20(i) and (ii)). Based on the area under the ROC curve, the average performance of TR P_{1+} is shown to be only marginally better than that of standard sonar processing. The marginal improvement in the average detection performance is evident by the area under the ROC curve of TR P_{1+} compared to that of standard sonar. The area under the ROC curve is 0.65 for TR P_{1+} and 0.58 for standard sonar processing. This implies the average detection performance of TR P_{1+} is marginally better than that of standard sonar.

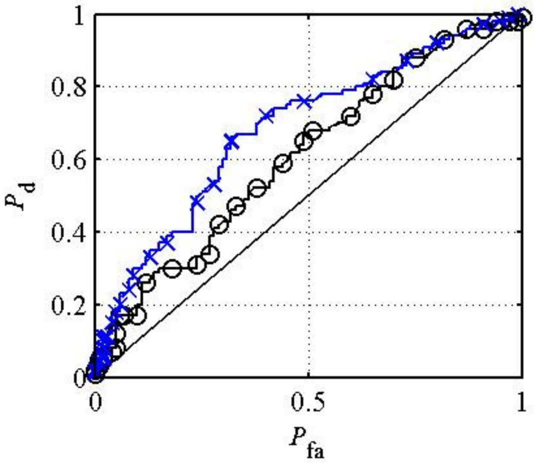

Figure 7.21. ROC curves of standard sonar processing compared with TR P_+ for simulated data shown in Figure 7.20 where the solid line with open circles is the ROC curve of the former and the solid line with crosses represents the ROC curve of the latter.

Both P_{1+} and standard sonar processing have very poor probability of detection (before giving a single false alarm) as measured by the ROC curves computed from the simulated data. Both have probability of detection (before giving a single false alarm) of 3%. For this particular case, while the simulation shows a marginally better average performance for TR P_{1+} compared to standard sonar processing as measured by the ROC curves (Figure 7.21), the ROC curves of the tank tests shows only comparable performance between TR P_{1+} and standard sonar processing (Figure 7.19). As in Section 5.2.3, these discrepancies between the absolute performances, as measured by the ROC curves, of the model relative to the experiment can be attributed to the spatial and temporal heterogeneity exhibited by the bubble cloud formed in the experiment which cannot be replicate precisely in the model used. Together with the simplification of a linear bubble cloud attenuation, exact agreement between the ROC curves of the simulations and measurements are thus not expected. The ROC curves from the experiment and simulation (Figures 7.19 and 7.21 respectively) show the average performance of TR P_{1+} is either comparable or marginally better than that of standard sonar. The probabilities of detection (before giving a single false alarm) for both sets of ROC curves are also very low, with values of 4% and 3% obtained from the experiments and simulations respectively.

7.6.3. Discussion

Both tank tests and the sonar simulation model have shown that the scattering of a linear scatterer (solid target) can be distinguished from the scattering of nonlinear scatterers (bubble cloud) with the use of a pair of time-reversed chirp signals. Here, this is referred to as the time-reversed (TR) pulse technique. The results of TR P_{1-} show the cancellations of the linear backscattered contribution of the target, with only nonlinear backscattered reverberation of the bubble cloud remaining. The results of TR P_{1+}, on the other hand, highlight the presence of the target in the bubble-filled environment.

The results of P_{1-} represent the resultant difference of the returned signals at the driving frequency. Hence P_{1-} can be considered to represent the energy which has leaked out of the first pulse into the higher harmonics. The function, P_{1+}, however, computes the sum of the returned signal of the pulse pair at the driving frequency. This represents the total amount of energy which remains at the fundamental frequency. This total amount of energy includes the linear backscattered contribution of both solid target and bubble cloud.

There is no significant improvement in the detection performance when results of P_{1+} are compared to the results of standard sonar processing. This is consistent with the results of the ROC curves (Figures 7.19 and 7.21). The ROC curves of P_{1+} and standard sonar processing computed from the results of both tank tests and sonar simulation model have comparable probability of detection, giving similar detection performance. This can be explained by re-examining the processing schemes of P_{1+} and standard sonar processing. The processing scheme of P_{1+} can be expressed as follow:

$$P_{1+} = Y_1(t) + Y_2(t) \tag{7.23}$$

For the standard sonar processing technique presented, the average of the absolute of the functions, $Y_1(t)$ and $Y_2(t)$, is computed and presented in the plots. For the function, P_{1+}, it represents the function, P_+, which is applied a filter matched to the frequency band of the driving pulse. To improve the probability of detection, the backscattered reverberation (from the bubbles) has to be lower compared to the backscattered contribution of the solid target when

P_{1+} is used. This will be significant only if the functions, $Y_1(t)$ and $Y_2(t)$, are incoherent. For a bubble cloud which consists of linear scatterers, the functions, $Y_1(t)$ and $Y_2(t)$, will be fully coherent with each other. In such a scenario, the backscattered contribution of the bubble relative to the target will be identical for both standard sonar processing and P_{1+} processing.

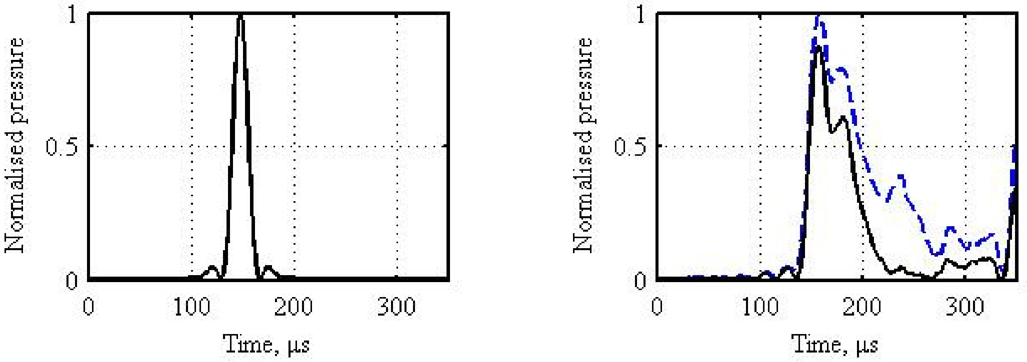

(a) 250 μm

(b) 50 μm

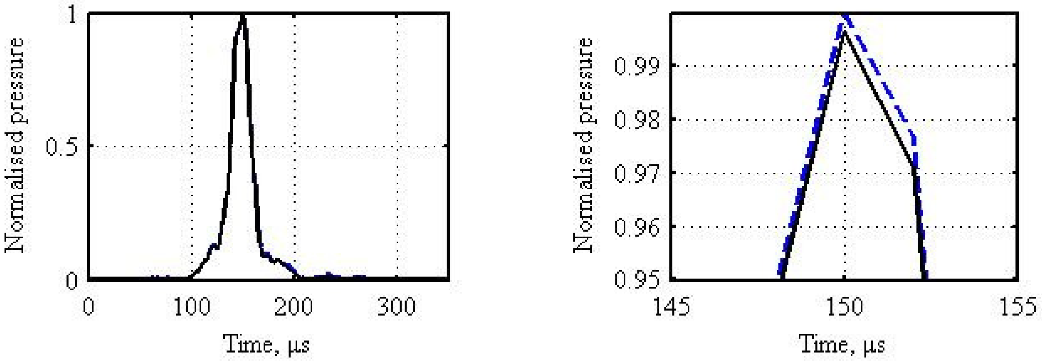

(c) 15 μm

(d) close-up of 15 μm

Figure 7.22. Standard sonar processing (denoted by the dotted line) and TR P_{1+} processing (denoted by the solid line) of the bubble response normalised by values of standard sonar processing. The bubble radius in (a) is 250 μm, (b) 50 μm, (c) 15 μm and (d) close-up of 15 μm.

The comparable probability of detection for both TR P_{1+} and standard sonar, as shown in the ROC curves, can be attributed to the wide distribution of bubble size present in the bubble cloud. This can be examined in detail with a single bubble analysis using the pulse used in the tank tests (Figure 7.16) as the driving pulse. Figure 7.22 shows the normalized pressure of the bubble backscattered response when processed using the standard sonar technique and TR P_{1+}. To prevent simple gains in the two processing scheme from affecting the comparison, the standard sonar and TR P_{1+} processing have been normalised such that both processing schemes give the same value for the backscattered response of a linear target.

For bubbles of resonant frequencies close to or higher than the driving frequency, TR P_{1+} processing will result in a reduced backscattered contribution of these bubble compared to standard sonar processing (Figures 7.22(b), (c) and (d)). It is also observed for the smaller bubbles (whose resonant frequencies are higher than the driving frequency), this reduction is not very significant as shown in Figure 7.22(d). If the bubble has a resonant frequency lower than that of the driving frequency, the backscattered contribution of the bubble from P_{1+} processing will be comparable to that of standard sonar as the bubble will behave close to that of a linear scatterer. When the bubble cloud has a wide bubble size distribution, the reduced backscattered contribution of the bubble cloud (from the resonant and smaller bubbles) has to be significant if there is to be a substantial improvement in the detection performance as measured by the ROC curves. From the single bubble analysis shown above, it appears that the reductions in backscattered contribution from the resonant and smaller bubbles are not significant enough for this particular case.

7.7. Comparison of the three two-pulse techniques

This chapter have described several new two-pulse techniques for distinguishing between linear and nonlinear scatterers for the scenario of a solid target in a bubble-filled environment. Here, two of these techniques, BiaPSS and TR pulse technique will be compared to TWIPS using the results from the tank tests, where the solid target would be placed close to or within the bubble cloud, depending on the natural evolution of the cloud in the tank. In the comparison, the TWIPS pulse pair used here will have a waveform and frequency band similar to that used in the tank tests of BiaPSS and TR pulse techniques, except that the TWIPS pulse pair will require one of the pulse pair to have a polarity opposite of the other.

So far in this thesis, the three techniques: TWIPS, BIAPPS and TR pulse technique, have been shown to have the primary advantage of being able to distinguish between the presence of the solid target and the bubble cloud easily. This is achieved by visually comparing the plots of the different combinations (sum and subtraction) of the returned signals from the respective pulse pairs. Such ability is absent in standard sonar technique.

The target detection performance of the three two-pulse techniques compared to standard sonar processing will now be compared. The plots of standard sonar processing and those of the TWIPS, BiaPSS and TR processing are now shown in Figure 7.23. For a fair comparison between the plots of the three techniques, the plots in Figure 7.23 are normalised to a common value as follows: the standard sonar technique plots are normalised to a common value while the plots of the two-pulse techniques are normalised to a common value. In this section, P_{1+} processing of BiaPSS will henceforth be referred to as BiaPSS processing for brevity. Likewise, P_{1+} processing of TR pulse pair will be referred to as TR processing and P_{1-} processing of TWIPS will be referred to as TWIPS processing.

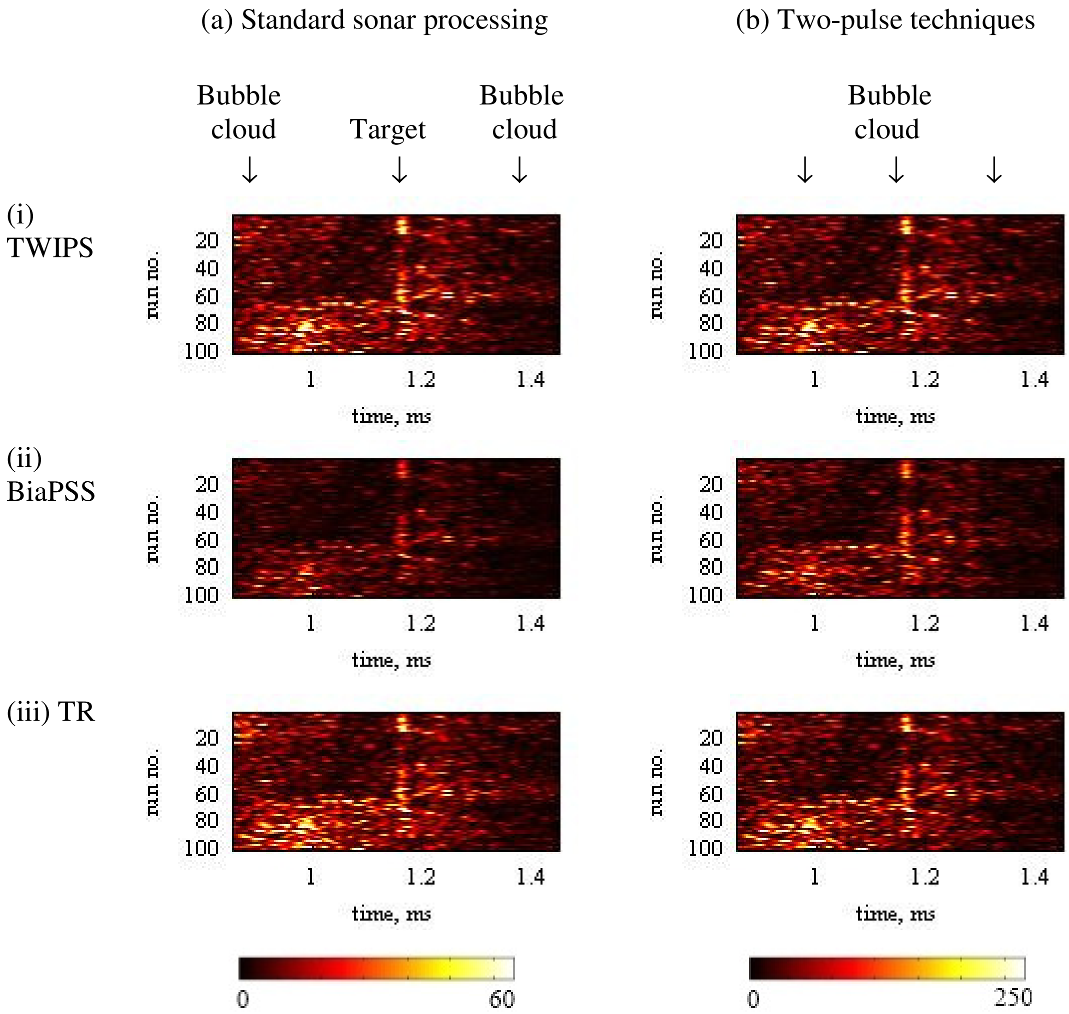

Figure 7.23. Measurement of a solid sphere (TS= -30 dB) placed in a bubble-filled environment with plots in (a) showing standard sonar processing and (b) two-pulse techniques. The target is located between 1.1 and 1.2 ms. TWIPS processing is shown in (i) with (ii) in BiaPSS and (iii) TR processing. Each colour scale is normalised to a common value, which for (a) and (b) are 60 and 2.5×10^2 respectively.

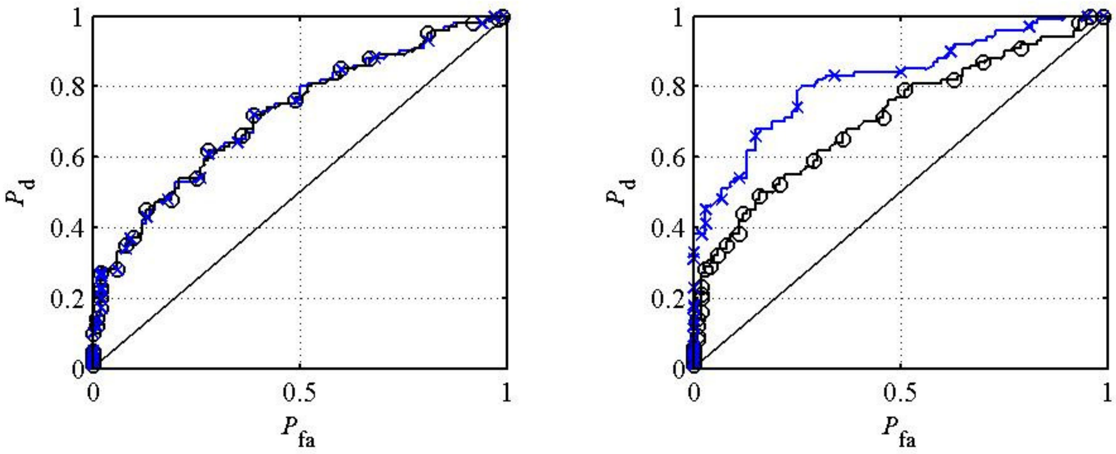
(a) TWIPS (b) BiaPSS

(c) TR

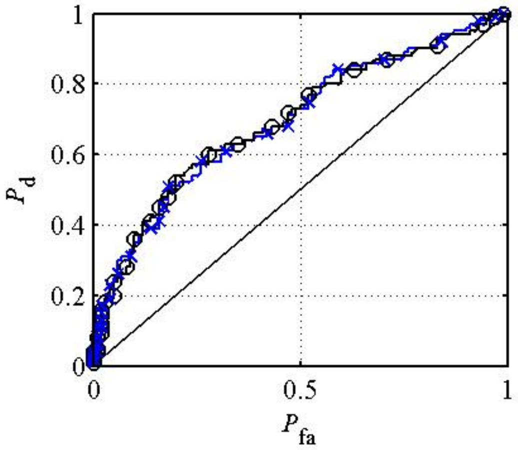

Figure 7.24. ROC curves of standard sonar processing compared with (a) TWIPS, (b) BiaPSS and (c) TR. Standard sonar processing is denoted by solid line with open circles while the respective two-pulse technique is denoted by solid line with crosses.

By comparing Figure 7.23(a) with (b) for each technique, the visual improvement in BiaPSS processing in the detection of the linear target compared to standard sonar processing is found to be greatest for a solid target placed close to or within a bubble cloud. This is consistent with the results of the ROC curves (Figure 7.24) which show the detection performance of BiaPSS outperforming that of standard sonar processing significantly while both performances of TWIPS and TR processing are found to be only comparable to that of standard sonar processing. The ROC curves computed for standard sonar processing using the three different types of pulse pair (TWIPS, BiaPSS and TR) also show the detection performance of standard sonar processing are comparable in all three cases.

(a) 250 µm (b) 50 µm

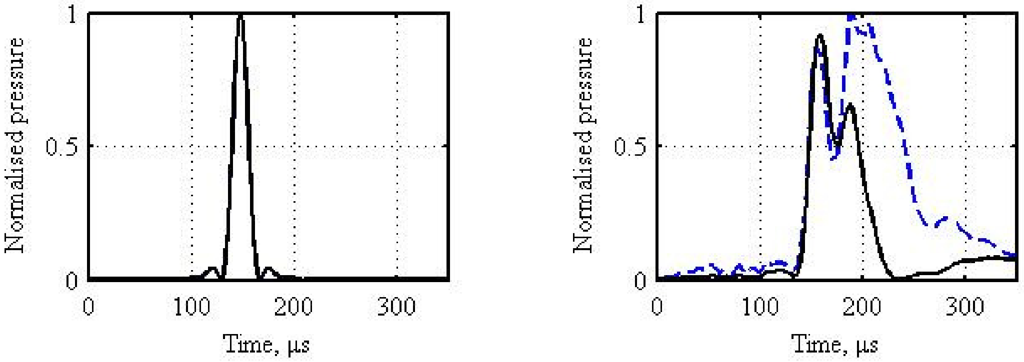

(c) 35 µm (d) 15 µm

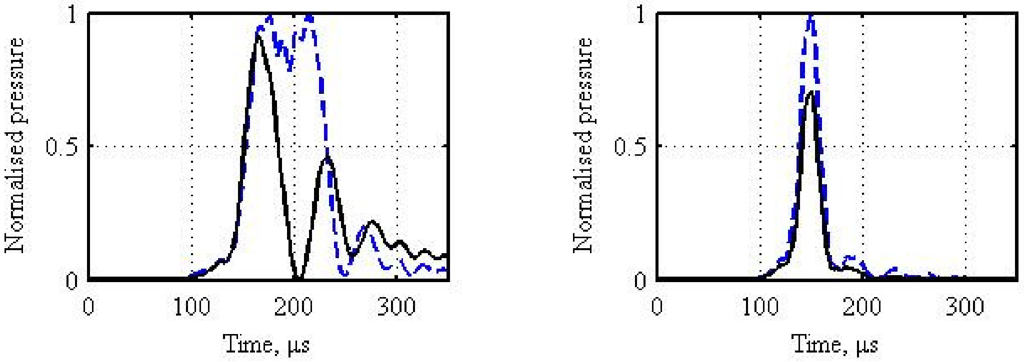

Figure 7.25. Standard sonar processing (denoted by the dotted line) and BiaPSS processing (denoted by the solid line) of the bubble response normalized by values of standard sonar processing. The bubble radius in (a) is 250 µm, (b) 50 µm, (c) 35 µm and (d) 15 µm.

The better BiaPSS performance can be attributed to the reduced backscattered contributions of the bubbles close to or higher than the frequency of the driving pulse. Using the nonlinear single bubble model, the bubble responses at four representative bubble radii are examined when driven by the same pulses used in the experiments. The normalized pressure of each bubble when processed using the standard sonar technique and BiaPSS processing is shown in Figure 7.25. Similar to Figure 7.22, simple gains in the two processing schemes are removed by normalising the standard sonar and BiaPSS such that both processing schemes give the same value for the backscattered pressure of a linear target.

For the larger bubbles, which can be treated as linear targets, the backscattered contributions for BiaPSS and standard sonar processing are of comparable levels as shown in Figure 7.25(a). This is expected because the backscattered response of a linear target will scale with amplitude of the input signal. The sum of the responses from a pair of BiaPSS signal will add up coherently, resulting in a comparable level to standard sonar processing.

As the resonant frequency of a bubble tends towards the driving frequency, the backscattered contribution of the bubble (processed using BiaPSS) decreases with respect to that processed using the standard sonar processing (Figures 7.25(b) and (c)).

For bubbles with resonant frequencies higher than the frequency of the driving pulse, the backscattered contributions of the bubbles (processed using BiaPSS) continue to be lower than that of standard sonar processing (Figure 7.25(d)). This suggests that the scattering of the bubble from the BiaPSS pulse pair tend to be incoherent, resulting in reduced scattering from the bubble with the linear sum of the signal responses (P_{1+}) from the BiaPSS pulse pair. This is because, for a bubble of such size, their behaviour tends towards that of a nonlinear system. For a nonlinear system, its response does not scale with the amplitude of its input signal. The responses of a nonlinear system (bubble) from a BiaPSS pulse pair will thus not be fully coherent with each other. This difference appears to be higher compared to TR and TWIPS processing. Hence, the combination of signal responses using BiaPSS results in a greater reduction of backscatter from the bubbles (compared to the other two-pulse techniques and standard sonar processing), and consequently, a relative higher level of backscatter from the linear target. This translates to a higher probability of detection in the ROC curve, and consequently better detection performance.

7.8. Summary

This chapter has presented several two-pulses techniques which can distinguish a solid target (linear scatterers) from bubble clouds (nonlinear scatterers). Two of these techniques were proposed based on observed pulses emitted by the dolphin during echolocation. The variation of frequency in the dolphin pulses, commonly referred to as a change in click types, yielded the Alternate Pulse (AP) technique while the variation in amplitude of the dolphin pulses within a click train formed the basis of Biased Pulse Summation Sonar (BiaPSS). While unrelated to dolphin, the use of a pair of time-reversed pulses was also investigated.

The AP technique and BiaPSS were initially studied using a pair of dolphin-like pulses in the sonar simulation model. Both two-pulse techniques were able to differentiate between the backscattered contribution of linear (solid target) and nonlinear scatterers (bubble cloud). However, only the target detection performance of BiaPSS was found to outperform standard sonar processing as measured by the ROC curves. Hence only BiaPSS was subsequently investigated with a series of tank tests and simulations using pulses which could be practically produced.

The results of the tank measurements confirmed the performance advantage of BiaPSS compared to standard sonar processing. The measurement results showed BiaPSS easily distinguished between linear and nonlinear scatterers and gave a better target detection performance compared to standard sonar processing. The use of a time-reversed pulse pair (derived from biomedical imaging) was also studied. Like the AP technique, it could successfully distinguish between linear and nonlinear scatterers. Unlike BiaPSS, the detection performance of the time-reversed pulse pair technique and the AP technique were comparable to standard sonar processing.

The chapter concluded with a comparison of the performance of BiaPSS, TWIPS and TR pulse technique for a solid target placed in a bubble-filled environment. In the scenario studied, the solid target was placed within or close to the bubble cloud, with different combinations (sum and subtraction) of the respective pulse pairs investigated for three two-pulse techniques. Using only the different combination (sum or subtraction) of the returned signals from the pulse pair, the performance advantage of BiaPSS relative to the standard sonar technique is found to be the greatest amongst the three two-pulse techniques studied. This suggests BiaPSS can improve the detection of a target in a bubbly environment for a greater number of applications, especially when the target is close to or within the bubble cloud.

Chapter 8. Conclusions

This thesis studies the Twin Inverted Pulse Sonar (TWIPS) and a range of techniques, including the proposal of a new one, Biased Pulse Summation Sonar (BiaPSS), for enhancing sonar performance in bubbly water. The study presented here adds to the limited number of proposed solutions [3, 6, 30, 31, 173] in this area. Of the other studies that have attempted to mitigate the effects of bubbles on sonar performance, only TWIPS [3, 6] has been developed from theoretical concept to sea trial. In TWIPS, a pair of pulses, with one the opposite polarity of the other, can be used to distinguish a solid target from bubble cloud, and improved detection of the solid target in some manifestations. Such effective classification and improved target detection are of importance in areas such as maritime security and underwater acoustics. For example, effective detection and classification of solid targets will be crucial for maritime security where the presence of a single naval mine could entail closure of a sea route and deployment of divers. The principles behind techniques like BiaPSS and TWIPS may be similarly applied to other sensor technologies such as radar [3, 6].

As part of the study to find solutions to enhance sonar performance in bubbly environment, the current state-of-the-art in ocean acoustics and biomedical imaging were also reviewed.

A sonar simulation model incorporated with a linear bubble cloud attenuation model has been developed to investigate a number of hypotheses raised. Current limitations of the model were also highlighted. These included a linear attenuation model (instead of a nonlinear one) as well as an absence of thermal damping in the nonlinear bubble model. The thermal damping in the nonlinear single bubble model was shown to be dominant for driving frequencies less than the bubble resonance. For the purpose of this study, thermal damping was excluded in the sonar simulation model with the consequence the total damping would be underestimated in some instances. The generalised trend of underestimation was noted. The inclusion of thermal damping in a bubble model is thus recommended as an area for future study. In addition, the bubble clouds formed in the experiments exhibit spatial and temporal heterogeneity that the model is unable to replicate precisely. The absolute performance, as measured by the ROC curves, of the model relative to the measurements suggests these features are not perfectly modelled, given these limitations. However, the relative performances of the various techniques to standard sonar processing, as measured by the ROC curves, from both model and measurements matched up well, suggesting the sonar simulation model is sufficient for the study here.

The two-pulse technique, TWIPS, was examined using a LFM waveform, a waveform different from the one extensively tested by Leighton *et al.* [3, 6]. The efficacy of TWIP was demonstrated using this waveform. The low frequency and high amplitude requirements of a pair of TWIPS pulse made it unlikely that odontocetes implement similar TWIPS-like techniques in nature, even though odontocetes like the shallow-water Hector's dolphin have been reported to produce multiple pulses of opposite polarity [118]. However, this conclusion could not categorically be made because of admittedly scarce data as these species of odontocetes are understudied and often endangered. Greater attention should therefore be paid to the abilities of these odontocetes which may yield results that will alleviate the pressing problem of sonar in shallow water [118].

On the other hand, the biosonar of dolphins like the Atlantic bottlenose dolphin, while not specifically on target echolocation in bubbly water, has been heavily studied with extensive data available. Current use of dolphins in military arena is a further testament of the superiority of their biosonar compared to man-made sonar [114]. Further consideration of the sonar problem was thus carried out with a review of the current understanding of the dolphin biosonar. The characteristics commonly associated with dolphin pulses were first examined, followed by studying how the observed change in the dolphin pulses within a click train during echolocation can enhance sonar performance in bubbly water.

The key characteristics (such as amplitude, chirp structure and duration) commonly associated with a typical dolphin pulse have been examined in both tank measurements and the sonar simulation models for possible sonar enhancement in bubbly water. In the scenario examined, increased amplitude was found to give only a marginal improvement in detection performance, showing a correspondence between amplitude and backscattered response of a bubble cloud might not be straightforward. Thus, caution will have to be exercised with regard to amplitude and bubble cloud backscattering or attenuation. Leighton *et al.* [173] have shown there is no simple correspondence of amplitude to the backscatter of a bubble cloud.

Another pulse characteristic examined was the chirp structure of a typical dolphin pulse. The backscatter of a bubble cloud to an up-chirp (a LFM waveform of increasing frequency) and down-chirp (a LFM waveform of decreasing frequency) signal were examined. A down-chirp was found to result in higher backscattered reverberation from a bubble cloud. Higher backscattered reverberation from the bubble cloud will result in high clutter, making it more difficult to detect the backscatter of any target. This inadvertently affects the detection performance of the target in the bubble-filled environment when such a pulse is used. This observation was corroborated with measurements and simulations. As measured by the ROC curves, it was shown there was significantly poorer detection performance when a down-chirp was used as the driving pulse. The main advantage appears to be the ease which a down-chirp can drive a bubble to a higher state of nonlinearity compared to an up-chirp of the same amplitude and frequency band. This begs the question of why some dolphins would use down-chirps for echolocation [106, 133].

The short pulse duration used by the dolphin was also investigated. The effects of varying the pulse duration were investigated in two ways. The first entailed varying the pulse duration while keeping the amplitude constant while the second varied the duration of the pulse with the total energy of the pulse kept constant. In both cases, a shorter pulse, of the order comparable to that of a typical dolphin pulse, was found to give the best detection performance. The better detection performance of a short pulse (about 70 μs long) was attributed to the nonlinear time-dependent characteristics of bubbles and bubble clouds prior to steady state. While this part of the study focused on the importance of pulse characteristics in sonar enhancement in bubbly water, the results could also be applied to a wide range of problems associated with the use of UCAs in biomedical imaging.

Studying the observed changes in certain parameters (like amplitude, and frequency) of dolphin-like pulses emitted or the possible strategies a dolphin might adopt during echolocation led to the proposal of a number of two-pulse techniques, including BiaPSS. The proposed technique, BiaPSS, is able to distinguish the linear backscattered contributions of a solid target from the nonlinear backscattered reverberation of the bubble cloud effectively. BiaPSS also has the secondary advantage of outperforming standard sonar processing in the detection of targets placed in a bubble-filled environment.

Other techniques like the Alternate pulse (AP) method and the time-reversed (TR) pulse technique have detection performances which were only comparable to standard sonar processing. While techniques like the AP and the TR pulse techniques gave only comparable performance to standard sonar processing, all the two-pulse techniques investigated were able to perform classification by distinguishing the linear backscattered contributions of a solid target from the nonlinear backscattered reverberation of the bubble cloud effectively. Such capability is inherently absent in standard sonar processing. Chapter 7 concluded with a comparison between BiaPSS, TR pulse technique and TWIPS. While the primary advantage of these three techniques lie in distinguishing the solid target (linear scatterer) from the bubble cloud (nonlinear scatterers), the secondary advantage of improving target detection was also studied. The reasons for the variation of their detection performance were discussed.

The techniques discussed all require some of form of nonlinear processing. Currently, there is no evidence dolphins perform any form of nonlinear processing, if at all. Questions thus remain, which would require data from dolphins to address. The characteristics of the pulses used in BiaPSS testing were similar in many ways to the pulses emitted by a dolphin. It has been shown in both tank tests and simulations that it was possible to distinguish a solid target from the bubble cloud with the frequency range close to that emitted by a dolphin using functions such as P_- in the fundamental frequency of the driving pulse. A dolphin also needs not be sensitive to energy at the second harmonic and the frequency range of the pulse used is well within the measured hearing sensitivity of the dolphin [113, 115, 132]. Sensitivity to the second harmonic, however, will raise the possibility of a wider range of processing capabilities as well as the issue of efficiency.

For BiaPSS to work efficiently, the receiver will be expected to have an upper frequency limit of at least twice the centre frequency of the pulse used. The upper frequency limit of the audiogram of the Atlantic bottlenose dolphin and the high peak frequency of a number of their echolocation clicks suggest dolphins cannot access the majority of the information in the signals necessary to exploit such strategies. Given that BiaPSS has been made to work in both simulations and measurements, it is justified to speculate if a dolphin uses BiaPSS or any other nonlinear technique to suppress bubble clutter and improve target detection. The reported use of a down-chirp, with an amplitude as high as 230 dB re 1 µPa m, as an echolocating pulse by some dolphins raises more questions. While speculative, it seems unlikely that a dolphin will want to use a pulse which will increase backscattered reverberation (increased sonar clutter) from the bubble cloud and consequently, poorer detection in such environment, unless it is required to drive a bubble cloud to a higher state of nonlinearity so as to exploit nonlinear processing. It should be noted dolphins will adapt their echolocation pulses to suit their environment [113, 115, 137, 155, 157]. For one, future tests will have to show dolphins adjusting their clicks to transmit significant energy below half of their upper frequency hearing limit when echolocating in bubbly water if they are using BiaPSS or another nonlinear technique. More data from dolphins is therefore needed to address the issues raised here.

Other areas of related research that may be of interest but have not been discussed in great detail include:

- Further work involving a greater variety of bio-inspired dolphin pulses, expanding on the current work, would be of benefit and may help improve the understanding of the dolphin biosonar. Current limitations of equipment also mean pulses used in the tank experiments have only some characteristics close to those of typical dolphin pulses.

- Experiments involving dolphins in bubble-filled environments to investigate how they adapt their pulses in target echolocation tasks. Particular attention should be paid to how a dolphin changes the frequency, amplitude and pulsing of its pulses during echolocation in bubbly water. This would be a valuable addition to the available data of dolphins performing this important task.

- The ultimate aim of the theoretical and experimental work conducted during this study is to yield results, and consequently solutions to enhance sonar performance in bubbly water in practical situations. It will be ideal to test these findings and solutions in sea trials or practical situations. Unfortunately, only simulations and controlled tank tests have been carried out in the course of this study. Hence, a fully successful trial of this nature would be of significant interest.

- More complicated underwater targets, other than solid targets, can be used. The study of a number of elastic waves present by many investigators [82-85, 107, 109, 133] show the possibility of exploiting these waves for detection and classification purposes. The interaction of these waves using two-pulse techniques would thus be of interest in the field of underwater target detection and classification.

- Implementation of the two-pulse techniques discussed in systems such as electromagnetic (radar) system should be investigated. Current understanding of the linear and nonlinear responses of practical targets to radar remains limited. Future work can study the responses of practical targets to radar to improve such understanding which may be useful in detection of objects like improvised explosive devices (IEDs).

This study proposed BiaPSS, a two-pulse technique for target discrimination in bubbly water, and yielded a number of results that can be considered for sonar enhancement in bubbly water. These include:

1. Development of a sonar simulation model which incorporated the nonlinear bubble behaviour coupled to a linear bubble cloud attenuation model. The relative performances of the various techniques studied to standard sonar processing, as measured by the ROC curves, from the simulations matched up well with the measurements.

2. The proposal of Biased Pulse Summation Sonar (BiaPSS), to distinguish solid targets from bubble clouds as the primary advantage with better target detection as the secondary advantage for sonar applications. Extensive testing through simulations and tank experiments indicate it holds possibilities for improved detection and classification of objects for practical situations.

3. The ingredients required for BiaPSS were similarly found in the pulses produced by some species of cetaceans which raised the possibility some form of BiaPSS-like techniques are performed in nature.

4. Assessment of the importance of pulse characteristics for sonar enhancement in bubbly water. These characteristics included amplitude, chirp structure, and duration of pulse. This knowledge can also be applied to biomedical imaging and possibly a variety of applications involving other sensor technologies such as radar.

5. Other two-pulse techniques such as the Alternate Pulse (AP) and Time-reversed (TR) pulse techniques were also proposed. These techniques have been shown to be effective in distinguishing linear scatterers from nonlinear ones. Such a capability is inherently absent in standard sonar technique.

References

1. Leighton, T.G., *From seas to surgeries, from babbling brooks to baby scans: The acoustics of gas bubbles in liquids.* International Journal of Modern Physics B, 2004. **18**(25): p. 3267-3314.

2. Leighton, T.G., D.C. Finfer, and P.R. White, *Sonar which penetrates bubble cloud*, in *The Second International Conference on Underwater Acoustic Measurements, Technologies and Results*, J.S. Papadakis and L. Bjorno, Editors. 2007: Heraklion, Crete. p. 555 -562.

3. Leighton, T.G., D.C. Finfer, P.R. White, G.H. Chua, and J.K. Dix, *Clutter suppression and classification using twin inverted pulse sonar (TWIPS).* Proc. R. Soc. A, 2010. **466**: p. 3453-3478.

4. Leighton, T.G., D.C. Finfer, and P.R. White, *Experimental evidence for enhanced target detection by sonar in bubbly water.* Hydroacoustics, 2008. **11**: p. 181-202.

5. Leighton, T.G., P.R. White, and D.C. Finfer. 2006 Target detection in bubbly water. UK patent application PCT/GB2006/002335, University of Southampton

6. Leighton, T.G., D.C. Finfer, G.H. Chua, P.R. White, and J.K. Dix, *Clutter suppression and classification using Twin Inverted Pulse Sonar in ship wakes.* J. Acoust. Soc. Am., 2011. **130**(5): p. 3431-3437.

7. Leighton, T.G., *Nonlinear bubble dynamics and the effects on propagation through near-surface bubble layers*, in *High Frequency Ocean Acoustics: High Frequency Ocean Acoustics Conference*, M.B. Porter, M. Siderius, and W. Kuperman, Editors. 2004: Melville, New York, American Institute of Physics. p. 180 -193.

8. Committee for Mine Warfare Assessment, N.S.B., National Research Council *Naval Mine Warfare: Operational and Technical Challenges for Naval Forces*. 2001, Washington, D.C.: National Academies Press.

9. Bachkosky, J.M., T. Brancati, D.R. Conley, J.W. Douglass, P.A. Gale, D. Held, L.R. Hettche, J.R. Luyten, I.C. Peden, R.L. Rumpf, and A. Salkind, *Unmanned Vehicles (UV) in Mine Countermeasures*, N.R.A. Committee, Editor. 2000: Arlington, VA.

10. Leighton, T.G., *The detection of buried marine targets.* Applied Acoustics, 2008. **69**(5): p. 385-386.

11. Biano, R., R.L. Croft, and W. Littlejohn, *Factors Affecting Modelling and Simulating the Surf Zone Region*, in *14th Distributed Interactive Simulation Workshop*. 2005.

12. Kozak, G., *Side scan sonar target comparative technique for port security and MCM Q-route requirements*, in *MINWARA Seventh International Symposium on Technology & the Mine Problem.* 2006: Naval Postgraduate School, Monterey, California, USA.

13. Kreisher, O., *Service Experts Eye 'Leap Ahead' in Mine Warfare Capabilities*, in *Seapower Magazine (September 2004).* 2004.

14. Medwin, H., *Counting bubbles acoustically, a review.* Ultrasonics, 1977. **15**: p. 7 -13.

15. Melville, W.K., E. Terrill, and F. Veron, *Bubbles and turbulence under breaking waves*, in *Natural Physical Processes Associated with Sea Surface Sound*. 1997. p. 135-145.

16. Leighton, T.G., *The Acoustic Bubble, Section 3.1*. 1994, London: Academic Press.

17. Leighton, T.G., *The Acoustic Bubble, Section 3.2.1*. 1994, Academic Press: London.

18. Ainslie, M.A. and T.G. Leighton, *Review of scattering and extinction cross-sections, damping factors, and resonance frequencies of a spherical gas bubble.* J. Acoust. Soc. Am., 2011. **130**(5): p. 3184-3208.

19. Devin, C.J., *Survey of thermal, radiation and viscuous damping of pulsating air bubbles in water.* J. Acoust. Soc. Am., 1959. **31**: p. 1654-1667.

20. Eller, A.I., *Damping constants of pulsating bubbles.* J. Acoust. Soc. Am., 1970. **47**: p. 1469-1470.

21. Leighton, T.G., *The Acoustic Bubble, Section 3.4.2*. 1994, London: Academic Press.

22. Kinsler, L.E., A.R. Frey, A.B. Coppens, and J.V. Sanders, *Fundamentals of Acoustics*. 1982, Wiley: New York, 3rd edn. p. 163-165.

23. Leighton, T.G., *The Acoustic Bubble, Section 3.2*. 1994, London: Academic Press.

24. Leighton, T.G., *The Acoustic Bubble, Section 4.4.2*. 1994, London: Academic Press.

25. Mallock, A., *The damping of sound by frothy liquid.* Procs R. Soc., 1910. **A84**: p. 391-395.

26. Leighton, T.G., S.D. Meers, and P.R. White, *Propagation through nonlinear time-dependent bubble clouds and the estimation of bubble populations from measured acoustic characteristics.* Proc. R. Soc. A, 2004. **460**: p. 2521-2550.

27. Leighton, T.G., *The Acoustic Bubble, Chapter 4*. 1994, Academic Press: London.

28. Walton, A.J. and R.G. T., *Sonoluminescence.* Adv Physics, 1984. **33**: p. 595-660.

29. Keller, J.B. and M. Miksis, *Bubble Oscillations of Large-Amplitude.* J. Acoust. Soc. Am., 1980. **68**(2): p. 628-633.

30. Clarke, J.W.L. and T.G. Leighton, *A method for estimating time-dependent acoustic cross-sections of bubbles and bubble clouds prior to the steady state.* J. Acoust. Soc. Am., 2000. **107**(4): p. 1922-1929.

31. Akulichev, V.A., V.A. Bulanov, and S.A. Klenin, *Acoustic Sensing of Gas-Bubbles in the Ocean Medium.* Soviet Physics Acoustics-Ussr, 1986. **32**(3): p. 177-180.

32. Suiter, H.R., *Pulse Length Effects on the Transmissivity of Bubbly Water.* J. Acoust. Soc. Am., 1992. **91**(3): p. 1383-1387.

33. Ainslie, M.A. and T.G. Leighton, *Near resonant bubble acoustic cross-section corrections, including examples from oceanography, volcanology, and biomedical ultrasound.* J. Acoust. Soc. Am., 2009. **126**(5): p. 2163-2175.

34. Pace, N.G., A. Cowley, and A.M. Campbell, *Short pulse acoustic excitation of microbubbles.* J. Acoust. Soc. Am., 1997. **102**(3): p. 1474-1479.

35. Meers, S.D., T.G. Leighton, J.W.L. Clarke, G.J. Heald, H.A. Dumbrell, and P.R. White. *The importance of bubble ring-up and pulse length in estimating the bubble distribution from propagation measurements*. in *Acoustical Oceanography* 2001, p. 235-241.

36. Shetzen, M., *The Volterra and Wiener theories of nonlinear systems*. 1980, New York: John Wiley.

37. White, P.R., W.B. Collis, T.G. Leighton, and J.K. Hammond, *Detection of bubbles via higher order statistics*, in *Natural Physical Processes Associated with Sea Surface Sound*, T.G. Leighton, Editor. 1997. p. 179 - 185.

38. Leighton, T.G., P.R. White, and D.C. Finfer. *Two hypotheses about cetacean acoustics in bubbly water*. in *3rd Int. Conf. on Underwater Acoustic Measurements, Technologies and Results*. Nafplion, Greece, 16-21 June 2009.

39. Tang, M.-X., J.-M. Mari, P.N.T. Wells, and R.J. Eckersley, *Attenuation correction in ultrasound contrast agent imaging. Elementary theory and perliminary experiment evaluation.* Ultrasound in Med. & Biol., 2008. **34**(12): p. 1998 - 2008.

40. Burns, P.N., D.H. Simpson, and M.A. Averkiou, *Nonlinear imaging.* Ultrasound in Med. & Biol., 2000. **26**(Supplement 1): p. S19-S22.

41. Simpson, D.H., T.C. Chien, and P.N. Burns, *Pulse inversion Doppler: a new method for detecting nonlinear echoes from microbubble contrast agents.* IEEE Transactions on Ultrasonics, Ferroelectrics and Frequency Control, 1999. **46**(2): p. 372 -382.

42. Burns, P.N., S.R. Wilson, and D.H. Simpson, *Pulse Inversion Imaging of Liver Blood Flow: Improved Method for Characterizing Focal Masses with Microbubble Contrast.* Investigative Radiology, 2000. **35**(1): p. 58 -71.

43. Brock-Fisher, G., M. Poland, and P. Rafter. 1996 Means for increasing sensitivity in nonlinear ultrasound imaging systems. patent application

44. Mor-Avi, V., E.G. Caiani, K.A. Collins, C.E. Korcarz, J.E. Bednarz, and R.M. Lang, *Combined assessment of myocardial perfusion and regional left ventricular function by analysis of contrast-enhanced power modulation images.* Circulation, 2001. **104**: p. 352-357.

45. Eckersley, R.J., C.T. Chin, and P.N. Burns, *Optimising phase and amplitude modulation schemes for imaging microbubbles contrast agents at low acoustic power.* Ultrasound in Med. & Biol., 2005. **31**(2): p. 213-219.

46. Bouakaz, A. 2005 Chirp reversal contrast imaging. France patent application PCT/IB06/02954, INSERM, Paris (FR)

47. Novell, A., S. van der Meer, M. Versluis, N. de Jong, and A. Bouakaz, *Contrast agent response to chirp reversal: simulations, optical Observations. and acoustical verification.* IEEE Transactions on Ultrasonics Ferroelectrics and Frequency Control, 2009. **56**(6): p. 1199-1206.

48. Sun, Y., D.E. Kruse, and K.W. Ferrara, *Contrast imaging with chirped excitation.* IEEE Transactions on Ultrasonics Ferroelectrics and Frequency Control, 2007. **54**(3): p. 520-529.

49. Sun, Y., S. Zhao, P.A. Dayton, and K.W. Ferrara, *Observation of contrast agent response to chirp insonation with a simultaneous optical-acoustical system.* IEEE

Transactions on Ultrasonics Ferroelectrics and Frequency Control, 2006. **53**(6): p. 1130-1137.

50. Commander, K.W. and A. Prosperetti, *Linear pressure waves in bubbly liquids - comparison between theory and experiments.* J. Acoust. Soc. Am., 1989. **85**(2): p. 732-746.

51. Leighton, T.G., *The Acoustic Bubble, Section 3.4*. 1994, London: Academic Press.

52. Leighton, T.G., *The Acoustic Bubble, Section 3.6*. 1994, London: Academic Press.

53. Commander, K.W. and R.J. McDonald, *Finite-element solution of the inverse problem in bubble swarm acoustics.* J. Acoust. Soc. Am., 1991. **89**(2): p. 592-597.

54. Francois, R.E. and G.R. Garrison, *Sound absorption based on ocean measurements. Part I: Pure water and magnesium sulfate contributions.* J. Acoust. Soc. Am., 1982. **72**(3): p. 896 -907

55. Francois, R.E. and G.R. Garrison, *Sound absorption based on ocean measurements. Part II: Boric acid contribution and equation for total absorption.* J. Acoust. Soc. Am., 1982. **72**(6): p. 1879-1890

56. Phelps, A.D. and T.G. Leighton, *Oceanic bubble population measurements using a buoy-deployed combination frequency technique.* IEEE Journal of Oceanic Engineering, 1998. **23**(4): p. 400-410.

57. Breitz, N. and H. Medwin, *Instrumentation for Insitu Acoustical Measurements of Bubble Spectra under Breaking Waves.* J. Acoust. Soc. Am., 1989. **86**(2): p. 739-743.

58. Farmer, D.M. and S. Vagle, *Waveguide propagation of ambient sound in the ocean-surface bubble layer.* J. Acoust. Soc. Am., 1989. **86**(5): p. 1897-1908.

59. Johnson, B.D. and R.C. Cooke, *Bubble populations and spectra in coastal waters - photographic approach.* Journal of Geophysical Research-Oceans and Atmospheres, 1979. **84**(NC7): p. 3761-3766.

60. Deane, G.B. and M.D. Stokes, *Air entrainment processes and bubble size distributions in the surf zone.* Journal of Physical Oceanography, 1999. **29**(7): p. 1393-1403.

61. Phelps, A.D. and T.G. Leighton. *Measurement of bubble populations near the sea surface using combination frequencies: adaptation and calibration of device between two sea trials*. in *Natural physical processes associated with sea surface sound.* Southampton, England, 1997, p. 198-210.

62. Culver, R.L., J.D. Park, T.G. Leighton, and D.G.H. Coles. *Variations in signal phase and beamformer gain due to bubble scattering*. in *Proceedings of the Fourth International Conference on Underwater Acoustic Measurements, Technologies and Results* Heraklion, Greece, 20 - 24 June 2011.

63. Leighton, T.G., D.C. Finfer, E.J. Grover, and P.R. White, *An acoustical hypothesis for the spiral bubble nets of humpback whales and the implications for whale feeding.* Acoustics Bulletin, 2007. **22(1)**: p. 17-21.

64. Chambers, C., *Acoustic measurement report for hydrophone D140 serial number: 18938*. 2006, Wraysbury Acoustic Calibration Laboratory, National Physical Laboratory.

65. Hayman, G., P. Theobald, G.B.N. Robb, S. Robinson, V. Humphrey, T.G. Leighton, J.K. Dix, and A.I. Best. *Hydrophone performance in sediment*. in *Proceedings of the Second International Conference on Underwater Acoustic Measurements, Technologies and Results*. Heraklion, Crete, Greece, 25-29 June 2007, p. 453-458.

66. Gutowski, M., J. Bull, T. Henstock, J. Dix, P. Hogarth, T. Leighton, and P. White, *Chirp sub-bottom profiler source signature design and field testing.* Marine Geophysical Researches, 2002. **23**(5-6): p. 481-492.

67. Bull, J.M., M. Gutowski, J.K. Dix, T.J. Henstock, P. Hogarth, T.G. Leighton, and P.R. White, *Design of a 3D Chirp sub-bottom imaging system.* Marine Geophysical Researches, 2005. **26**(2-4): p. 157-169.

68. Harris, F.J., *On the use of windows of harmonic analysis with discrete Fourier transform.* Proc IEEE, 1978. **66**: p. 51-83.

69. Schock, S.G., L.R. LeBlanc, and S. Panda, *Spatial and temporal pulse design considerations for a marine sediment classification sonar.* IEEE Journal of Oceanic Engineering, 1994. **19**(3): p. 406-415.

70. Mole, J.H., *Filter design data for communication engineers.* 1952, Spon Ltd: London. p. 233-246.

71. Fano, R.M., *Theoretical limitations on the broadband matching of arbitrary impedances.* Proceedings of J. Franklin Institute, 1950. **249**: p. 57-83.

72. Dishal, M., *Design of dissipative bandpass filters producing desired exact amplitude-frequency characteristics.* Proceedings of the IRE, 1949: p. 1050-1069.

73. Doust, P.E. 2000 Equalising transfer functions for linear electro-acoustic systems. UK patent application 0010820.9,

74. Doust, P.E. and J.F. Dix. *The impact of improved transducer matching and equalisation technique on the accuracy and validity of underwater acoustic measurements*. in *Acoustical Oceanography*. Southampton Oceanography Centre, UK, 2001, p. 100-109.

75. Jones, P., *Test Certificate MS1 HF Pump*. 2006, Neptune Sonar Ltd. p. 14.

76. Kinsler, L.E., A.R. Frey, A.B. Coppens, and J.V. Sanders, *Fundamentals of Acoustics*. 2000, John Wiley & Sons, Inc.: New York, 4th edn. p. 188-193.

77. Finfer, D.C., *Use of a twin-inverted pulse sonar (TWIPS) to discern between solid objects and bubbles.* Institute of Sound and Vibration Research, University of Southampton, 2009, PhD thesis.

78. Clift, R., J.R. Grace, and M.E. Weber, *Bubbles, drops and particles*. 1978, San Diego: Academic Press.

79. Swets, J.A., R.M. Dawes, and J. Monahan, *Better decisions through science.* Scientific American, 2000. **283**: p. 82-87.

80. Egan, J.P., *Signal detection theory and ROC analysis*. Series in Cognition and Perception. 1975, New York: Academic Press.

81. Fawcett, T., *ROC graphs: notes and practical considerations for researchers*, in *Technical Report HPL-2003-4*. 2004, Hewlett Packard Laboratories.: Palo Alto, USA.

82. Junger, M. and D. Feit, *Sound, Structures and Their Interaction*. 2nd ed. 1986, Cambridge, MA: MIT Press.

83. Skelton, E.A. and J.H. James, *Theoretical Acoustics of Underwater Structures*. 1997, London: Imperial College Press.

84. Tesei, A., P. Guerrini, and G. Canepa. *Tank measurements of elastic scattering by a resin-filled fiberglass spherical shell.* in *2nd International Conference and Exhibition on Underwater Acoustic Measurements: Technologies and Results, IACM - FORTH*. Heraklion, Greece, 25-29 June 2007.

85. Hickling, R., *Analysis of echoes from a solid elastic sphere in water.* J. Acoust. Soc. Am., 1962. **34**(10): p. 1582-1592.

86. Kaye, G.W.C. and T.H. Laby, *Tables of Physical and Chemical Constants and Some Mathematical Functions*. 13th ed. 1968, London: Longmans.

87. Fawcett, T., *An introduction to ROC analysis.* Pattern Recogn. Lett., 2006. **27**(8): p. 861-874.

88. Arif, M. and S. Freear, *Fractional fourier transform with pulse inversion for second harmonic pulse compression* IEEE International Ultrasonic Symposium Proceedings, 2009: p. 1227-1230.

89. Borsboom, J., C.T. Chin, A. Bouakaz, M. Versluis, and N. De Jong, *Harmonic chirp imaging method for ultrasound contrast agent.* Ultrasonics, Ferroelectrics and Frequency Control, IEEE Transcation on,, 2005. **52**(2): p. 241-249.

90. Leighton, T.G., *Transient excitation of insonated bubbles.* Ultrasonics, 1989. **27**(1): p. 50-53.

91. Leighton, T.G., A.J. Walton, and J.E. Field, *High-speed photography of transient excitation.* Ultrasonics, 1989. **27**: p. 370-373.

92. Leighton, T.G., A.D. Phelps, D.G. Ramble, and D.A. Sharpe, *Comparison of the abilities of eight acoustic techniques to detect and size a single bubble.* Ultrasonics, 1996. **34**(6): p. 661-667.

93. Leighton, T.G., D.G. Ramble, and A.D. Phelps, *The detection of tethered and rising bubbles using multiple acoustic techniques.* J. Acoust. Soc. Am., 1997. **101**(5): p. 2626-2635.

94. Gabor, D., *Theory of communication.* Journal of IEE, 1946. **93**: p. 429-457.

95. Leighton, T.G., *What is ultrasound?* Progress in Biophysics and Molecular Biology, 2007. **93**(1-3): p. 3-83.

96. Medwin, H., *In situ acoustic measurements of bubble populations in coastal ocean waters.* Journal of Geophysical Research, 1970. **75**(3): p. 599-611.

97. Stokes, M.D. and G.B. Deane, *A new optical instrument for the study of bubbles at high void fractions within breaking waves.* IEEE Journal of Oceanic Engineering, 1999. **24**(3): p. 300-311.

98. Burdic, W.S., *Underwater acoustic system analysis*. Prentice-Hall Signal Processing Series, ed. A.V. Oppenheim. 1984, Englewood Cliffs, NJ: Prentice-Hall, Inc.

99. Waite, A.D., *Sonar for Practising Engineers*. 1998, Dorchester: Epic Printing Services.

100. Urick, R.J., *Principles of underwater sound*. 3rd ed. 1983, New York: McGraw-Hill.

101. Kroszczynski, J.J., *Pulse compression by means of linear-period modulation.* Proc IEEE, 1969. **57**(7): p. 1260-1266.

102. Au, W.W.L., B.K. Branstetter, K.J. Benoit-Bird, and R.A. Kastelein, *Acoustic basis for fish prey discrimination by echolocating dolphins and porpoises.* J. Acoust. Soc. Am., 2009. **126**(1): p. 460-467.

103. Au, W.W.L. and D.A. Pawloski, *Cylinder wall thickness discrimination by an echolocating dolphin.* Journal of Comparative Physiology A, 1992. **170**: p. 41-47.

104. Au, W.W.L. and C.W. Turl, *Material composition discrimination of cylinders at different aspect angles by an echolocating dolphin.* J. Acoust. Soc. Am., 1991. **89**: p. 2448-2451.

105. Brown, K., C. Capus, Y. Pailhas, Y. Petillot, and D. Lane, *The application of bioinspired sonar to cable tracking on the seafloor.* EURASIP Journal on Advances in Signal Processing, 2011. **2011**: p. 1-18.

106. Pailhas, Y., C. Capus, K. Brown, and P.W. Moore, *Analysis and classification of broadband echoes using bio-inspired dolphin pulses.* J. Acoust. Soc. Am., 2010. **127**(6): p. 3809-3820.

107. Capus, C., Y. Pailhas, K. Brown, and D. Lane. *Detection of buried and partially buried objects using a bio-inspired wideband sonar.* in *OCEANS 2010 IEEE*. Sydney, 24-27 May 2010, p. 1-6.

108. Capus, C., Y. Pailhas, K. Brown, J. Evans, and D. Willins. *Underwater detection, classification and tracking using wideband sonar.* in *3rd Int. Conf. on Underwater Acoustic Measurements, Technologies and Results*. Nafplion, Greece, 16-21 June 2009.

109. Pailhas, Y., C. Capus, K. Brown, and Y. Petillot, eds. *BioSonar: a bio-mimetic approach to sonar systems concepts and applications*. On Biomimetics, ed. L. Pramatarova. 2011, InTech. 469-488.

110. Ainslie, M.A., *Principles of Sonar Performance Modelling, Chapter 5*. 1st ed. 2010: Springer Berlin Heidelberg. 191-249.

111. Leighton, T.G., P.R. White, H.A. Dumbrell, and G.J. Heald, *Nonlinear propagation in bubbly water: theory and measurement in the surf zone*, in *Proceedings of the International Conference: Underwater Acoustic Measurements: Technologies & Results*. 2005: Heraklion, Crete, Greece.

112. Cox, H., *Navy applications of high-frequency acoustics*, in *High Frequency Ocean Acoustics: High Frequency Ocean Acoustics Conference*, M.B. Porter, M. Siderius, and W. Kuperman, Editors. 2004: Melville, New York, American Institute of Physcis.

113. Au, W.W.L., *The Sonar of Dolphins*. 1993, New York: Springer-Verlag.

114. Au, W.W.L., *The dolphin sonar: excellent capabilities in spite of some medicore properties*, in *High Frequency Ocean Acoustics*, M.B. Porter, M. Siderius, and W. Kuperman, Editors. 2004, AIP Conference Proceedings.

115. Au, W.W.L. and M.C. Hastings, *Principles of marine bioacoustics*. 2008, New York: Springer.

116. Leighton, T.G., D.C. Finfer, and P.R. White, *Bubble acoustics in shallow water: possible applications in Nature*, in *International conference on boundary influences in high frequency, shallow water acoustics*. 2005: Bath. p. 433-440.

117. Leighton, T.G., D.C. Finfer, and P.R. White, *Cavitation and cetacean.* Revista de Acustica, 2007. **38**(3-4): p. 37-74.

118. Finfer, D.C., P.R. White, G.H. Chua, and T.G. Leighton, *Review of the occurrence of multiple pulse echolocation clicks in recordings from small odontocetes.* IET Radar Sonar Navig., 2012. **6**(6): p. 545-555.

119. Leighton, T.G., D.C. Finfer, and P.R. White. *Bubble acoustics: What can we learn from cetaceans about contrast enhancement?* in *IEEE International Ultrasonics Symposium.* Rotterdam, 18-21 September 2005, p. 964-973.

120. Chou, Y.-L., *Statistical Analysis with Business and Economic Applications*. 1970, Holt, Rinehart and Winston: London. p. 61-67.

121. Parkhurst, D.F., *Arithmetic versus geometric means for environmental concentration data.* Environ Sci Techno, 1998. **32**(3): p. 92a-98a.

122. Kamminga, C. and H. Wiersma, *Investigations on cetacean sonar II. Acoustical similarities and differences in odontocete sonar signals.* Aquatic Mammals, 1981. **8**: p. 41-62.

123. Goodall, R.N.P., K.S. Norris, A.R. Galeazzi, J.A. Oporto, and I.S. Cameron, *On the Chilean dolphin, Cephalorhynchus eutropia (Gray, 1846).* Rep. Int. Whal. Commn. Spec. Issue, 1988. **9**: p. 197-257.

124. Evans, W.E., F.T. Aubrey, and H. Hackbarth, *High frequency pulse produced by free ranging Commerson's dolphin (Cephalorhynchus commersonii) compared to those of phoceonids.* Rep. Int. Whal. Commn. Spec. Issue, 1988. **9**: p. 173-181.

125. Dawson, S.M., *The high-frequency sounds of free-ranging Hector's dolphin, Cephalorhynchus hectori.* Rep. Int. Whal. Commn. Spec. Issue, 1988. **9**: p. 339-341.

126. Dawson, S.M. and C.W. Thorpe, *A quantitative analysis of the sounds of Hector's dolphin.* Ethology, 1990. **86**: p. 131-145.

127. Li, S., K. Wang, D. Wang, and T. Akamatsu, *Origin of the double- and multi-pulse structure of echolocation signals in Yangtze finless porpoise (Neophocaena phocaenoides asiaeorientialis).* J. Acoust. Soc. Am., 2005. **118**(6): p. 3934 - 3940.

128. Medwin, H., *Specular scattering of underwater sound from a wind-driven surface.* J. Acoust. Soc. Am., 1967. **41**(6): p. 1485-1495.

129. Tindle, C.T., G.B. Deane, and J.C. Preisig, *Reflection of underwater sound from surface waves.* J. Acoust. Soc. Am., 2009. **125**(1): p. 66-72.

130. DeRuiter, S.L., M. Hansen, H.N. Koopman, A.J. Westgate, P.L. Tyack, and P.T. Madsen, *Propagation of narrow-band-high-frequency clicks: measured and modeled transmission loss of porpoise-like clicks in porpoise habitats.* J. Acoust. Soc. Am., 2010. **127**(1): p. 560-567.

131. Kastelein, R.A., P. Bunskoek, M. Hagedoorn, W.W.L. Au, and D. Haan, *Audiogram of a harbor porpoise (Phocoena phocoena) measured with narrowband frequency-modulated signals.* J. Acoust. Soc. Am., 2002. **112**(1): p. 334-344.

132. Au, W.W.L. and P.E. Nachtigall, *Acoustics of echolocating dolphins and small whales.* Marine and Freshwater Behaviour and Physiology, 1997. **29**(1): p. 127 - 162.

133. Capus, C., Y. Pailhas, K. Brown, and D.M. Lane, *Bio-inspired wideband sonar signals based on observations of the bottlenose dolphin (Tursiops truncatus).* J. Acoust. Soc. Am., 2007. **121**(1): p. 594-604.

134. Gotz, T., R. Antunes, and S. Heinrich, *Echolocation clicks of free-ranging Chilean dolphins (Celphalorhynchus eutropia) (L).* J. Acoust. Soc. Am., 2010. **128**(2): p. 563-566.

135. Li, S., K. Wang, D. Wang, and T. Akamatsu, *Echolocation signals of the free-ranging Yangtze finless porpoise (Neophocaena phocaenoides asiaeorientialis).* J. Acoust. Soc. Am., 2005. **117**(5): p. 3288-3296.

136. Lammers, M.O. and L. Castellote, *The beluga whale produces two pulses to form its sonar signal.* Biology Letters, 2009. **5**: p. 297 - 301.

137. Houser, D.S., D.A. Helweg, and P.W. Moore, *Classification of dolphin echolocation clicks by energy and frequency distribution.* J. Acoust. Soc. Am., 1999. **106**(3): p. 1579-1585.

138. Houser, D.S., S.W. Martin, E.J. Bauer, M. Philips, T. Herrin, M. Cross, A. Vidal, and P.W. Moore, *Echolocation characteristics of free-swimming bottlenose dolphins during object detection and identification.* J. Acoust. Soc. Am., 2005. **117**(4): p. 2308-2317.

139. Evans, W.E., *Echolocation by marine delphinids and one species of fresh-water dolphin.* J. Acoust. Soc. Am., 1973. **54**: p. 191-199.

140. Au, W.W.L., P.W.B. Moore, and D.A. Pawloski, *Echolocation transmitting beam of the Atlantic bottlenose dolphin.* J. Acoust. Soc. Am., 1986. **80**: p. 688-694.

141. Au, W.W.L., R.W. Floyd, and J.E. Haun, *Propagation of Atlantic bottlenose dolphin echolocation signals.* J. Acoust. Soc. Am., 1978. **64**: p. 411-422.

142. Moore, P.W., L.A. Dankiewicz, and D.S. Houser, *Beamwidth control and angular target detection in an echolocating bottlenose dolphin (Tursiop truncatus).* J. Acoust. Soc. Am., 2008. **124**(5): p. 3324-3332.

143. Harley, H.E. and C.M. Delong, *Echoic object recognition by the bottlenose dolphin.* Comparative Cognition & Behaviour Reviews, 2008. **3**: p. 46-65.

144. Ibsen, S.D., W.W.L. Au, P.E. Nachtigall, C.M. Delong, and M. Bresse, *Changes in signal parameters over time for an echolocating Atlantic bottlenose dolphin performing the same target discrimination task.* J. Acoust. Soc. Am., 2007. **122**: p. 2446-2450.

145. Moore, P.W.B., H.L. Roitblat, R.H. Pnner, and P.E. Nachtigall, *Recognizing successive dolphin echoes with an Integrator Gateway Network.* Neural Networks, 1991. **4**: p. 701-709.

146. Au, W.W.L., R.W. Floyd, R.H. Penner, and A.E. Murchison, *Measurement of echolocation signals of the Atlantic bottlenose dolphin Tursiops truncatus Montagu, in open waters.* J. Acoust. Soc. Am., 1974. **56**: p. 1280-1290.

147. Au, W.W.L., R.H. Penner, and J. Kadane, *Acoustic behaviour of echolocating Atlantic bottlenose dolphins.* J. Acoust. Soc. Am., 1982. **71**: p. 1269-1275.

148. Thomas, J.A. and C.W. Turl, *Echolocation characteristics and range detection by a false killer whale (Pseudorca crassidens)*, in *Cetacean sensory systems: field and laboratory evidences.*, J.A. Thomas and R.A. Kastelein, Editors. 1990, Plenum Press: New York. p. 321-334.

149. Thomas, J.A., N. Chun, W.W.L. Au, and K. Pugh, *Underwater audiogram of a false killer whale (Pseudorca crassidens).* J. Acoust. Soc. Am., 1988. **84**: p. 936-940.

150. Au, W.W.L., J.L. Pawloski, P.E. Nachtigall, M. Blonz, and R. Gisner, *Echolocation signals and transmission beam pattern of a false killer whale (Pseudorca crassidens).* J. Acoust. Soc. Am., 1995. **98**: p. 51-59.

151. Turl, C.W., D.J. Skaar, and W.W.L. Au, *The echolocation ability of the beluga (Delphinapterus leucas) to detect targets in clutter.* J. Acoust. Soc. Am., 1991. **89**: p. 896-901.

152. Au, W.W.L., D.A. Carder, R.H. Penner, and B.L. Scronce, *Demonstration of adaption in beluga whale echolocation signals.* J. Acoust. Soc. Am., 1985. **77**: p. 726-730.

153. Ketten, D.R., S. Ridgway, J.J. Arruda, J.T. O'Malley, S.R. Cramer, and M. Dunn. *Mature mammal hearing loss: a natural experiment in presbycusis (abstract only).* in *18th Biennial Conference on the Biology of Marine Mammals*. Quebec, Canada, 12-16 October 2009.

154. Houser, D.S. and J.J. Finneran, *Variation in the hearing sensitivity of a dolphin population determined through the use of evoked potential audiometry.* J. Acoust. Soc. Am., 2006. **120**(6): p. 4090-4099.

155. Au, W.W.L. and R.H. Penner, *Target detection in noise by echolocating Atlantic bottlenose dolphins.* J. Acoust. Soc. Am., 1981. **70**: p. 687-693.

156. Roitblat, H.L., R.H. Penner, and P.E. Nachtigall, *Matching-to-sample by an echolocating dolphin (Tursiop truncatus).* Journal of Experimental Psychology: Animal Behaviour Processes, 1990. **16**: p. 85-95.

157. Au, W.W.L., P.W.B. Moore, and D.A. Pawloski, *Detection of complex echoes in noise by an echolocating dolphin.* J. Acoust. Soc. Am., 1988. **83**: p. 662-668.

158. Moore, P.W.B., R.W. Hall, W.A. Friedl, and P.E. Nachtigall, *The critical interval in dolphin echolocation: What is it?* J. Acoust. Soc. Am., 1984. **76**(314-317).

159. Herman, L.M. and W.R. Arbeit, *Frequency discrimination limens in the bottlenose dolphins: 1-70 Ks/c.* J. Auditory Research, 1972. **2**: p. 109-120.

160. Au, W.W.L., D.W. Lemonds, D.W. Vlachos, and P.E. Nachtigall, *Atlantic bottlenose dolphin (Tursiop truncatus) hearing thresholds for brief broadband signals.* J. Comp. Psychol., 2002. **116**: p. 151-157.

161. Delong, C.M., W.W.L. Au, D.W. Lemonds, H.E. Harley, and H.L. Roitblat, *Acoustic features of objects matched by an echolocating bottlenose dolphin.* J. Acoust. Soc. Am., 2006. **119**(3): p. 1867-1879.

162. Altes, R.A., L.A. Dankiewicz, P.W. Moore, and D.A. Helweg, *Multiecho processing by an echolocating dolphin.* J. Acoust. Soc. Am., 2003. **114**(2): p. 1155-1166.

163. Dankiewicz, L.A., D.A. Helweg, P.W. Moore, and J.M. Zafran, *Discrimination of amplitude-modulated synthetic echo trains by an echolocating bottlenose dolphin.* J. Acoust. Soc. Am., 2002. **112**(4): p. 1702- 1708.

164. Altes, R.A., *Synthetic aperture and image sharpening models for animal sonar*, in *Echolocation in Bats and Dolphins*, J.A. Thomas, C.F. Moss, and M. Vater, Editors. 2003, University of Chicago Press: Chicago. p. 492-500.

165. Herzing, D.L., ed. *Social and nonsocial uses of echolocation in free-ranging Stenella frontalis and Tursiops truncatus*. Echolocation in bats and dolphins, ed. J.A. Thomas, C.F. Moss, and M. Vater. 2004, The University of Chicago Press: Chicago.

166. Helweg, D.A., W.W.L. Au, H.L. Roitblat, and P.E. Nachtigall, *Acoustic basis for recognition of aspect-dependent three dimensional targets by an echololocating bottlenose dolphin.* J. Acoust. Soc. Am., 1996. **99**: p. 2409-2420.

167. Imaizumi, T., M. Furusawa, T. Akamatsu, and Y. Nishimori, *Measuring the target strength spectra of fish using dolphin-like short broadband sonar signals.* J. Acoust. Soc. Am., 2008. **124**(6): p. 3440-3449.

168. Martin, S.W., M. Phillips, E.J. Bauer, P.W. Moore, and D.S. Houser, *Instrumenting free-swimming dolphins echolocating in open water.* J. Acoust. Soc. Am., 2005. **117**(4): p. 2301-2307.

169. Herzing, D.L. and M.E. dos Santos, eds. *Functional aspects of echolocation in dolphins*. Echolocation in bats and dolphins, ed. J.A. Thomas, C.F. Moss, and M. Vater. 2004, The University of Chicago Press: Chicago.

170. Leighton, T.G., M.J.W. Pickworth, A.J. Walton, and P.P. Dendy, *Studies of the cavitation effects of clinical ultrasound by sonoluminescence: 1 correlation of sonoluminescence with the standing-wave pattern in an acoustic field produced by a therapeutic unit.* Physics in Medicine and Biology, 1988. **33**(11): p. 1239-1248.

171. Pickworth, M.J.W., P.P. Dendy, T.G. Leighton, and A.J. Walton, *Studies of the cavitional effects of clinical ultrasound by sonoluminescence: 2 Thresholds for sonoluminescence from a therapeutic ultrasound beam and the effect of temperature and duty cycle.* Physics in Medicine and Biology, 1988. **33**(11): p. 1249-1260.

172. Pickworth, M.J.W., P.P. Dendy, T.G. Leighton, E. Worpe, and R.C. Chivers, *Studies of the cavitional effects of clinical ultrasound by sonoluminescence: 3 Cavitation from pulses a few microseconds in length.* Physics in Medicine and Biology, 1989. **34**(9): p. 1139-1151.

173. Leighton, T.G., H.A. Dumbrell, G.J. Heald, and P.R. White. *The possibility and exploitation of nonlinear effects in the near-surface oceanic bubble layer*. in *Proceedings of the Seventh European Conference on Underwater Acoustics*. Delft, Holland, 5-8 July 2004, p. 205-210.

174. Thomas, J.A., C.F. Moss, and M. Vater, *Echolocation in bats and dolphins*. 2004, Chicago: The University of Chicago Press.

175. Chua, G.H., P.R. White, and T.G. Leighton, *Use of clicks resembling those of the Atlantic bottlenose dolphin (Tursiops truncatus) to improve target discrimination in bubbly water with Biased Pulse Summation Sonar (BiaPSS).* IET Radar Sonar Navig., 2012. **6**(6): p. 510-515.

176. Leighton, T.G., G.H. Chua, and P.R. White, *Do dolphins benefit from nonlinear mathematics when processing their sonar returns?* Proc. R. Soc. A, 2012, doi: 10.1098/rspa.2012.0247.

177. Au, W.W.L., K.J. Benoit-Bird, and R.A. Kastelein, *Modeling the detection range of fish by echolocating bottlenose dolphins and harbour porpoises.* J. Acoust. Soc. Am., 2007. **121**: p. 3954-3962.

178. Leighton, T.G., P.R. White, and D.C. Finfer. *Hypotheses regarding exploitation of bubble acoustics by cetaceans*. in *Proceedings of 9th European Conf. on Underwater Acoustics (ECUA2008)*. Paris, France, 29 June - 4 July 2008, p. 77-82.